

MIT OpenCourseWare
<http://ocw.mit.edu>

16.89J / ESD.352J Space Systems Engineering
Spring 2007

For information about citing these materials or our Terms of Use, visit: <http://ocw.mit.edu/terms>.

ASTRO

Architecting the Search for Terrestrial planets and Related Origins

Document No:	ASTRO-002
Revision:	--
Title:	TPF MISSION ARCHITECTURE ANALYSIS DOCUMENT
Date:	May 17, 1999
Document Manager:	Andrew Curtis
Authors:	Andrew Curtis, Olivier de Weck, Emilio Frazzoli, André Girerd, Troy Hacker, Cyrus Jilla, Edmund Kong, Brian Makins, Sangwoo Pak

RELEASE HISTORY		
Revision	Date	Description
--	May 17, 1999	Initial Release

Course 16.89 -- Space Systems Engineering
Department of Aeronautics and Astronautics
Massachusetts Institute of Technology

This page intentionally left blank.

Abstract

A fundamental activity during the conceptual design phase for a large project is the comparison of competing system architectures. The ASTRO team has developed a process and a software tool, based on a quantitative systems engineering methodology, to conduct trade studies during the conceptual design phase of the Terrestrial Planet Finder (TPF) mission, which is scheduled to launch in 2010. The TPF mission analysis software (TMAS) package consists of 6 macro-modules that model the physics and processes that distinguish between competing system architectures, including structurally connected (truss) and separated spacecraft (formation flying) concepts. Ultimately, each design is evaluated by a performance assessment module (GINA), which computes the capability, performance, and cost of each architecture. The cost per image metric is the primary metric used to trade architectures against each other. This metric represents the ratio of the total lifecycle cost of the mission divided by the number of useful "images" returned, where "images" represent the total number of surveys and spectroscopic observations accomplished during the mission lifetime. Limited resources, in the form of personnel and time, determined the level of fidelity incorporated into the model. The team focused on developing models for the processes with the greatest likelihood to contribute to the differentiation between architectures. After using benchmark spacecraft configurations, previously developed by industry teams, to validate the TMAS package, the team conducted one dimensional trade studies from a baseline spacecraft configuration to evaluate general trends.

It is premature to propose a specific spacecraft architecture for the TPF mission based on the current results -- further exploration of the trade space is required. Furthermore, a critical review of the assumptions and the modeling approach in each software module is necessary to validate the process beyond the benchmark cases. Nevertheless, the TMAS is a comprehensive, modular, expandable, and robust tool for trading TPF mission architectures using unified and quantitative metrics.

This page intentionally left blank.

Acknowledgements

The team would like to thank and acknowledge the following people for their time and assistance in realizing this project:

Professor David Miller, Professor Walter Hollister and Dr. Joyce Warmkessel for their advice and guidance throughout the project;

Dr. Raymond Sedwick for giving us a lecture on propulsion and orbits, and also his continuous support and guidance throughout the project;

Dr. Christian Lindensmith, Jet Propulsion Laboratory, for taking the time to ensure that we got the required information;

Professor Charles Biechmann, Caltech, for taking the time to answer our questions pertaining to the signal to noise module;

Mr. Dave Gross, Able Engineering, for answering our questions on truss designs;

Col. Pete Young for giving us a lecture on launch vehicle operations;

Mr. Maurice Martin, Air Force Research Laboratory, for giving us a lecture on systems engineering in the Techsat21 program;

Alvar Saenz Otero, for his exceptional network administration support; and

Dr. Graeme Shaw, Orbital Sciences Corporation, for taking the time to review our project at CDR.

This page intentionally left blank.

Contents

ABSTRACT.....	3
ACKNOWLEDGEMENTS.....	5
CONTENTS.....	7
FIGURES.....	9
TABLES	12
1.0 EXECUTIVE SUMMARY.....	13
2.0 PROJECT OVERVIEW	15
3.0 THE TERRESTRIAL PLANET FINDER MISSION	17
3.1 MISSION DESCRIPTION.....	17
3.2 TPF SCIENCE	18
3.3 PREVIOUS WORK AND RESOURCES	20
4.0 TPF MISSION REQUIREMENTS.....	23
4.1 TPF MISSION SCIENCE REQUIREMENTS.....	23
4.2 TPF MISSION SYSTEM REQUIREMENTS.....	23
4.3 TPF MISSION DESIGN REQUIREMENTS	23
4.4 ADDITIONAL TPF MISSION REQUIREMENTS	24
4.5 REQUIREMENTS DOCUMENT ELECTRONIC FORMAT.....	24
4.6 QUALITY FUNCTION DEPLOYMENT (QFD).....	24
5.0 ARCHITECTURAL DESIGN OPTIONS	27
5.1 INFRARED NULLING INTERFEROMETER TECHNIQUE	27
5.2 SPACECRAFT OPERATIONS SCENARIO.....	28
5.2.1 <i>Mission Timeline</i>	28
5.2.2 <i>Science Operations Functional Flow</i>	30
5.2.3 <i>Spacecraft Science Operations Functional Flow</i>	31
5.3 STRUCTURALLY CONNECTED INTERFEROMETER	32
5.4 SEPARATED SPACECRAFT INTERFEROMETER.....	33
5.5 TETHERED SPACECRAFT INTERFEROMETER	34
5.6 HYBRID INTERFEROMETER.....	35
5.7 CELESTIAL BODY INTERFEROMETER	35
6.0 ARCHITECTURAL DESIGN APPROACH.....	37
6.1 IDENTIFY ARCHITECTURE METRICS.....	37
6.2 DEFINE THE ARCHITECTURE TRADE SPACE.....	39
6.3 INITIAL DOWNSELECT TO TWO SPACECRAFT ARCHITECTURES	41
6.4 DETERMINE MEANINGFUL TPF MODEL COMPONENTS (MACRO-MODULES)	43
6.5 ANALYSIS SOFTWARE DEVELOPMENT PROCESS	44
6.6 MODULE DEVELOPMENT STEPS.....	45
6.7 MODULE INTEGRATION.....	46
7.0 ARCHITECTURAL DESIGN EVALUATION MODULES	49

7.1	ENVIRONMENT MACRO-MODULE.....	49
7.2	APERTURE CONFIGURATION MACRO-MODULE	53
7.3	SPACECRAFT MACRO- MODULE.....	60
7.3.1	<i>Payload Module</i>	62
7.3.2	<i>Communications Module</i>	66
7.3.3	<i>Power Module</i>	70
7.3.4	<i>Propulsion Module</i>	75
7.3.5	<i>Thermal Module</i>	86
7.4	DYNAMICS, OPTICS CONTROLS, AND STRUCTURES (DOCS) MACRO-MODULE	88
7.4.1	<i>Structural Design Module</i>	89
7.4.2	<i>Optics Control Module</i>	94
7.4.3	<i>Attitude Determination and Control Module</i>	96
7.4.4	<i>Integration Module</i>	101
7.4.5	<i>Disturbance Analysis Module</i>	103
7.4.6	<i>DOCS Macro-Module Trades</i>	107
7.5	OPERATIONS MACRO-MODULE	109
7.5.1	<i>Orbit Module</i>	109
7.5.2	<i>Launch Module</i>	113
7.5.3	<i>Operations Module</i>	115
7.6	GINA MACRO-MODULE.....	125
7.6.1	<i>Capability Module</i>	126
7.6.2	<i>Performance Module</i>	133
7.6.3	<i>Cost Module</i>	138
7.6.4	<i>Cost per Function Module</i>	139
7.6.5	<i>Adaptability Module</i>	140
8.0	ARCHITECTURAL DESIGN EVALUATION RESULTS	143
8.1	BENCHMARK CONFIGURATION RESULTS	143
8.2	TRADE STUDY RESULTS.....	147
8.2.1	<i>Orbit Trade Study</i>	148
8.2.2	<i>Number of Apertures Trade Study</i>	151
8.2.3	<i>Interferometer Type Trade Study</i>	158
8.2.4	<i>Aperture Diameter Trade Study</i>	161
8.2.5	<i>Summary of Trade Studies</i>	163
8.2.6	<i>Combined Case Results</i>	164
8.2.7	<i>Operational Trade Results</i>	165
9.0	CONCLUSIONS.....	167
9.1	TPF ARCHITECTURE.....	167
9.2	TMAS	167
9.3	LESSONS LEARNED	168
9.4	RECOMMENDATIONS AND FUTURE WORK.....	168
10.0	ACRONYMS	171
11.0	REFERENCES	173
12.0	AUTHORS.....	175
	APPENDIX A. ELECTRONIC REQUIREMENTS DOCUMENT	A1
	APPENDIX B. RESULTS OF THE APERTURE CONFIGURATION MODULE	B1
	APPENDIX C. TMAS N² DIAGRAM.....	C1

Figures

FIGURE 1. HERTZSPRUNG-RUSSELL DIAGRAM FOR NEARBY STARS.....	19
FIGURE 2. DISTANCE TO PARENT STAR AND POSITION OF PLANETS	20
FIGURE 3. QUALITY FUNCTION DEPLOYMENT FOR THE TPF MISSION.....	25
FIGURE 4. TPF MISSION OVERVIEW TIMELINE.....	29
FIGURE 5. TPF SCIENCE OPERATIONS FUNCTIONAL FLOW.....	30
FIGURE 6. TPF SPACECRAFT SCIENCE OPERATIONS FUNCTIONAL FLOW	31
FIGURE 7. STRUCTURALLY CONNECTED INTERFEROMETER EXAMPLE	32
FIGURE 8. SEPARATED SPACECRAFT INTERFEROMETER EXAMPLE.....	33
FIGURE 9. TETHERED SPACECRAFT INTERFEROMETER EXAMPLE.....	34
FIGURE 10. HYBRID INTERFEROMETER EXAMPLE	35
FIGURE 11. CELESTIAL BODY INTERFEROMETER EXAMPLE.....	36
FIGURE 12. INITIAL ARCHITECTURE DOWNSELECT MATRIX.....	41
FIGURE 13. MODEL COMPONENT IDENTIFICATION MATRIX.....	44
FIGURE 14. TMASS N ² DIAGRAM.....	47
FIGURE 15. SOLAR FLUX VS. SOLAR DISTANCE	50
FIGURE 16. LOCAL ZODIACAL INTENSITY VS. SOLAR DISTANCE.....	51
FIGURE 17. INTERPLANETARY METEROID FLUX AT 1 AU VS. METEROID DIAMETER.....	52
FIGURE 18. OASES TRANSMISSIVITY FUNCTION ALONG $\theta = 0$	57
FIGURE 19. SIMULATED ANNEALING FLOW CHART (KONG, 1998).....	59
FIGURE 20. SPACECRAFT MACRO-MODULE DATA FLOW	61
FIGURE 21. COMMUNICATIONS MODULE INPUTS AND OUTPUTS.....	67
FIGURE 22. INITIAL POWER ESTIMATE DETERMINATION FOR 1 AU SEPARATION CASE	69
FIGURE 23. TRADESPACE FOR ANTENNA MASS, DATA RATE, AND DISTANCE.....	70
FIGURE 24. SOLAR ARRAY AND RTG POWER SYSTEM MASSES.....	75
FIGURE 25. PROPULSION MODULE DATA FLOW.....	76
FIGURE 26. THRUST TIME VS. MOMENT OF INERTIA.....	78
FIGURE 27. THRUST LEVEL REQUIREMENTS FOR AN SSI MISSION	81
FIGURE 28. SIMPLIFIED ION THRUSTER DIAGRAM.....	82
FIGURE 29. PROPULSION SYSTEM MASS FOR A GIVEN INTEGRATION TIME	86
FIGURE 30. THERMAL MODULE INPUTS AND OUTPUTS	87
FIGURE 31. DOCS MACRO-MODULE FLOW DIAGRAM.....	88
FIGURE 32. DESIGN OF HUB BASE PLATE	89
FIGURE 33. LOOKUP TABLES FOR TRUSS PROPERTIES	90
FIGURE 34. GRAPHIC REPRESENTATION OF AN ASSEMBLED FINITE ELEMENT MODEL.....	91
FIGURE 35. OPTICS MODELING DIAGRAM	95
FIGURE 36. ITHACO E-WHEEL	99
FIGURE 37. GENERALIZED PLANT	100
FIGURE 38. BLOCK DIAGRAM OF THE TPF INTEGRATED DYNAMICS MODEL	101
FIGURE 39. TRANSFER FUNCTION TO ILLUSTRATE THE EFFECTS OF OPEN LOOP, ADCS, AND OPTICAL CONTROL ON OPD DISTURBANCES	103

FIGURE 40. ASSUMED REACTION WHEEL DISTURBANCE PSD'S FOR THE TPF MISSION	104
FIGURE 41. PERFORMANCE POWER SPECTRAL DENSITY FUNCTION FOR OPD _i	105
FIGURE 42. NORMALIZED CUMULATIVE AREA PLOT FOR OPD1-2 (TPF BASELINE CONFIGURATION)	105
FIGURE 43. CRITICAL MODES FOR OPD1-2 OF THE TPF BASELINE DESIGN	106
FIGURE 44. MODE SHAPE REPRESENTATIONS FOR THREE CRITICAL SYSTEM MODES	106
FIGURE 45. DEMONSTRATION OF "WASHOUT" EFFECT DUE TO RWA NOISE (RIGHT SIDE).....	107
FIGURE 46. EFFECT OF OPTICAL CONTROLLER BANDWIDTH ON THE TRANSMISSIVITY FUNCTION.....	108
FIGURE 47. HILL'S TRANSFER TO L2 ORBIT	110
FIGURE 48. HOHMANN'S TRANSFER.....	112
FIGURE 49. TOTAL DELTA V AND FLIGHT TIME VS. ORBITAL RADIUS.....	112
FIGURE 50. LAUNCH VEHICLE MODULE INPUTS AND OUTPUTS	114
FIGURE 51. OPERATIONS MODULE INPUTS AND OUTPUTS	116
FIGURE 52. DETERMINATION OF LABOR COSTS	121
FIGURE 53. MISSION INEFFICIENCY FROM A SINGLE ANOMALY	123
FIGURE 54. OPERATIONAL DIFFICULTY TRADESPACE	125
FIGURE 55. MISSION INEFFICIENCY TRADESPACE	125
FIGURE 56. OVERVIEW OF THE GINA MACRO-MODULE	126
FIGURE 57. FAULT TREE FOR AN EIGHT COLLECTOR TPF ARCHITECTURE.....	134
FIGURE 58. MARKOV MODEL STATE DIAGRAM FOR THE 8 COLLECTOR TPF ARCHITECTURE	135
FIGURE 59. MARKOV MODEL RESULTS FOR THE EIGHT COLLECTOR TPF ARCHITECTURE.....	136
FIGURE 60. BALL DESIGN FOR TPF.....	143
FIGURE 61. TRW DESIGN FOR TPF.....	145
FIGURE 62. IMAGE DISTRIBUTION VS. ORBIT	148
FIGURE 63. COST DISTRIBUTION VS. ORBIT.....	149
FIGURE 64. TOTAL MASS DISTRIBUTION VS. ORBIT	150
FIGURE 65. TOTAL MASS VS. ORBIT	150
FIGURE 66. COST PER IMAGE VS. ORBIT.....	151
FIGURE 67. SCI IMAGE DISTRIBUTION	152
FIGURE 68. SCI TOTAL MASS DISTRIBUTION	153
FIGURE 69. SCI COST DISTRIBUTION	153
FIGURE 70. SSI IMAGE DISTRIBUTION.....	154
FIGURE 71. SSI TOTAL MASS DISTRIBUTION.....	155
FIGURE 72. SSI COST DISTRIBUTION.....	155
FIGURE 73. TOTAL MASS DISTRIBUTION	156
FIGURE 74. COST DISTRIBUTION.....	157
FIGURE 75. COST PER IMAGE.....	157
FIGURE 76. NUMBER OF IMAGES	158
FIGURE 77. TOTAL MASS (KG)	159
FIGURE 78. COST DISTRIBUTION (\$M)	160
FIGURE 79. COST PER IMAGE (\$M/IMAGE)	160
FIGURE 80. COST VS. APERTURE SIZE (SCI)	162
FIGURE 81. COST VS. APERTURE SIZE (SSI)	162
FIGURE 82. CREW SIZE VS TIME (YEARS)	165

FIGURE 83. OPERATIONS COST BREAKDOWN 166
FIGURE 84. MISSION INEFFICIENCY VS. ORBIT..... 166

Tables

TABLE 1. RANGE OF INPUTS ACCEPTED BY THE APERTURE CONFIGURATION MODULE	54
TABLE 2. OUTPUT MATRIX FROM APERTURE CONFIGURATION MODULE.....	55
TABLE 3. PROPERTIES OF THE C&DH AND ADCS SUBSYSTEMS	63
TABLE 4. PROPERTIES OF THE C&DH AND ADCS SUBSYSTEMS	63
TABLE 5. MASS AND POWER DEMANDS FOR THE PAYLOAD COMPONENTS.....	65
TABLE 6. SOLAR ARRAY PROPERTIES.....	72
TABLE 7. RTG PROPERTIES	73
TABLE 8. BATTERY PROPERTIES	74
TABLE 9. MOMENTUM DUMPING INFORMATION	79
TABLE 10. ATTITUDE CONTROL THRUSTER TRADE SPACE.....	79
TABLE 11. ELECTRONIC PROPULSION SUMMARY [SUTTON]	81
TABLE 12. BASELINE MISSION SUMMARY	83
TABLE 13. TPF SPACECRAFT THERMAL REQUIREMENTS	87
TABLE 14. LAUNCH VEHICLE SELECTION.....	115
TABLE 15. TRANSITION TIMES FOR GENERIC SINGLE SPACECRAFT.....	118
TABLE 16. BASIC AUTOMATION LEVEL FOR EVENTS	119
TABLE 17. AVERAGE SALARIES FOR OPERATIONS PERSONNEL.....	121
TABLE 18. AVERAGE FAILURE RECOVERY TIME PER OPERATIONS FUNCTION (DATA FROM [SCHWARZ, 1997])	124
TABLE 19. DETECTION REQUIREMENTS FOR THE DIFFERENT SPECTROSCOPY MODES.....	128
TABLE 20. PROPERTIES OF THE ZODIACAL CLOUD (BEICHMAN ET. AL., 1999).....	130
TABLE 21. SIGNAL AND NOISE SOURCE COMPONENTS FOR THE OASES INTERFEROMETER.....	131
TABLE 22. IMAGING TIME COMPONENTS.....	132
TABLE 23. SURVEYING IMAGING RATES (SURVEYS PER MONTH) FOR EACH OPERATIONAL STATE OF A 6 COLLECTOR TPF ARCHITECTURE	132
TABLE 24. TPF SCIENTIFIC UTILIZATION PLAN (BEICHMAN ET. AL. 1999)	137
TABLE 25. TPF DAILY MISSION PROFILE (CUMULATIVE FROM MISSION START).....	137
TABLE 26. LAUNCH VEHICLE COSTS.....	139
TABLE 27. BALL SCI BENCHMARK.....	144
TABLE 28. TRW SCI BENCHMARK.....	145
TABLE 29. TRW SSI BENCHMARK	146
TABLE 30. LOCKHEED MARTIN SCI BENCHMARK	146
TABLE 31. BASELINE CASES	147
TABLE 32. RANGE OVER WHICH EACH PARAMETER VARIES	148
TABLE 33. RESULTS FOR COMBINED CASES.....	164
TABLE 34. BEST COST PER IMAGE FOR SAMPLE CASES	167

1.0 Executive Summary

As part of a series of NASA's Origins missions to answer fundamental questions regarding the origin of life, the Terrestrial Planet Finder (TPF) is the first mission that will directly detect the existence of Earth-like planets in our stellar neighborhood. To do so, TPF will need to suppress the light from the parent star by a factor of one million while maintaining good transmissivity in the habitable zone between 0.5 and 3 AU. The existence of these planets is confirmed through the detection of various key compounds in the mid-infrared spectrum. These key compounds will serve as "Markers for life" in this TPF mission.

The level of star light suppression required can be achieved through the use of a Bracewell nulling interferometer. Such an instrument is very similar to conventional interferometers except for the introduction of a 180° phase shift to create a required null at the center of the interferometer's transmissivity. In either case, the success of an interferometer depends on the ability to place accurately the apertures in their respective locations. The precise placement of the apertures can be achieved through several proposed interferometer types such as a structurally connected interferometer (SCI), a separated spacecraft interferometer (SSI), a tethered interferometer, a hybrid architecture, and a celestial body interferometer. The question then, is which of these interferometers would be best for the TPF?

To best answer the proposed question, the ASTRO team developed a process, based on a quantitative systems engineering methodology, to conduct trade studies during the conceptual design phase of TPF. However, a qualitative analysis was performed first to determine the physics and competing factors that would distinguish the different architectures. The analysis led to the development of the six macro-modules, which model the physics and processes for two system architectures, namely the structurally connected and formation flying concepts. These six macro-modules form the TPF mission analysis software (TMAS) package. Ultimately, each design architecture, which is distinguished by its operating orbit, the number of apertures, the size of its apertures, and the type of interferometer, is evaluated by the performance assessment module (GINA), which computes the capability, integrity, and life cycle cost. In this study, the cost per image metric is the primary metric used to trade the different architectures. This metric represents the ratio of the total lifecycle cost of the mission divided by the number of useful "images" returned, where "images" represent the expected number of surveys and spectroscopy observations accomplished during the mission lifetime.

In order to validate the TMAS package, several benchmarking cases were performed and compared against configurations previously developed by industry teams. In these benchmarking cases, only mass figures for the different configurations were compared. Even though the results obtained were not exactly the same, comparisons between these configurations indicated that the TMAS package is accurate within an order of magnitude.

The level of detail was chosen based on the limited resources of this class project and the necessity to accurately predict relevant differences between architectures. Initial trade studies were conducted, where one parameter at a time was varied from a nominal design

case involving 4 apertures in a linear-symmetric array with 2m apertures. From the results of the trades, very interesting relationships and trends were observed. As an example it was found that the optimal cost performance relationship seems to be achieved at a heliocentric altitude around 2.5 AU. At lower altitudes the local zodiacal dust cloud leads to increased integration times for a given SNR. At higher altitudes, the launch costs exceed the benefits gained from the reduced local noise environment. Another interesting observation was that the number of images generally increases as more apertures are added to the architecture. In the SSI case, however, an exceedingly large number of apertures (> 10) reduces the number of images produced due to the larger mission inefficiency of a complex separated spacecraft architecture.

To formally conclude the trade studies, two more case studies were performed. The different one-dimensional parameters that led to a local minima for cost per image were combined for both the SSI and SCI. The resultant architectures gave the lowest cost per image metric among all the cases that have been performed. Unfortunately, these architectures were found to be more massive and expansive. Their lower cost per image metric was due primarily to the higher number of expected images attainable.

It is premature to propose a particular architecture for TPF based on the current results since further exploration of the trade space should be conducted first. Furthermore, a critical review of the assumptions and the modeling approach in each software module is necessary to validate the process beyond the benchmark cases. Nevertheless, this study has succeeded in producing a useful and robust tool for trading TPF mission architectures based on unified and quantitative metrics.

The team learned a number of lessons throughout the course. In the trade analysis phase, the team learned a great deal about the systems engineering process ranging from initial definition of the system design space to down-selecting the best potential options. In the preliminary design phase, balancing between the complexity of the analysis model and the limited time available became an important issue. Finally, in the critical design phase, the proper maintenance of an Interface Control Document enabled the integration of the different modules into one functional software package. In general, team members gained the experience of participating in an integrated design team, including design and programming tasks, sharing responsibilities for making presentations, and creating engineering documentation.

2.0 Project Overview

The objectives of the TPF mission architecture analysis are identified in the following ASTRO mission statement:

“To conduct a trade study of mission architectures for NASA’s Terrestrial Planet Finder mission using a quantitative systems engineering methodology. One fundamental objective will be to develop a methodology for the comparison of the design architectures spanning from structurally connected to separated spacecraft interferometers.”

The goal is not to come up with a single point design that would satisfy the TPF mission requirements, but to develop a technique to fairly evaluate the relative merits of intrinsically different design concepts.

Consideration of a single point design to satisfy the mission requirements has been performed previously by different industrial teams such as Ball, TRW, and Lockheed Martin. Thus far, only a structurally connected system has been thoroughly considered and proposed. Comparisons between a structurally connected (SCI) and a separated spacecraft interferometer (SSI) have been performed at the MIT Space Systems Laboratory by Surka and Stephenson. Since the scope they considered was rather limited, it is not possible to conclude from their studies that one spacecraft architecture should be chosen over the other, though the more recent study by Stephenson tends to favor the SSI design for longer interferometer baselines.

The level of detail in modeling the physics, costs, operations, etc, in the TPF Mission Analysis Software (TMAS) was determined to permit meaningful comparisons of the relative merits of competing architectures. The team members do not claim that the level of design detail presented in this project is highly accurate in an absolute sense or that the current methodology provides sufficient information to begin the fabrication phase for a future TPF mission. However, the methodology is useful for understanding the fundamental relationships and sensitivities between TPF mission design parameters.

This page intentionally left blank.

3.0 The Terrestrial Planet Finder Mission

3.1 Mission Description

The National Aeronautics and Space Administration (NASA) and the scientific community have recently initiated the Origins Program to roadmap future space astronomy and astrophysics for the next 20 years. The Origins Program will develop the technologies that will enable putting in space a succession of sophisticated telescopes, each building on scientific and technological achievements of the prior missions. The purpose of the Origins Program is to help answer fundamental questions regarding the origins of life and the universe such as:

- How did the first galaxies form?
- How do stars and planetary systems form?
- Are there any planets outside our solar system that are capable of sustaining life?
- How did life originate on Earth?
- Is there life (however primitive or evolved) outside our solar system?

Augmented with ground-based observatories and research and analysis, NASA's Origins program will give our civilization a better sense of the universe around us and our place in it.

The Terrestrial Planet Finder (TPF) mission is one in a series of missions designed to provide answers to the questions regarding extra-solar planets. It will leverage new technologies and techniques demonstrated on earlier missions in the road map such as the Space Infrared Telescope Facility (SIRTF), the Space Interferometry Mission (SIM), the Next Generation Space Telescope (NGST), and Space Technology 3 (ST3 – formerly Deep Space 3, DS3). SIRTF will demonstrate improvements in infrared detection technology. SIM will demonstrate hardware and software packages for a space-based interferometer as well as star-light nulling, precision pathlength control, and general interferometer operations. NGST will demonstrate technologies for cryogenic actuators and for precision wavelength control. TPF will serve as a precursor for yet another series of exploration missions including the Planet Imager (PI) mission.

The primary objective of the TPF mission is to detect and to characterize Earth-like planets orbiting nearby stars. This objective requires the capability to detect radiation emitted from extra-solar planets and to be able to discriminate this radiation from that of the parent star. The proposed technique for performing this function is to use a spaceborne interferometer. By combining the high sensitivity of space telescopes with the sharply detailed pictures from a nulling interferometer, TPF will be able to reduce the glare of parent stars by a factor of more than one hundred-thousand to see planetary systems as far away as 50 light years.

In addition to measuring the size, temperature, and location of planets as small as the Earth in the habitable zones of distant solar systems, TPF will be used to gather spectroscopic data that will allow atmospheric chemists and biologists to study the concentrations of gasses like

carbon dioxide, water vapor, ozone and methane to determine whether a planet someday could, or even now does, support life.

As well as studying planets around nearby, mature stars like the sun, TPF will be used to advance our understanding of how planets and their parent stars form. The disks of forming stars are a few astronomical units (AU) across. TPF will image planetary accretion disks with a resolution of a few tenths of an AU to investigate how gaseous (Jupiter-like) and rocky (Earth-like) planets form out of disk material. By studying the heat glow from dust, ice, and gasses such as hydrogen and carbon monoxide, TPF will investigate whether, as theory predicts, rocky planets form in warmer regions and gaseous planets in colder regions while a solar system is being born.

3.2 TPF Science

The science requirements of the astrophysics community and the properties of the parent stars are crucial in designing the TPF and drive the engineering requirements for the mission. Specifically TPF will be designed for direct planet detection and for spectroscopy in the infrared regime. The three single most critical factors that drive the scientific performance are:

- Suppression of parent star light (nulling) by a factor of 10^6 over the entire diameter of the star,
- Retention of maximum transmissivity in the habitable zone (0.5 to 3 AU) around a star,
- Maintenance of the spacecraft optics and detectors at adequately cold temperatures to maximize the SNR in the 7-17 μ m range.

The properties of a particular star in the target star population are very important, since they are directly related to the engineering requirements that must be met to design viable TPF architectures and to conduct trade studies. Specifically, the four properties of the parent star that will be investigated are:

- Absolute stellar magnitude [M], which drives the depth of null needed,
- Average surface temperature [K], which defines the Planck spectrum and drives observation wavelength selection,
- Distance from the observer [pc], which drives angular resolution and baseline length,
- Absolute star diameter [km], which drives the width of null.

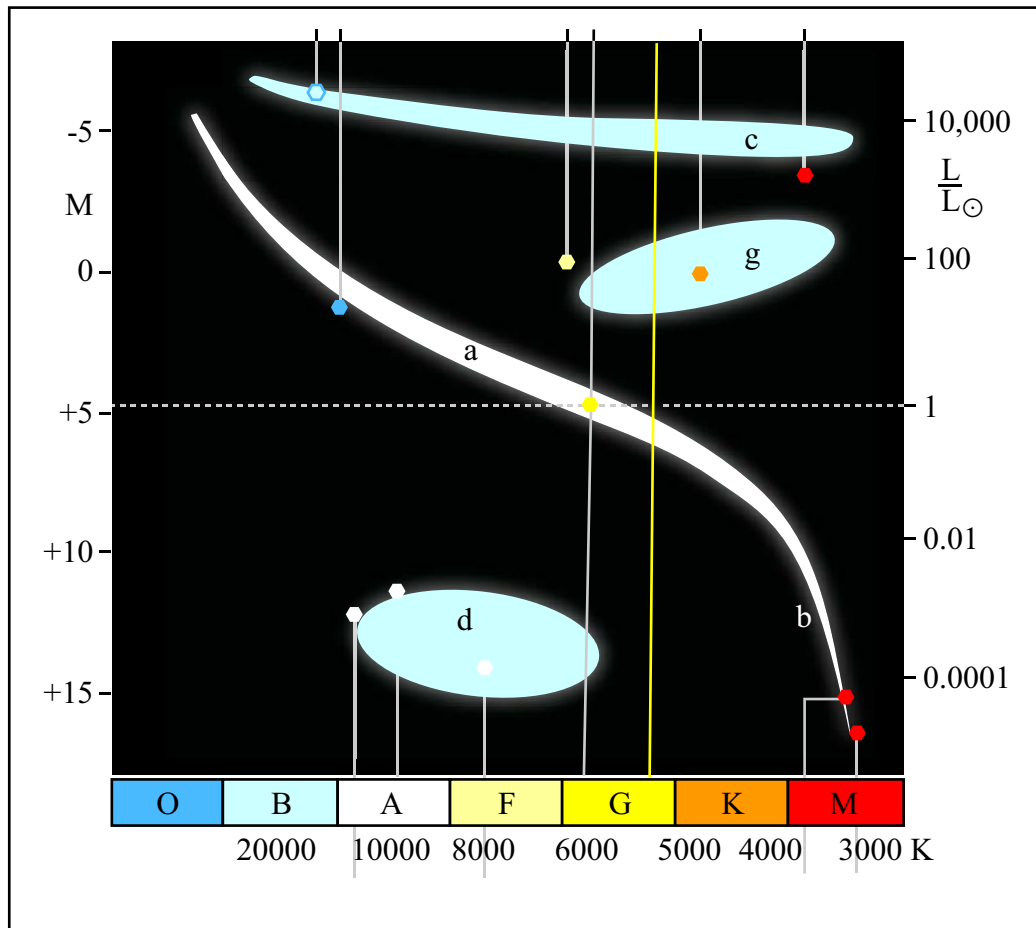


Image by MIT OpenCourseWare.

Figure 1. Hertzsprung-Russell Diagram for Nearby Stars

Figure 1 shows the so-called Hertzsprung-Russell Diagram. This diagram is useful because it identifies a correlation between the evolutionary state of nearby stars and a combination of their surface temperature and their luminosity. The temperature of a star, in degrees Kelvin, decreasing from left to right, is represented on the X-axis. The stars are grouped into spectral classes according to their temperature: O, B, A, F, G, K, and M. G class stars are referred to as being “sunlike”. The luminosity metric (L/L_{\odot}) on the right side is the ratio of the luminosity of a star to the luminosity of the Sun. The scale on the left represents the luminosity as the absolute stellar magnitude M (not to be confused with relative magnitude that amateur astronomers care about). Astrophysical observations show that stars are not scattered randomly in the HR-diagram, but that they are grouped in certain clusters or “sequences”. The largest number of stars can be found in the “main sequence” in the middle of the diagram (a); the Sun is thus part of the main sequence of stars. There is also a considerable number of stars in the “Giants” branch (g) and a smaller number of stars in the “Supergiants” branch (c). The number of “White Dwarfs” (d) and “Red Dwarfs” (b) that can be observed is limited due to their relatively small luminosity, even though red dwarfs are believed to comprise the majority of the total stellar population in the galaxy. TPF will be searching for “earthlike” planets around “sunlike” stars. This limits the surface temperatures of the observed parent stars to be in the 4000-8000 K range and excludes Supergiants and Dwarfs as candidates.

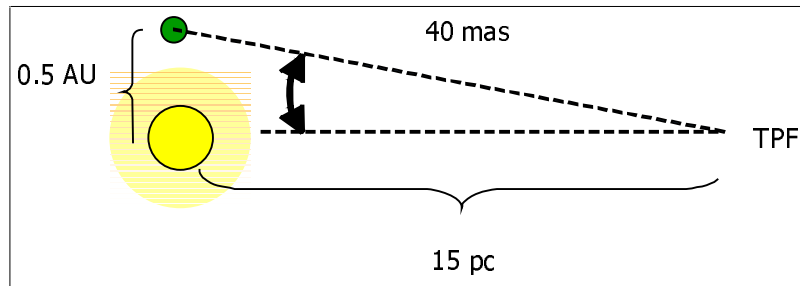


Figure 2. Distance to Parent Star and Position of Planets

The maximum distance to a target star drives the angular resolution that will be necessary to isolate a planet. The maximum distance has been set at 15 parsecs (about 50 light years) for the TPF mission to allow for a sufficiently large number of candidate stars without making the technical requirements overly difficult. This results in a required angular resolution of 40 milliarcseconds to detect a planet as close to the star as 0.5 AU (see Figure 2). After the additional exclusion of binary star systems, there are approximately 150 candidate stars that meet both the temperature and distance requirements identified above.

3.3 Previous Work and Resources

Between 1997 and 1998, three contracts were awarded to three industry teams to design a system that would meet the TPF objectives. All three teams developed proposed conceptual designs based on the structurally connected interferometer (SCI) spacecraft architecture. The other spacecraft architectures, such as the separated spacecraft interferometer (SSI) were either considered to be too technologically challenging or were not considered at all.

Comparisons between a SCI concept and a SSI concept for TPF were studied at the MIT Space Systems Laboratory by Surka (1996) and Stephenson (1998). Surka reported that the SCI concept is generally preferable to the SSI unless spacecraft separations of greater than hundreds of meters are required. In contrast, the report by Stephenson concludes that the cross-over point where the SSI concept is “better” occurs for space interferometer baselines of less than one hundred meters.

The JPL maintained TPF website provides a broad overview of the TPF program that includes a statement of the mission and goals of the TPF as well as a description of the underlying science and technology concepts involved in the design and the operation of the system. There are sections that discuss the detection of Earth-like planets, interferometer design issues, precursor missions, and possibilities for astrophysical imaging. Also, there is a library on this website that is periodically updated with new publications that are relevant to TPF, including topics such as infrared surveying of starburst galaxies, investigations of planetary formation, and zodiacal dust gaps caused by the presence of planets.

In addition to the TPF website, JPL maintains a TPF book available in PDF format on the web that provides a more technical and detailed description of the topics that are pertinent to the TPF mission. This book contains chapters that discuss the important issues behind the

design of TPF, including interferometer properties, star-light nulling, target stars, and precursor missions that will provide TPF with the necessary technology to detect and to characterize planets around nearby stars.

This page intentionally left blank.

4.0 TPF Mission Requirements

The first activity of the ASTRO project was to develop the system and design requirements for the TPF mission from the stated science objectives in enough detail to allow for the development of viable competing mission architectures. These requirements are organized into three successively more engineering-oriented levels. The first level, Science Requirements / User Needs, includes a formal definition of the stated scientific objectives of the mission. The second level consists of TPF mission System Requirements derived from the Science Requirements. The third level contains Design Requirements derived from the previous two levels. The requirements have been documented in PDF format for electronic distribution over the internet.

Additionally, a Quality Function Deployment (QFD) analysis was performed to examine the correlation between and among the System Requirements and the Science Requirements. This activity is documented in section 4.6 below.

4.1 TPF Mission Science Requirements

Also referred to as user needs, the science requirements define the mission objective. They define what the system must do and are the criteria by which mission success will be measured. For TPF, the system requirements are science objectives defined by the scientists who will be the primary end users of the system. It is important to note that user needs specify “function” not form. User needs should not be architecture dependent and should avoid defining specific technologies unless they are deemed essential for the successful execution of the mission.

4.2 TPF Mission System Requirements

The system requirements are the highest level engineering requirements that describe how the system should perform. They define the physical limitations of the system without specifying the “form” the design should take. System requirements are driven by user needs, which is expected, but they are also driven by external factors. Some of these factors include constraints due to public opinion, NASA budgets, launch schedules, etc. These requirements fall outside the scope of the ASTRO project, but the influential external factors that influence the mission timeline and budget have been considered.

4.3 TPF Mission Design Requirements

Design requirements are the next lower level of engineering requirements that begin to define the “form” of the system. They are driven by the laws of physics and by standard engineering practices.

4.4 Additional TPF Mission Requirements

In addition to the science community, which is the principle stakeholder for this mission, there are a number of other sources that may contribute to the definition of user needs and system requirements. For a NASA science mission such as this, the U.S. tax payers, students, teachers, subcontract engineers, etc. will have vested interests that are likely to impose additional constraints on the system design. While this influence is recognized, it is outside the scope of the ASTRO project and has not been explicitly included in the analysis.

4.5 Requirements Document Electronic Format

The TPF Mission Requirements Document has been implemented in an electronic format that takes advantage of hypertext capabilities. The advantages of this format are that it enables a more user friendly interaction with the document, it can simplify configuration control, and it can provide easy access to additional contextual information regarding the source, intent, and verification methods for each requirement.

Typical requirements documents have the requirements listed sequentially, proceeding to the lowest, most complex requirement before returning to the next high level requirement. This organization provides an easy way to trace changes in requirements, but is somewhat cumbersome. The end user is not always interested in the detailed requirements. A document with hypertext links allows the end user to navigate at the level of complexity of interest without being encumbered by lower level details.

The hypertext electronic format can improve document configuration control. Since each requirement has a well defined parent-child relationship with the other requirements, it becomes easier to trace the impact of a proposed change to a particular requirement.

The context of any requirement is essential to its effectiveness. Users of the TPF mission electronic requirements document can easily determine the intent, source, and intended verification method of requirements by following the appropriate hypertext link. This capability will provide for program continuity despite staff turnover and for better informed decisions when the requirements are reviewed and potentially revised.

4.6 Quality Function Deployment (QFD)

Quality Function Deployment (QFD) is a graphical technique that translates customer needs into the parameters or attributes of the product and its manufacturing and Quality Control (QC) processes, a key element of Integrated Product Process Development (IPPD), see Boppe. The QFD technique can help to minimize human biases, prioritize technical requirements, provide requirements traceability, and provide a communication mechanism.

Customer requirements are the top-level Science Requirements stated in the TPF Mission Requirements Document. They are listed on the left side of the QFD (see Figure 3) and are assigned a number that indicates their relative importance (10 is the most important) among the customer requirements. Across the top of the QFD chart are listed the high-level

to 10 (10 being most important). As can be seen in the QFD for the TPF Mission (Figure 3), Baseline Separation, Maximize Spectral Resolution, Increase Level of Sensitivity, Collector Aperture, Combiner Optics, and Infrared Imaging Device have been identified as the most important technical requirements.

Another useful section of the QFD chart is the Correlation Matrix, which is the top triangle section that indicates interactions among the technical requirements. An 'x' symbol in the Correlation Matrix identifies technical requirements that are interdependent such that both may not be optimized at the same time. These represent some of the primary trades that must be considered during the mission design process.

5.0 Architectural Design Options

With the requirements defined, a number of mission architectures were identified and briefly examined as candidates for further evaluation.

An important assumption about the design is that an infrared nulling interferometer will be used to accomplish the TPF mission. A brief discussion of this technique including some justification for this assumption is included in section 5.1 below.

One of the most important trades with regard to the TPF mission is to determine the best architecture to carry out the mission. The apertures can be located on a single structurally connected spacecraft or on a number of different spacecraft. Therefore, in addition to developing a generic spacecraft operations scenario (section 5.2), five potential spacecraft architecture types were identified: Structurally Connected, Separated Spacecraft, Tethered, Hybrid, and Celestial Body. Sections 5.3 through 5.7 provide brief descriptions of each spacecraft concept with its perceived benefits and liabilities.

5.1 *Infrared Nulling Interferometer Technique*

To achieve the goal of directly detecting and characterizing terrestrial planets located in the habitable zones of other solar systems, the TPF mission must use some technique to prevent the parent star's light from concealing the light emitted by the planets. Typically, the intensity of the light from a parent star must be reduced by a factor of about a billion (in optical wavelengths) to a million (in thermal infrared wavelengths) to allow for the direct detection of the radiation from a planet. Consequently, the TPF mission will be designed to operate in the thermal infrared regime to take advantage of the higher relative intensity of the planets to their parent stars at these wavelengths. The scientific community has selected the nulling interferometer technique over other methods, such as a coronagraph or an occultation spacecraft, as the most viable technique for this mission.

The concept of using an interferometer to null out a bright parent star while simultaneously detecting a planet was first proposed by Bracewell and Macphie in 1979. A nulling interferometer is very similar to a conventional Michelson interferometer except for the introduction of phase delays to obtain a zero response at the center of the interferometer fringe pattern. Thus, the light from a parent star at the center of the interferometer field of view will be "nulled" out. For the TPF interferometer to detect a planet in a star system located at a distance of 10 parsecs, an interferometer with a baseline of 250 meters is required [Beichman, et. al., 1999] to provide the minimum starlight suppression of 10^6 at the inner boundary of the habitable zone. Since terrestrial interferometers consisting of modest sized telescopes and baselines on the order of hundreds of meters are currently under construction or are already in operation, there clearly exists a technological path to a similar, space-based platform.

An alternative method for masking the light from the parent star involves the use of a coronagraph. This technique employs an occulting mask in the center of the focal plane to

suppress the on-axis light. Additionally, a second filter, called a Lyot stop, is frequently inserted before the detector to mask the light at the edges of the image to further increase the signal to noise ratio. However, this technique has a typical suppression capability of only 10^3 , which is not enough for the TPF mission, and is most applicable to filled aperture telescopes, which would need to be very large (~100s of meters) to satisfy the TPF mission requirements.

The occultation concept involves the placement of a large disk in front of the telescope such that the light from the parent star will be occluded. To implement this concept, a 100 meter disk must be located a few hundred thousand kilometers away from an NGST-class telescope before an Earth-like planet in nearby systems could be detected. To achieve the required star-light suppression for the TPF mission, both the size of the occulting disk and the distance to the telescope would need to be scaled up by a factor of 100.

By choosing to conduct observations at thermal infrared wavelengths using a nulling interferometer with a sufficiently long baseline, the TPF mission can achieve the starlight suppression and resolution levels required to successfully detect and spectrographically analyze terrestrial planets orbiting nearby stars.

5.2 Spacecraft Operations Scenario

A generic mission operations scenario was developed to provide guidance during the system architecture design phase. The level of detail in the scenario is purposely selected to be general enough to accommodate all potential spacecraft architectures while being specific enough to assist with the selection of subsystem components capable of satisfying the mission requirements. In addition to an overview mission timeline, a science operations scenario was developed that focuses on spacecraft operations.

5.2.1 Mission Timeline

Figure 4 shows an overview timeline for the TPF mission. The mission has been divided into four phases: Pre-launch, Launch and Cruise, Deployment and Science Mission, and Extended Mission and Spacecraft Termination.

The Pre-launch phase includes spacecraft design, construction, test, and integration activities as well as the development of operations procedures and infrastructure. There will be a substantial flow of information from the spacecraft design team to the operations team to facilitate the development of the operational procedures. By the end of this phase, the spacecraft failure modes and effects should be well documented, the operational procedures for the Launch and the Cruise segments should be mature, and the operational procedures for the Deployment and Science segments should be started.

There is a large degree of variability in length of the Launch and Cruise phase due to the system architecture selected. First, there may or may not be the need for spacecraft integration in Earth orbit following launch. Second, the length of the Cruise segment is strongly dependent on the selected solar orbit altitude and the final mass of the spacecraft.

During the Cruise segment, the operational procedures for the Deployment and Science Phase will be matured and updated based on actual spacecraft health and simulation.

Once the spacecraft arrives at the science orbit, there will be an initial period dedicated to the deployment of the spacecraft elements from the Cruise segment configuration, initial calibration of the science instruments, and testing of the ground segment elements of the system with transmitted data. Afterward, the active science phase of the mission will be conducted. The first observations will be selected and scheduled to maximize the expected data value in the event of a spacecraft failure early in the Science Mission Phase.

During the extended mission phase, operations will continue much as they did during the Science Mission Phase except that there will be a continuing evaluation of the cost of continuing operations given the value of the science data being gathered. When the ratio falls below an acceptable level (this could be due to component failures, rising operations costs, or lack of qualitatively new data), the mission will be terminated. Afterwards, the operations team will still be responsible for completing the permanent archival of science data and the maintenance of processes to access that data.

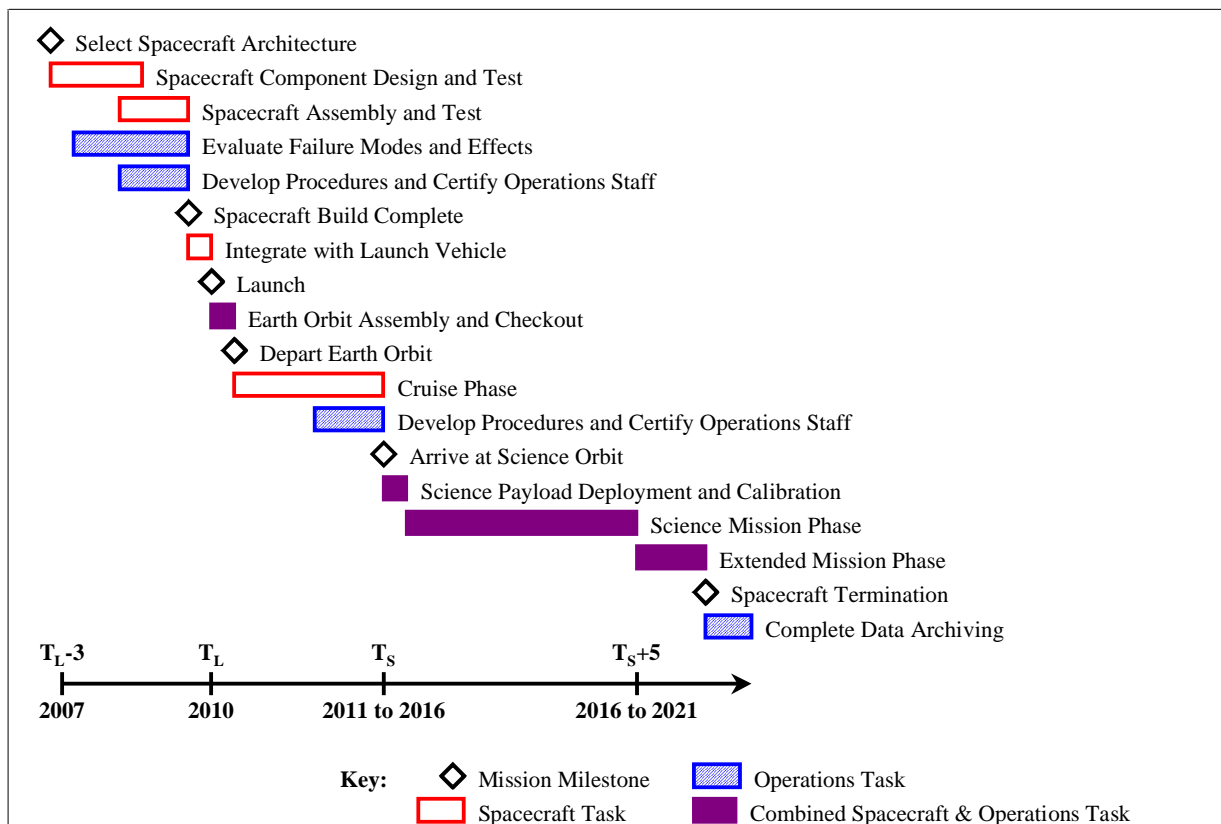


Figure 4. TPF Mission Overview Timeline

5.2.2 Science Operations Functional Flow

Science operations consist of the ground support activities required to fulfill the science requirements of the TPF mission during the Science Mission Phase. The primary duties of the TPF operations group will be to schedule science activities, to disseminate science data, and to maintain the health of the spacecraft. A diagram of the functional flow is shown in Figure 5 and is described below.

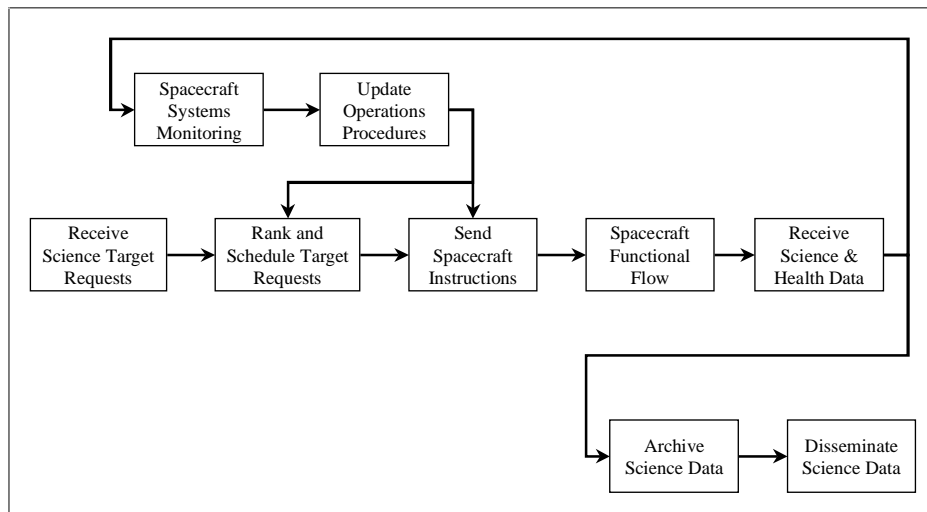


Figure 5. TPF Science Operations Functional Flow

A process must be established to receive science target requests from the research community and then to rank and schedule them for observation by the spacecraft. Early in the mission, there will be a focus on acquiring the most valuable subset of data as soon as possible to protect against an early failure of the spacecraft. Later in the mission, factors such as fuel and power management will more heavily influence target scheduling.

Following appropriate commanding of the spacecraft, the spacecraft functions will be executed to obtain the requested data and transmit it back to Earth. The transmitted data will consist of both the science data and the spacecraft status and engineering data. The science data must be permanently archived once it has been verified to be free of transmission defects. Then, the science data may be distributed to both the research community and to the public through various means such as the Internet or its successor.

The spacecraft status data will be used to monitor expected spacecraft performance including failures and consumable margins. This data can be used to update the simulation models of the spacecraft performance to assist with the evaluation of updated operations procedures that would be designed to prolong the operational life of the spacecraft or to improve the science instrument capabilities. These updated procedures would then influence subsequent scheduling and spacecraft commanding.

5.2.3 Spacecraft Science Operations Functional Flow

Once on station at the destination orbit, the TPF spacecraft will need to perform a series of coordinated activities to accomplish the science gathering objectives. These activities are shown in Figure 6 and are discussed below.

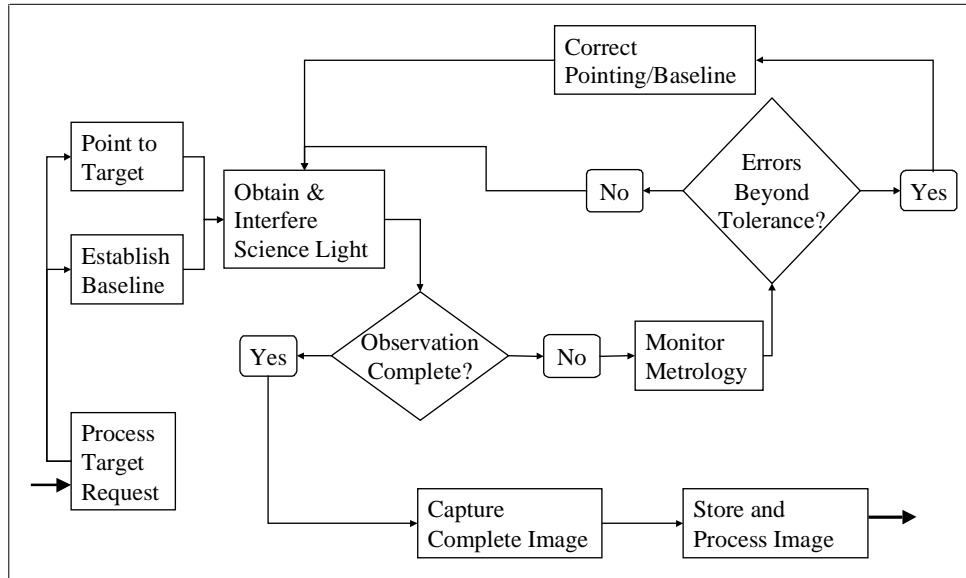


Figure 6. TPF Spacecraft Science Operations Functional Flow

The cycle begins with the reception of instructions for a science target. This can be from either a single, dedicated ground instruction, or from a sequenced list of targets. In addition, the format of this request may vary depending on the established ground control/spacecraft automation balance. This request must be stored in the spacecraft's memory in case a repeat of the operation is needed.

The next steps are to establish the required baseline separation distances of the apertures and to point them at the requested target. This will require periodic re-calibration of the attitude control system using reference stars to maintain the desired level of pointing accuracy.

Once the imaging cycle starts, it will be necessary to control the pointing accuracy and the internal metrology to within tight tolerances while the collectors move through a predetermined pattern (usually circular) to collect the science light. During this time, the integrated image data is captured by the optical instruments.

When the imaging cycle is completed, the integrated image data must be captured, stored, and processed (labeled, compressed, etc.) in preparation for transmission back to Earth. The spacecraft must be reasonably capable of detecting and correcting errors in this process so as to maximize its capacity to deliver the highest possible data fidelity. The process will be concluded with the transmission of science data, either one image at a time or after several have been accumulated.

5.3 Structurally Connected Interferometer

This spacecraft architecture consists of a single spacecraft that incorporates trusses or other rigid members to locate the interferometer components. The configuration may be linear or nonlinear and may or may not be symmetric.

Deployable trusses have been used on a number of other spacecraft and have been proposed for both the Space Interferometry Mission (SIM) and the Next Generation Space Telescope (NGST) missions.

The perceived advantages of using this technique include:

- The truss provides passive coarse positioning and angular pointing control of the interferometer components.
- Assuming the optical instruments can be placed near the spacecraft center of mass, this architecture requires less propellant usage during rotational maneuvers (such as during science operations.)
- Previous studies have favored the use of a truss architecture, especially for short baseline separation requirements.

The perceived disadvantages associated with this architecture are:

- Truss deployment may be complicated.
- The variability of aperture configurations is limited, including maximum separation and minimum separation.
- More effort (propellant) may be required to retarget the array.
- Less graceful degradation since component replacement would likely involve the entire truss.

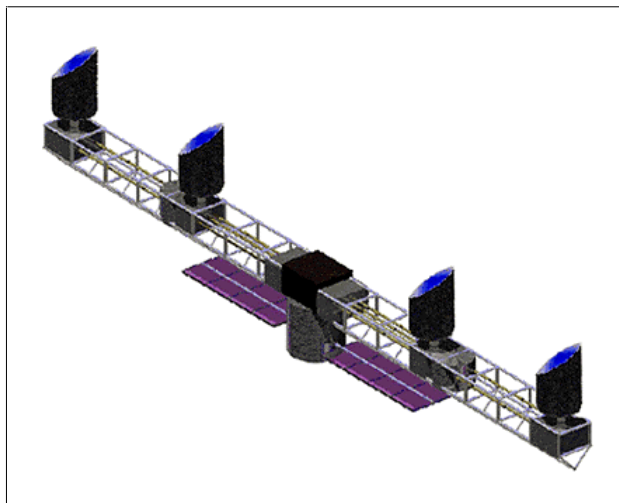


Figure 7. Structurally Connected Interferometer Example

5.4 Separated Spacecraft Interferometer

A separated spacecraft architecture places the apertures and the combiner optics on independent spacecraft platforms. Obviously, this architecture can accommodate the greatest variability of collector configurations spanning the range of linear, nonlinear, symmetric, and non-symmetric.

In the communications industry, systems that use a large number of satellites to provide global coverage have been proposed, developed, and utilized. The use of a separated spacecraft architecture for interstellar imaging is currently being undertaken by the NASA Space Technology 3 (ST3, formerly Deep Space 3, DS3) mission that is planned to conduct interferometry using two formation flying spacecraft. Separations of up to 1000 m are currently envisioned for this mission. The formation flying and the interferometer operation strategies developed for the ST3 mission are directly applicable to a TPF mission that uses this spacecraft architecture.

The perceived advantages of this architecture include:

- The collectors can be reconfigured to virtually any formation provided that a minimum separation distance is maintained.
- This architecture can exhibit graceful degradation and can accommodate incremental upgrades more easily than most other configurations since each spacecraft is independent.
- There will be increased flexibility in launching the array since these smaller spacecraft can be launched separately.
- Re-targeting maneuvers require minimal effort (propellant) since each spacecraft can be re-oriented individually.

The perceived disadvantages of this architecture are:

- Active formation flying sensors and controls must be developed for this architecture. To date, spacecraft formation flying technology has yet to be demonstrated.
- Propellant expenditure to maintain formation may cause contamination of the infrared optics.
- The mission lifetime will be dependent on onboard propellant loads.

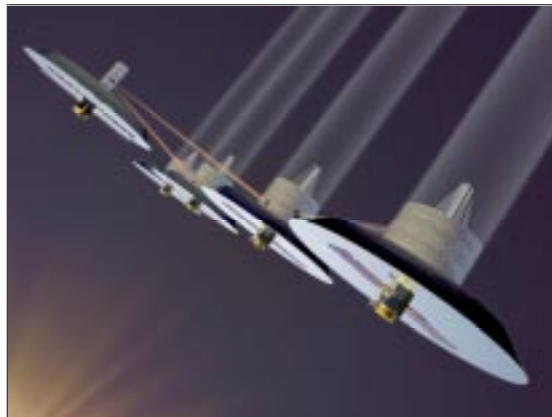


Figure 8. Separated Spacecraft Interferometer Example

5.5 Tethered Spacecraft Interferometer

A tethered architecture consists of separate collector and combiner platforms connected by tethers. In this application, a tether is considered to be a structural element that may only transmit tension loads.

Tethered satellites have been flown as part of the TSS-1 and TSS-1R (Reflight) , with somewhat dubious success. Even though science data was collected, both the spacecraft have been lost. In many respects, however, the application of the space tethers technology to the TPF is new, as tethers will be used mainly for formation flight.

The perceived advantages of the tethered architecture include:

- Tethers can provide the forces required to maintain the required relative separation distances between the collectors and the combiner.
- Tethers have a lower aspect ratio and a lower mass than an equivalent length of truss.
- The collector baseline length can also be easily varied using appropriate reeling mechanisms and maneuvers.
- The tethers provide a sort of ‘umbilical cord’ to the main spacecraft through which signals, or even power, can flow, thus lowering the complexity of the collector platform.

The perceived disadvantages of the tethered architecture include:

- This architecture is characterized by extremely complex dynamics that may be impossible to deterministically model, simulate, or control.
- The angular momentum of the system must be carefully managed during operations to maintain the correct spin axis, rotation rate, tether tension, and spacecraft separation.
- Collector configurations may be more limited than for the separated spacecraft case – non-symmetric and non-planar configurations may be particularly difficult.

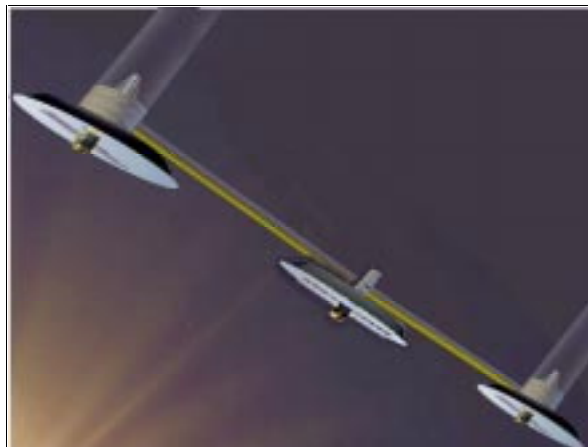


Figure 9. Tethered Spacecraft Interferometer Example

5.6 Hybrid Interferometer

The hybrid architecture can consist of any combination of structurally connected, tethered, and separated spacecraft elements. One simple example configuration is a pair of short baseline, structurally connected interferometers flown in formation to create a longer combined baseline. The potential advantage of a hybrid design is that it could make use of the best characteristics of the different designs, while at the same time reducing the effect of their weaknesses. However, this benefit may come with the cost of increasing the complexity of both the spacecraft design and of the operations processes.

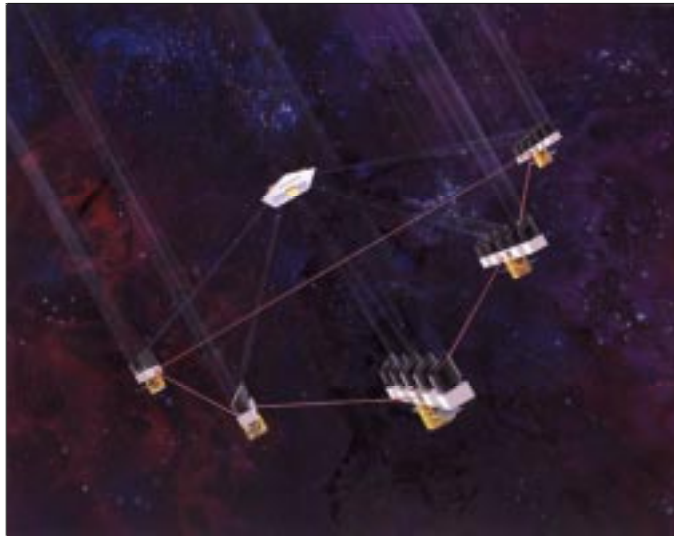


Figure 10. Hybrid Interferometer Example

5.7 Celestial Body Interferometer

The final architecture considered was the use of the Moon or an appropriate asteroid as a platform for the TPF interferometer. The interferometer elements would be landed and deployed on the surface of the celestial body.

A significant amount of expertise has been developed to conduct Earth based interferometry. This experience may be directly applied to the operation of an interferometer located on another astronomical body. However, a major engineering project on the surface of another celestial body has never been realized.

The perceived advantages of this technique include:

- The celestial body itself provides coarse position control. If the body is not seismically active, only minor effects, such as thermal deformations, will occur.
- A telescope on a celestial body could be operated in the same manner as an Earth-based one, but without the obstacle to astronomical observations represented by a significant atmosphere.
- The absence of a need for fuel once the components have been configured means that the primary limit on spacecraft lifetime is removed: the mission can nominally last much longer than a spacecraft-based mission.

- Graceful degradation and incremental upgrades are assured by allowing for component addition and removal from the array.
- The host body may provide a virtually infinite capacity heat sink for the thermal control subsystem.

The perceived disadvantages of this technique include:

- There are significant technical difficulties associated with landing, deploying and assembling an interferometer on a celestial body.
- The apertures will be fixed, or moving on some kind of tracks: in both cases, the baseline range may be significantly limited.
- The line of sight of the interferometer will be limited by the orbital and rotation properties of the host body. At least half of the sky will be obscured by the host body itself, and a significant part of the sky will be at very low elevation angles throughout the year. This means that even if an object is observable, the projected baseline will be very small, thus limiting the achievable resolution.
- In the case in which a massive body is selected as the host, additional structures may be required to sustain the weight of the optics.



Figure 11. Celestial Body Interferometer Example

6.0 Architectural Design Approach

6.1 Identify Architecture Metrics

A need exists to develop a uniform framework to compare different TPF architectures - structurally connected, separated spacecraft, tethered, and their permutations. The systems engineering methodology chosen to develop this framework is GINA - the Generalized Information Network Analysis methodology for Distributed Satellite Systems [Shaw, 1998]. The foundation behind the GINA methodology is the belief that all satellite systems are information disseminators that can be represented as information transfer networks [Shaw, 1998]. A summary of the procedural steps in the GINA methodology is listed below.

1. *Define Customer Requirements*
 - Identify the customer.
 - Define the customer requirements.
2. *Define Capability Requirements*
 - Translate the customer requirements into the four Capability “Quality of Service” parameters: isolation, rate, integrity, and availability.
3. *A) Develop System Metrics*
 - Define the performance, cost per function, and adaptability metrics by which all proposed system architectures will be compared and evaluated.

B) Perform Functional Analysis

 - Develop a functional flow diagram of the system.
4. *Derive Top-Level Architecture(s)*
 - Allocate values to the key design parameters identified in 3B.
5. *Evaluate Architecture(s)*
 - Perform a system abstraction by defining the simplest models that still quantitatively capture these tradable design parameters.
 - Using these models, calculate the capability, performance, cost per function, and adaptability of each architecture that meets or exceeds the specified capability “Quality of Service” parameters.
6. *Select Final Architecture*
 - Select the architecture that provides the best overall system value in terms of the cost per function metric.

Through these steps, GINA allows the systems engineer to make meaningful, quantitative trades at the conceptual design level by directly relating lifecycle performance to lifecycle cost.

Capability Requirements

In the GINA methodology, the capability of an architecture is characterized by four “Quality of Service” parameters that relate to the detection process, and to the quantity, quality, and availability of the information that is processed through the network. These four parameters are signal isolation, information rate, information integrity, and the availability of these services over time [Shaw, 1998]. Once formulated, these four parameters serve as the minimum instantaneous capability requirements the system must meet to satisfy the customer. These metrics assess how well the aforementioned customer requirements are met.

- **Isolation**

Isolation refers to the ability of a system to isolate and distinguish information signals from different sources within the field of view. For TPF, the system’s angular resolution, which is a function of the maximum vector baseline between a pair of collectors, determines the smallest sized objects the SSI can image and discriminate between in the field of view.

- **Rate**

Rate measures the speed at which the system transfers information between the sources and sinks in the network. In TPF, the imaging rate is simply the total number of images the system can produce per unit time and varies for each of the three modes of operation - surveying, imaging, and spectroscopy.

- **Integrity**

Integrity is a measure of the quality of the information being transferred through the network. In the case of TPF, the integrity of an individual image is a function of the signal-to-noise ratio (SNR) and the u-v coverage used to obtain that image. The u-v coverage can be quantitatively evaluated by calculating the mean square error (MSE) of the image, which is a comparison between an idealized point spread function (PSF) and the true PSF for a particular u-v coverage [Kong, 1998]. TPF architectures with greater integrity will produce images with less ambiguity.

- **Availability**

Finally, availability characterizes the instantaneous probability that information symbols are being transferred through the network between all of the sources and sinks. TPF targets close to the sun, or other targets whose imaging needs violate sun avoidance angles within the optical train, reduce the availability of the system. The actual imaging time versus the time to complete other tasks such as calibration and retargeting also affects the availability of the system.

System Metrics

To compare all the different architectural concepts that are formulated in the design iteration loop, GINA uses a quantifiable set of metrics – capability, performance, cost per function, and adaptability [Shaw, 1998]. The capability metrics have been already covered. The remaining three metrics are discussed below. These are the metrics that will be used to evaluate and compare all of the TPF architectures.

- Performance

While the four capability “Quality of Service” parameters introduced in the previous slide measure how well the architecture meets the capability requirements at any instantaneous point in time, the performance metric measures how the architecture satisfies the demands of the market over the entire life of the mission. For TPF, the performance may be expressed as the total number of images the system produces over the mission design life.

To calculate this quantity, however, the additional complication of taking into account all of the possible failures that may occur within the different components of the system must be taken into account. As individual payloads or satellites fail over time, the imaging rate of the system will decrease while attempting to maintain the same pre-failure level of integrity (image ambiguity). Conversely, an identical imaging rate could be maintained, but only by sampling fewer spatial frequencies (u-v points) in each image, thus reducing the integrity of the images. To take into account potential failures and the effect they have on system performance, a reliability model is needed.

- Cost Per Function

The cost per function metric provides a clear measure of the cost of an architecture versus its performance. It is a measure of the cost to achieve a common level of performance and includes expected development, launch, failure compensation, and operations costs. Examples include the cost per billable minute of a telecommunications system or the cost per megabyte of data for a weather reconnaissance system. For TPF, the cost per function is defined as the cost per image, and is calculated by dividing the total lifecycle cost of TPF by the total number of images it produces over its mission life.

- Adaptability

In GINA, adaptability is a measure of how flexible an architecture is to changes in design assumptions and mission requirements. In one sense, adaptability may be thought of as the sensitivity or elasticity of the cost per function of a particular architecture to incremental changes in an assumption or requirement. For the TPF mission, potential assumptions that could be altered to measure architecture sensitivity include component costs, learning curve slopes, and component reliabilities. In another sense, adaptability may be thought of as the flexibility of a particular architecture to a new set of mission requirements, such as the mission design life. An example of flexibility for TPF might be the ability of an architecture to transition from a planetary detection mission to a mission of astrophysical imaging.

6.2 Define the Architecture Trade Space

Trade Analysis

A trade analysis helps to identify the dependencies between different aspects of the system design. The analysis typically begins by defining top-level system trades and continues to lower level trades for a comparison of different subsystem components if fidelity needs require it. During the trades, metrics are used that quantify the trade analysis to determine the performance capability of each candidate architecture. The trade studies identify the

aspects of the system design that have a significant impact on the overall performance. More importantly, the overall goal of the trade analysis is to indicate the best alternatives for the system design to clarify the choice of architecture(s) that will be carried through the remainder of the design process.

Top Level System Trades

The first step in the trade analysis is to identify the major top-level trades that drive the general system design. The fundamental system trade that has the greatest impact on the overall design is the architecture comparison. Each option implies substantial differences in system design and operation that must be identified and understood before overall performance and cost can be evaluated.

There are other important top-level trades that involve the comparison of different design alternatives to find the best balance between performance and cost. First of all, the selected orbit, as well as the requirements on the observation time and image quality, strongly influence the interferometer configuration (aperture number, diameter, and location). The orbit is related to the noise sources that TPF must overcome, including the local zodiacal cloud and the Sun. The observing time and image quality requirements affect the number and diameter of the apertures. A larger number of apertures and a greater aperture diameter tend to decrease the observing time and increase the image quality.

Another trade concerns the impact of mission lifetime, noise sources, and user needs on target selection. The mission lifetime places a maximum limit on the number of targets that can be observed.

Noise sources such as zodiacal clouds, the Sun, close binary star systems, and other bright astrophysical objects limit the number of target stars that can be observed. Finally, the user ultimately decides which targets have the highest priority and in what order they will be observed.

Additional trades are more specific to the spacecraft design. Parameters such as orbit, architecture, specific functional requirements, and mission lifetime impact the spacecraft bus subsystem and thus impose a minimum bus performance level needed to maintain the functionality of the total spacecraft. Also, the system architecture is limited by the maximum mass and size of the system due to requirements set by the launch and transit vehicle, deployment method, general operation, and overall performance.

The final top-level trades concern on-board autonomy versus ground control and overall system cost versus capability and reliability. On-board autonomy allows for minimal maintenance of the spacecraft and a small operations crew but software complexity is sometime difficult to handle. Ground control helps increase the system flexibility but increases costs due to a large operations crew. Finally, The trade concerning overall cost, common to all space systems, seeks to find a balance between cost and performance. All of these trades form the initial analysis of each proposed system design.

Initial Trade Analysis Indications

An initial examination of the top-level system trades identified certain design alternatives that were significant design drivers. The system architecture drives every other level of system design by defining the general design framework that will set the bounds for all subsequent system engineering. The interferometer configuration, which includes the aperture number, diameter, and location, directly affects the ability of the system to obtain useful images thereby driving overall performance. The system orbit determines the noise sources that must be factored in to the system design as well as the spacecraft bus requirements concerning power, communications, GNC, etc. Mission lifetime defines the minimum capability and reliability of all system components to ensure that the system will have an adequate level of performance throughout its lifetime. Image quality requirements impact the system configuration as well as the payload systems so that the incident science light is synthesized to a useful image. Finally, the cost drives the maximum capability and reliability that can be included in the final system design.

6.3 Initial Downselect to Two Spacecraft Architectures

The ASTRO team, limited by time and manpower constraints, chose to concentrate on two architectures for further evaluation. The following chart was used to justify the downselect.

	Celestial Body	SCI	STI	SSI
Performance	Limited by many factors	Single Point Failure	Complicated Dynamics	Quick Reconfiguration and Graceful Degradation
Cost per Function	Construction Cost, Deployment Risk	Structure Cost	Risk of Tethers Breaking, Interacting	Thrust Cost, Replaceable
Isolation	Very Difficult to Vary Baseline	Limited Baseline	Moderate Variability of Baseline	Easy to Vary Baseline
Rate	Constrained by Body Dynamics	No Distinguishable Difference in Rate		
Integrity	Seismic, Thermal, Debris	Onboard Disturbance & Vibration	Tether Dynamics	Exhaust Plumes
Availability	Determined Field of Regard	Structural Vibrations	Tether Dynamics	Spacecraft Motions
Adaptability	Very Difficult to Vary Baseline	Non-Trivial to Change Baseline	Risk in Varying the Baseline	Easy to Vary Baseline and Graceful Degradation

Figure 12. Initial Architecture Downselect Matrix

Narrow Down to SCI and SSI

Once the system design was narrowed down to two architectural options, SCI and SSI, certain top-level system trades specific to the chosen architecture needed to be defined. The trades for the structurally connected interferometer concern the impact of structure material, dynamics, and system construction on the number and location of the apertures as well as

the dependency of baseline range, image quality, and mission lifetime on the precision system deployment range and structural stability and rigidity. Trades specific to a separated spacecraft interferometer involve the same system performance parameters but relate them to formation flying strategy and control, optical delay line range and capability, and available propellant for station keeping and maneuvering. These trades, along with the general top level system trades, aided in the selection of a specific system architecture.

SCI Trade Space

In the structurally connected architecture, in particular a truss structure, some of the available truss types are the traditional boom truss and the innovative scissoring truss. In both these trusses, the components (such as collector) are generally locked down onto the truss, though they can be placed on different truss segments. In a traditional truss, the truss segments remain fixed relative to each other. Hence, it is not possible to physically change the relative separation between the collector mirrors without affecting the truss segments. One possible method to change the baseline separation between the collector mirrors is to vary the projection of the truss onto a plane perpendicular to the array's line-of-sight (LOS). In this case, the LOS of the array is no longer normal to the array. This method requires delay lines in order to interfere the same wavefront coming from the target as the LOS of the array is changed. If TPF were to use a truss structure, one possibility is to build on the Able Engineering's ADAM truss developed for use on the International Space Station. The scissoring truss is an idea of placing the pivot of the different truss segments on the combiner module. In this case, the baseline separation between the apertures can be varied by changing the angle between the truss segments while the pathlength from the collector to the combiner module remains the same (assuming that the LOS of the array is still perpendicular to the array). Though an interesting idea, the operation of a scissoring truss remains to be demonstrated.

In the case where more than three modules (coll. and comb.) are required, deployment of a multi-element structure may prove to be complicated. Since the separation between the apertures is fixed by the truss, the maximum separation between the apertures is somewhat limited by the maximum extension of the truss.

SSI Trade Space

In order to detect a planet using a nulling interferometer, the interferometer must be rotated in order to increase the probability of detecting the planet. This is especially true if a linear array is used. Hence, in the separated spacecraft architecture, the best maneuver profiles that will give us the best chances to detect a planet should be determined.

Two different types of maneuvering profiles that were considered by Stephenson (though there are many more). A circular maneuvering profile allows the separation between the collector apertures to remain constant - which is also a feature of rotating the traditional truss. However, in order to maintain the same separation at all times, constant thrusting of the spacecraft is required.

A square maneuvering profile, however, requires the spacecraft to follow square trajectories. The two square trajectories considered by Stephenson are squares inscribed in circular trajectories (equal diagonal) and square trajectories having the same perimeter as circular trajectories (equal perimeter). In this case, the baseline separation between the spacecraft varies since the combiner spacecraft remains stationary at the center. The science light pathlength from the target, however, remains the same. The propellant expenditure in this profile may not be as high since propellant is required to change the spacecraft directionality only at the corners of the squares. This, however, assumes that observations can be made while the spacecraft are in motion, a technology that has yet to be proven but may be demonstrated in the DS3 mission.

In order to formation fly these separated spacecraft, active formation flying controls to centimeter levels of accuracy are required. Propellant expenditure to provide this active control may be high and may result in contamination of the infrared optics. The propulsive system must be able to provide a large enough impulse to change the heading of the spacecraft at the corners of the squares as well as the small impulses for centimeter level control.

6.4 Determine Meaningful TPF Model Components (Macro-Modules)

The chart in Figure 13 is a cornerstone of the approach taken since it establishes the relationship between the trade space for TPF and the metrics by which competing architectures were judged. It contains the attributes that distinguish individual architectures. Notice the fundamental relationships between the elements of the design vector and the capability metrics. For example, the number of apertures in the system will directly affect the ability to shape the transmissivity function. This dictates the sharpness in the rise of the transmissivity at the boundary between the exo-zodi and the habitable zone. Hence, the number of apertures drives the isolation metric (angular resolution).

The different attributes can be lumped into groups of modeling needs that allow the recognition of important differences between competing architectures. These groups directly determined the macro-modules that would be required to capture the TPF-relevant relationships of physics, cost and systems engineering trades. Thus, the level of modeling detail is high only for aspects that matter to TPF and help distinguish trends within the trade space. As mentioned before, the shape of the transmissivity function, dynamic stability and thermal control are very important for the success of TPF. The communication system, on the other hand, was only modeled to the level of detail necessary to obtain a complete mission design. For example, a link budget is included but not a detailed analysis of time vs. frequency division multiplexing. This might be a key driver for other trade analyses, such as for a satellite communications constellation, but not for TPF.

Top Trades Capability Metrics	Heliocentric Orbital Altitude (1 to 6 AU)	Aperture Maintenance (SCI vs. SSI)	Number of Apertures (4 to 12)	Size of Apertures (1 to 4 m)
Isolation (Angular Res.)	N/A	SSI allow more freedom in baseline tuning	Fine tuning of transmissivity function	N/A
Rate (Images/Life)	Noise reductions increase rates. Different operation delays	SSI power and propulsion requirements highly sensitive	Increased collecting area improves rate	Increased collecting area improves rate
Integrity (SNR)	Different local zodiacal emission and solar thermal flux	SCI: passive alignment but complex flexible dynamics	Tuning of transmissivity for exo-zodiacal suppression	Smaller FOV collects less local zodiacal noise
Availability (Variability)	N/A	Different safing complexity and operational events	Different calibration and capture complexity	N/A
				

Figure 13. Model Component Identification Matrix

6.5 Analysis Software Development Process

The development of the TPF Mission Analysis Software (TMAS) entailed eight discreet steps, some of which were executed in parallel:

1. Define S/W Objectives and Requirements
2. Define S/W Macro-Modules
3. Define All Interfaces
4. Define S/W Sub-Modules
5. Code Modules
6. Test Code
7. Integrate Code
8. Benchmark Sanity Check

The first step entails defining exactly what the user would like the software to do. For this project, the objective was to create a software tool to enable comparisons of different TPF designs on order to map out the system trade-space. The required software inputs are the elements of the design vector (orbit, number of apertures, architecture, and aperture diameter), and the desired outputs are the GINA metrics.

After defining the S/W objectives and requirements, the S/W macro-modules must be defined. Macro-modules represent distinct aspects of the design which have high coupling within each other, but low coupling between each other, allowing each macro-module to be coded individually by an individual/team with expertise in that area. TMAS contains six macro-modules: Environment, Aperture Configuration, Spacecraft (Payload and Bus), Structures/Control/Dynamics, Operations, and GINA.

Once these macro-modules are defined, the interfaces (variable inputs and outputs) between them must be explicitly agreed upon by all of the programmers. This ensures compatibility between modules and speeds up the integration process. Interface definition is carried out in parallel with the selection of the macro and sub-modules, and is documented in the N2 diagram.

The sub-modules are a division of each macro-module into its core components. For example, each spacecraft subsystem is a sub-module in the spacecraft macro-module. It is important that all of the code be thoroughly documented at this stage for later understanding and easy modification.

As the modules are completed, they are integrated into a single "Master" code. In parallel with both the coding and the integration, every module is continuously tested, both for correctness and for compatibility.

Finally, after all of the code has been integrated, simulations are run for existing TPF designs. By comparing the TMAS results with this independent source of design data, modeling errors are identified and the fidelity of the entire simulation is improved through an iterative process. Once the user is comfortable with the fidelity of the software, simulations may be run to map out the system trade-space.

6.6 Module Development Steps

A module is a Matlab m-file that models a specific subsystem or function within the mission. The purpose of the modules is to develop a systematic tool that sizes the subsystems within an architecture for a given set of inputs. If implemented correctly, the modules should also aid in the systems analysis methodology by computing the system metrics for a given architecture. This allows for rapid evaluations and comparisons of alternative architectures. The four steps in the development of the TPF modules are listed and explained below.

1) Explore all possible options and perform preliminary trade studies to identify a candidate architecture for the subsystem.

This step primarily entails background research into each subsystem. First, a list of all the candidate architectures for a subsystem or function is made. Next, the advantages and disadvantages of each candidate architecture are defined. If enough information is known at this point, a design decision is made on the subsystem architecture (ex. solar power vs. nuclear power).

2) Develop the subsystem modules.

Once an architecture has been decided on for a given subsystem, the module for that subsystem may be developed. This includes explicitly defining inputs required by the module, the outputs the module will deliver, and the mathematical relationships between these inputs and outputs. Once the module has been developed, the engineer may use it to explore the trade-space of the subsystem (ex. How does solar array area scale with orbital radius?). The importance of taking the time to understand the trade-space of each subsystem cannot be overstressed. For if the relationships between the inputs and outputs of each module are not understood before the modules are linked, then the engineer will not understand why certain architectures perform better in terms of the system metrics than other architectures. By understanding the trade-space of each subsystem, the engineer will be better prepared to make intelligent system architecting decisions and to interpret the results of any attempts to optimize a design. This step also provides an opportunity to debug the module before linking it with the other modules.

3) Code the module as a Matlab Function, connect it to the other modules, and analyze an entire architecture at once.

Once the subsystem module has been debugged, it may be coded up as a Matlab Function. A “master” m-file then links the modules together. The outputs from each module serve as inputs to one or more successive modules to size the system architecture and evaluate it on the basis of the system metrics. At this point, a simulation tool has been created. For any given set of architectural inputs, the Matlab “master” m-file will use the modules to size and evaluate that architecture. The results from different simulations may then be used to compare different architectures.

4) Apply an algorithm to systematically explore the system trade-space and search for “optimal” designs on the basis of a given metric.

This final step is optional. The design team may decide to use the simulation tool to compare a small number of different architectures. If, however, the design team deems it necessary to evaluate a large number of different architectures rapidly, then an optimization algorithm may be applied to systematically explore the global trade-space.

6.7 Module Integration

The TPF design process was divided into six macro-modules:

- Environment
- Aperture Configuration
- Spacecraft
- Dynamics, Control, & Structure
- Deployment & Operations
- Systems Analysis - GINA

Certain macro-modules were further subdivided into sub-modules. This modular division of the TPF design process reduces software development risk by reducing coupling and simplifies the simulation code development as each module is separately testable.

An N^2 diagram is an $N \times N$ matrix used by systems engineers to develop and organize interface information (Boppe, 1998). The sub-modules (Matlab m-file functions) are located along the diagonal of the matrix. The inputs to each sub-module are vertical and the outputs are horizontal. The aggregation of the sub-modules into macro-modules is illustrated by the black boxes enveloping different sections of the diagonal.

The N^2 diagram in Figure 14 provides a visual representation of the flow of information through the conceptual design process and will be used to connect all of the Matlab functions to enable an automated simulation of different TPF architectures.

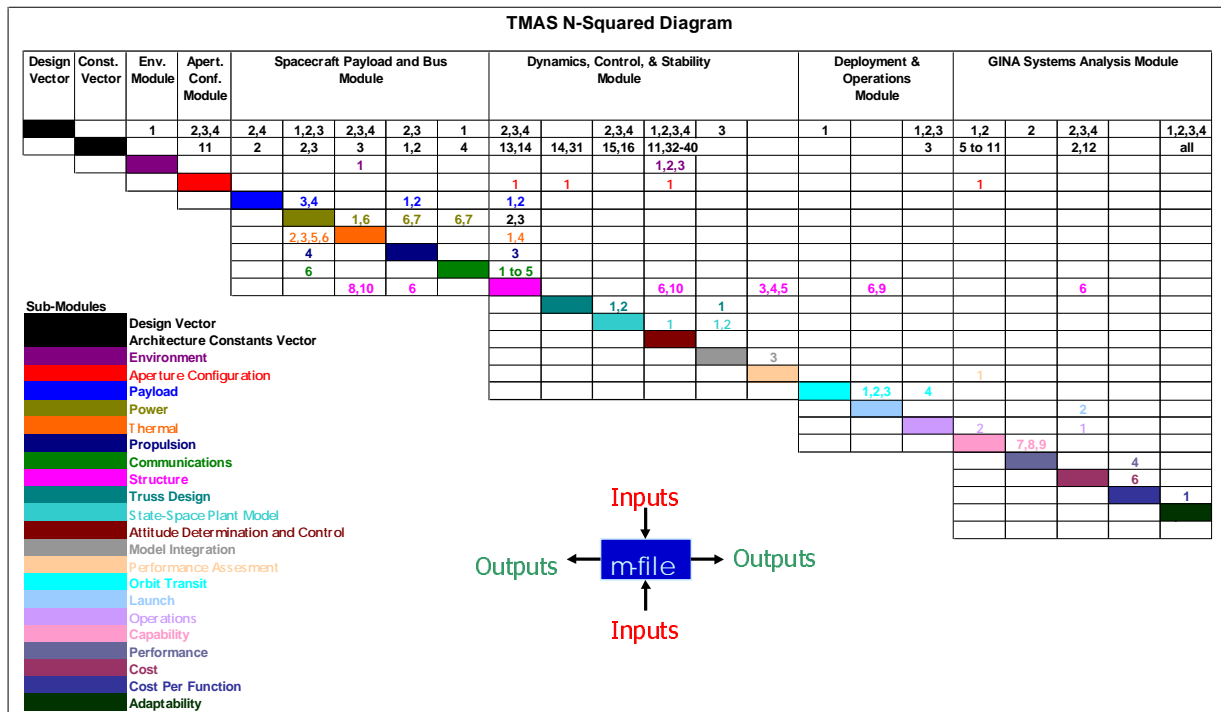


Figure 14. TMAS N^2 Diagram

This page intentionally left blank.

7.0 Architectural Design Evaluation Modules

The following sections discuss how the Matlab modules have been designed to perform comparisons of competing TPF mission architectures. Details regarding the intent, design, and trade space for each module are provided.

7.1 Environment Macro-Module

Module Motivation:

The local space environment will influence the thermal, power, aperture size, mission lifetime, and spacecraft attitude control components of the spacecraft and must be considered when evaluating if the proposed design meets the TPF mission requirements. The solar flux at the operational orbit is one of the major issues for thermal control and is a potential source of power. Therefore, the solar flux information will be calculated by this module and will be used as an input to the thermal and power modules. The local zodiacal environment influences aperture size. The aperture size must be larger to detect a planet through thicker local zodiacal dust. The calculated local zodiacal information will be used as an input to the payload module in order to calculate the minimum required aperture size. Micrometeoroid impacts can cause physical or plasma-related damage to the payload and the bus. Most damage to the TPF will be the result of cumulative degradation of the mirrors and other structures from micrometeoroid impacts over a long period of time. The calculated meteoroid flux will be input to the payload module to permit calculation of shielding parameters and to the GINA module to help estimate end of mission performance and failure rates. The solar pressure and gravity gradient data output by this module will be used by the ADCS module. When the TPF is close to the Sun, the effects of these two outputs may be significant.

Module Description:

The solar flux as a function of solar orbit radius is calculated using Equation 1, which shows that the solar flux varies as the inverse square of the distance from the Sun. The solar flux information is used as an input to the thermal and power modules to calculate the sizes of thermal shielding and of solar arrays. Figure 15 is a plot of this function for the orbital range under consideration for the TPF mission.

$$G_s = \sigma T_s^4 \frac{R_s^2}{R_o^2} \quad \text{Equation 1}$$

where

G_s : Solar Flux (W/m²)

σ : Stefan - Boltzmann constant (W/m² / K⁴)

T_s : Temperature of Sun (K)

R_s : Radius of Sun (m)

R_o : Orbital Radius (m)

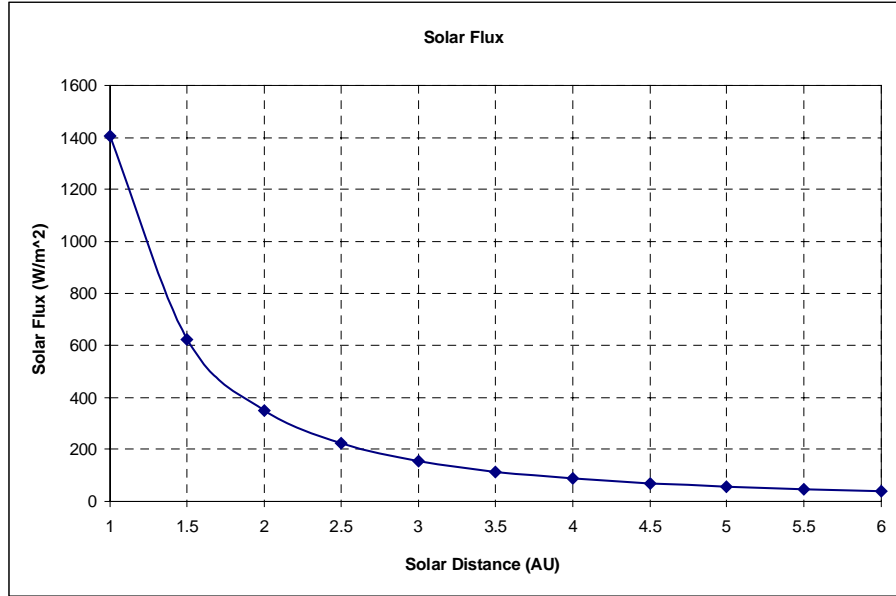


Figure 15. Solar Flux vs. Solar Distance

Zodiacal dust is composed of very tiny particles ever present in our own and other solar systems. These particles are remnants of the construction of the planets and of collisions among comets, asteroids, and other small bodies. The local zodiacal dust is the dust in our own solar system and the exo-zodiacal dust is the dust around candidate stars. Zodiacal dust creates a diffuse glow at infrared wavelengths that makes it more difficult to detect planets. Due to the gravitational attraction of the Sun, more dust exists near the Sun. Therefore, the TPF will experience different levels of local zodiacal dust depending on the orbit. On the other hand, the level of exo-zodiacal dust has little or no dependence on the TPF orbit. According to the TPF Book, the exo-zodiacal dust emission is expected to be smooth, with less than 1% random variations, except for rings and wakes due to gravitational trapping by planets or bands due to recent asteroid or comet collisions. As a result, the Environment Module provides the information on the local zodiacal dust only as function of the TPF orbit.

The local zodiacal intensity information generated from the Environment Module is used to calculate the signal to noise ratio which will determine the minimum aperture size. The following equations are used to calculate the local zodiacal intensity, which is plotted in Figure 16 for the orbital range under consideration for the TPF mission.

$$W_{T\lambda} = RE(T_{LZ}, \lambda)\tau_{LZ}10^{-6} \quad \text{Equation 2}$$

$$RE(T_{LZ}, \lambda) = 2\pi c^2 \frac{h}{\lambda^5 \left(e^{\frac{hc}{\lambda T_{LZ}k}} - 1 \right)} \quad \text{Equation 3}$$

$$T_{LZ} = 265 L_s^{.25} R_{au}^{-0.4} \quad \text{Equation 4}$$

$$\tau_{LZ} = 6 \times 10^{-8} R_{au}^{-0.8} \quad \text{Equation 5}$$

where

$W_{T\lambda}$: Local Zodiacal Intensity (W/m²/micron)

T_{LZ} : Local Zodiacal Temperature (K)

τ_{LZ} : Local Zodiacal Optical Depth

R_{au} : Orbital Radius (AU)

L_s : Solar Luminosity(J/sec)

c : speed of light(m/s)

h : Plancks constant(J * S)

λ : wavelength (μm)

k : Boltzmanns constant(J/K)

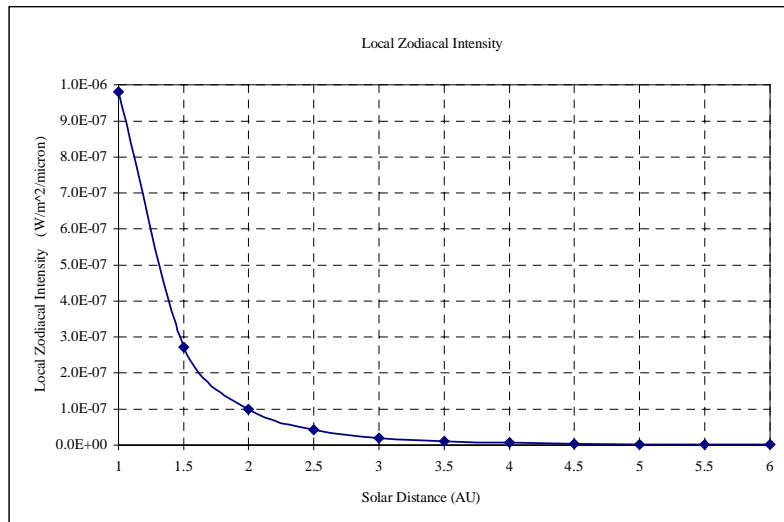


Figure 16. Local Zodiacal Intensity vs. Solar Distance

The meteoroid flux can be calculated in terms of the cumulative flux, which is the number of particles per m² per year for a mass greater than or equal to that mass, against a randomly tumbling surface. The interplanetary flux at 1 AU is described by Equation 6 for masses less than 10 g. A focusing factor (Equation 7) that accounts for the gravitational influence of the Sun on meteoroid density must be applied to Equation 6 to estimate the flux for other orbits. The cumulative meteoroid flux at 1 AU is plotted in Figure 17.

$$F_r(m) = c_0 [c_1 m^{0.306} + c_2]^{-4.38} + c_3 (m + c_4 m^2 + c_5 m^4)^{-0.36} + c_6 (m + c_7 m^2)^{-0.85}$$

Equation 6

where

$F_r(m)$: Cumulative Flux (number / m² / year)

$$\begin{aligned} c_0 &= 3.156 \times 10^7 & c_4 &= 10^{11} \\ c_1 &= 2.2 \times 10^3 & c_5 &= 10^{27} \\ c_2 &= 15 & c_6 &= 1.3 \times 10^{-16} \\ c_3 &= 1.3 \times 10^{-9} & c_7 &= 10^6 \end{aligned}$$

$$\text{FocusFactor} = 1 + \frac{R_s}{r}$$

Equation 7

where

R_s : Sun's radius

r : orbital radius

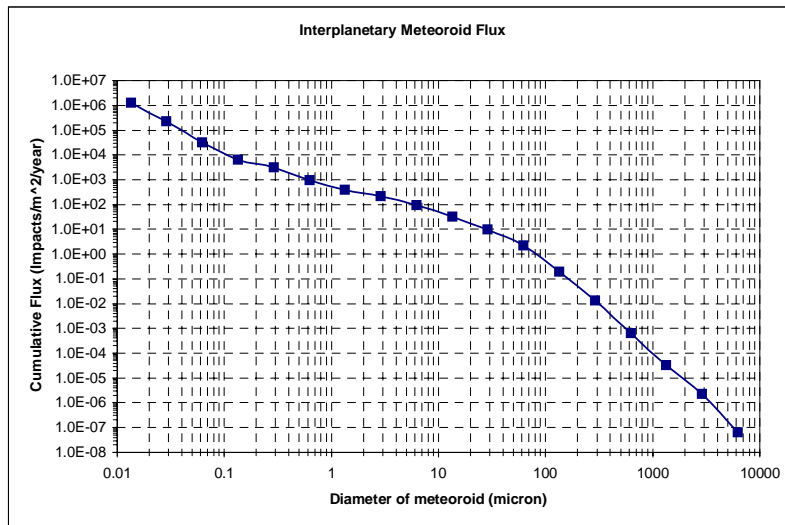


Figure 17. Interplanetary Meteoroid Flux at 1 AU vs. Meteoroid Diameter

Solar radiation pressure causes spacecraft orbital perturbations and is used as an input to the ADCS module. At 1 AU, the solar pressure is $4.5 \times 10^{-8} \text{ N/m}^2$. Equation 8 was derived from the observation that solar pressure varies as the inverse square of the distance from the Sun.

$$P = \frac{4.5 \times 10^{-8}}{R^2}$$

Equation 8

where

P : Solar Pressure (N/m²)

R : Orbital Radius (AU)

In orbit, the TPF will experience gravity gradient torques due to the distribution of mass along (among) the spacecraft and the distances of those masses from the center of mass of the Sun. Equation 9 is used to calculate the magnitude of these disturbances given the spacecraft orbit and principle moments of inertia. These results represent additional perturbation data that will be used by the ADCS module.

$$M_G = \frac{3\mu_s}{R^3} \begin{Bmatrix} (I_{zz} - I_{yy}) \sin \phi \cos \phi \cos^2 \theta \\ -(I_{xx} - I_{zz}) \sin \theta \cos \theta \cos \phi \\ -(I_{yy} - I_{xx}) \sin \theta \cos \theta \sin \phi \end{Bmatrix} \quad \text{Equation 9}$$

where

M_G : gravity gradient moment

μ_s : GM_{Sun}

R : orbital radius

I : moment of inertia

ϕ, θ : perturbation angles

Trade Space:

The outputs from this module contribute to the trade between solar and nuclear power and provide inputs for the determination of aperture size, thermal and debris protection schemes, mission lifetime, and ADCS capabilities. All of these factors are evaluated as functions of the chosen operational orbit for the TPF mission.

7.2 Aperture Configuration Macro-Module

Module Motivation:

As discussed in section 5.1 above, the TPF mission will be implemented using a number of sparse apertures operating as an interferometer. Unlike conventional interferometers, the goal of this mission is to null out the parent star. This will be done using the Bracewell nulling interferometer concept. However, similar to any conventional interferometer, the response of the TPF interferometer will be highly dependent upon the locations and the relative sizes of the individual apertures. This module will ensure that the evaluated designs meet the TPF mission's star light nulling requirement.

Module Description:

The goal of the Aperture Configuration Module is to capture the effects of the environment surrounding the planetary system of interest. Taking into account all the possible external noise sources that can effect the capability of the interferometer to detect a planet, the optimal transmissivity function for the given number of apertures in the interferometer is then determined.

The inputs to this module come directly from the Design Vector. Specifically, the module must be provided with the type of interferometer, the number of apertures to be used in the interferometer design, and the size of the apertures. The types of interferometers can be divided into the four types listed in Table 1. Note that this module does not distinguish between Structurally Connected (SCI) or Separated Spacecraft (SSI) architectures. Linear configurations limit the placement of apertures to a single line. Two dimensional configurations arrange the apertures in a plane normal to the pointing direction. Symmetric configurations require an even number of apertures and that each pair of apertures is the same size and is located symmetrically about the center of the array. The number of apertures in the array can be between four and twelve, subject to the limitation that symmetric configurations must have an even number. The range of aperture diameters is between 0.5 meters and 4.0 meters. When the size of the apertures is specified, it is assumed that all the apertures will have the same size. However, when the aperture size is left as a free parameter, an optimization routine is used to choose the optimum individual aperture sizes. These inputs are summarized in Table 1.

Table 1. Range of Inputs Accepted by the Aperture Configuration Module

Interferometer Type	Number of Apertures	Aperture Diameter Size
SCI/SSI Linear Symmetric	{4,6,8,10,12}	{0.5,1.0,1.5,2.0,2.5,3.0,3.5,4.0, Multi-Size}
SCI/SSI Linear	{4,5,6,7,8,9,10,11,12}	{0.5,1.0,1.5,2.0,2.5,3.0,3.5,4.0, Multi-Size}
SCI/SSI 2-D Symmetric	{4,6,8,10,12}	{0.5,1.0,1.5,2.0,2.5,3.0,3.5,4.0, Multi-Size}
SCI/SSI 2-D	{4,5,6,7,8,9,10,11,12}	{0.5,1.0,1.5,2.0,2.5,3.0,3.5,4.0, Multi-Size}

For each set of inputs, this module produces a single N by 6 output matrix, where N is the number of apertures in the design. An example of the module output is shown in Table 2. The first column in the matrix lists the number of apertures in the design. The locations of the apertures are then given in columns two and three, in polar coordinates. The sizes of these apertures are given in column four. Column five shows the phasing angles that must be provided to the reflected light beam from the apertures before being combined to provide the required nulling depth and width. In general, these phasing angles are chosen arbitrarily but can also be set as a free parameter in the optimization routine. The last column in the output shows the length of delay lines required to ensure that the same wavefront from the target is interfered when no phasing angles are introduced. The values in this column are generated by subtracting each value in the second column from the aperture that is furthest away from the center of the array.

Table 2. Output matrix from Aperture Configuration Module

Aperture Number	Distance from Center (m)	Clock Angle (rad)	Aperture Diameter (m)	Phasing Angle (rad)	Required Delay Length (m)
1	5.0000	0.0000	2.0000	0.0000	10.0000
2	5.0000	3.1416	2.0000	6.2832	10.0000
3	15.0000	0.0000	2.0000	3.1416	0.0000
4	15.0000	3.1416	2.0000	9.4248	0.0000

The optimal aperture configurations obtained from this module were determined prior to running the integrated software. The different possible interferometer types were first identified and separate routines were used to determine their optimal configurations. The mechanics behind this optimization are described below following a brief summary of the concept and the fundamental equations of a nulling interferometer.

The concept of using a nulling interferometer to detect an Earth-like planet by reducing the glare from its parent star, was first proposed by Bracewell and MacPhie (1979). Their two aperture concept is essentially similar to the Michelson interferometer except for introducing a 180° phase shift to one of the two light beams before they are interfered at the combiner. This, in essence, creates a zero response at the center of the interferometer's fringe pattern. However, it is possible to null out the parent star using more than two apertures. The first interferometer that was proposed for the TPF mission actually has four apertures (Angel and Woolf 1997) arranged in a linear array. This interferometer is better known as OASES. The first two-dimensional aperture configuration using five apertures was proposed by Mennesson and Mariotti (1997) for the Darwin project. Essentially, given the locations of the apertures and the amount of phase shift to be introduced into each collector beam, the response of the interferometer is given by Equation 10.

Note that the form of the transmissivity function in Equation 10 is essentially the same as for an ordinary Michelson interferometer, except for the independent phase shift term. By expanding the cosine term in the equation, one can quickly recognize that the $L_k \cos(\delta_k)$ and $L_k \sin(\delta_k)$ are actually the x and y coordinates of aperture k . As in an ordinary interferometer, it is the relative position between the apertures that is of importance, not their absolute coordinates.

$$\Theta = \left| \sum_{k=1}^N D_k \exp(j2\pi(L_k r / \lambda) \cos(\delta_k - \theta)) \exp(j\phi_k) \right|^2 \quad \text{Equation 10}$$

where

- D_k - the diameter of the aperture k (m)
- L_k - the distance between the aperture k and the center of the array (m)
- δ_k - clock angle of aperture k measured from a given aperture (radians)
- λ - observation wavelength (m)
- r - angular separation of the source from the center of the interferometer's fringe pattern (radians)
- θ - azimuthal angle of the source from the first interferometric arm (radians)
- ϕ_k - independent phase shift introduced to beam k (radians)
- N - number of apertures in the array

The transmissivity function for the OASES interferometer design operating at 12 microns is plotted in Figure 18. This interferometer consists of four apertures arranged in a 1-2-2-1 configuration. The 1-2-2-1 interferometer notation is interpreted as having two 1 meter apertures located at the extreme ends of the interferometer and two 2 meter apertures between them. The distance between each aperture, in this case, is the same throughout. By introducing a phase shift of 180° to one aperture in each of the two pairs, the transmissivity function in Equation 10 can be reduced to Equation 11. A value of $B = 75$ meters was used in Equation 12 to generate Figure 18.

$$\Theta = 4 \sin^2 \gamma \sin^4(\gamma/2) \quad \text{Equation 11}$$

where

$$\gamma = 2\pi r \cos \theta (0.5B) / \lambda \quad \text{Equation 12}$$

where

B - the overall dimension of the interferometer

Since the OASES array is actually linear and symmetric, the response shown in Figure 18 is only for the $\phi = 0^\circ$ sky angle. Clearly seen in the figure is the very low response of the interferometer for small angular separations about the origin ($r = 0^\circ$). From the figure, at $r = 7.5 \times 10^{-4}$ arcsec, the normalized response of the interferometer is only 2.8×10^{-10} , which is very small compared to some of the responses for angular separations that are greater than 0.1 arcsec. In fact, the response shown here actually meets the nulling requirement to detect an Earth-like planet orbiting a Sun-like star located 10 parsecs away. The aperture configurations determined in this module are optimized for an observation wavelength of 12 microns and a target distance of 10 parsecs. The six order of magnitude star light suppression that is required is indicated by the solid red box in the figure. The dashed line in the figure represents an area between the surface of the parent star to the 0.5 AU inside limit of the habitable zone. Signals received from this area will be pre-dominantly from the zodiacal cloud surrounding the star. Therefore, it makes sense to also null out this region. Unfortunately, it is almost impossible to null out such a large region using a limited number of apertures and maintaining the desired high transmissivity in the habitable region. Hence, the dashed lines represent a soft constraint where it is preferable to have the interferometer exhibit a low transmissivity, but it is not a "hard" requirement.

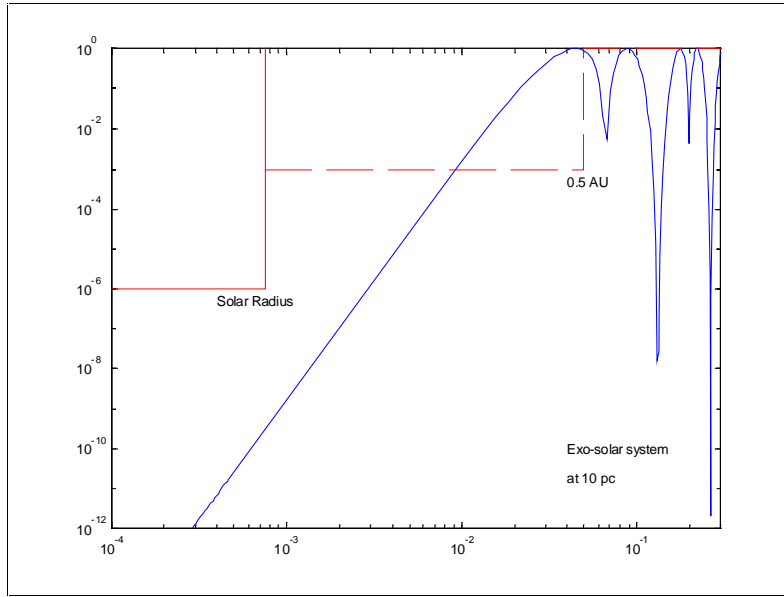


Figure 18. OASES Transmissivity Function Along $\phi=0^\circ$

For the optimization process, the ideal transmissivity function is defined using the hard and soft constraints shown in Figure 18 together with the desired unity response in the habitable range. A simple objective function is formed by taking the absolute difference between the ideal transmissivity function and the response generated by the interferometer. However, in order to ensure that the transmissivity response obtained from the optimization actually meets the nulling requirement, several modifications were made to the objective function. Since the transmissivity function deals with relatively small values, the algorithm uses the logarithmic difference between the transmissivity functions instead of the simple difference. For the low transmissivity constraints, the configuration will be penalized if the transmissivity lies above these constraints in the violation region. To ensure that the optimal solution does not violate the hard constraint, the logarithmic difference between the transmissivity functions is multiplied by a large coefficient (10,000). Hence, the objective function of this optimization problem is defined by Equation 13.

$$\min \left\{ 10000 \int_0^{7.5 \times 10^{-4}} \int \max(0, \log \Theta + 6) r dr d\theta + \int_{7.5 \times 10^{-4}}^{0.05} \max(0, \log \Theta + 3) r dr d\theta + \int_{0.05}^{0.3} |\log \Theta| r dr d\theta \right\} \quad \text{Equation 13}$$

Due to time constraints, the aperture configurations in this project were optimized for imaging an Earth-Sun system located 10 parsecs away. This value was chosen because it lies half way between the 5 and 15 parsecs where the different planetary systems are to be observed with the TPF interferometer. The observational wavelength chosen for this optimization, 12 microns, was also chosen because it lies halfway between the 7 and 17 micron band that TPF will be observing. Hence, the only variables left to determine in Equation 10 are the physical properties of the apertures and their phasing angles. To simplify the optimization, the phasing angles of the apertures are calculated using Equation 14.

$$\phi_k = \frac{4\pi(k-1)}{N}$$

Equation 14

Except for $N = 2$, these sets of phasing angles allow the interferometer to achieve a zero response in its transmissivity function to within first order. This can be verified by taking the summation of the complex exponentials of all the phasing angles. For a more detailed discussion of this matter, the reader is referred to Mennesson and Mariotti (1997).

The only variables that are left to consider in the optimization process are the physical properties of the apertures, namely their locations and sizes. The possible aperture locations chosen for this problem are mapped onto a circular grid with a minimum radius of 5 meters, a maximum radius of 60 meters, and a minimum radial separation of 5 meters between locations. The angular separation between the imaging locations is fixed at 10° , which gives a total of 432 possible imaging locations.

For the aperture diameter, the minimum allowable aperture size is 0.5 meters, the maximum is 4 meters, and the increment between aperture sizes is 0.5 meters. The maximum diameter is a consequence of the limitation imposed by the circumferences of currently available launch vehicles. In this project, the possibility of using deployable apertures was not considered.

The global optimum for this optimization problem can only be determined if all the possible solutions are considered, or if the optimization space is proven to be convex. Given the 432 possible imaging locations and N apertures, the number of possible aperture configurations is $432!/(432-N)!$, which can be approximated as 432^N . Assuming that it takes approximately 1 ms of computational time to consider each possible configuration, the time required to consider all the possible combinations for $N = 4$ is 404 days! Hence, from a computational standpoint, it is impractical to try to search the entire optimization space.

In this module, a heuristic optimization method, namely simulated annealing, is used to determine the best aperture configurations. The use of heuristic methods cannot guarantee that the solution obtained is the global minimum, but in general, offers a reasonable solution requiring short computational time. Due to the limited time allocated to this project, the use of heuristics can be justified in that the goal is to first obtain a feasible solution (one that doesn't violate the hard constraint) and then to improve the solution by further iteration.

The basic premise behind the simulated annealing technique can be found in Kirkpatrick, Gelatt and Vecchi (1983). Applications of this method in the determination of optimal aperture configurations can be found in both Cornwell 1988 and Kong 1998, which are similar to what is being done in this case. Essentially, this optimization method uses a statistical approach by starting with a randomly selected configuration of aperture locations and aperture diameters. A new configuration is then chosen randomly by either swapping a point that is already in the set of imaging points with a new point chosen randomly from the total available set of imaging locations, or by randomly changing the size of a particular

aperture. This new configuration is then compared with the current best configuration and is accepted as the new current best if its objective function is the lower of the two. However, the current best configuration can still be replaced by a higher objective function configuration if this configuration has an $e^{(-\Delta/T)}$ value that is greater than a number randomly drawn between 0 and 1, where Δ is the difference in objective function values between the configurations. The variable T is called the "temperature" of the system and is decreased each time a new configuration is accepted. This ensures that for a system that is at a low temperature, the probability of accepting a configuration with a higher objective function is low. The key feature in this optimization technique is that it reduces the chance that the system will get stuck at a local minimum solution.

The starting temperature chosen for this optimization algorithm is $T = 10,000$. The temperature is reduced by multiplying by the temperature multiplication factor $g = 0.99$ each time a new configuration is accepted. The temperature multiplication factor must be set such that the temperature is reduced in small enough steps to prevent convergence to a non-optimal, or "quench," solution. The temperature is also reduced in the same manner when a particular configuration does not get replaced after 7,500 additional trials. The optimization process is completed when a configuration becomes "frozen," which means that it has had its temperature reduced three times without being replaced by another configuration. A flow chart of this optimization strategy is shown in Figure 19.

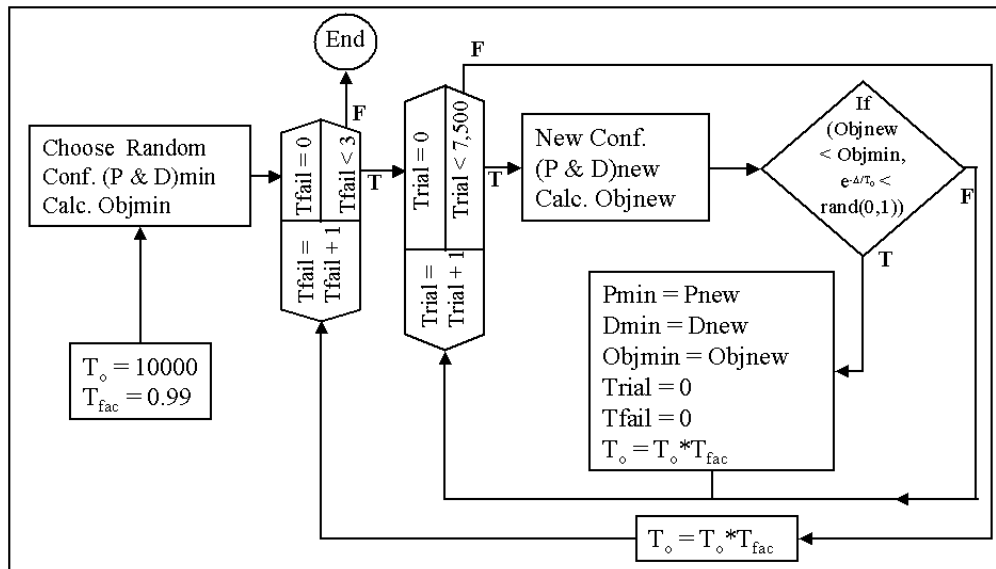


Figure 19. Simulated Annealing Flow Chart (Kong, 1998)

The optimization algorithm in this module does not distinguish between the two types of interferometer (SCI or SSI) considered in this study. Rather, constraints are used to limit the total number of possible configurations. The two classes of configurations considered in this study are the linear and the two-dimensional configurations. For each of these configurations, the apertures may or may not be constrained to be placed symmetrically about the center of the array. Furthermore, only one optimization is required for a given

ratio of aperture sizes, since the actual aperture sizes effect only the required integration time and not the characteristics of the normalized transmissivity function. The integration time effects are handled by the GINA macro-module.

An additional constraint on the placement of apertures is imposed by the desire to avoid collisions between spacecraft in the SSI case. A minimum separation of 10 meters between the centers of the apertures is imposed to ensure that none of the apertures overlap. Since this module does not differentiate between SSI and SCI configurations, this 10 meter minimum separation constraint will be applied to all configurations.

The module outputs for the different aperture configurations are tabulated in Appendix B.

Trade Space:

By defining the required baseline length, relative aperture placement, and in some cases the aperture diameters, the aperture configuration module plays a significant role in defining the image integrity and the total size and mass of the TPF spacecraft. All of these factors contribute to the cost per image metric that is used to compare configurations.

7.3 Spacecraft Macro- Module

The Spacecraft Macro-Module consists of the five modules that represent the science payload instruments and the spacecraft bus subsystems that support payload operations. Namely, the five modules are the Payload, Communications, Power, Propulsion, and Thermal modules. The Spacecraft Macro-Module is responsible for scaling the relative size and power characteristics of the four bus subsystems to optimize the TPF spacecraft design.

The Spacecraft Macro-Module reads in inputs from the Design Vector and from the Aperture Configuration and Environment Modules. Using these inputs the bus module estimates the structural mass and imaging integration time, sizes the payload, and minimizes the total bus mass by varying the peak and average power allocated to the bus subsystems. Figure 20 depicts the data flow of the module. The precise data flow into and out-of the bus module is inherently complicated and is described in more detail in the sub-module sections.

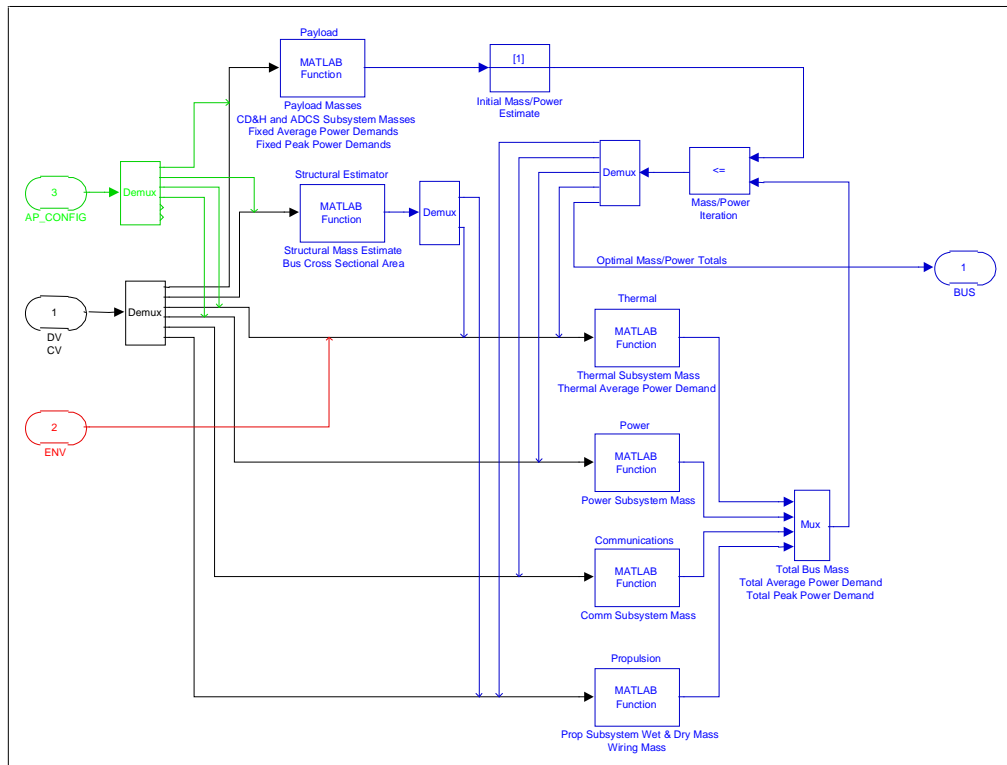


Figure 20. Spacecraft Macro-Module Data Flow

There is a fundamental mass trade between the power system and the other bus subsystems. To minimize mass, the power subsystem always wants to have a minimum power, while the other subsystems want more power to drive their respective masses down. The bus algorithm iterates through a reasonable power range to find the equilibrium point between these competing goals. For each peak power, there are several different average power configurations. The bus module iterates through a process of allocating average power to each subsystem and keeps track of the resulting mass calculations in a matrix.

The minimum bus mass configuration is returned to the general TMAS routine. In order to satisfy the DOCS module finite element module, the point masses of the subsystems are also provided. Future versions of the bus module should include the DOCS and the ADCS in the bus optimization because a low mass system may not be the best performing system. Future versions should also consider a simplification of the optimization algorithm. Currently, the bus completely maps the entire power trade space, which takes a significant amount of time, especially for the multiple bus design of a separated spacecraft (SSI) mission.

7.3.1 Payload Module

Module Motivation:

In any space mission, the payload drives the system design for the entire spacecraft because the payload components gather, process, and transmit the information needed by the end user to fulfill the mission objectives. The remaining spacecraft subsystems exist to support the operation and maintenance of the payload. Therefore, it is important to first define the payload requirements so they can be accounted for in the overall system design. In the case of the TPF mission, the goal is to directly detect planets around parent stars within fifteen parsecs. Additionally, the TPF spacecraft must be able to image a wide range of astrophysical sources. To meet these goals, the TPF spacecraft will be an interferometer designed to observe in the mid-infrared spectrum with a tunable baseline [Beichman et. al., 1999]. This will allow the spacecraft to successfully image a planet with milliarcsecond angular resolution while nulling the light from the parent star. Also, the interferometer baseline can be expanded to permit precise imaging of astrophysical sources. To support this mission, the TPF payload must be able to collect science light from a target source, convert it to a useful image/spectrum, and store it for later transmission to Earth for scientific use.

The payload components required for TPF fall into four main categories: the collector mirrors, the optical train, the beam combiner, and the infrared detectors. The collector mirrors and a portion of the optical train (fast steering mirrors and beam collimators) are located on the collector spacecraft, where science light from the target source is collected and fed to the combiner. The remainder of the optical train (delay lines), the beam combiner, and the IR instruments are found on the combiner spacecraft, where the science light is combined to synthesize either an image or a spectrum [Beichman et. al., 1999, Chapter 11]. The TPF payload places many requirements on bus subsystems to ensure that it performs as designed. First, the power subsystem must meet the power demand of the payload to ensure its proper function. Also, successful combination of the different beams of light from the collectors requires that the ADCS, GNC, and propulsion subsystems precisely control the relative positions of the spacecraft as well as continuously provide a high level of disturbance rejection during an imaging session. The thermal subsystem must use a combination of cryocoolers and sunshields to cool the payload components to the point where their sensitivity is maximized. Finally, the communications subsystem must be able to successfully transmit stored images back to Earth.

The main function of the payload module is to provide mass and power demand estimates for the various payload components. These values impact the power and propulsion modules within the Spacecraft Macro-Module as well as the spacecraft structural model and disturbance analysis in the DOCS Macro-Module. Also, the thermal and communications demands for the payload are directly specified in each of these modules. In addition to the payload properties, this module uses mass and power estimates for the Command and Data Handling (C&DH) and the Attitude Determination and Control (ADCS) subsystems because masses and power demands of these subsystems are relatively independent of the overall TPF design.

Module Description:

In general, the TPF payload module is relatively straight forward because most of the mass and power demand estimates for the payload components and for the C&DH subsystem are based on the estimates made by the Jet Propulsion Laboratory (JPL) in their analysis of the TPF mission [Beichman et. al., 1999]. The inputs to this module are the diameters of the collector mirrors and the type of interferometer used. The module consolidates the mass and power demand estimates for the payload components as well as for the C&DH and ADCS subsystems and outputs this information in vector form to give the mass and power distribution for each TPF spacecraft. The payload module is integrated with the spacecraft bus modules to create the Spacecraft Macro-Module that optimizes the allocation of mass and power to the bus subsystems.

The initial task of the payload module is to provide the mass and power demand estimates for the C&DH and the ADCS subsystems. These subsystem estimates are placed in the payload module because it is assumed that their values are fixed with respect to the spacecraft architecture. The C&DH subsystem is responsible for processing and distributing spacecraft commands as well as monitoring the health and status of the spacecraft [Wertz & Larson, 1992]. The mass and power distribution for this subsystem was based on the estimates determined by JPL for an SSI architecture [Beichman et. al., 1999]. The ADCS subsystem provides determination and control of attitude and orbit position [Wertz & Larson, 1992]. In this case, the mass and power demand estimates came from the ADCS module. Table 3 and Table 4 specify the mass and power demand estimates, based on architecture type, used in the payload module for the C&DH and ADCS subsystems.

Table 3. Properties of the C&DH and ADCS Subsystems

SSI Architecture	Mass (kg)	Average Power (W)	Peak Power (W)
Collector Spacecraft			
C&DH Computer	12	48	15
ADCS Subsystem	37	90	0
Combiner Spacecraft			
C&DH Computer	21	71	20
ADCS Subsystem	37	90	0

Table 4. Properties of the C&DH and ADCS Subsystems

SCI Architecture	Mass (kg)	Average Power (W)	Peak Power (W)
Collector Spacecraft			
C&DH Computer	0	0	0
ADCS Subsystem	37	90	0
Combiner Spacecraft			
C&DH Computer	33	119	35
ADCS Subsystem	37	90	0

Certain assumptions concerning the estimates in Table 3 and Table 4 need to be addressed. First, there are different approaches used to assess the impact of architecture type (SSI or SCI) on the mass and power demand estimates for these subsystems. The estimates made by JPL for the C&DH subsystem were based on an SSI architecture where each spacecraft requires its own bus subsystems, including a C&DH computer. However, an SCI architecture needs only one C&DH computer because the spacecraft bus can be centrally located on the bus. This single C&DH computer for the entire spacecraft will require more mass and power than the combiner spacecraft estimate for the SSI architecture, but less than the combined total for all SSI spacecraft. Consequently, the mass and power demand estimates for the C&DH subsystem in an SCI architecture are the sum of the estimates for the combiner and a single collector. On the other hand, the mass and power distribution for the ADCS subsystem was assumed to be independent of interferometer type because the collectors and the combiner require a control system regardless of spacecraft architecture. This assumption is valid for the most cases, but there probably are some functions of this subsystem that could be centralized in an SCI architecture, which would reduce the overall mass and power demand of the ADCS subsystem.

Another assumption is that the number of apertures and the aperture diameter have a negligible impact on the masses and power demands of the C&DH and ADCS subsystems. While such an assumption is generally valid for initial estimates, further analysis of the C&DH and ADCS subsystems are expected to show increases in their mass and power demands when the number of apertures or the aperture diameter is increased. For instance, these subsystems should require more mass and power when they must maintain control over eight instead of four apertures or when they need to maneuver collector spacecraft with four-meter diameter mirrors instead of two. Further revisions of the payload module should account for all elements of the design vector when estimating the masses and power demands of the C&DH and ADCS subsystems, but the estimates currently used are good first-order approximations for this analysis.

With the mass and power demand estimates for the C&DH and ADCS subsystems known, the last task of the payload module is to make the same estimates for the different components of the payload. The estimates, listed in Table 5, are separated based on the payload distribution between the collector and combiner spacecraft [Beichman et. al., 1999].

Table 5. Mass and Power Demands for the Payload Components

	Mass (kg)	Average Power (W)	Peak Power (W)
Collector Spacecraft			
Optical Train	125	133	0
Mirror	$14 \cdot A_{\text{mir}}$	-- [†]	0
Combiner Spacecraft			
Optical Train	150	133	15
Instruments	320	415	0
Data Storage Computer	15	40	0

† - The average power demand for the collector mirror is included with the collector optical train

Most of these estimates are taken directly from JPL, but there are a few important differences. First, the mass of the collector mirror is estimated by multiplying the area of the mirror with the approximate areal density of the material used to construct it [TPF Technology Inheritance Matrix, 1999]. Also, the estimates for the combiner optical train were decreased because the JPL estimate includes cryocooler mass and power requirements, whereas the Spacecraft Macro-Module separates the thermal control devices from the components of the payload. Finally, the estimates for the data storage computer are based on rough mass and power demand approximations for twenty gigabytes of storage space [TPF Technology Inheritance Matrix, 1999].

The mass and power demand estimates for the TPF payload include many assumptions concerning the technology available in the next decade and the properties of the payload components. TPF will incorporate a wide range of advanced technology including lightweight mirrors, a laser metrology system, a beam combiner, an infrared detector/spectrometer, and other technology systems that will allow TPF to interfere beams of light with accuracy to a tiny fraction of a wavelength. Many of these technologies are still on the drawing board and have yet to be demonstrated or tested in an environment similar to TPF. In the end, the actual impact of the technological assumptions on the payload estimates will not be known for some time, so educated guesses based on past technology but adjusted for future advances must be used for the time being. However, certain other assumptions can be relaxed by refining the mass and power demand estimates for certain payload components. For example, the maximum baseline of the configuration and the required delay line length should be included in the optical train estimates for the collectors and the combiner. The collector optical train may have to be changed to factor in the distance that the beam of science light must travel to get to the combiner. Also, the combiner optical train should have some sort of dependence on delay line length (kg/m) similar to the areal density of the collector mirrors. Another example concerns the impact of the number and location of the apertures on the design of the beam combiner. It's certainly reasonable to conclude that the complexity of the beam combiner increases with the number of apertures because it must be able to interfere a greater number of beams of light to synthesize the final image. In addition, a two-dimensional configurations require a more sophisticated beam combiner than a linear configuration. The point is that additional design

parameters need to be included in the mass and power demand estimates for the TPF payload components so that a better understanding can be gained concerning the payload impact on the overall system design.

Trade Space:

Due to the fact that the TPF payload is not well understood, there is not a significant level of trade space analysis that can be conducted for this module at this time. However, the mass and power distribution for the payload is a significant contributor to the mass/power trade for the bus subsystems and the overall spacecraft. Although the payload trade space is currently quite limited, it should be expanded once certain technologies have been demonstrated and the actual design of the payload components is better understood. The technology assessment will validate some of the assumptions concerning the payload design but will also point out certain errors and discrepancies in this design. These results must be used to correct not only the payload design but also the overall design of the entire spacecraft. In addition, further details in the design of the payload components will demonstrate how certain top-level design considerations, such as the interferometer type and configuration, number of apertures, and maximum baseline, will affect the mass and power demand estimates of the payload. As the TPF payload design progresses, the payload module can be expanded to include the impact of instrument noise sources on the overall signal-to-noise ratio of the system as well as a reliability analysis of each individual component of the payload.

7.3.2 Communications Module

Module Motivation:

The communications system allows the transfer of TPF data to the science community and the capability of spacecraft control to the operations team. It is optimized for minimum mass.

The communications capability of the TPF consists of a high rate data transfer system and one or more low rate data links. Since the high rate system is most affected by changes in mission design parameters, the communications module concentrates exclusively upon it for use as a design differentiation tool. The low rate systems are envisioned as a backup command link in case of high rate failure, will operate under non-stressing conditions, and can be safely assumed to offer negligible changes in mass and required power throughout the trade space. The power and mass of the inter-spacecraft links between elements of a separated spacecraft interferometer, while addressed, can be safely neglected due to their low size.

Module Description:

The communications module computes the size, mass, and simple configuration of the communication system, while satisfying the physical constraints of the link equation. There are four inputs into the module, two of which (orbital altitude and power allocation) are the main system drivers. The outputs from the communications module are the antenna

diameter, the antenna mass, the transmitter mass, and the minimum gimballed distance. The first time the communications module is called in the bus macro module, it provides a minimum power output. Thereafter, the communications module takes a power allocation input during the power distribution iteration of the bus macro module. The inputs and outputs are shown in Figure 21.

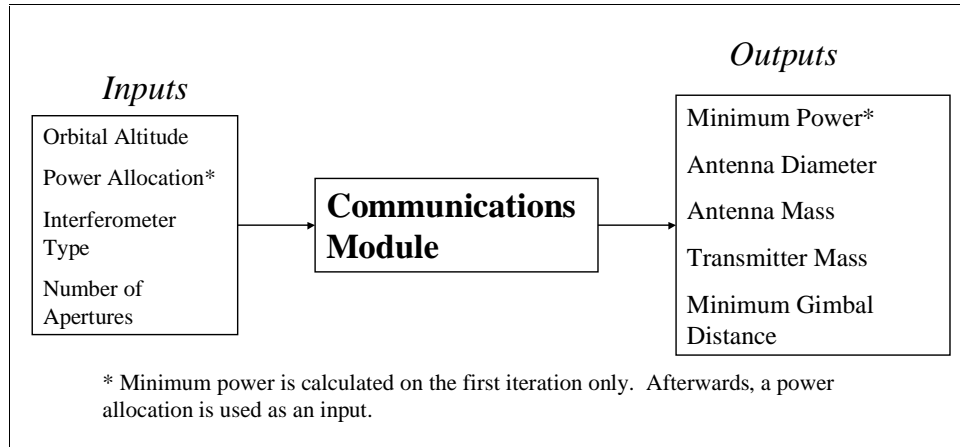


Figure 21. Communications Module Inputs and Outputs

The module finds the minimum antenna size and mass for a given power, data rate, and orbital altitude. This is accomplished using the link equation and Shannon's bound for error-free transmission. First, the physical limit of the signal to noise ratio is found according to the equation

$$\left(\frac{C}{N}\right)_{Limit} = 10^{\left(\frac{R \log_{10}(2)}{B}\right)} - 1 \quad \text{Equation 15}$$

where $\left(\frac{C}{N}\right)_{Limit}$ is the signal to noise ratio, R is the data rate, and B is the bandwidth.

This constrains the intra-module tradespace and offers a criterion for maximum attainable performance. Then the physical limit is raised to a design limit by including the coding loss and link margin. For TPF, the system is power limited, not bandwidth limited, so highly efficient techniques like BPSK Reed-Solomon with Viterbi encoding will be necessary to approach the Shannon bound. Coding loss values were taken from deep space missions as reference (at data rates less than 100kbps), and can be assumed applicable for higher data rates (~400kbps) with the improvement of encoding due to processor performance increases in the years before the TPF is launched. In addition, emerging advances in amplifiers will lower the receiving noise temperature [Posner, 1988]. Results from the link equation drive the minimum antenna diameter. This process is shown by the following three equations:

$$EIRP = \left(\frac{E_b}{N_o} \right)_{DesignLimit} - L_s - L_a - G_r + k + T_s + R + M \quad \text{Equation 16}$$

where $EIRP$ is the effective isotropic radiated power, $\left(\frac{E_b}{N_o} \right)_{DesignLimit}$ is the design limit ratio of received energy-per-bit to noise-density, L_s is the space loss, L_a is the transmission path loss, G_r is the gain of the receive antenna, k is Boltzmann's constant, T_s is the system noise temperature, R is the data rate, and M is the link margin. All variables are in decibels for this formulation.

$$G_t = EIRP - P - L_t \quad \text{Equation 17}$$

where G_t is the gain of the spacecraft transmitting antenna, P is the power supplied, and L_t is the transmitter to antenna line loss.

$$D_t = 10^{\left(\frac{(G_t - 17.8 - 20 \log_{10}(f))}{20} \right)} \quad \text{Equation 18}$$

where D_t is the diameter of the spacecraft antenna and f is the operational frequency. This equation is from an estimated relationship between antenna diameter, gain, and frequency for a parabolic shape given in [Larson & Wertz, 1992].

The link design assumes use of NASA's 70meter DSN for the ground segment and its associated 8.4GHz operational frequency.

The module calculates the antenna mass by multiplying the surface antenna area by the area density of a lightweight mesh material. Typical fiberglass/composite options are heavier and experience a mass penalty due to deployment mechanisms if the diameter exceeds a given payload fairing size. The mesh antenna is always assumed to be launched in a stowed condition, with a small deployment mass penalty.

The first time the communications module is called, it must provide a minimum power to the bus macro module. In reality, there is no power constraint in this determination. Theoretically, any low power level will work, as long as the antenna diameter can grow as large as possible. Figure 22 shows the relationship between power and antenna mass for the 1 AU separation case. Clearly, there exists a bend in the curve before which the mass is prohibitively high, and after which the additional power has a diminishing effect. The module captures this "bend in the curve" and uses it as the initial minimum power estimate.

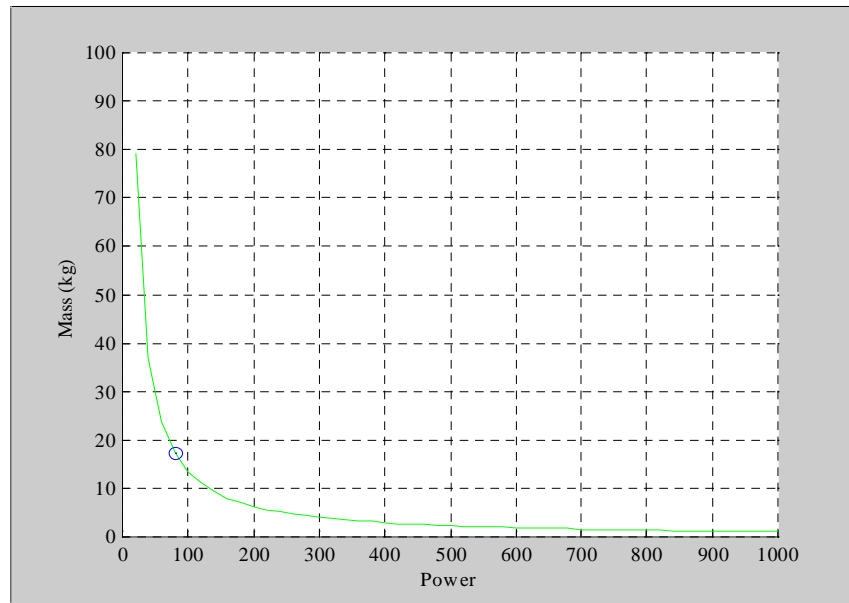


Figure 22. Initial Power Estimate Determination for 1 AU Separation Case

The TPF spacecraft, with its extremely high pointing accuracy, can keep the radiated signal on its earth target well within the half-power beamwidth with a body-fixed antenna, despite the narrow “spot-beam” nature of the high data rate downlink. However, communications may be desired during spacecraft maneuvers, or at deliberate pointing offsets for operational efficiency, so a required gimbal configuration is calculated.

Laser communication systems have not been incorporated into the code because of their inability to penetrate the Earth’s atmosphere satisfactorily. With the onset of earth-orbiting laser-to-RF relay satellites, laser communications might become attractive, but using a conservative estimate of the available infrastructure in the TPF operational timeframe, RF communications were found to be the only feasible communications approach. In addition, only a simple (yet highly effective) parabolic antenna configuration was used, although some alternative technologies like flat-plate planar arrays could provide marginal mass benefits.

Trade Space:

Figure 23 below shows the effect on antenna mass of variations in distance and data rate for a constant power level.

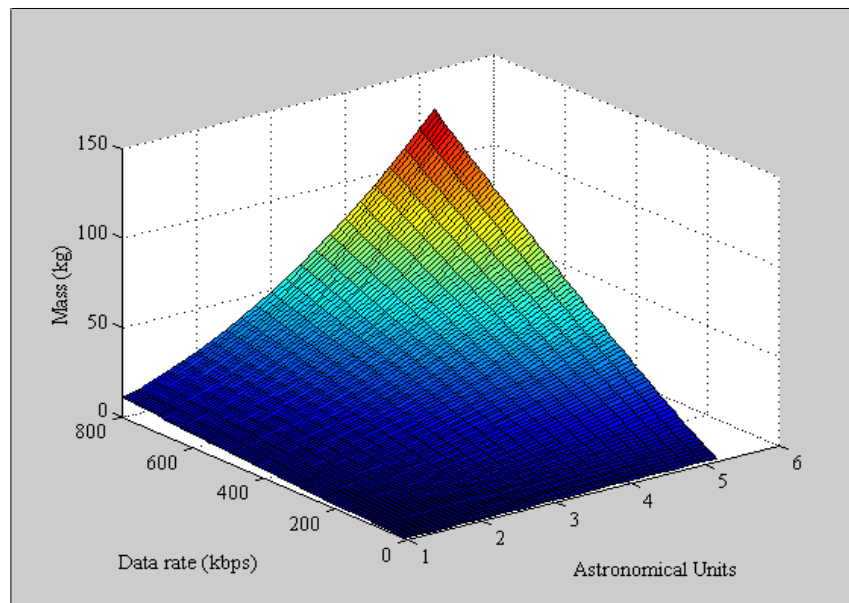


Figure 23. Tradespace for Antenna Mass, Data Rate, and Distance

As seen from the figure, the highest mass occurs when the distance and data rate are highest. The current 400 kbps data rate is specified in the TPF requirements, but should that stipulation be relaxed in the future, variations in the data rate would affect the mass/distance relationship as shown.

7.3.3 Power Module

Module Motivation:

The electrical power subsystem performs many functions for the spacecraft to ensure that all subsystems have an adequate power supply. First, it conditions and regulates the power supply for the spacecraft. Certain bus and payload components may require different or strictly regulated input voltage levels. Some of these components may require DC power while others may need AC power. The power subsystem must be able to provide all of these subsystems with the type and level of power they need to operate properly. Second, the power subsystem must store power for use during periods of peak power demand. The peak power requirements drive battery selection to ensure an adequate power storage capability to satisfy the peak power demands for the entire spacecraft. Third, the power subsystem must distribute power throughout the spacecraft. In addition to these primary functions of the power subsystem, it must also perform secondary functions such as switching equipment on or off, protecting against short circuits, and isolating faults [Larson & Wertz, 1992]. All of these functions must be factored into the overall design of the spacecraft bus.

The power module will choose a power source from among the two main power sources that are used in modern spacecraft: solar arrays and radioisotope thermoelectric generators (RTGs). The power subsystem design must trade between the two power sources available to determine which one is best suited to the specified TPF architecture.

To design the power subsystem, certain design parameters for the entire spacecraft must first be defined. To begin with, the average and peak power demands for all the bus and payload subsystems need to be known. The average power requirement determines the size and type of power source selected while the peak power level affects the size, number, and type of batteries used to store power for peak power periods. Other important design parameters that impact the power subsystem include the mission lifetime, the orbital profile, and the spacecraft configuration. The mission lifetime defines the level of redundancy needed to account for solar array degradation or the amount of fuel that is required to run an RTG for a specific amount of time. The orbital profile specifies the radiation environment for the spacecraft (solar flux, eclipse periods, etc.). Finally, the spacecraft configuration impacts the physical location and dimensions of the power subsystem [Larson & Wertz, 1992]. Once all of these design parameters have been considered, the detailed design of the power subsystem can take place.

The main purpose of the TPF power module is to assess the different design options available for the power subsystem and to select the one that is best suited to the TPF spacecraft design. This module estimates the masses of the various components of the power subsystem including the power source, batteries, and miscellaneous devices such as the power control unit and regulators/converters. The power module is incorporated into the spacecraft bus and payload macro-module which determines the optimal mass and power combination for the bus subsystems.

Module Description:

The overall function of the power module is to estimate the mass requirements for both solar array and RTG power sources based on the average and peak power requirements for the bus and payload subsystems and on the mission lifetime, interferometer type, and orbital radius. The first function of this module is to size the solar arrays and RTG needed to satisfy the average power demand for the TPF spacecraft. For this particular mission, average power is provided when the spacecraft is imaging a target star or an astrophysical source. The selection of a power source involves a trade between the merits and the faults of solar arrays and RTGs. Solar arrays convert incident solar radiation to electrical energy while RTGs generate electrical power by using either a radioisotope heat source through thermoelectrics or by providing thermal energy to a rotating generator. Solar arrays benefit from having an unlimited power source and a well-understood technology. However, they suffer because the array material degrades over the mission lifetime and the available solar radiation decreases as orbital radius increases, forcing an increase in the solar array area to provide adequate output power. RTGs provide a constant power source independent of orbital location but have a limited source of fuel and the technology is not very mature. Therefore, multiple mission parameters must be considered to help select the power source.

The calculation of the mass estimate for solar arrays requires a series of steps that apply power generation, conversion, and manufacturing efficiencies as well as the lifetime degradation to the solar flux and the maximum sun incidence angle. The properties of the solar arrays used in the power module are shown in Table 6 [Larson & Wertz, 1992].

Table 6. Solar Array Properties

Properties	Estimated Values
Solar Panel Efficiency	40 %
Secondary Power Conversion Efficiency	90 %
Manufacturing Efficiency	77 %
Degradation per Year	2.5 %
Areal Density	2.45 kg/m ²

The first step in sizing the solar arrays is to calculate the total power available based on the solar flux (SF) and the solar panel (η_{sp}) and secondary power conversion (η_{2nd}) efficiencies (Equation 19).

$$P_o = \eta_{sp} * \eta_{2nd} * SF \quad \text{Equation 19}$$

It is assumed that the solar arrays on the TPF will not experience an eclipse period because the orbits under consideration are heliocentric and far from any potential eclipsing bodies. The next steps identify the power requirements for beginning-of-life (BOL) and end-of-life (EOL) operations. The calculation of the power per unit area of the solar array at BOL accounts for the manufacturing efficiency of the solar panels (I_d) as well as the maximum sun incidence angle (θ_I) (Equation 20). At EOL, lifetime degradation is applied to the BOL calculation to determine the power per unit area required by the spacecraft to conduct operations and the end of the mission lifetime (Equation 21).

$$P_{BOL} = P_o * I_d * \cos \theta_I \quad \text{Equation 20}$$

$$P_{EOL} = P_{BOL} * (1 - \text{degradation}/\text{year})^{\text{lifetime}} \quad \text{Equation 21}$$

Another assumption is made concerning the maximum sun incidence angle. The value used for θ_I in the power module is 45°, which is the worst case condition allowed by the requirement to avoid contamination of the science light by the sun. The final step in sizing the solar arrays is to calculate the area and the mass required to provide adequate output power. The area is found by dividing the total average power requirement (P_{avg}) for the entire spacecraft by the power per unit area at EOL (Equation 22). The mass is calculated by multiplying the solar array area with the areal density (AD_{sa}) of the material used to construct the panels (Equation 23).

$$A_{sa} = P_{avg} / P_{EOL} \quad \text{Equation 22}$$

$$M_{sa} = AD_{sa} * A_{sa} \quad \text{Equation 23}$$

The power module also calculates the estimated mass of an RTG power source. Table 7 describes the properties of the RTGs used in this module [Larson & Wertz, 1992].

Table 7. RTG Properties

Property	Estimated Values
Power Conversion Efficiency	30 %
Specific Power	20 W/kg

The mass calculation for RTGs is much simpler than for solar arrays because this power source provides a constant level of output power independent of orbital radius. Therefore, the required output power for the RTG is found by simply dividing the average power requirement (P_{avg}) for the spacecraft by the power conversion efficiency (η_{RTG}) of the RTG (Equation 24). The mass is calculated by dividing the required output power with the RTG specific power (SP_{RTG}) (Equation 25).

$$P_{RTG} = P_{avg} / \eta_{RTG} \tag{Equation 24}$$

$$M_{RTG} = P_{RTG} / SP_{RTG} \tag{Equation 25}$$

The end result is the mass estimate for the RTG. It is important to note that the architecture type is included in the mass estimates for the different power subsystem sources. The issue is that only one power subsystem, located on the central bus, is required for an SCI architecture while an SSI architecture requires each spacecraft to have its own power subsystem. Since the impact of architecture type on average and peak power demands are taken into account by the other bus modules, the power subsystem mass is simply the sum of the mass estimates for the collector and combiner spacecraft. However, the overall power subsystem mass will be higher for an SSI architecture because the average and peak power demands will be higher to reflect the fact that each spacecraft requires its own bus.

Once the mass estimates for the different power sources have been determined, the power module moves on to the power storage requirements. The amount of power storage capability required for the power subsystem is dictated by the peak power demand for the spacecraft. Peak power is provided during certain periodic spacecraft operations such as slewing to a new target, transmitting data back to Earth, etc. The peak power demand affects the type, number, and size of the storage batteries. The properties of the batteries used in the power module are listed in Table 8 [Larson & Wertz, 1992].

Table 8. Battery Properties

Property	Estimated Values
Specific Energy Density	200 W-hr/kg
Depth of Discharge	60 %
Transmission Efficiency	90 %

The first step in finding the mass of the batteries is to calculate the required battery capacity based on the peak power load (P_{peak}), the time length of the peak power cycle (T_{peak}), the depth of discharge (DOD), the number of batteries (N), and the transmission efficiency (n) between battery and load (Equation 26).

$$C_r = \frac{P_{peak} * T_{peak}}{(DOD) * N * n} \quad \text{Equation 26}$$

In this module, the number of batteries is estimated based on the architecture type. A total of three batteries, located on the central bus, are used for an SCI architecture while two batteries for the combiner spacecraft and one battery for each of the collector spacecraft are used for an SSI architecture. The number of batteries can be adjusted to trade between battery mass and volume. The mass of the batteries is found by dividing the required capacity with the specific energy density (SED_b) of the battery (Equation 27).

$$M_b = C_r / SED_b \quad \text{Equation 27}$$

The last step in determining the total mass for the power subsystem is to estimate the masses of certain miscellaneous components such as the power control unit and the regulators/converters (the wiring mass is estimated in the propulsion module). This miscellaneous mass is combined with the power source and battery mass estimates to yield the total mass of the power subsystem. The power source and battery properties used in the power module were adjusted in favor of certain technological advances that are expected to happen before the construction of TPF. Some of these include higher power conversion efficiencies, specific power, and specific energy density as well as lower lifetime degradation. Most of these assumptions are within reason but certain advances still need to be demonstrated before they are completely valid. The mass estimates for the power subsystem are used by the spacecraft bus and payload macro-module to determine the best power source based on thermal considerations (solar arrays provide a certain level of heat shielding) as well as to optimize the mass and power distribution for the entire spacecraft bus.

Trade Space:

The trade space that is specific to the elements of the power module is somewhat limited. An initial trade of the power source used in this subsystem can be conducted to make a first

guess at the orbital radius where the source should be switched from solar arrays to RTGs. Figure 25 illustrates the mass relationship between the different power sources.

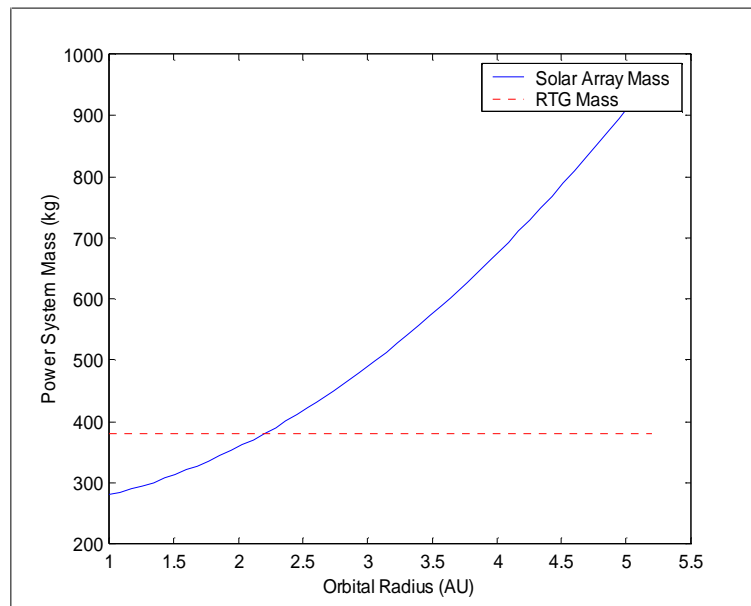


Figure 24. Solar Array and RTG Power System Masses

This plot shows that at orbits lower than about 2.25 AU, solar arrays should be used as the power source, while at orbits outside this limit, RTGs will provide the same amount of power with a lower subsystem mass. However, solar arrays can provide a certain amount of thermal shielding, which would increase the solar array/RTG crossover point based on the combined mass of the power and thermal subsystems. Because of this, the trade between solar arrays and RTGs is conducted in the Spacecraft bus and payload Macro-Module, where the power and thermal mass estimates can be combined. Additionally, the power subsystem mass is incorporated into the mass and power trade between the communications and the propulsion subsystems. This trade attempts to find the optimal mass and power estimates for all the components of the spacecraft bus.

7.3.4 Propulsion Module

Module Motivation:

The propulsion system provides the energy to maneuver the spacecraft system between targets and to dump built up momentum. In a separated spacecraft (SSI) mission, the propulsion system must also provide the energy to rotate each collector spacecraft about the combiner, maintaining a constant angular velocity and the system line of site. The purpose of the propulsion module is to estimate the mission V requirements and to chose the appropriate attitude control thrusters. For an SSI mission, the primary purpose of the propulsion module is to design a continuous low, thrust system.

The time required to transfer between targets influences the imaging rate of the science mission. From a propulsion standpoint, it requires less energy and propellant if more time is spent coasting between targets. The coasting time is limited by the baseline mission requirement and by the minimum mass philosophy of the bus. So, as with any propulsion system, there is a trade between mass, energy and time. The current baseline mission, however, does not appear to be time limited. This will be demonstrated in more detail in the module description section.

The primary driver for the propulsion system in a structurally connected (SCI) mission is the location of the thrusters. The thruster plumes are restricted from infringing into the line of site of the science instruments, and are required to be in the general vicinity of the propulsion tanks. That is, the thrusters could not be placed on the end of a deployable truss without an adjoining tank. The tank location restriction was established to simplify the deployment strategy.

On the other hand, the primary driver for the propulsion system in the SSI mission is the amount of time spent in continuous thrust. The thrust time is determined by the number of targets in the mission baseline and the total time spent integrating the science data at each target. Indirectly, the signal to noise ratio (SNR) requirement of the science data drives the SSI propulsion module development. The SNR is the most influential factor for determining the integration time, and therefore the continuous thrust requirement and propellant mass. The integration time is described in more detail in the aperture configuration module section.

Module Description:

The propulsion module takes the following inputs: the mission architecture, the mass estimate of the spacecraft, the integration time, the allotted subsystem power, and the momentum storage capacity of the momentum wheels. The source for the inputs are the design vector, the structural mass estimator module, the aperture configuration module, the power module, and the ACDS module. Using these inputs, the propulsion module calculates the dry mass of the propulsion system, the propellant mass, and the wiring mass of the power system, which depends on the final system dry mass. The module inputs and outputs are shown in Figure 30.

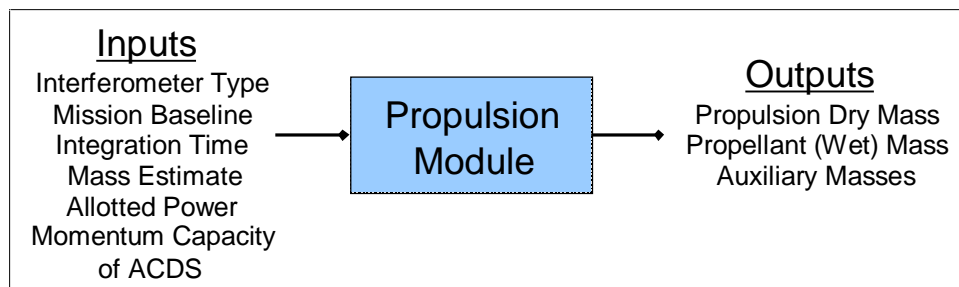


Figure 25. Propulsion Module Data Flow

SCI Architecture

The focus of the SCI propulsion model is on selecting and modeling the attitude control thrusters. These thrusters are sized to maneuver the spacecraft between targets, while satisfying the imaging rate requirement and the low mass philosophy of the bus. For the SCI mission, reaction wheels maintain the angular momentum of the spacecraft. To slew between targets, an appropriate set of thrusters will fire and the spacecraft line of site will precess to the next target. To ensure the thrusters are designed for the worst case scenario, the propulsion system will be able to slew the momentum biased spacecraft from a resting position. This is equivalent to slewing the spacecraft in a direction which none of the angular momentum can be utilized for the precession. The worst case thrusting times for a slew maneuver are calculated using Equation 28.

$$t_d = \frac{(I_{zz}\omega_{imaging})\omega_{transfer}}{lF} \quad \text{Equation 28}$$

The variable t_d is the thruster duty cycle, I_{zz} is the moment of inertia of the spacecraft about its spin axis, l is the moment arm of the thruster, $\omega_{imaging}$ is the angular velocity of the imaging and transfer stage, respectively.

If the thrusters are placed on the deployable truss, the moment arm length and the moment are known. The angular velocity of the imaging session is set to one revolution for every two hours, a reasonable integration time estimate. The force level of the thrusters is set to 5 Newtons and the transfer slew rate is set to 0.05 degrees per second, which will have a minimal dynamic effect on the spacecraft. The worst case transfer time is determined by the angle between the targets. The baseline mission includes 150 targets. If these targets are scattered along the celestial sphere -- as far away from one another as possible -- the transfer angle is 15 degrees. A 15-degree transfer will take 5 minutes, which defines the thrust time when multiplied by the thruster duty cycle. The thrust time was calculated for a reasonable range of spacecraft inertias (estimated from the structural module). This relationship is plotted in Figure 26.

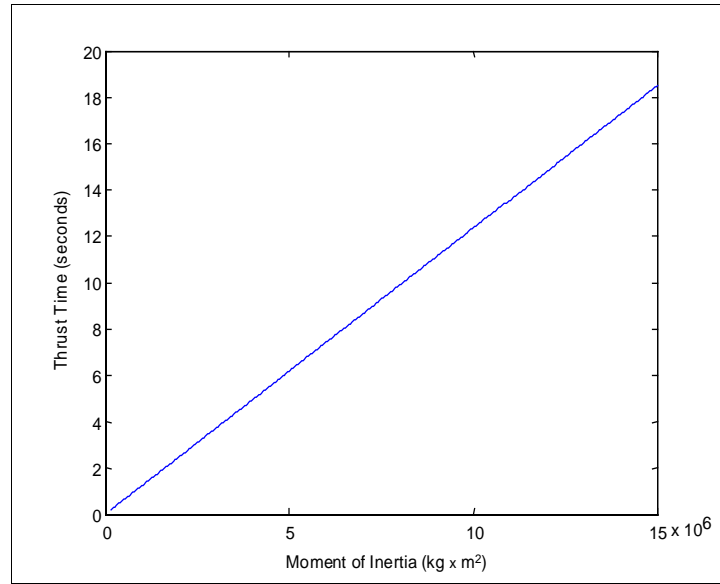


Figure 26. Thrust time vs. Moment of Inertia

Figure 26 shows a reasonable range of thrusting times for a 5-minute transfer. The baseline mission consists of 150 surveys, 50 coarse spectroscopy and 5 fine spectroscopy sessions. Assuming the scientists will not know whether a surveyed planet is a candidate for spectroscopy until all the surveys are completed, there will be a total of 205 transfers. Even if 5 minutes elapse for each transfer, the total transfer time for the mission is still less than one day, which is negligible compared to a 5-year mission.

A total of 12 thrusters, placed in suites of 3, will provide simultaneous, three axis translation and rotation capability. The ΔV expenditure for a target transfer maneuver was calculated using the simplified plane change formula in Equation 29.

$$\Delta V_{plane\ change} = 2V \sin(\theta/2) \quad \text{Equation 29}$$

ΔV is the change in velocity required by the propulsion system, θ is the angular distance between the targets, and V is the current tangential velocity of the deployed truss.

Note that plane change propellant was allotted for each spacecraft imaging session, even for situations where the plane change may be slight or nonexistent. This margin was included to ensure that a reasonable amount of propellant would be left for astrophysical imaging operations, which begin after the primary mission has been completed.

The plane change equation is typically applied to a single spacecraft held in orbit by gravity. In an SCI mission, the analog is two thrusters (180 degrees out of phase) held in place by the spacecraft structure. A factor of 4 will be applied to Equation 29 in order to calculate the total transfer ΔV . One factor of 2 was included because the spacecraft must start and stop; the other factor of 2 was included because the two thrusters must be fired simultaneously to maintain a constant angular velocity. This ΔV calculation is valid if the combiner section

mass is distributed very close to the center of gravity, and the deployed truss mass is not a major contributor to the spacecraft inertia. (This is not necessarily a good assumption.) Furthermore, the three-axis dynamics of the problem have been simplified in Equation 28, which assumes that the thrusters fire without disturbing the body fixed angular velocities.

A certain amount of V was allocated for spinning up the spacecraft for the cruise phase, for stopping the rotation prior to interferometer deployment, and for the initial rotation of the extended configuration. The propellant expenditure for momentum dumping is based on the total impulse that must be applied to unload a reaction wheel at its saturation limit. The propellant mass required for momentum dumping was calculated using Equation 30.

$$M_{dump} = \frac{(H/l)t_{total}}{I_{sp}g} \quad \text{Equation 30}$$

H is the momentum limit of the reaction wheels, l is the moment arm, t is the pulse time for one pulse, t_{total} is the total length of time spent pulsing over the entire mission, I_{sp} is the specific impulse of the thruster, and g is the acceleration of gravity. The impulse required to de-saturate the reaction wheels was approximated in the ACDS module and is summarized in Table 9. The moment arm was based on the average distance to the thruster suite positions because the momentum saturation could occur in any direction. The worst case scenario requires the momentum to be dumped once per day, for each of the four reaction wheels.

Table 9. Momentum Dumping Information

Interferometer Type	Spacecraft Type	Major Disturbance	De-saturation Impulse
SCI	combiner / collector	solar torque	7.2 N m s
SSI	combiner	solar torque	7.2 N m s
SSI	collector	thruster misalignment	28.7 N m s

Due to the relatively high force level of the thruster, electric thrusters were eliminated from the design space. The attitude control thrusters considered for operation are summarized in Table 10.

Table 10. Attitude Control Thruster Trade Space

Thruster Type	Propellant Type	Isp Estimate
Cold Gas	Nitrogen	70 seconds
Mono-propellant	Hydrazine	240 seconds
Bi-propellant	Tetra-oxide, Mono-Methyl-Hydrazine	290 seconds

The propulsion module considers the specific impulse of the thruster, the total mission V , and the total impulse required for momentum dumping when determining the propellant (wet) mass required for the baseline mission. For simplicity, the dry mass of the system was

assumed to 15% of the wet mass -- a reasonable estimate for chemical systems. This method favors the higher impulse of the bi-propellant engine, but in practice these systems are more complicated and have higher dry masses. In future versions of the TMAS, the propulsion module should include a comprehensive look-up table of off-the-shelf thruster systems, which have known thruster and valve mass values. The propulsion model would then size the volume and mass of the propellant tanks, and determine the total dry mass.

Collecting the total impulse requirements for momentum dumping and the total mission ΔV , the propulsion module solves the following system of equations for each thruster option.

$$M_{p|transfer} / M_o = 1 - \exp(-\Delta V_{total} / I_{sp} g) \quad \text{Equation 31}$$

$$M_{p|total} = M_o (M_{p|transfer} / M_o) + M_{p|dumping} \quad \text{Equation 32}$$

$$M_o = 1.04(M_{d|estimate} + 0.15(M_{p|transfer} + M_{p|dumping})) + M_{p|total} \quad \text{Equation 33}$$

M_o is the initial spacecraft mass, $M_{p|transfer}$ is the propellant required for slewing from target to target and for rotating the spacecraft, $M_{p|dumping}$ is the propellant required for dumping momentum, and $M_{d|estimate}$ is the initial dry mass estimate. The factor 1.04 is included in Equation 33 because the power system wiring is about 4 percent of the total system dry mass.

The propulsion module code then finds the minimum mass system and returns this value to the Spacecraft Macro-Module. In future versions of the propulsion code, a trade of complexity versus mass could be incorporated. This would return a more practical design value. The aforementioned dry mass simplification and the neglected complexity effects are an example of compromising fidelity for quick (and working) simulation.

SSI Architecture

The focus of the SSI propulsion model is on selecting and designing a continuous, low thrust system. (The centrifugal force provided by the structure in an SCI mission is replaced by a propulsion system in an SSI mission.) The required thrust value is a function of the collector spacecraft mass and the distance that the collector spacecraft is rotated about the combiner spacecraft. The thrust calculation is included as Equation 34.

$$T = M (\omega_{imaging} R)^2 / R \quad \text{Equation 34}$$

T is the thrust, ω is the angular velocity of an imaging maneuver, and R is the radial distance the collector spacecraft orbits about the combiner spacecraft. This relationship is plotted for a reasonable range of collector spacecraft masses in Figure 27. The dynamics of Equation 34 are quite simple because circular orbits are assumed. A more detailed analysis of the orbit's influence on an SSI mission is available in [Stephenson, et al].

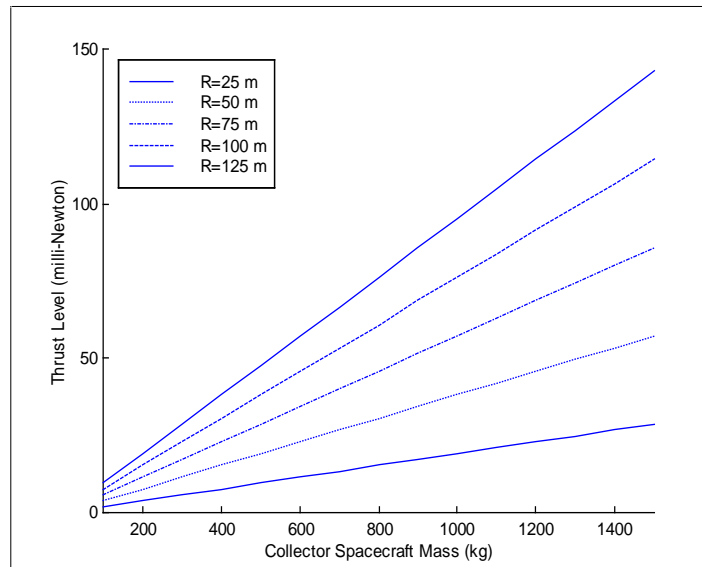


Figure 27. Thrust Level Requirements for an SSI Mission

The thrust range depicted in Figure 27 is conveniently within the range of electric propulsion engines. Table 11 lists the feasible electric engines, their thrust ranges, efficiencies, advantages and disadvantages.

Table 11. Electronic Propulsion Summary [Sutton]

Thruster Type	Thrust (mN)	<i>Isp</i> Range	Thruster Efficiency	Advantages	Disadvantages
Arcjet	2-700	400-1500	40-50%	Relatively high thrust Low power consumption Low plume divergence	Very high thermal noise Relatively low efficiency
Hall Thruster	0.001-2000	3000-5000	30-50%	High efficiency Easy to vary thrust	Low US flight experience Complex
Ion Bombardment	0.01-200	1500-5000	60-80%	Very high efficiency Easy to vary thruster Low plume divergence	Complex
PPT (Pulsed Plasma)	0.05-10	1000-2000	5-15%	Simple operation	Low thrust range Low efficiency

The ion bombardment engine was selected for the SSI mission because it meets all the requirements and because it can be implemented quite easily as a functional design. The ion engine has the following traits.

- Negligible effect on the thermal sub-system.
- Little plume impact on the science gathering instruments.
- A relatively simple operation throughout the thrust range.
- A considerably high efficiency.
- Wide support and interest within the industry.

The ion engine works by accelerating positive ions, produced by bombarding a neutral gas propellant with electrons emitted from a cathode. The electrons are influenced by a weak magnetic field, so they spiral towards the anode. The spiral motion is necessary because it slows the electrons down so that they actually collide and ionize a neutral propellant atom. The ions are accelerated through a pair of grids because a strong electric field is applied between them. Electrons are ejected into the ion stream, so that the plume remains neutral. A simple ion engine is sketched in Figure 28.

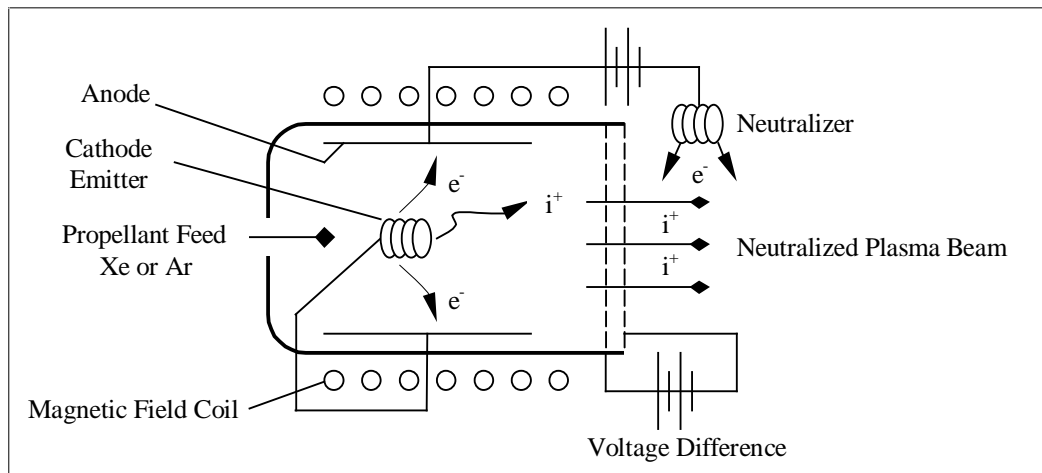


Figure 28. Simplified Ion Thruster Diagram

Varying the voltage applied across the accelerating grid controls the electric field strength. By varying the electric field strength, one effectively controls the thrust. Note that it is inefficient to operate an ion engine at off-nominal conditions. This inefficiency was taken into account in the modeling of the propulsion system.

Future versions of the propulsion module should consider adding Hall thrusters into the trade space. Hall thrusters are generally much less massive and more compact than their ion engine counterparts. Hall thrusters have some lifetime degradation issues, but are being developed quite extensively in the US. Hall thrusters were not included in this version of the code because the analysis is still quite well guarded, so there is relatively little information available to the public.

The propellant mass of the low thrust engine was dominated by the length of time the engine was operated. The first design decision was to determine whether it required more propellant to stop between imaging sessions or to continue to thrust and precess to the next target. The pause duration time for which it is more efficient to start and stop rather than to continuously thrust is determined by Equation 35.

$$t_{cutoff} = 2V / (V^2 / R) = 2 / \omega_{imaging} \quad \text{Equation 35}$$

The variable t_{cutoff} is the cutoff time, and $\omega_{imaging}$ is the angular velocity of an imaging maneuver. For the nominal integration time, the cutoff time is on the order of 30 minutes, which is a reasonably short period of time. Considering the housekeeping procedures that will be necessary during an SSI mission, it appears that start-stop operation is feasible. This assumption was carried throughout the SSI propulsion module development.

The attitude control thruster design for the combiner spacecraft matches the procedure outlined in the SCI section, assuming that the combiner remains fixed in space. Note that the 5 Newton thrusters can easily apply the ΔV needed to start and stop the collector spacecraft. So, the attitude control thruster design of the collector spacecraft is similar to that of the SCI spacecraft, except that the plane changes become simple rotations, start-stop pulses are included, and the impulse required for momentum dumping increased. (See Table 9.)

The continuous thrust time calculation is straightforward, assuming start-stop operation of the collectors. The continuous thrust is based on the baseline mission and the nominal integration times summarized in Table 12.

Table 12. Baseline Mission Summary

Science Category	Number of Sessions	Nominal Integration Time
Detection	150 x 6	> 2 hours
Coarse Spectroscopy	50	> 2.3 days
Fine Spectroscopy	5	> 15.1 days
Astrophysical Imaging	750+	unknown

According to the baseline mission, the total continuous thrust requirement totals 265 days. (This does not include the astrophysical imaging.) In order to include enough propellant for astrophysical imaging and off-nominal operations, a margin of 3 was included in the continuous thrust calculation. This amount of continuous thrust is more realistic in terms of the 5 year mission, but can lead to a relatively large propulsion system mass. The continuous thrust calculation is potentially a large source of error in the system, and can be a cause for discrepancies in benchmark cases.

While, the image integration time is calculated in the Aperture Configuration module, there is no limit to its length. So, the continuous thrust value is calculated as a function of the

actual integration times. This way, longer integration times are penalized in terms of the propulsion system. Furthermore, the Aperture Configuration module assumes that longer integration times occur in one long period, which corresponds to an extremely slow angular velocity. The ADCS and propulsion modules assume that this integration time is broken into two hour periods because the ADCS can not maintain the strict pointing requirement for days on end. Momentum will have to be dumped. The prime concern in long integration times, from a propulsion standpoint, is the slow angular velocity. According to Figure 27, a substantial decrease in angular velocity will result in a decrease of the thrust level below the available range of all electric thrusters. This restriction should be applied in future versions of the propulsion module.

The low thrust section of the propulsion module takes the power allocated to the system to make a mass estimate of the system and to calculate the corresponding specific impulse of the ion engine using Equation 36.

$$I_{sp} = \frac{Fg}{2\eta P} \quad \text{Equation 36}$$

F is the thrust force, η is the efficiency of the engine, P is the allocated power, and g is the acceleration of gravity. The I_{sp} of the engine is only valid between 1500 and 5000 seconds, so large mass penalties were assessed to systems where the power is either too low or too high. The engine efficiency was intentionally chosen closer to the low end (of ion engines) because of the wide range of operating thrusts. The thruster force, F , is a function of the mass, as shown in Equation 34. The mass was based on the initial dry mass fraction, multiplied by a corrective factor. The corrective factor can be back calculated using the following set of equations.

$$M_{p|ct} / M_o = 1 - \exp(-\Delta V_{total} / I_{sp} g) \quad \text{Equation 37}$$

$$M_{p|total} = M_o (M_{p|ct} / M_o) + M_{p|dumping} \quad \text{Equation 38}$$

$$M_o = 1.04(M_{d|estimate} + 0.15(M_{p|ct} + M_{p|dumping}) + M_{d|ct}) + M_{p|total} \quad \text{Equation 39}$$

$$f = M_o / M_{d|estimate} \quad \text{Equation 40}$$

M_o is the initial spacecraft mass, $M_{p|ct}$ is the propellant required for continuous thrusting, for slewing from target to target, $M_{p|dumping}$ is the propellant required for dumping momentum, $M_{d|estimate}$ is the initial dry mass estimate, $M_{d|estimate}$ is the dry mass of the electric engine, and f is the mass corrective factor. These equations were iterated until the corrective factor converged to within one percent of its previous result.

The dry mass of an electric engine must include a power processing unit, a thermal isolation system, a propellant flow system, structural components and the electric thruster. The dry mass values generally increase with power, as the propellant mass decreases. The dry mass

model was approximated using an empirical model provided by Electric Propulsion Laboratory, Inc. This model, summarized in the following equations, is not guaranteed to be accurate, but is a good first approximation.

$$M_e = 17.307 + 7.082 \ln(D) \quad \text{Equation 41}$$

$$M_{fs} = 4.707 + 2.62N \quad \text{Equation 42}$$

$$M_{pp} = 0.397(1000P)^{0.544} \quad \text{Equation 43}$$

$$M_s = 0.30(N)Me + 2.77(N)P \quad \text{Equation 44}$$

$$M_{d/ct} = N(M_{pp} + Me) + M_s + M_{fs} \quad \text{Equation 45}$$

M_e is the engine mass, D is the diameter of the engine, M_{fs} is the flow system mass, M_{pp} is the power processor mass, P is the power in Watts, M_s is the structural mass, and $M_{d/ct}$ is the total dry mass estimate of the ion engine. Future versions of the propulsion module could incorporate a look-up table of working engines, whose dry masses would be known.

Trade Space:

There are no fundamental design trades for the SCI propulsion system. The primary driver in the SCI system mass is the baseline mission, which is set. A future trade for the SCI propulsion system could be additional propellant versus additional imaging sessions. Because the baseline mission is so generously margined, this trade will not be useful until the entire mission (including astrophysical imaging) becomes more definite.

The fundamental design trade for the SSI propulsion system is mass versus power. The dry mass components of the propulsion system will slowly increase with power, while the propellant mass decreases as the specific impulse increases.

Using the propulsion module code, the relationship between mass and power for a collector spacecraft is plotted in Figure 29. The combiner spacecraft does not have an electric propulsion system and is not included in this trade.

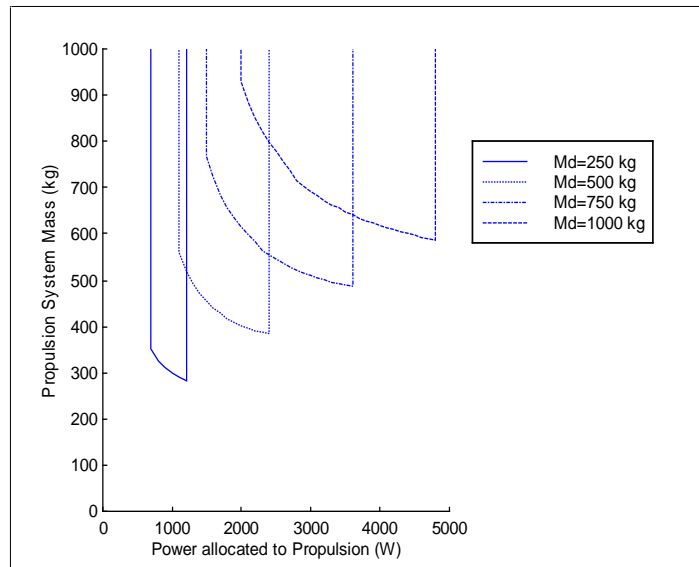


Figure 29. Propulsion System Mass for a Given Integration Time

Figure 29 demonstrates the expected trend – a decreasing system mass for increasing power. This indicates that the wet mass savings outweigh the dry mass gain, which corresponds with intuition. The vertical lines in Figure 29 correspond to the mass penalties at the technology limits (in terms of specific impulse) of the ion engines. Notice that the larger the dry mass estimate is, the larger the propulsion system mass ranges. This demonstrates the direct impact mass has on thrust and hence on specific impulse, as indicated in Equation 34 and in Equation 36. The higher the mass, the larger the corresponding power must be to span the specific impulse range of ion engines.

The propulsion system module does not try to choose the optimal points in Figure 29. Instead it allows the spacecraft bus algorithm to perform a bus-wide optimization. However, in most cases, the minimum bus mass corresponds to a minimum propulsion system mass.

7.3.5 Thermal Module

Module Motivation:

Three thermal requirements have been derived from the system requirements for the TPF mission and are shown in Table 13 below. The Optical Detector and Optical Train temperature requirements are derived from the specifications for the instrument sensitivity in the near IR frequencies. The Spacecraft Electronics temperature requirement is derived from the operating temperature range for space qualified electronic components. The ambient blackbody temperature for the spacecraft is expected to be between 100 and 200 K for the range of solar orbits under consideration, indicating a need for both cooling and heating capabilities for different parts of the spacecraft.

Table 13. TPF Spacecraft Thermal Requirements

Component Description	Temperature
Optical Detector	4-6 K
Optical Train Components	~35 K
Spacecraft Electronics	~300 K

Module Description:

A schematic of the thermal module indicating the module inputs and outputs is shown in Figure 30. Many of the assumptions made in the module processing were made following evaluations of the designs for other spacecraft such as the Space Infra-Red Telescope Facility (SIRTF), the Infra-Red Space Observatory (ISO) and its proposed follow-on mission, the Far Infra-Red and Sub-millimeter Telescope (FIRST).

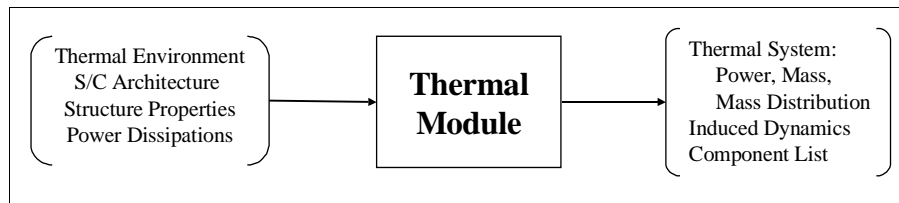


Figure 30. Thermal Module Inputs and Outputs

The spacecraft is(are) assumed to have a hot side and a cold side, separated by some combination of thermal shields and Multi-layer insulation (MLI). The amount of shielding required for each collector is calculated using the collector size, the incident solar radiation, typical properties of MLI (absorptivity, emissivity, etc.), and an assumed radiative shape factor of 0.5 between successive shields. The initial number of shields (2 or 3) is selected to meet the optical train cooling requirement. Most calculations are based on the Stefan-Boltzmann equation (Equation 46). For cases that use solar arrays to generate spacecraft power, the outermost thermal shield is eliminated since the solar array can provide an equivalent shielding effect.

$$G = \alpha \epsilon \sigma T^4 \quad (\text{W/m}^2) \tag{Equation 46}$$

where

- α : absorptivity
- ϵ : emissivity
- σ : Stefan-Boltzmann constant
- T : Temperature

For the detector, the thermal shields are assumed to be part of the bus structure. The final stage of cooling to the optical detector requirement temperature is assumed to be accomplished using a cryocooler. The simplifying assumption was made that the thermal shields could be appropriately designed such that this final stage cryocooler will have essentially the same requirements regardless of operational orbit and onboard power dissipation thermal loads.

Trade Space:

The fundamental trade in the thermal module is between mass and power. The initial configuration is generated to use the minimum power by maximizing the use of passive cooling techniques. Subsequent thermal system configurations are generated by replacing thermal shield elements, starting with the most massive, with a generic active cooling element assumed to be a cryocooler (mass of 40 kg and continuous power requirement of 150 W). This information is used by the bus integration module to conduct a bus level power vs. mass optimization.

7.4 Dynamics, Optics Controls, and Structures (DOCS) Macro-Module

The Dynamics, Optics Controls, and Structures (DOCS) Module provides the link between aperture physics and the performance modeling in the GINA module. The motivation for this module is the desire to model the difficulties in maintaining a nanometer precision optical pathlength between the apertures and the combiner of the TPF for SCI and SSI spacecraft architectures. Figure 31 provides an overview of the DOCS module, including inputs, data flow, and outputs. The following sections describe the modules in the order they are executed in the TMAS: Structures, Optics Control, ADCS, Integration, and Disturbance Analysis.

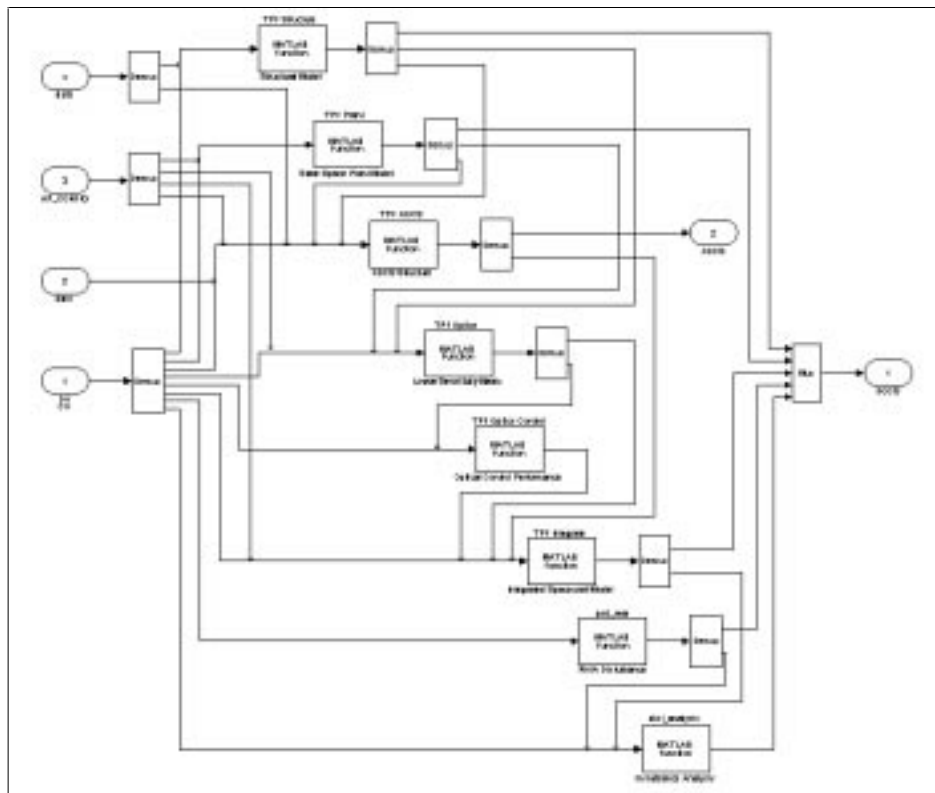


Figure 31. DOCS Macro-Module Flow Diagram

7.4.1 Structural Design Module

Module Motivation:

The purpose of the structural design module is to automatically create reasonable structural models for structurally connected (SCI) and separated spacecraft (SSI) interferometer concepts.

Module Description:

The generic spacecraft design is based on the simple concept of a central hub, which contains the combiner, the spacecraft bus, and the high-gain communications antenna. The apertures are located in a plane around the hub and are identified by their radius from the hub and their clock angle. This information is provided by the aperture configuration module. In the structurally connected case, a deployable truss connects each aperture with the central hub or with another aperture that is located on the same radial spoke. Each truss and its associated canister are dimensioned based on existing empirical engineering relationships for truss diameter and mass. The design is parameterized and scales with the number of apertures and with the number of radial spokes from the central hub; this includes the shape of the hub itself.

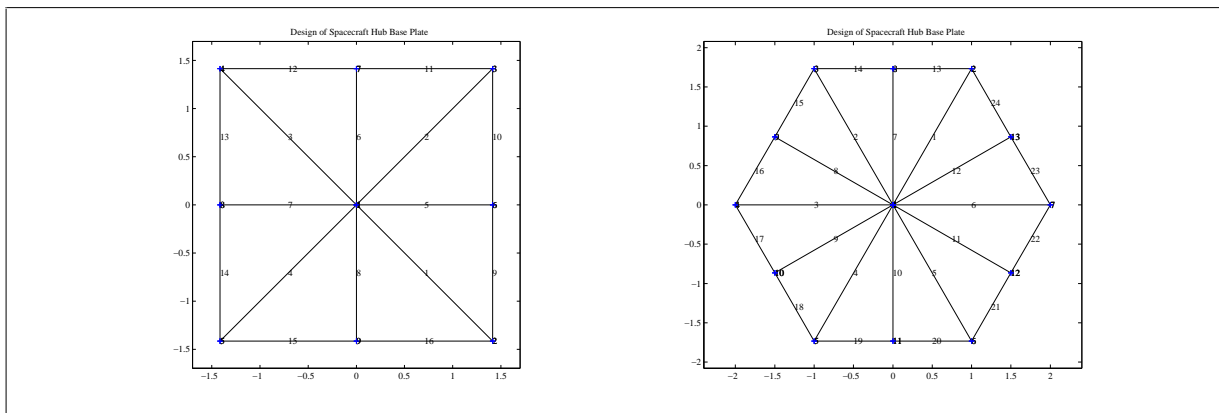


Figure 32. Design of Hub Base Plate

The first step in the structural design module is the design of the hub base plate. Figure 32 shows the configuration for 2 and 4 radial spokes on the left and for 6 radial spokes on the right. The number of radial spokes does not necessarily correspond to the number of apertures, since several apertures may be located along the same radial direction. Next, the bottom and top plates and the vertically connecting structure (truss elements) are designed. Again, the dimensions are parameterized based on the Lockheed-Martin A2100 bus design [Lockheed Martin]. The high gain antenna is added as a circular parabolic dish. The antenna diameter and point mass are obtained from the bus macro-module and are computed based on the orbital radius. The apertures are modeled as simple siderostat bays with crossbars to improve rigidity. The central node contains the collector mass and, in the SSI case, the additional mass due to the separate bus components that support each collector spacecraft.

In the SCI case, the code proceeds with the truss design and calculates the truss system mass, the corresponding mast diameter, and the canister mass fraction for a deployable articulated truss of a given baseline and bending stiffness. These functions are based on the ABLE Deployable Articulated Mast (ADAM) System [ADAM Technology Manual] and consists of 2D-lookup tables for these critical truss and canister design parameters. The 2D-lookup tables were created from a plot in the AEC-ABLE technical manual: "ADAM System Mass, Corresponding Mast Diameter and Canister Mass Fraction vs. Bending Stiffness for 25m, 50m, 100m and 500m Deployment Lengths." The data for the 10 meter baseline was extrapolated. Figure 33 provides a graphical representation of these lookup tables.

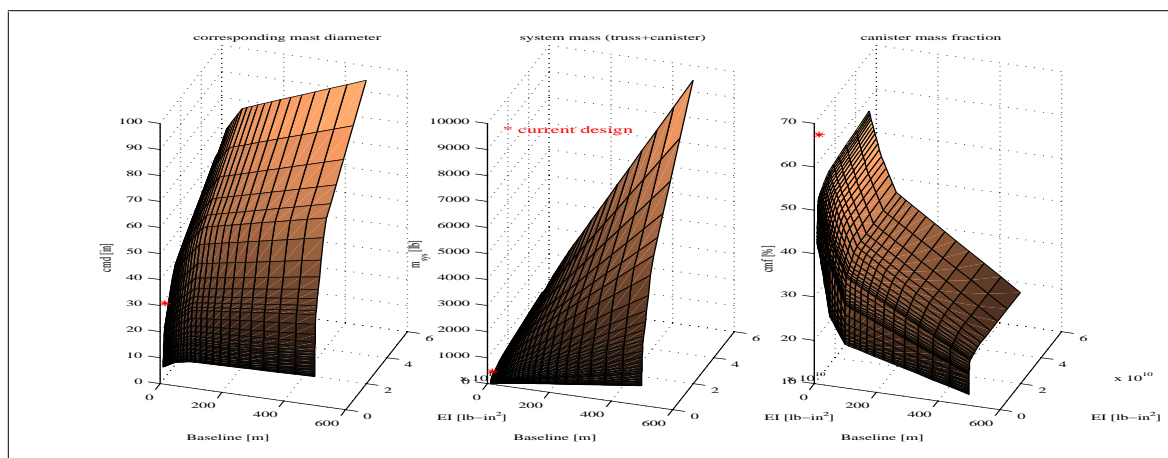


Figure 33. Lookup Tables for Truss Properties

Due to the large dimensions of the separations between apertures in the SCI case, it would be difficult to model the deployable trusses between the apertures in such detail that each truss member (joints, longerons, battens, diagonals) would be represented by one or several finite elements. Such an approach would lead to an extremely large order FEM. Consider, for example, a truss with 20 bays and 16 nodes per bay. This would lead to $20 \cdot 16 \cdot 6 = 1920$ degrees of freedom for only a single truss. Therefore, it is standard practice to represent the truss with equivalent Bernoulli-Euler (BE) beam elements. This is acceptable up to an aspect ratio of bay diameter/length of ~ 25 . For very long slender beams a Timoshenko beam representation is preferable.

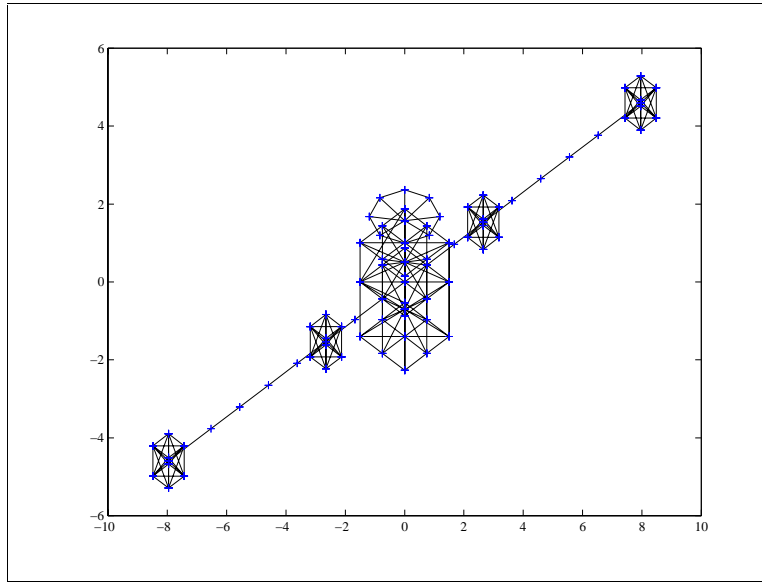


Figure 34. Graphic Representation of an Assembled Finite Element Model

The BE beams capture bending in 2 directions: torsional and axial tension and compression. However, it is important that realistic material properties are used for the equivalent beam elements. A special effort was made in this respect. Other beam properties such as torsional stiffness, GJ, were determined from the bending stiffness, EI, based on the equivalent ratios for the SRTM mission [Gross and Messner]. Once the truss elements are designed, the entire FEM is assembled, including the associated material properties, the boundary conditions, and the global mass and stiffness matrices, M and K. The FEM can be displayed by the user as shown in Figure 34.

The FEM model is compatible with and requires access to the IMOS V2.0 toolbox. The following functions from IMOS are called from within the Structures Module: posunique.m, trans.m, mkboom.m, genrot.m, unit.m, bcond.m, conm.m, truss.m, beam.m, cg_calc.m, wtcg.m, viewfem.m, iso.m, scale.m, rotx.m, fourvu.m. An effort was made to restrict the utilized element types to bars, beams (Bernoulli-Euler formulation), generalized stiffnesses (celas) and to concentrated masses (conm's). The current version only uses beams, rods and conm's. The structural design module also computes the CG location, the total system mass, and the tensor of inertia in spacecraft coordinates.

Following the finite element model, the plant model is responsible for creating a state space representation of the spacecraft (plant) structural dynamics. The generalized eigenvalue problem [Craig] is shown in Equation 47, where $\lambda = \omega^2$ are the eigenvalues, which correspond to the squares of the natural frequencies of the system.

$$[\mathbf{K} - \lambda_i \mathbf{M}] \cdot \phi_i = 0$$

Equation 47

The variable λ_i is the i^{th} eigenvalue of the structure and ϕ_i is the i^{th} eigenvector. The ϕ_i 's are the columns of the matrix Φ , that is sometimes referred to as the mode shape matrix. The eigenvalues are computed by setting the determinant of $[\mathbf{K} - \lambda_i \mathbf{M}]$ to zero.

$$\det[\mathbf{K} - \lambda \mathbf{M}] = 0 \quad \text{Equation 48}$$

The result, after evaluating the determinant and some algebra, is a polynomial of degree n equal to the number of degrees of freedom of the system, that can be solved for the eigenvalues, λ . The eigenvalues with a value of zero correspond to the rigid body modes (6 total). These are critical for the design of the TPF attitude determination and control system.

The next step consists of computing the eigenvectors, ϕ_i . The physical interpretation of the eigenvectors as mode shapes is based on the underlying notion that the relative magnitudes of the components of the eigenvector correspond to the dynamic displacements occurring at that particular natural frequency.

It is useful and customary to normalize the columns of the eigenvector matrix, Φ . For structural dynamics purposes, the mass matrix \mathbf{M} is used for this normalization. In the normal coordinate frame, arbitrary motions of the system are represented by linear combinations of the (orthogonal set of normalized) eigenvectors. The modal mass matrix $\tilde{\mathbf{M}}$ is obtained by pre-multiplying \mathbf{M} with the transpose of Φ and by post-multiplying with Φ (see Equation 49).

$$\Phi^T \mathbf{M} \Phi = \tilde{\mathbf{M}} = \tilde{\mathbf{M}}^{1/2} \cdot \tilde{\mathbf{M}}^{1/2} \quad \text{Equation 49}$$

Thus, the normal modes of an undamped structure are orthogonalized by the mass matrix. $\tilde{\mathbf{M}}$ is the matrix containing the modal masses on the main diagonal. Pre- and post-multiplication with $\tilde{\mathbf{M}}^{-1/2}$ is shown in Equation 50.

$$\underbrace{(\tilde{\mathbf{M}}^{-1/2})^T}_{\text{}^o\Phi^T} \Phi^T \mathbf{M} \Phi \underbrace{\tilde{\mathbf{M}}^{-1/2}}_{\text{}^o\Phi} = (\tilde{\mathbf{M}}^{-1/2})^T \tilde{\mathbf{M}}^{1/2} \cdot \tilde{\mathbf{M}}^{1/2} \tilde{\mathbf{M}}^{-1/2} = \mathbf{I} \quad \text{Equation 50}$$

$\text{}^o\Phi$ is called the mass normalized mode shape matrix. Invoking the orthogonality relationships, as with the mass matrix, the stiffness matrix \mathbf{K} is pre- and post-multiplied with $\tilde{\mathbf{M}}^{-1/2}$ to obtain Equation 51.

$$\underbrace{(\tilde{\mathbf{M}}^{-1/2})^T}_{\text{}^o\Phi^T} \Phi^T \mathbf{K} \Phi \underbrace{\tilde{\mathbf{M}}^{-1/2}}_{\text{}^o\Phi} = \Lambda = \text{}^o\Phi^T \mathbf{K} \text{}^o\Phi = \Lambda = \Omega^2 \quad \text{Equation 51}$$

The eigenvectors, as a linearly independent, orthogonal set of $N = 3$ vectors, can be used as a basis for the N space. Thus, the transformation from physical coordinates to modal

coordinates is represented by Equation 52 and the equations of motion in normal (modal) space are represented by Equation 53.

$$\mathbf{x} = {}^o\Phi \xi \quad \text{Equation 52}$$

$$\mathbf{M} \ddot{\mathbf{x}} + \mathbf{K} \mathbf{x} = \mathbf{M}^o\Phi \ddot{\xi} + \mathbf{K}^o\Phi \xi = \mathbf{F} \quad \text{Equation 53}$$

Pre-multiplication of Equation 53 with ${}^o\Phi^T$ yields Equation 54.

$$\underbrace{{}^o\Phi^T \mathbf{M}^o\Phi}_{\mathbf{I}} \ddot{\xi} + \underbrace{{}^o\Phi^T \mathbf{K}^o\Phi}_{\Omega^2} \xi = \underbrace{{}^o\Phi^T \mathbf{F}}_{\mathbf{Q}} \quad \text{Equation 54}$$

The modal form of the equations of motion is especially convenient because the coupled 2nd order differential equations are now decoupled, which makes them easy to solve. At this point, it is convenient to add damping to the TPF system design by setting the damping coefficient, ζ , to 0.001.

In practice, the modal damping coefficients are often different for every mode and typically vary between 0.1% and 3% for lightly damped space structures. The equations of motion in modal coordinates can be expressed using a state vector of modal coordinates and modal velocities, as shown in Equation 55.

$$\mathbf{q}_p = \begin{bmatrix} \xi \\ \dot{\xi} \end{bmatrix} \quad \text{Equation 55}$$

The subscript p indicates states of the structural plant. The modal force matrix \mathbf{Q} can be broken up into contributions from control inputs \mathbf{u} and disturbances \mathbf{w} , where β_u and β_w are the control and disturbance influence coefficient matrices, respectively. \mathbf{B}_u and \mathbf{B}_w are matrices that usually contain only ones or zeros to indicate at which degrees of freedom of the structural plant the forces act (Equation 56).

$$\mathbf{Q} = {}^o\Phi^T \mathbf{F} = {}^o\Phi^T \mathbf{F}_u + {}^o\Phi^T \mathbf{F}_w = {}^o\Phi^T \beta_u \mathbf{u} + {}^o\Phi^T \beta_w \mathbf{w} \quad \text{Equation 56}$$

Then, the equations of motion (the “dynamics”) for a particular TPF configuration can be written in 2nd order modal form, with the assumption that the structure exhibits linear behavior (Equation 57).

$$\frac{d\mathbf{q}_p}{dt} = \underbrace{\begin{bmatrix} \mathbf{0} & \mathbf{I} \\ -\Omega^2 & -2\mathbf{Z}\Omega \end{bmatrix}}_{\mathbf{A}_p} \mathbf{q}_p + \underbrace{\begin{bmatrix} \mathbf{0} \\ {}^o\Phi^T \beta_u \end{bmatrix}}_{\mathbf{B}_u} \mathbf{u} + \underbrace{\begin{bmatrix} \mathbf{0} \\ {}^o\Phi^T \beta_w \end{bmatrix}}_{\mathbf{B}_w} \mathbf{w} \quad \text{Equation 57}$$

The other important relationships that complete the state space representation are the output \mathbf{y} and the performance \mathbf{z} equations. In general, the outputs are given as a linear combination of the coordinates in physical space (Equation 58), or as a combination of states in modal space (Equation 59).

$$\mathbf{y} = \mathbf{C}_{yx}\mathbf{x} + \mathbf{C}_{y\dot{x}}\dot{\mathbf{x}} = \mathbf{C}_{yx}^o\Phi\xi + \mathbf{C}_{y\dot{x}}^o\Phi\dot{\xi} = \begin{bmatrix} \mathbf{C}_{yx}^o\Phi & \mathbf{C}_{y\dot{x}}^o\Phi \end{bmatrix} \mathbf{q}_p \quad \text{Equation 58}$$

Output equation:
$$\mathbf{y} = \underbrace{\begin{bmatrix} \mathbf{C}_{yx}^o\Phi & \mathbf{C}_{y\dot{x}}^o\Phi \end{bmatrix}}_{\mathbf{C}_y} \mathbf{q}_p + \underbrace{\begin{bmatrix} \mathbf{0} \\ \mathbf{0} \end{bmatrix}}_{\mathbf{D}_{yu}} \mathbf{u} + \underbrace{\begin{bmatrix} \mathbf{0} \\ \mathbf{0} \end{bmatrix}}_{\mathbf{D}_{yw}} \mathbf{w} \quad \text{Equation 59}$$

Performance equation:
$$\mathbf{z} = \underbrace{\begin{bmatrix} \mathbf{C}_{zx}^o\Phi & \mathbf{C}_{z\dot{x}}^o\Phi \end{bmatrix}}_{\mathbf{C}_z} \mathbf{q}_p + \underbrace{\begin{bmatrix} \mathbf{0} \\ \mathbf{0} \end{bmatrix}}_{\mathbf{D}_{zu}} \mathbf{u} + \underbrace{\begin{bmatrix} \mathbf{0} \\ \mathbf{0} \end{bmatrix}}_{\mathbf{D}_{zw}} \mathbf{w} \quad \text{Equation 60}$$

The vector \mathbf{y} contains all the outputs of the system that are captured by sensors, i.e. they are actually measured, whereas \mathbf{z} contains the metrics by which the performance of the system is assessed.

The strategy for the SSI case is to solve the generalized eigenvalue problem for each spacecraft individually and then to append them into the overall system as completely parallel systems. The only thing that ties them together is the performance metric and the ADCS.

Trade Space:

A consolidated discussion of the DOCS module trades is included in Section 7.4.6 below.

7.4.2 Optics Control Module

Module Motivation:

The optics control module is responsible for computing the optics linear sensitivity matrix, which relates the physical displacements and rotations of the combiner and the apertures to the optical performance metrics. Currently the only optical performance metric included is the optical pathlength difference (OPD). Future work could include line-of sight (LOS) jitter, wavefront tilt (WFT) and differential beam shear (DBS).

Module Description:

Figure 35 shows how the OPD is computed based on the pathlength difference between the reference aperture and the i^{th} aperture.

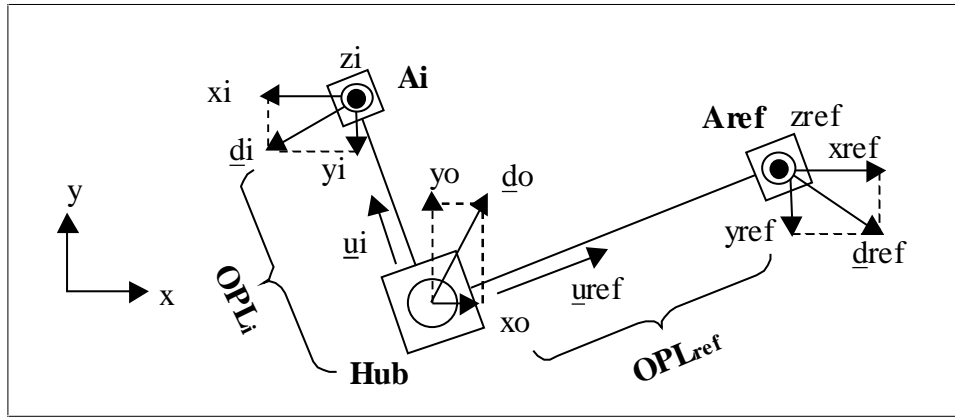


Figure 35. Optics Modeling Diagram

The optical pathlength difference is defined as $OPD_i = OPL_{ref} - OPL_i$ and can be computed as a linear combination of the displacement degrees of freedom from the hub, the reference aperture, and the i^{th} aperture, as indicated in Equation 61.

Reference pathlength:
$$OPL_{ref} = R - z_{ref} + r_{ref} + \bar{d}_{ref} \cdot \bar{u}_{ref} - \bar{d}_o \cdot \bar{u}_{ref} \quad \text{Equation 61}$$

OPL_{ref} is the optical pathlength from the reference aperture to the hub. The reference aperture is the aperture with the *largest radial distance from the hub* and appears first in the sorted aperture list. R is the distance of the aperture to the reference plane of the incoming stellar wavefront. The quantity z_{ref} is the z displacement of the reference aperture. The quantity r_{ref} is the nominal radius of the reference aperture from the hub. Furthermore, d_{ref} is the displacement vector of the reference aperture, u_{ref} is the unit normal vector along the radial of the reference aperture, and d_o is the displacement vector of the hub.

Pathlength of i^{th} aperture:
$$OPL_i = R - z_i + r_i + r_{ODL_i} + \bar{d}_i \cdot \bar{u}_i - \bar{d}_o \cdot \bar{u}_i \quad \text{Equation 62}$$

In Equation 62, OPL_i is the optical pathlength of the i^{th} aperture, z_i is the z displacement of the i^{th} aperture, r_i is the radial distance of the i^{th} aperture, r_{ODL_i} is the fixed delay introduced by the optical delay line (ODL) of the i^{th} aperture, d_i is the displacement vector of the i^{th} aperture, and u_i is the unit normal vector along the radial belonging to the i^{th} aperture. The ODL located within the combiner section is assumed to be able to compensate for the nominal pathlength difference between the hub and the reference aperture, resulting in Equation 63.

$$r_{ref} = r_i + r_{ODL_i} \quad \text{Equation 63}$$

Based on this assumption, only the relative displacements of the hub and apertures with respect to each other will enter into the OPD metric. The C_z matrix is computed based on the above relationships. Optical control through ODL's and fast steering mirrors (FSM) has

not been modeled in great detail, but the effect of optical control on the OPD has been approximated. This is done by passing the optical performance metrics through a low order high pass filter, which treats each channel independently as shown in Equation 64.

$$G_{ODL} = \frac{K_{odl}s}{s + \omega_{odl}} \quad \text{Equation 64}$$

Trade Space:

A consolidated discussion of the DOCS module trades is included in Section 7.4.6 below.

7.4.3 Attitude Determination and Control Module

Module Motivation:

In order to provide the nulling performance needed for planet detection, the geometry of the TPF optical instruments must be maintained within very strict accuracy requirements. To satisfy this goal and to allow for the limited bandwidth and dynamic range of available sensors and actuators, a layered control system is designed. In the current design, two decoupled control loops are envisaged. The Attitude Determination and Control System (ADCS) will be responsible for controlling the optics position and attitude with centimeter and arc-second accuracies. The main purpose of the ADCS is to stabilize rigid body motions, and to reject disturbances at low frequencies. This is achieved by sensing the current attitude (and relative position in the SSI case) using an appropriate suite of sensors and providing control torques and forces using thrusters and angular momentum control/storage devices.

The ADCS subsystem design is strongly coupled with the spacecraft configuration, and with other subsystems, such as the propulsion subsystem. The purpose of the ADCS design module is to characterize the achievable performance in the face of the foreseen worst-case environmental disturbance and the spacecraft disturbances injected into the system by the ADCS actuators themselves (namely, the effects of static and dynamic imbalances in the Reaction Wheel Assemblies). The results of the ADCS module are also used to size the reaction wheel assemblies (RWAs).

Module Description:

Due to the wide range of variability of several key options in the TPF system design, care has been taken in the design of this module to automatically determine an “optimal” ADCS system, with no direct intervention by the human operator. The ensuing ADCS design is only locally (to the ADCS) optimal, and no claims are made about optimality in the broader system sense. However, some consideration and constraints following from physical intuition and engineering insight have influenced the design process, at least as far as the coupling with closely related modules is concerned (DOCS).

During TPF mission lifetime, the spacecraft will operate in different attitude control modes, namely

- emergency, or safe mode (e.g. sun pointing),
- transfer orbit mode,
- formation change/slew mode,
- science observation mode.

These modes are characterized by different requirements in terms of accuracy and robustness to other subsystems failures or anomalies, and consequently will usually require the use of different sensors and possibly different actuators.

The ADCS module has been developed to meet the most difficult requirements, corresponding to the science observation mode. For the science mode, the mission requirements can be met only by a three-axis stabilization technique (even though the TPF spacecraft in the envisioned operational profile will be spinning, the rotation rate of 2 rpm is far from enough to provide any consequential gyroscopic stiffness).

At the TPF operational orbit, the (external) disturbance torques will be dominated by the solar radiation pressure effect, and to a lesser extent, by the tidal or gravity gradient effect. The torque due to the solar radiation pressure can be expressed as Equation 68.

$$T_{sp} = F(c_{ps} - c_g) \tag{Equation 65}$$

where

$$F = \frac{F_s}{c} A_s (1 + q) \cos i \tag{Equation 66}$$

F_s is the solar constant (1358 W/m² at the Earth's orbit), c is the speed of light, A_s is the cross-section area, c_{ps} is the center of solar pressure, c_g is the center of gravity, q is the reflectance factor (assumed to be 0.6), and i is the angle of incidence of the Sun (taken to be 0).

The actual computation of the location of the solar center of pressure can be an extremely difficult task. Since all attitude configurations with respect to the Sun should be considered, interactions between different parts of the system should be taken into account (e.g. shadows), and specific details about the system implementation would be needed (e.g. reflectance factor for the different materials). To reduce the complexity of the system performance evaluation, only a worst case deviation due to solar pressure of 5% of the maximum baseline length is considered.

The maximum torque due to the differential gravity forces can be expressed as Equation 70, where μ is the gravitational parameter of the Sun, R , is the orbital radius, and I_{\max} and I_{\min} are respectively the maximum and minimum moments of inertia.

$$T_g = \frac{3\mu}{2R^3} (I_{\max} - I_{\min}) \tag{Equation 67}$$

The mass property data are readily available from the structural design module (at least their nominal values). For the TPF, the effect of the gravity gradient is noticeable only for the SCI case with very long baselines.

Apart from externally generated disturbances, some on-board systems will generate indigenous disturbance torques and forces. The main sources of such disturbances will be the reaction wheel assemblies and the cryocoolers (described in the disturbance analysis module).

The generation of disturbances by the RWA presents an interesting control problem, in that the use of RWA for stabilizing the rigid body modes results in an effective transfer of disturbances power from low frequencies to higher frequencies corresponding to the harmonics of the RWA revolution speed.

Moreover, in the SSI case, the thrusters will be firing during observations to maintain formation. Since the operational scenario calls for a rotating baseline, the thrusters will be constantly providing the required centripetal acceleration. This continuous thrusting will inevitably translate into some torque disturbance due to misalignments. A worst case misalignment angle is assumed to be 1 degree.

The main attitude sensing devices for high accuracy requirements are star trackers. To improve the achievable performance of the closed-loop ADCS system, the additional use of rate gyros is suggested. The resulting attitude sensing is very similar to the current design for the NGST [Mosier and Fermiano, 1999]. The NGST ADCS design team claims that such a system will provide an attitude steady state error (1 σ) of 0.3 to 0.4 arcsec when combined with a Kalman filter. The sensor sample rate is assumed to be 10 Hz for the rate gyros, and 2 Hz for the star trackers. For the TPF mission, it is reasonable to assume a better performance since the star trackers can be sampled at a relatively high rate. This is due to the fact that the optics boresight will be pointed at a rather close and bright star, in contrast to NGST, which will be looking at very faint objects. As a consequence, the integration times required from the star trackers on the TPF can be considerably lower.

The attitude actuators on the TPF will consist of reaction wheel assemblies (RWAs) for angular momentum control and storage, and thrusters for slewing maneuvers, for momentum dumping, and for formation flying in the SSI case.

The RWA design in this module is dictated by several factors. First, the RWA torque capability must be greater than the maximum expected environmental torque. Second, the RWA must be able to store enough momentum to reduce the frequency of momentum dumping operations below a given threshold (e.g. once a day). Momentum dumping requires the use of thrusters, and hence could disrupt the attitude accuracy attained during science observations. Third, rather than fine tuning the available "free parameters" that characterize the momentum wheels (i.e. mass properties, max speed, max torque), a "COTS" approach is taken. The most appropriate commercially available RWA that

satisfies the minimum torque and momentum storage requirements is selected from a range of RWAs produced by Ithaco, as reported in their web site, <http://www.ithaco.com>. The number of RWAs required is usually four, mounted in such a way as to provide three independent directions with any three RWAs, to maintain full control authority in the event of a single failure.

Image removed due to copyright restrictions.

Figure 36. Ithaco E-Wheel

The TPF ADCS design is based on methods adapted from [Mosier and Fermiano, 1999], [Athans, 1998], and [Dahleh and Diaz-Bobillo, 1995]. The interested reader should refer to these sources and to textbooks on advanced linear control for mathematical details. A brief discussion follows.

To perform an automated control system design for the TPF spacecraft, the structural model must be reduced to a manageable size without losing any relevant dynamics information. First, the uncontrollable and unobservable modes are removed. One such mode is the rigid body translation mode of the entire TPF spacecraft. This mode is (linearly) unobservable, since it requires accurate orbit determination, which can not be determined directly from the attitude and relative position measurements. However, there is no requirement for the TPF spacecraft to remain at an exactly specified location in space, only that the collectors are kept in the nominal position with respect to the combiner during science gathering operations. Thus, the rigid body modes involving translations of the combiner may be safely removed from the controller model.

Even after the removal of these modes (3x2 states), the structural model is still too large for effective controller design. A model reduction is required. A popular method for model reduction involves balancing the plant. Common (i.e. available in MATLAB) numerical algorithms for finding a balanced realization (that is, a realization for which the controllability and observability gramians are equal and diagonal) require strictly stable plants, whereas the TPF structural plant still includes all the rigid body modes (attitude and collector translations). To address this issue, the rigid body modes are converted to low-frequency, lightly damped modes by adding “virtual springs” between the spacecraft model and fixed points in space.

Once there is a balanced realization, a reduced order model can be obtained by (balanced) truncation, or by finding the optimal Hankel norm approximation (via the *Nehari's theorem*, see [Dahleh and Diaz-Bobillo, 1995]). The option is left to the user, who can set the appropriate flag in the TMAS software, together with the maximum number of modes to retain.

Once a reduced order model is obtained, a generalized plant is constructed that takes into account the translation in the frequency domain of performance requirements (command tracking, disturbance rejection, etc.). This is done by the standard technique of adding performance weights, effectively designing an “obstacle course” for the loop transfer function, see [Athans, 1998]. Frequency weights are added to the OPD error (the metric that must be minimized), as a low-pass filter to obtain good tracking at low frequencies. Additionally, frequency weights in the form of a high pass filter are added to the control channels to enhance the robustness to noise, unmodeled dynamics, and time delays by avoiding high control bandwidth. The high pass filter’s gain increases starting at a frequency that is 10% of the first non-zero frequency of the original plant (the first flexible mode). This design process is an automated version of the “LQR control cost tweaking” technique for controller bandwidth selection.

Finally, some comments about the attitude sensing subsystem. To avoid dealing with details such as raw data filtering and attitude reconstruction (quaternion propagation, etc.), the attitude estimation process is simulated by the addition of a frequency varying noise to the attitude measurement channels. Again, this is a high-pass filter, with a steady state gain given by the expected steady state error of the attitude Kalman filter [Mosier and Fermiano, 1999]. The increase in noise power at frequencies higher than 5Hz ensures that the controller will not respond to (or, in fact, require) higher rate signals.

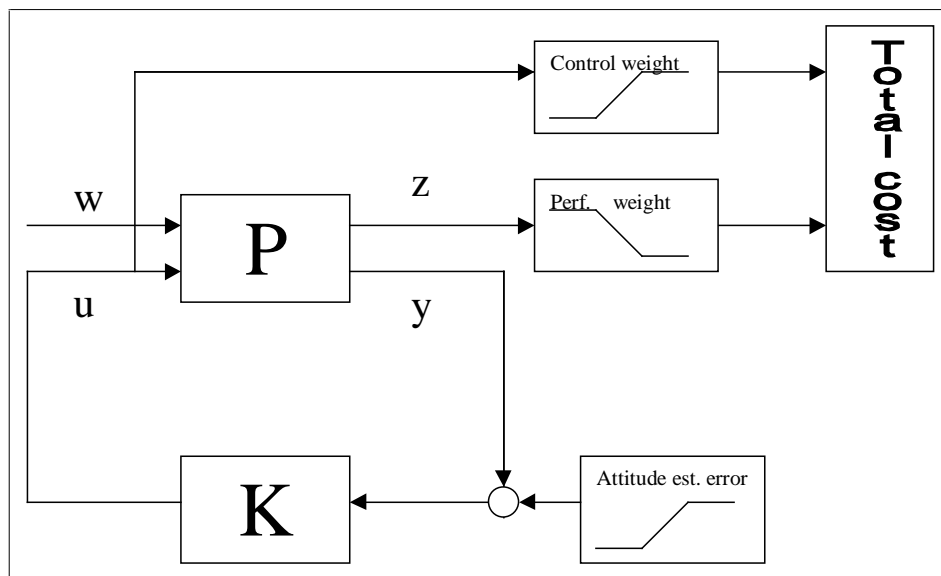


Figure 37. Generalized Plant

Once the generalized plant is built, the control system design process can proceed. The H_2 and H_{∞} optimal controllers are derived and are output to the rest of the DOCS module. Some plots of the resulting loop transfer functions and closed-loop transfer functions are included in the discussion of the ADCS performance in the following sections.

Trade Space:

A consolidated discussion of the DOCS module trades is included in Section 7.4.6 below.

7.4.4 Integration Module

Module Motivation:

The purpose of this module is to assemble the integrated model based on the previous designs of the structure, the optical train and the control loops. The integrated model is represented in LTI state space form and can be used for the subsequent dynamic performance analysis. The integrated model contains the structural plant, ADCS, and optical controllers, as well as the linear sensitivity matrix C_z that relates the physical degrees of freedom of the opto-structural system to the performance metrics of interest.

Module Description:

The inputs to the integrated model are: the input matrix B_w , the FEM dynamics state space system, the ADCS controller in state space form, the optics linear sensitivity matrix C_z , and the optical control state space system. This is represented in the block diagram in Figure 38.

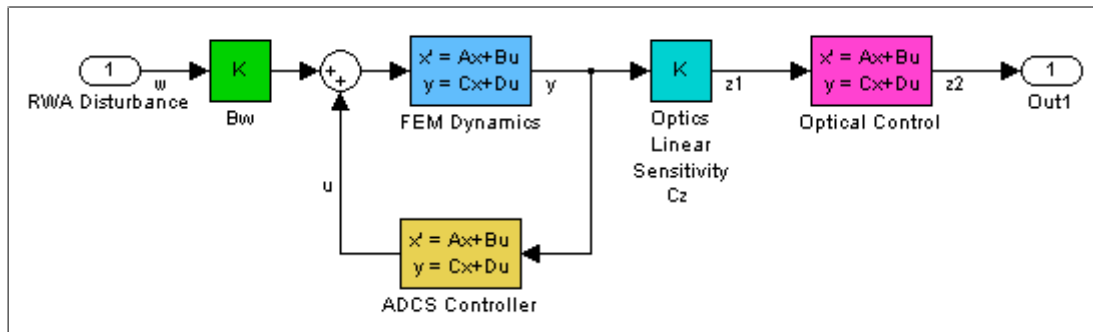


Figure 38. Block diagram of the TPF Integrated Dynamics Model

The main equations for obtaining the integrated dynamics model are given below. The plant dynamics are given by Equation 68.

$$\begin{aligned} \dot{q}_p &= A_p q_p + B_p w + B_u u \\ y &= C_p q_p + D_p w + D_p u \end{aligned} \tag{Equation 68}$$

The ADCS controller in state space form is represented by Equation 69.

$$\begin{aligned} \dot{q}_k &= A_k q_k + B_k y \\ u &= C_k q_k + D_k y \end{aligned} \quad \text{Equation 69}$$

The output metrics of interest (OPD) before optical control are calculated with Equation 70.

$$z_1 = C_{z1} y \quad \text{Equation 70}$$

The optical controller is modeled as Equation 71.

$$\begin{aligned} \dot{q}_l &= A_l q_l + B_l z_1 \\ z_2 &= C_l q_l + D_l z_1 \end{aligned} \quad \text{Equation 71}$$

Assembling the closed loop state space system results in the following equations.

$$\begin{aligned} \dot{q} &= \begin{Bmatrix} \dot{q}_p \\ \dot{q}_k \\ \dot{q}_l \end{Bmatrix} = \underbrace{\begin{bmatrix} A_p + B_u D_k C_p & B_u C_k & 0 \\ B_k C_p & A_k & 0 \\ B_l C_{z1} C_p & 0 & A_p \end{bmatrix}}_{A_{zw}} \begin{Bmatrix} q_p \\ q_k \\ q_l \end{Bmatrix} + \underbrace{\begin{bmatrix} B_p + B_u D_k D_p \\ B_k D_p \\ B_l C_{z1} D_p \end{bmatrix}}_{B_{zw}} w \\ z_2 &= \underbrace{\begin{bmatrix} D_l C_{z1} C_p & 0 & C_l \end{bmatrix}}_{C_{zw}} \begin{Bmatrix} q_p \\ q_k \\ q_l \end{Bmatrix} + \underbrace{\begin{bmatrix} D_l C_{z1} D_p \end{bmatrix}}_{D_{zw}} w \end{aligned} \quad \text{Equation 72}$$

The effect of the ADCS system and of the optical controller on the stability of the science light passing through the TPF system is extremely important. The effects can be seen by examining the sample transfer function in Figure 39. The top curve shows the rigid body behavior of the TPF if there were no active ADCS. This is clearly not acceptable and the system must be stabilized. The effective bandwidth of the ADCS controller is 1 decade below the first flexible mode of the system. The optical control (third curve from top) provides significant attenuation of the disturbances.

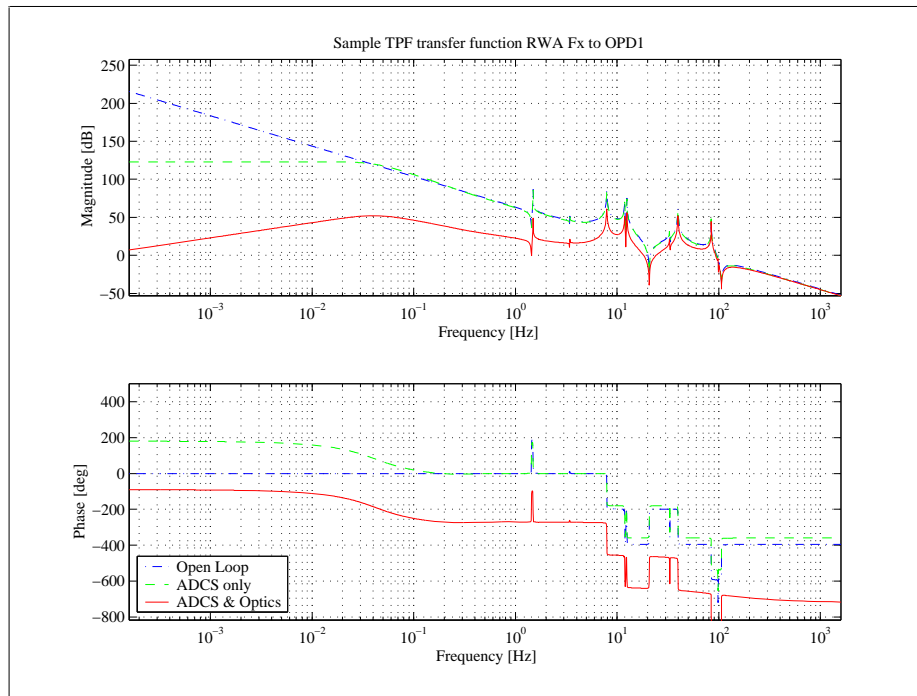


Figure 39. Transfer Function to Illustrate the Effects of Open Loop, ADCS, and Optical Control on OPD Disturbances

Trade Space:

A consolidated discussion of the DOCS module trades is included in Section 7.4.6 below.

7.4.5 Disturbance Analysis Module

Module Motivation:

It is assumed that the two principal dynamic disturbances will be on-board and that the major contributions are from the reaction wheel assembly (RWA) and from the cryocoolers, which are necessary to cool the IR detectors. Two separate routines compute the RWA and Cryocooler disturbance spectra. In the current version of the TMAS, only RWA disturbances have been implemented.

Module Description:

Reaction wheel disturbances are modeled as power spectral densities (PSD's) that describe the disturbance energy frequency content. The RWA disturbance function generates RWA disturbance PSD's in spacecraft axes for an arbitrary number of wheels and an arbitrary orientation of the RWA. It uses [Melody]'s model of the disturbance PSD's for a single wheel. These reaction wheel disturbances are injected into the system and their effect on the optical pathlength difference is determined in the disturbance analysis module.

Figure 40 depicts the RWA disturbances generated by a reaction wheel assembly with four wheels in a pyramid configuration. This is the configuration chosen for the TPF structurally connected model (SCI). The wheel speed is assumed to vary uniformly between 0 and 2000 RPM. For the SSI model, each spacecraft is assumed to have its own RWA that produces noise. This is one of the reasons why maintaining equal pathlength in the SSI case is more challenging.

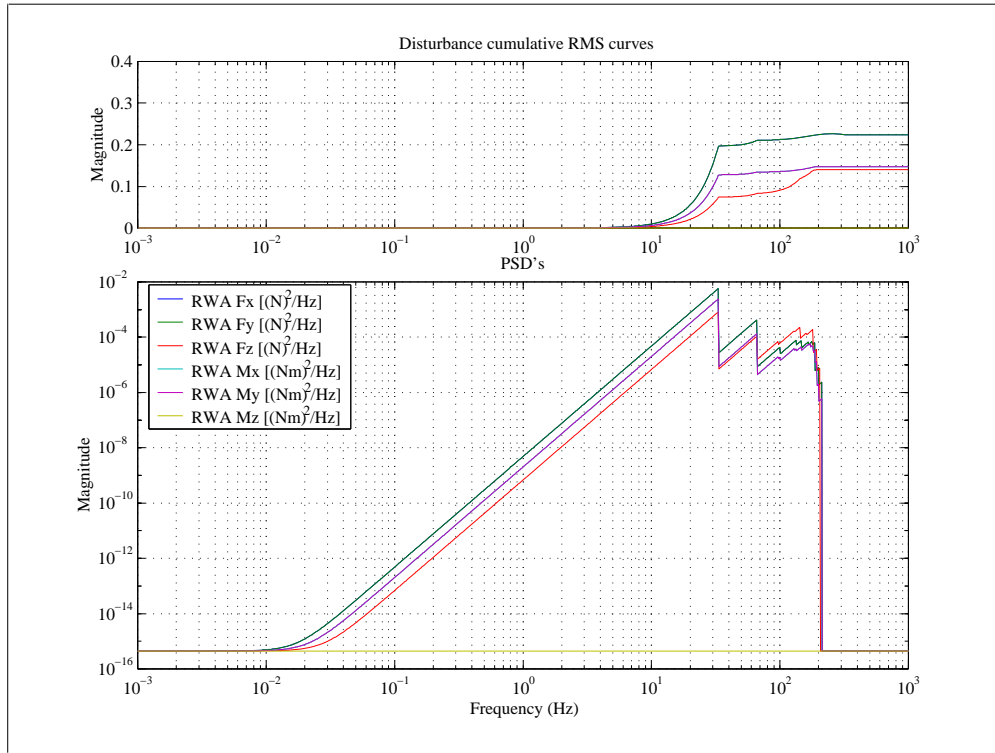


Figure 40. Assumed Reaction Wheel Disturbance PSD's for the TPF Mission

The disturbance analysis returns a PSD for the OPD of each aperture with respect to the reference aperture. The reference aperture is defined by the optics modeling routine. The OPD of the reference aperture with respect to itself is obviously zero. Figure 41 shows an example OPD PSD for aperture #1 with respect to the reference aperture #2. The top plot shows the cumulative RMS curve of the OPD, the middle curve shows the performance OPD $S_{zz}(\)$, and the bottom curve shows the relative contributions of the RWA disturbance components.

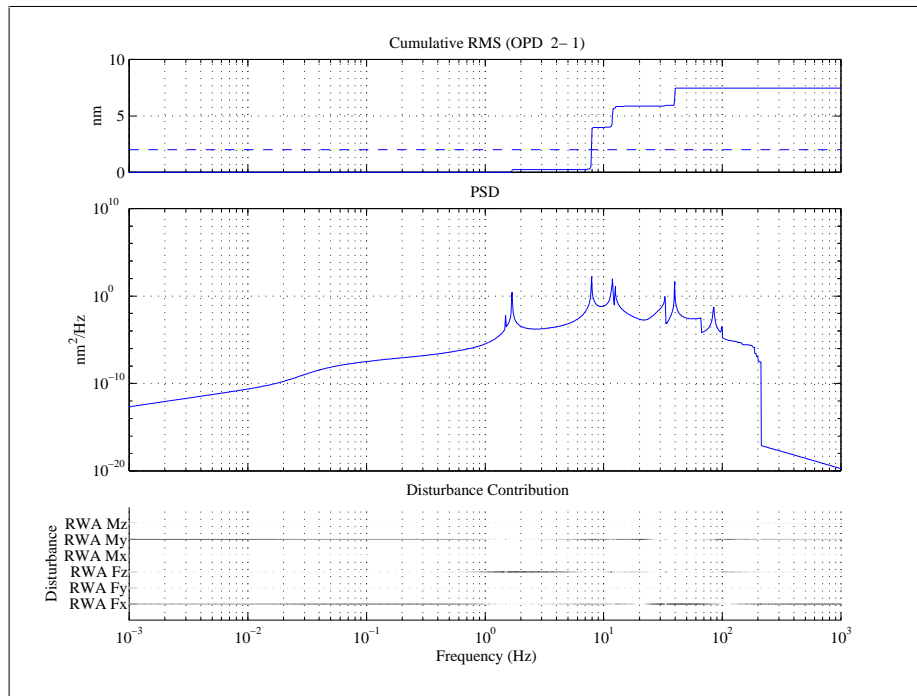


Figure 41. Performance Power Spectral Density Function for OPD₁

It is interesting to note that there is significant dynamic amplification over certain frequency regions. The top subplot shows the cumulative RMS curve that is obtained by integrating under the performance PSD. It can be observed that most of the RMS errors are accumulated in a frequency regime between 7 and 40 Hz. This is typical for space based structures with these dimensions and physical properties. The normalized cumulative area plot (Figure 42) can be used to determine the critical modes of the system.

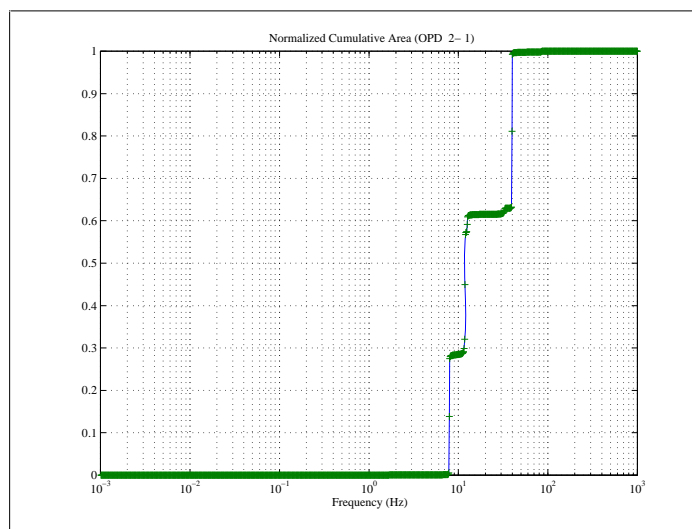


Figure 42. Normalized Cumulative Area Plot for OPD1-2 (TPF Baseline Configuration)

Almost 100 % of the RMS error is caused by only three modes of the system. This is an interesting and surprising result. Figure 43 illustrates the relative contribution of the RWA components at these modes for this OPD metric. The results shown are applicable to the SCI baseline design case documented in the Trade Studies section below.

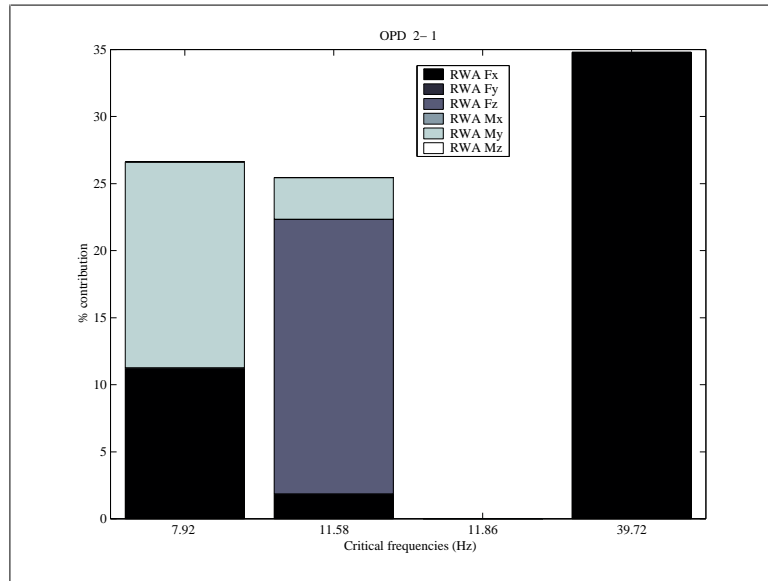


Figure 43. Critical Modes for OPD1-2 of the TPF Baseline Design

The mode shapes corresponding to the three critical frequency modes are shown in Figure 44. The first mode is a coupled truss bending and high-gain antenna mode. The F_x contribution, acting along the truss, is the dominant component to the third mode, and results in an axial truss mode.

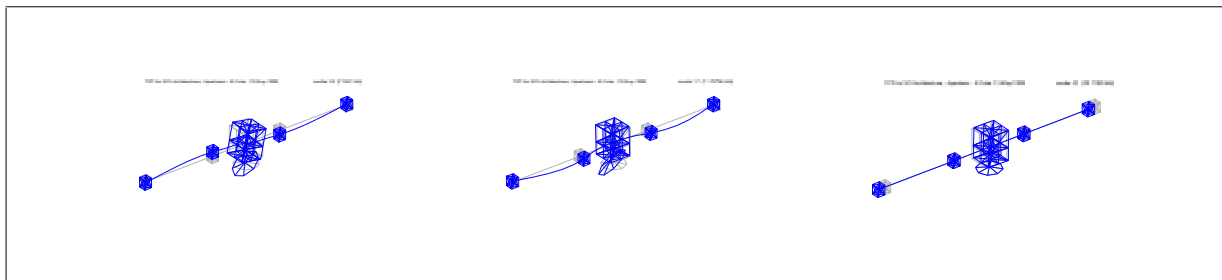


Figure 44. Mode Shape Representations for Three Critical System Modes

Trade Space:

A consolidated discussion of the DOCS module trades is included in Section 7.4.6 below.

7.4.6 DOCS Macro-Module Trades

This section describes just two of the many trades that are possible using parameters in the DOCS module. The two parameters discussed are the RWA disturbance level and the optical control bandwidth. Changing these values will have a fundamental impact on the dynamics, the transmissivity function, the resulting integration times for a given SNR, and ultimately the cost per image of the observatory.

The first trade shows the effect that reaction wheel imbalances can have on the transmissivity function, and ultimately on the signal to noise ratio. The reaction wheel disturbance data was obtained from a test of the ITHACO E-Wheel conducted at NASA GSFC in 1998 [Mosier and Brown]. The wheel speed distribution was assumed to be uniform between 0 and 2000 RPM. The combined effect of 4 wheels in a pyramidal configuration is taken into account. The left subplot in Figure 45 shows the effect of the reaction wheel imbalances that were obtained from the test without any modification to the test data. The transmissivity image has four symmetric lobes (fringes of peak intensity) and the suppression of starlight meets the specification of 10^{-6} out to the star diameter.

The right subplot demonstrates the effect of scaling up the wheel imbalances by a factor of 10. This could occur if the wheels are poorly balanced or if a ball bearing fails during operations. The effect on the transmissivity image is dramatic. First, one pair of fringes is being washed out by the vibrations. Second, the nulling of the starlight at the center of the image is no longer meeting the requirements. In the nominal case, the σ_{OPD} (average) is 76 nm. It is 762 nm in the second case, which corresponds to roughly $\lambda/16$. For non-interferometric systems, such a wavefront error might be acceptable, but for TPF, it clearly is not. This is an illustration of why the requirement for the OPD is $\lambda/6000$.

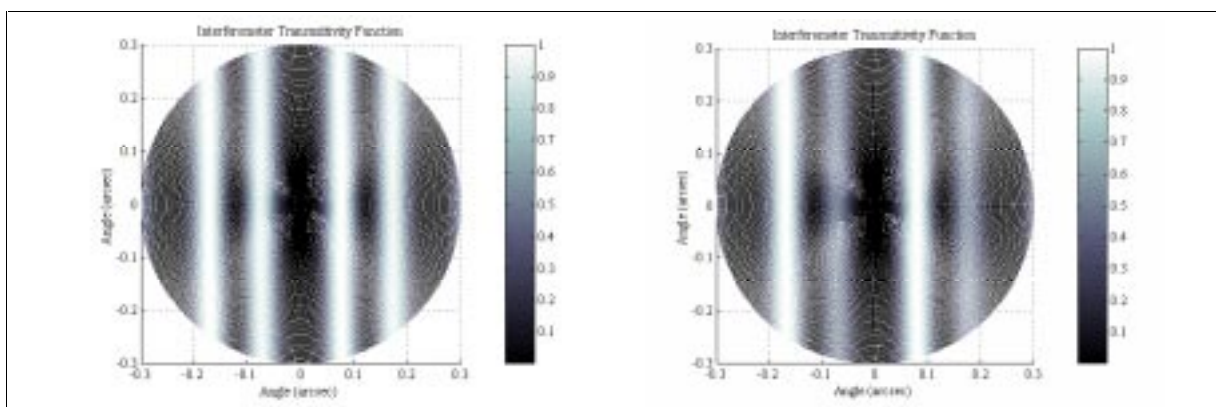


Figure 45. Demonstration of “Washout” Effect Due to RWA Noise (Right Side)

A second interesting trade concerns the optical control bandwidth. This trade provides an indication of the fidelity of the DOCS macro-module. The effect of optical control bandwidth limitations on the system is modeled using a high-pass filter approach. Each OPD channel is attenuated by the optical controller at low frequencies but not at high frequencies due to assumed limitations on sensor and actuator bandwidths.

Figure 46 shows the effect on the transmissivity function of changing the optical controller bandwidth. If the optical controller bandwidth is too low, the optical pathlength differences between the apertures create a time-varying phase difference ϕ_i between the light beams at the combiner. This phase shift disturbs the +/- 180-degree phase shift requirement for perfect nulling. A simplifying assumption is that the OPDs, which are the square roots of the variance of a stochastic random signal, are added to the phase shift used to compute the transmissivity as if they were deterministic. Thus, the perturbations from the perfect transmissivity shown above are to be understood in a 1 sigma sense. This calculation is shown in Equation 73.

$$\text{Computation of RMS OPD: } \sigma_z^2 = \frac{1}{\pi} \int_0^{\infty} G_{zw}(\omega) S_w(\omega) G_{zw}^H(\omega) d\omega \quad \text{Equation 73}$$

The σ_z value for the i^{th} aperture is then converted into a phase delay, ϕ_k , which is injected into the transmissivity function. It can be said that dynamic disturbances degrade the transmissivity function, especially the nulling performance of the parent star, when the ϕ_k 's are injected into the transmissivity equation (Equation 74).

$$T = \left| \sum_{k=1}^n D_k \exp[j2\pi(L_k \theta/\lambda)\cos(\delta_k - \phi)] \exp(j\phi_k) \right|^2 \quad \text{Equation 74}$$

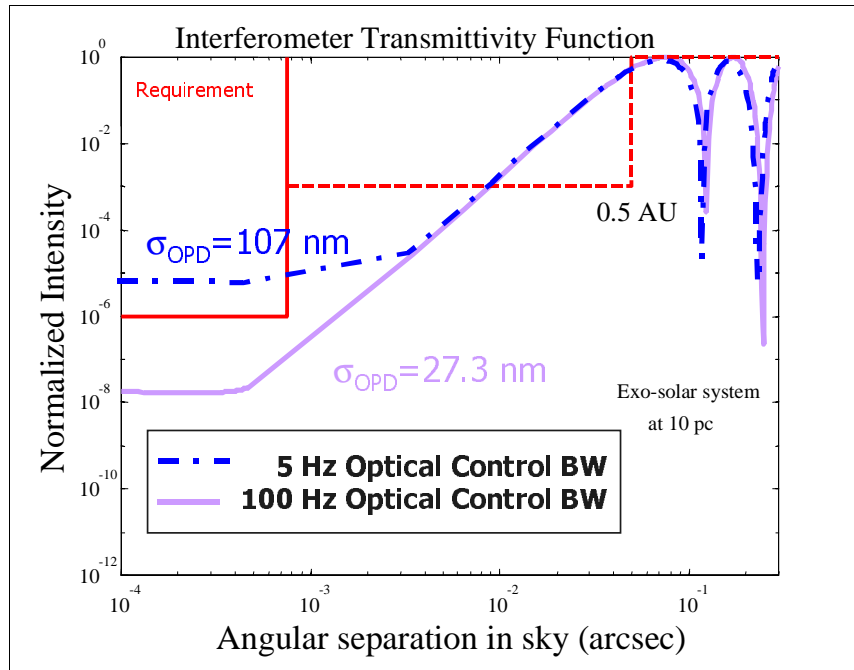


Figure 46. Effect of Optical Controller Bandwidth on the Transmissivity Function

Preliminary results indicate that the science requirements can not be met with an optical bandwidth of 5 Hz, but that increasing the bandwidth to 100 Hz leads to sufficient suppression of the onboard dynamic disturbance sources.

7.5 Operations Macro-Module

7.5.1 Orbit Module

Module Motivation:

According to the TPF Book, orbit selection is one of the principal mission development issues. Earlier studies by Ball, Lockheed Martin, and TRW suggested that the orbital radius for TPF should be between 1 AU (Earth orbit) to 5.2 AU (Jupiter orbit). Orbit selection influences many areas of the TPF mission, including aperture size, power, communications, thermal control, launch vehicle, and flight time to the operational orbit.

Module Description:

The Orbit Module takes orbit as an input and provides information about delta V and flight time. Delta V is the velocity change required for orbit transfer and the flight time is the time to get to the desired orbit from the Earth. The Orbit Module calculates three delta Vs: the departure delta V, the arrival delta V, and the total delta V. The departure delta V is the delta V needed at the initial point of transfer orbit, the arrival delta V is the delta V needed at the final point of the transfer orbit, and the total delta V is the sum of departure and arrival delta Vs. The delta V outputs will be used by the propulsion and launch vehicle modules to calculate thrust levels and to select the launch vehicle. The flight time information will be used as an input by the operations and the GINA modules to estimate time dependent functions such as operations cost.

According to the previous studies, the most favorable candidate location for the TPF in a 1 AU orbit is at the L2 point, which is 60 degrees ahead of the Earth, as shown in Figure 47. Hill's transfer method is used to calculate the delta V and the flight time required to reach this orbit. The Hill transfer method is accomplished by entering an elliptical orbit with a shorter period than the initial orbit so that when the spacecraft reaches its next apogee, it will be separated from the Earth by the desired phase (see Figure 47). The departure delta V and arrival delta V are equal and opposite and the flight time is approximately equal to the period of the new orbit. The following equations were used to calculate the departure delta V, arrival delta V, and the flight time. Both departure and arrival delta V are about 2.17 km/s and the estimated flight time is about 0.82 year.

$$\Delta V_{total} = |\Delta V_{departure}| + |\Delta V_{arrival}| \quad \text{Equation 75}$$

$$|\Delta V_{departure}| = |\Delta V_{arrival}| = V_e - V_{apogee} \quad \text{Equation 76}$$

$$V_e = \sqrt{\frac{GM_{Sun}}{R_e}} \quad \text{Equation 77}$$

$$V_{apogee} = \sqrt{GM_{Sun} \left(\frac{2}{R} - \frac{1}{a} \right)} \quad \text{Equation 78}$$

$$a = \left(GM_{Sun} \left(\frac{300 \times 24 \times 60 \times 60}{2\pi} \right)^2 \right)^{\frac{1}{3}} \quad \text{Equation 79}$$

$$Flighttime = \frac{300}{365} \text{ year} \quad \text{Equation 80}$$

where

ΔV_{total} : total delta V(km/s)

$\Delta V_{departure}$: departure delta V(km/s)

$\Delta V_{arrival}$: arrival delta V(km/s)

V_e : orbital velocity of Earth(km)

R_e : orbital radius of Earth(km)

V_{apogee} : velocity at apogee of transfer orbit(km/s)

GM_{Sun} : constant(km³ / sec²)

R : desired orbital radius(km)

a : semimajor axis of transfer orbit

$Flighttime$: time to achieve L2 orbit

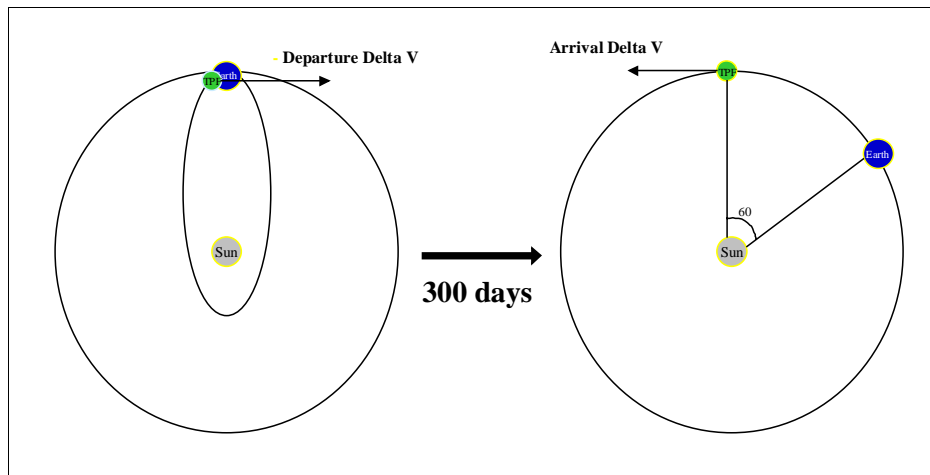


Figure 47. Hill's Transfer to L2 Orbit

If the desired orbit is greater than 1AU, an interplanetary Hohmann transfer method is used to estimate departure delta V, arrival delta V, total delta V, and flight time. The approximate flight time is about one half of the period of the transfer orbit. All transfers are assumed to start from a 300 km LEO parking orbit. As illustrated in Figure 48, the Hohmann transfer technique consists of performing a departure delta V at the perigee of the transfer orbit followed by an arrival delta V when it reaches apogee to circularize the final orbit. The following equations show how to calculate the arrival delta V, departure delta V,

and the flight time using Hohmann's transfer method. These calculations do not use the gravity assist technique, which may help to reduce the delta V requirements by using a planet's gravity to redirect the spacecraft. The plots in Figure 49 show the total delta V and the flight time as functions of orbital radius.

$$a_t = \frac{R_e + R}{2} \quad \text{Equation 81}$$

$$V_{perigee} = \sqrt{GM_{Sun} \left(\frac{2}{R_e} - \frac{1}{a_t} \right)} \quad \text{Equation 82}$$

$$V_{\infty} = V_{perigee} - V_e \quad \text{Equation 83}$$

$$C_3 = V_{\infty}^2 \quad \text{Equation 84}$$

$$E_e = \frac{C_3}{2} \quad \text{Equation 85}$$

$$\Delta V_{departure} = \sqrt{2 \frac{GM_{earth}}{E_{radius} + h} + E_e} \quad \text{Equation 86}$$

$$V_{apogee} = \sqrt{GM_{Sun} \left(\frac{2}{R} - \frac{1}{a_t} \right)} \quad \text{Equation 87}$$

$$\Delta V_{arrival} = V_R - V_{apogee} \quad \text{Equation 88}$$

$$V_R = \sqrt{\frac{GM_{Sun}}{R}} \quad \text{Equation 89}$$

$$\Delta V_{total} = |\Delta V_{departure}| + |\Delta V_{arrival}| \quad \text{Equation 90}$$

$$\text{Flighttime} = \frac{\pi \left(a_t^{\frac{3}{2}} \right)}{\sqrt{GM_{Sun}}} \left(\frac{1}{60 * 60 * 24 * 365} \right) \quad \text{Equation 91}$$

where

a_t : semimajor axes of transfer orbit(km)

R_e : orbital radius of Earth(km)

R : desired orbital radius(km)

$V_{perigee}$: velocity at perigee of transfer orbit(km/s)

V_{∞} : velocity needed to exit from Earth orbit(km/s)

C_3 : characteristic energy (km^2 / s^2)

E_e : energy (km^2 / s^2)

C_3 : characteristic energy (km^2 / s^2)

E_e : energy (km^2 / s^2)

ΔV_{total} : total delta V(km/s)

$\Delta V_{departure}$: departure delta V(km/s)

$\Delta V_{arrival}$: arrival delta V(km/s)

E_{radius} : radius of Earth(km)

h : altitude of parking orbit(km)

V_e : orbital velocity of Earth(km)

V_R : orbital velocity at the desired orbit(km/s)

R_e : orbital radius of Earth(km)

V_{apogee} : velocity at apogee of transfer orbit(km/s)

GM_{Sun} : constant ($\text{km}^3 / \text{sec}^2$)

GM_{earth} : constant ($\text{km}^3 / \text{sec}^2$)

Flighttime : time to get to the desired orbit(year)

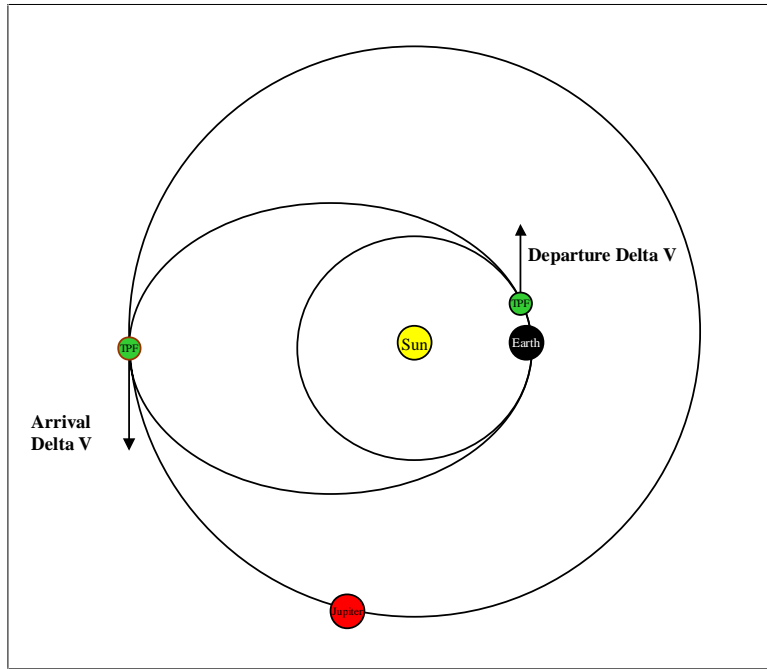


Figure 48. Hohmann's Transfer

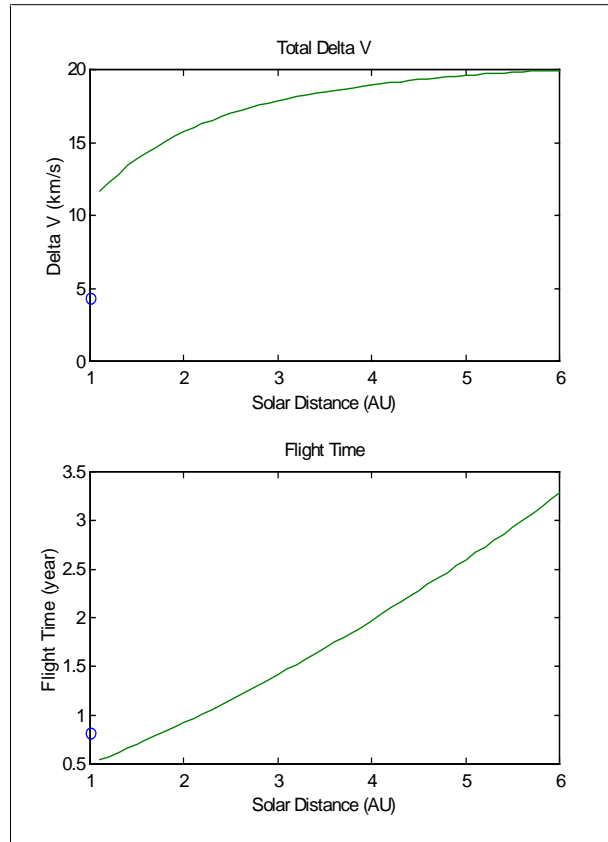


Figure 49. Total Delta V and Flight Time vs. Orbital Radius

Trade Space:

The following trade studies show the importance of orbit selection and describe how the orbit influences different areas of the TPF mission.

- Orbit vs. Apertures Size: Since the Sun's gravity attracts gas and dust, the local zodiacal environment at smaller orbits will cause greater interference with TPF observations and will force the use of larger apertures.
- Orbit vs. Solar Power: The option to use solar power for the TPF mission becomes less viable as the orbit increases.
- Orbit vs. Communication: The communications system size and power requirements increase with increased TPF orbit.
- Orbit vs. Thermal Control: The load on the thermal control system becomes greater for lower orbits.
- Orbit vs. Launch Cost and Flight Time: If the orbit is further away from the Earth, the launch cost and flight time will be increased.

7.5.2 Launch Module

Module Motivation:

The launch vehicle places TPF into the desired orbit. The launch vehicle selection is an important part of the Operations Macro-Module because it contributes to a significant part of the total mission cost. A launch vehicle incorporates one or more upper stages which provide necessary delta Vs, calculated by the Orbit Module. Although the launch process can severely constrain spacecraft design for most of space missions, the Launch Vehicle Module does not drive the design process for TPF. Rather, it provides a launch vehicle according to the total mass calculated by the TMAS.

Module Description:

The Launch Vehicle Module takes the mass of TPF and the arrival delta V as inputs, selects a launch vehicle, and provides the cost associated with the launch vehicle. Although both mass and volume of TPF should be used as inputs, only mass was used as an input because TMAS does not calculate the exact volume of a stowed TPF. The Launch Vehicle Module only considers using a single launch vehicle. However, it is possible that SSI missions can be launched using multiple vehicles because they consist of more than one spacecraft. Therefore, comparing the multiple launch vehicle scenario to the single vehicle scenario for SSI missions is recommended as a future work.

The departure delta V and arrival delta V are the delta Vs needed at the perigee and the apogee of a transfer orbit. There are two ways to provide these velocity changes. One way is to use two different upper stages, one for the perigee kick and one for the apogee kick. The other way is to have the launch vehicle provide the perigee kick necessary to meet the departure delta V requirement and to have only one upper stage for the arrival apogee kick. This second option is called a 'direct insertion.' While direct insertion involves some

complicated scheduling and maneuvers, the total mass is smaller since the launch vehicle must only carry one upper stage instead of two. Since the total launch cost is directly proportional to the total launch mass, the Launch Vehicle Module for TPF has been designed to use the direct insertion case to minimize the launch cost. Figure 50 summarizes the inputs and outputs of the Launch Vehicle Module.

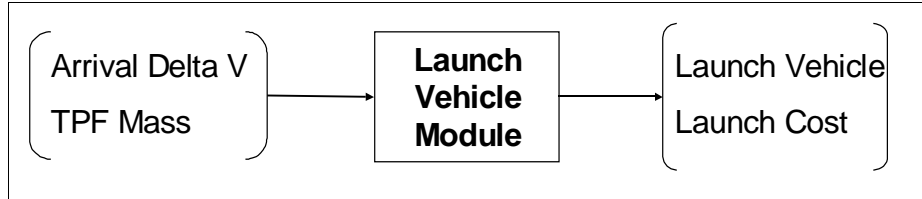


Figure 50. Launch Vehicle Module Inputs and Outputs

The size and mass of the upper stage, which provides the apogee kick, increase as the required arrival delta V increases. The arrival delta V increases as the orbital radius from the Sun increases. Therefore, a bigger and more powerful launch vehicle is required to carry the upper stage and the TPF to the desired orbit as the orbital distance from the Sun increases. Using the following equations, the mass of an apogee kick upper stage is calculated according to the required arrival delta V. The upper stage is assumed to use liquid oxygen and hydrogen for propellant in order to generate high specific impulse, I_{sp} , of 400 seconds.

$$\Delta V_{arrival} = I_{sp} g \ln \left(\frac{M_{TPF} + M_{AKUS}}{M_{TPF} + M_{AKUS} - M_{AKUS, Fuel}} \right) \quad \text{Equation 92}$$

$$M_{AKUS} = M_{AKUS, Structure} + M_{AKUS, Fuel} \quad \text{Equation 93}$$

where

$\Delta V_{arrival}$ = arrival delta V (km/s)

I_{sp} = specific impulse, assumed for 400 (sec)

M_{TPF} = mass of TPF (kg)

M_{AKUS} = mass of apogee kick upper stage (AKUS) (kg)

$M_{AKUS, Structure}$ = mass of AKUS structure, assumed for 500 (kg)

$M_{AKUS, Fuel}$ = mass of AKUS fuel (kg)

After calculating the mass of an apogee kick upper stage, the total mass inside the launch vehicle fairing can be calculated by adding the mass of the TPF and the mass of the upper stage. According to the total mass, the Launch Vehicle Module selects a launch vehicle and provides the launch cost. Table 14 shows the list of launch vehicles that were considered by the module.

Table 14. Launch Vehicle Selection

Total Mass, M (kg)	Launch Vehicle	Launch Cost (million \$)
4800 M	Delta II	50
4800 < M 6500	Zenit	85
6500 < M 7900	Delta III	85
7900 < M 13200	Delta IV	100
13200 < M 18000	Ariane V	150
18000 < M 21640	Titan IV	250
21640 < M	TBD	>300

The launch vehicles listed in the above table are selected based on the maximum mass that can be carried by that vehicle. If the total mass exceeds 21,640 kg, the Launch Vehicle Module does not provide a launch vehicle and assumes the launch cost will be higher than 300 million dollars.

Trade Space:

- **Launch Cost vs. Mass of TPF:** As the mass of the TPF increases, it requires a larger and more powerful launch vehicle. Therefore, the launch cost increases as the mass of the TPF increases.
- **Launch Cost vs. Orbit:** If the orbital radius from the Sun increases, the TPF requires higher delta V to achieve the desired orbit. Higher delta V means that the TPF will require a larger and more powerful upper stage for the apogee kick. This will increase the total mass. Therefore, increasing the orbital radius from the Sun also increases the launch cost.
- **Launch Cost vs. Number of Launch Vehicles:** Although the option of using multiple launch vehicles for the SSI case was not considered for this module due to time constraints, it will be interesting to see the relationship between the total launch cost and the number of launch vehicles. It may or may not decrease the total launch cost if the SSI spacecraft are launched by multiple launch vehicles. This trade study is recommended for future work.

7.5.3 Operations Module

Module Motivation:

Operations costs comprise a significant portion of total mission costs, especially over long duration missions like the TPF. They are sometimes considered “hidden” costs since they accrue over time in an unobtrusive manner after high profile, high-ticket items such as development, construction, and launch. Traditionally, operational issues are relegated to the tail end of a spacecraft design process, and rarely influence the decision criterion of key system trades that they directly affect. This is not to imply that operations crews do not attempt to optimize their efficiencies throughout the mission, but rather that some spacecraft are inherently more difficult to operate than others. Higher operational difficulty leads to larger costs. Therefore, the inclusion of operations costs into the TPF trade analysis allows a

more thorough systems examination, with the twofold result of lower total costs and improved discrimination between alternate designs.

Operational issues also affect the TPF design trade in an important area besides cost. Dissimilar TPF configurations generate different rates of anomalies along with varying anomaly response times. While not directly affecting cost, the anomaly frequency and response capability influences overall system performance. This is very important in scientific missions with an established design life, but traditionally has not been captured during early system studies. Thus, the inclusion of operationally-derived adjustments to TPF performance indices contributes needed fidelity to the design trades.

Incorporating the impact of operations into the rest of the TPF design code required the formulation of operations issues into quantifiable forms. In addition, a necessity arose to develop a method to translate differences in TPF configurations to differences in operational difficulty. The size of this challenge became apparent after the discovery that most of the sparsely existing spacecraft operations literature embraced specific case studies and qualitative descriptions. In short, no previous example or methodology existed to compare the operational differences between alternate spacecraft choices of an unprecedented astronomy mission with a launch date several years in the future.

Module Description:

The operations module provides two main types of output to the TMAS software: cost and performance. The costs are split between development costs and operations costs, and the performance is given by mission inefficiency. Figure 51 shows the module's inputs and outputs.

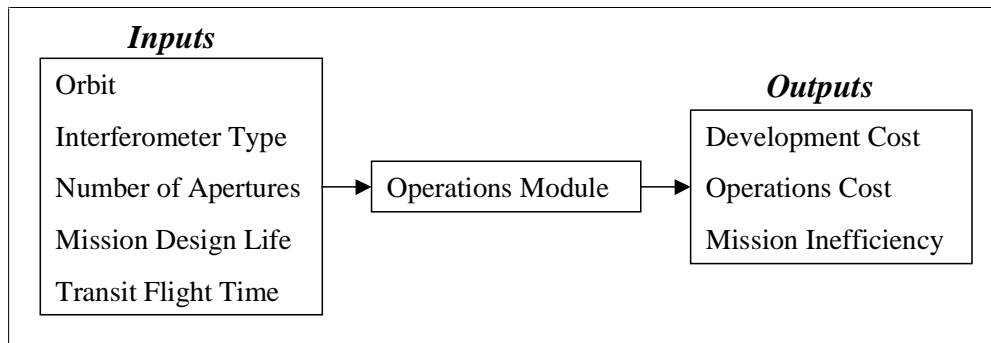


Figure 51. Operations Module Inputs and Outputs

Development costs represent the total mission expenditure before launch, excluding the costs of launch and the theoretical first unit costs of the TPF payload and bus. More complex missions require longer flight and ground software codes, which have a snowball effect on other key development costs. The individual components of the development cost are:

- Flight Software
- Ground Software
- Facilities
- Equipment
- Logistics
- Management
- Systems Engineering
- Product Assurance
- Integration and Test

Operations costs consist of labor and maintenance costs, and affect the mission throughout its useful life. Labor costs are a function of crew size and salary that the module determines from estimated operational complexity and failure recovery complexity. Maintenance costs are modeled on the size and complexity of the flight operations center.

Mission Inefficiency represents the performance output. It represents the science imaging time lost from transmission delay time and anomaly resolution time.

Labor Cost Approach

The key to capturing the operational differences between TPF architectures lies in a quantifiable complexity value that is quasi event-rate based. The module arrives at operations complexity by manipulating estimates for mean time to event, mean time to false event, and mean time to non-permanent failure. Examples of events, false events, and non-permanent failures for an antenna subsystem are slew movements, false indications of critical temperature, and gimbal jamming by an overheated turntable, respectively. Permanent failures are not utilized to determine complexity since direct operational interaction is impossible afterwards. Thus, the operational complexity experienced by the TPF operations crew is defined as:

$$J = J_e + J_{fe} + J_f = \sum_{i=1}^n \frac{1}{mte_i} (1 + f_i(N))(1 - A_i) + X_{fe} \sum_{i=1}^n \frac{1}{mtfe_i} (1 + f_i(N)) + X_f \sum_{i=1}^n \frac{1}{mtf_i} (1 + f_i(N)) \quad \text{Equation 94}$$

where mte_i , $mtfe_i$, and mtf_i represent the mean times to event, false event, and non-permanent failures, respectively, for a specific operations function i , N is the number of additional spacecraft beyond one, $f_i(N)$ is the relative increase in the event rate as a function of N , A_i is the basic onboard automation percentage, and X_{fe} and X_f are the complexity adjustment factors for false events and non permanent failures. Notice that basic automation savings only apply to events. Also notice that J_e , the complexity from events, represents a true event rate, whereas J_{fe} and J_f represent quasi event rates because they are adjusted by X_{fe}

and X_f . This adjustment provides a higher fidelity estimate of total system complexity by accommodating the inherently higher difficulty of anomalous incidents over routine events.

Table 15 gives the transition times for a generic single spacecraft, which served as a baseline for complexity. The numbers are from “A Probabilistic Model of the Effects of Satellite System Automation on Availability and Costs” [Schwarz, 1997]. It is important to note that as TPF development proceeds, higher fidelity estimates of transition times for TPF-specific functions will become available, which may or may not diverge significantly from the generic model given here.

Table 15. Transition Times for Generic Single Spacecraft

Operations function i	$mtte$	$mttfe$	$mttf$
Archiving	4 min.	-	4 yrs.
Tracking	1 day	-	3 yrs.
Control Center Comm.	6 hrs.	-	10 mo.
Attitude Control	10 min.	1 wk.	6 yrs.
Power Generation	30 min.	1 wk.	1 yr.
Power Distribution	30 min.	1 wk.	4 yrs.
Telemetry	4 min.	-	6 yrs.
Command Handling	6 hrs.	-	7.5 yrs.
Orbit Control	1 mo.	1 yr.	6 yrs.
Payload Receive	1 mo.	-	1 mo.
Payload Transmit	1 wk.	-	1 mo.
Thermal Control	12 hrs.	2 mo.	4 yrs.

It is important to realize the benefit of automation on total operations costs. At this point, basic automation has only been applied to routine operation events (although false-events are exempted from the recovery complexity calculation by anticipated advances). Since each TPF architecture is equally amenable to higher order automation efficiencies, like self-corrective failure capability, such technology was not included as a tradespace differentiator. Furthermore, the readiness of such tools, while being vigorously pursued, is open to question for TPF utilization. Currently, the costs of any higher order automation could be considered as labor costs, but if some TPF architectures are found to exhibit greater cost savings than others from this type of automation, the module could incorporate the necessary separate functionality in the future.

Table 16. Basic Automation Level for Events

Operations function i	Automation Percentage
Archiving	0
Tracking	0
Control Center Comm.	0
Attitude Control	95
Power Generation	98
Power Distribution	98
Telemetry	80
Command Handling	20
Orbit Control	0
Payload Receive	0
Payload Transmit	0
Thermal Control	98

Efficiencies result from operating several spacecraft from a single control facility. To model this, a 90% learning curve was applied to the complexity J . The adjusted complexity is defined by

$$\tilde{J} = JL \tag{Equation 95}$$

where \tilde{J} is the adjusted complexity, J is the complexity, and L is the gain, defined by

$$L = \frac{(1+N)^B}{(1+N)}, \quad B = 1 - \frac{\ln\left(\frac{100}{S}\right)}{\ln 2} \tag{Equation 96}$$

where N is the number of spacecraft beyond one, and S is the learning curve of 90%. Therefore, each additional spacecraft causes the total operational complexity to rise, but at a proportionally reduced rate.

The adjusted complexity is used as a discriminator for crew sizing. The adjusted complexity level for the least operationally complicated TPF (structurally-connected) is baselined against steady-state staffing sizes for a Hubble-class astronomy mission using input from industry. Then the change in adjusted complexity from additional spacecraft causes increases in certain segments of the crew. The three primary crew types considered are flight operations (Fops), ground operations (Gops), and technical experts (techexperts). The Fops crew is further broken down into the three segments of mission planners (MP), spacecraft controllers (SC), and engineering and analysis personnel (E&A). The total Fops crewsize during the steady-state staffing phase is defined by

$$\text{Steady-State Fops Crew Size} = 4 \left[\left(1 + \left(\frac{\tilde{J}}{K} \right) \right) + \left(2 + \left(\frac{\tilde{J}}{K} \right) \right) + \left(1 + 1.5 \left(\frac{\tilde{J}}{K} \right) \right) \right] \quad \text{Equation 97}$$

Where K represents the baselined adjusted complexity, the factor 4 represents the number of 12 hour shifts required for continuous operation, and the three summed bracketed quantities represent the single-shift crew requirements for MP, SC, and E&A, respectively.

The steady-state Gops crew size, in contrast to Fops, does not exhibit the same dependency on complexity, and can be modeled as a constant. Any cluster of separated spacecraft will fly close enough together to represent collectively a single target for ground-based antenna pointing and contact scheduling. The operations module uses a “Great Observatory” Gops crew size of 18 people during the steady-state phase.

The steady-state crew levels, both Fops and Gops, represent the staff requirements for the science-gathering mission of the TPF. This stipulates the estimated constant technical human resource level for the required mission design life of 5 years. However, the two other mission phases, transit and checkout, have different staffing requirements.

The transit phase starts at launch and ends when the TPF reaches its destination orbit. Due to the lack of science operations, and correspondingly lower operational tempo, the required Fops and Gops staffing levels will be less. However the operations crew will not operate in as lean a manner as theoretically possible, due to the practical necessity of retaining a core of qualified operators for the later mission phases without causing programmatically difficult large-scale personnel ramp-ups. Therefore, the transit phase staffing levels for both the Fops and Gops components were modeled as half of their steady-state science phase levels.

The checkout phase follows the transit phase and precedes the science phase. From the written TPF requirements, it lasts 73 days. The Fops and Gops crew sizes are the same as in the later science phase, but an additional staffing component of techexperts is added. These techexperts provide support to validate the proper functionality of each TPF subsystem. Their number is directly affected by the adjusted complexity value and is defined by

$$\text{Checkout Techexpert Crew Size} = \left(50 + 50 \left(\frac{\tilde{J}}{K} \right) \right) \quad \text{Equation 98}$$

Traditionally, complexity estimates dictate Fops crew sizes and skill levels, but this module differentiates between them. The requisite skill level does not depend completely on the adjusted complexity, but rather the recovery complexity of operational hiccups like false events and non-permanent failures. Therefore, a more trouble-prone TPF will require operators with a higher average skill level, not merely more operators. For example, a geostationary communications satellite with a high event rate would require a lower operator skill level than a Pluto flyby mission with a lower event rate but more difficult recovery profile. Assuming advancements in automation technology during the intervening years

before official TPF program start, all false events were modeled as transparent to the operations crew, because of anticipated low-cost, multiple-path onboard state detection algorithms. However, non-permanent failures would still require the intervention of the operations crew. The daily rate of non-permanent failures found by summing the daily failure rates of each operations function represents the recovery complexity of a TPF configuration. This recovery complexity determines the skill level of the Fops crew. Differences in skill level can cause a salary variation of up to \$10,000 for a Fops employee. Table 17 shows the salaries for the different operations personnel.

Table 17. Average Salaries for Operations Personnel

Personnel Type	Average Salary
Flight Operations (Fops)	\$70,000 - \$80,000
Ground Operations (Gops)	\$70,000
Technical Experts (Techexperts)	\$100,000

Knowing the crew sizes for the different operations groups, their respective salaries, and the time spent in each operational phase, the total labor cost for a TPF configuration is calculated. Figure 52 recaps the approach used to arrive at the labor cost.

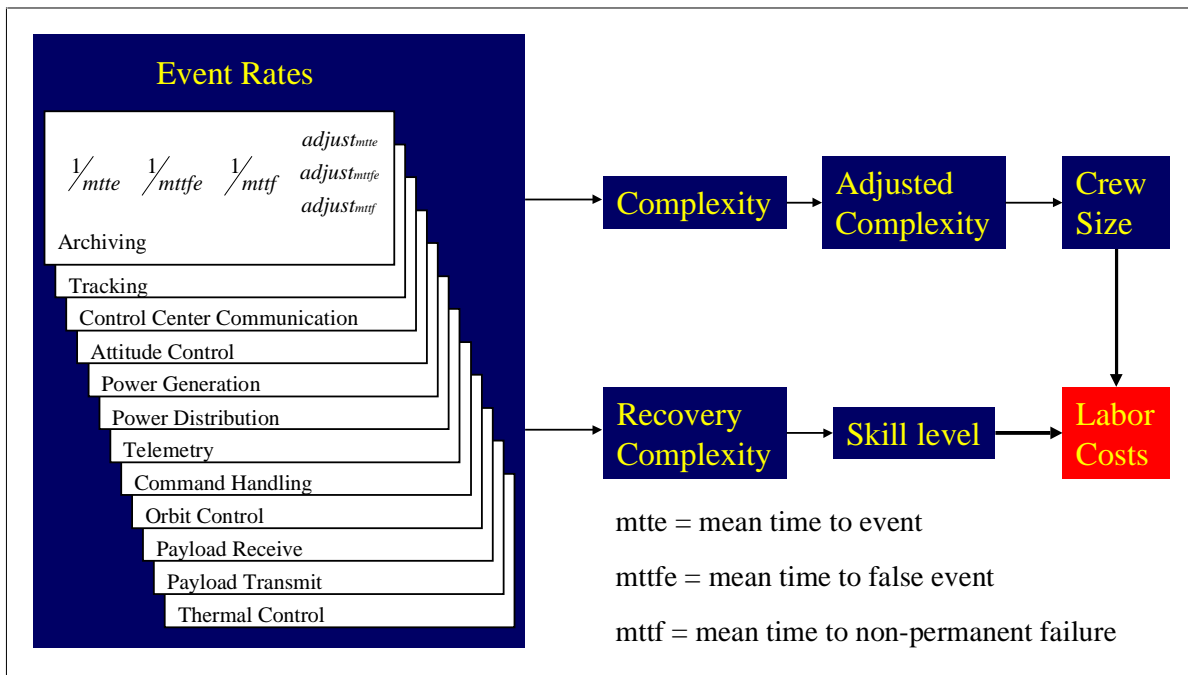


Figure 52. Determination of Labor Costs

Development Cost Approach

While the key to capturing the labor cost differences between TPF architectures lies in a quantifiable complexity value, the development cost is estimated in a more traditional manner. The module arrives at this cost by first estimating the flight and ground software

sizes. It then estimates the ground segment development cost as a function of the ground software cost using a cost estimating relationship (CER) approach from “Space Mission Analysis and Design” [Larson & Wertz, 1992].

The flight and ground software size estimates attempt to account for the differences in required software for alternate TPF configurations. In each case a baseline length of Ada source lines of code (SLOC) for the least complex TPF configuration is harmonized with one from a “Great Observatory” class astronomy mission. Additional spacecraft add flight software length due to 1) new model introduction, and 2) increased complexity of safe mode logic for multiple vehicles. For ground software, the length increases with 1) new model introduction, and 2) increased data filtering and archiving. The following two equations display the flight and ground software sizing estimates:

$$\text{Flight S/W SLOC} = 40000 \text{ base} + 20000 \text{ second platform} + 150N^2 \text{ safing logic} \quad \text{Equation 99}$$

$$\text{Ground S/W SLOC} = 1000000 + 200000 \text{ second platform} + 500N^2 \text{ filtering \& archiving} \quad \text{Equation 100}$$

where N is the number of additional spacecraft. Notice that the software size increase from a second platform is only a fraction of the initial baseline. This results from the relative simplicity of the combiner spacecraft and some software re-use with the collector spacecraft. It is assumed that the software differences between combiner spacecraft of different sized apertures will be negligible.

Maintenance Cost Approach

Maintenance represents the continual requirement to support necessary operational elements over the course of the TPF mission. Using a CER from [Larson & Wertz, 1992], it is modeled by

$$\text{Maintenance} = 0.1 \times (\text{GSW} + \text{EQ} + \text{FAC}) \quad \text{Equation 101}$$

where GSW is the ground software development cost, EQ is the equipment development cost, and FAC is the facility development cost.

Mission Inefficiency

Three main components affect mission inefficiency, the signal delay time, the operational failure rate, and the recovery time per failure. Figure 53 shows the mission inefficiency contribution from a single anomaly.

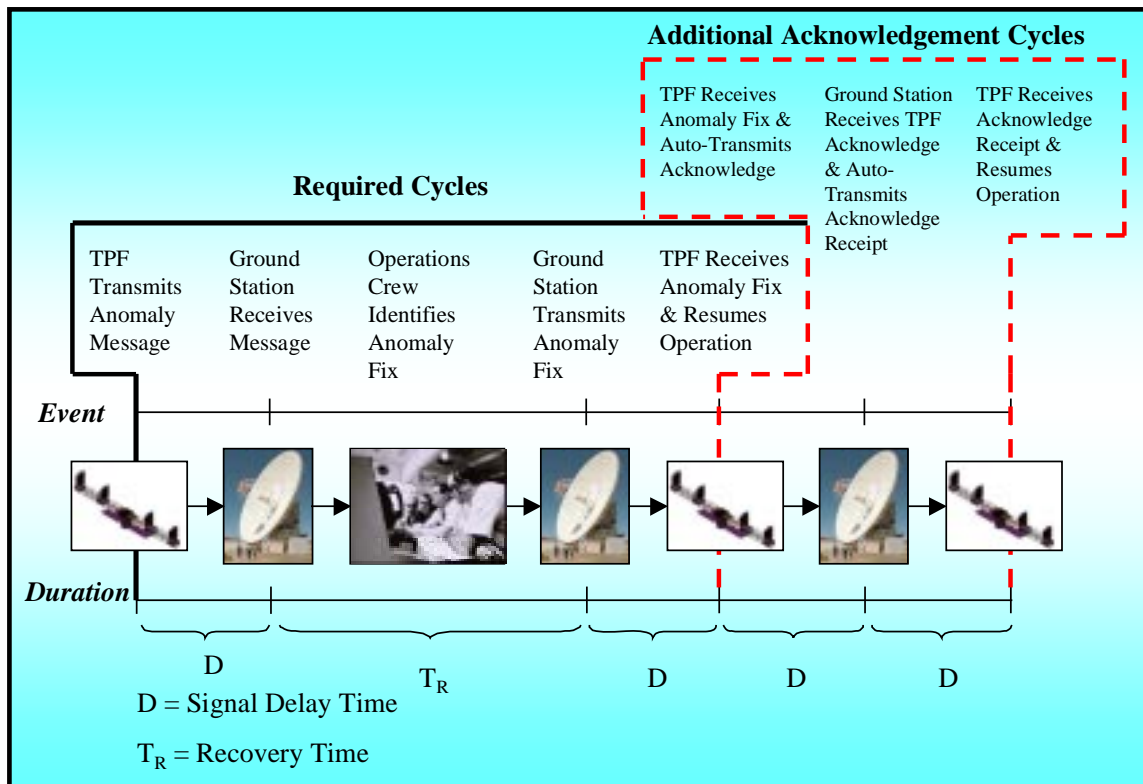


Figure 53. Mission Inefficiency from a Single Anomaly

In Figure 53, the additional mission inefficiency from an acknowledgment cycle is shown. This extra cycle, comprised of two transmission cycles, will not always be necessary, and is up to the operator's judgement or established operations protocol. The average number of transmission cycles, assuming an equal distribution of required and acknowledgement cycles, is therefore 3.

The signal delay time is the one-way straight-line communications travel time between the TPF and the ground station. It is captured by

$$D = S/c \tag{Equation 102}$$

where D is the signal delay time, S is the distance between the TPF and ground station, and c is the vacuum speed of light.

Failures of different operations functions have different average failure recovery times. The breakdown is shown in Table 18.

Table 18. Average Failure Recovery Time per Operations Function (Data from [Schwarz, 1997])

Operations Function i	Average Failure Recovery Time (min.)
Archiving	60
Tracking	10
Control Center Comm.	10
Attitude Control	60
Power Generation	20
Power Distribution	30
Telemetry	20
Command Handling	30
Orbit Control	120
Payload Receive	240
Payload Transmit	240
Thermal Control	20

With this information, the module provides a mission inefficiency output according to the equation

$$I = \bar{C}_y DF_{total} + \sum_i^n F_i \bar{r}_i \quad \text{Equation 103}$$

where \bar{C}_y is the average number of transmission cycles for anomaly resolution (assumed to be 3), D is the signal delay time, F_{total} is the total failure rate, n is the total number of operations functions considered, and F_i and \bar{r}_i are the failure rate and average recovery time for a specific ops function, respectively.

Trade Space:

Operational difficulty leads to increased cost and is driven by system complexity. System complexity is driven, to a large degree, by the number of additional spacecraft to control, and the attendant increase in difficulty to ensure their cooperative functionality. Therefore, a structurally connected spacecraft is easier to operate than a small cluster of separated spacecraft, which, in turn, is easier to operate than a more numerous cluster of separated spacecraft. It should be pointed out that operating the five spacecraft of a 4 aperture SSI is not four or five times as complex as a single spacecraft SCI, since each additional collector spacecraft is comparatively simple with respect to the main combiner spacecraft. Furthermore, operational efficiencies, learning curve effects, and automation attenuate the complexity increase from each additional spacecraft. The operational difficulty trade is shown in Figure 54.

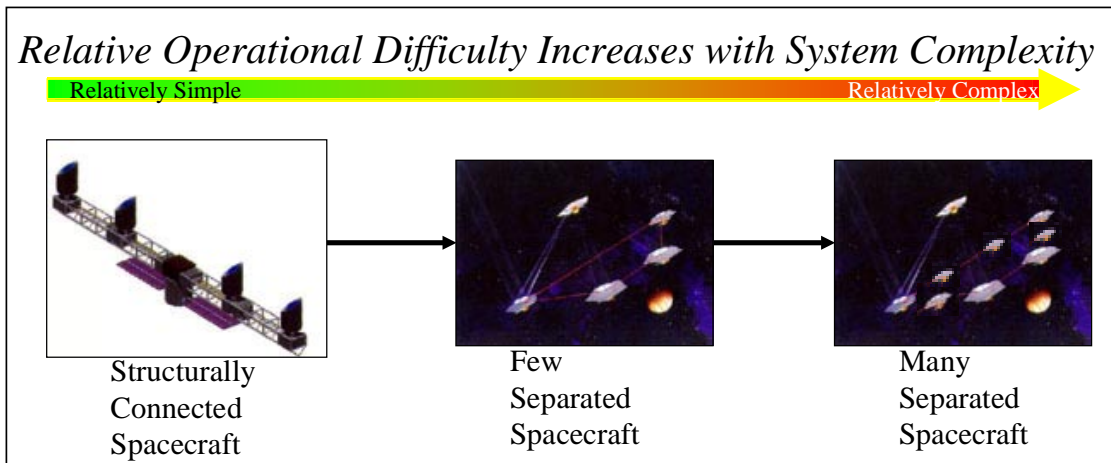


Figure 54. Operational Difficulty Tradespace

Mission inefficiency impacts system performance (primarily imaging rate) and is affected by two factors, system unreliability and distance. A less complex system will generate less anomalies, requiring less time to resolve those anomalies. A closer system will suffer less transmission delay time. Therefore, a close and reliable system reacts quickly to relatively few anomalies, while a distant and unreliable system reacts slowly to frequent anomalies.

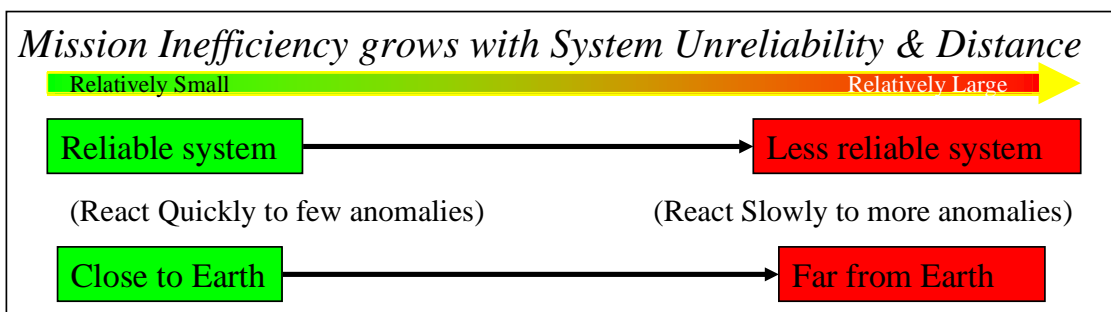


Figure 55. Mission Inefficiency Tradespace

7.6 GINA Macro-Module

The final macro-module in TMAS is the systems analysis macro-module, named GINA. Recall that the primary objective of this project was to “Develop a methodology for the comparison of architectures, spanning from structurally connected to separated spacecraft interferometers.” Therefore a need exists to develop a uniform framework for comparing different TPF architectures on the same basis. The systems engineering methodology chosen to develop this framework is GINA - the Generalized Information Network Analysis methodology for Distributed Satellite Systems [Shaw, 1998].

Figure 56 illustrates the order in which each module is called by the GINA macro-module. First, GINA calls the Capability module. This function reads in the orbit, the number of apertures, the signal-to-noise ratio (SNR), the spectral resolution required for each of the

three modes of operation, the aperture configuration matrix, the dynamic noise (OPD delays), and the mission inefficiency. The outputs include the surveying, medium spectroscopy, and deep spectroscopy imaging rates. Next, GINA calls the Performance module. This function requires the total number of apertures, the correct Markov Model, and the imaging rate in each of the three modes of operations. With these inputs, the performance module estimates the total number of images the TPF will take over its mission lifetime. GINA then calls the Cost module, which requires the total number of apertures, the architecture type, the aperture diameters, the number of combiner payloads, the science light beam diameter, the total bus mass, the launch cost, and the operations cost as inputs. The Cost module computes the system's total lifecycle cost. After reading in the total lifecycle cost and the mission performance, the Cost Per Function module calculates the cost per image. Finally, the adaptability module may be used to calculate the sensitivity of the cost per image to variations in different parameters.

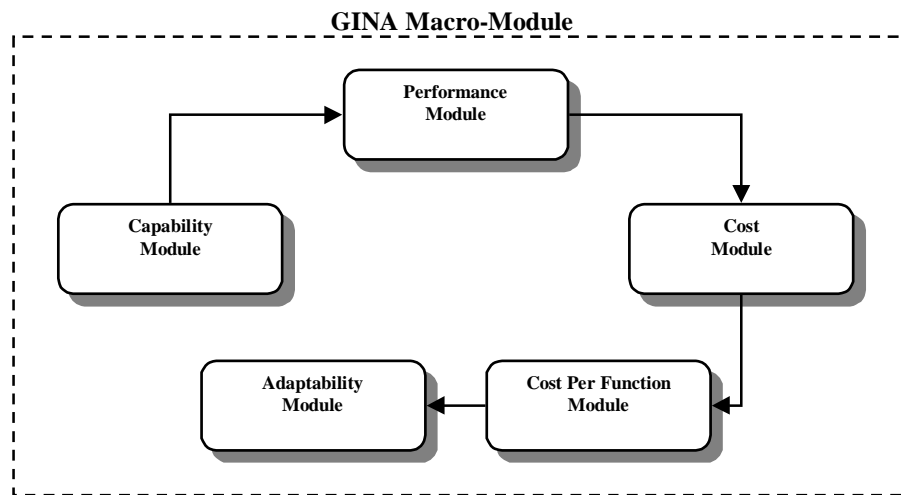


Figure 56. Overview of the GINA Macro-Module

7.6.1 Capability Module

Module Motivation

In the GINA methodology, the capability of an architecture is characterized by the “Quality of Service” parameters that relate to the detection process and to the quantity, quality, and availability of the information that is processed through the network. These parameters are signal *isolation*, information *rate*, information *integrity*, and the *availability* of these services over time [Shaw, 1998]. Once formulated, these parameters serve as the minimum instantaneous capability requirements the system must meet to satisfy the customer.

Module Description

Isolation refers to the ability of a system to isolate and distinguish information signals from different sources within the field of view. For TPF, the system's angular resolution, which is a function of the maximum vector baseline between a pair of collectors, determines the

smallest sized objects the SSI can image and discriminate between in the field of view. Rate measures the speed at which the system transfers information between the sources and sinks in the network. In TPF, the imaging rate is simply the total number of images the system can produce per unit time and varies for each of the three modes of operation - surveying, imaging, and spectroscopy. Integrity is a measure of the quality of the information being transferred through the network. In the case of TPF, the integrity of an individual image is a function of the SNR. TPF architectures with greater integrity will produce images with less uncertainty. Finally, availability characterizes the instantaneous probability that information symbols are being transferred through the network between all of the sources and sinks. For TPF, targets close to the sun, or those whose imaging violates sun avoidance angles within the optical train, reduce the availability of the system. The actual imaging time versus calibration, retargeting, and other tasks also affect the availability of the system.

For TPF, the isolation capability (necessary angular resolution) for the TPF mission is mandated in the requirements document. All simulated architectures meet this requirement, which may be verified by looking at the transmissivity function. Similarly, the minimum integrity (required SNR) needed for planetary detection is also mandated in the requirements document. This SNR, combined with the inputs to the capability module, allows for the calculation of the imaging time for each mode of operation by solving the SNR equation (Equation 116) for time t . The inverse of t yields the TPF architecture imaging rate. By calculating this imaging rate for each unique functioning state of the TPF and passing this information to the performance module, the GINA module is able to calculate the total number of images the architecture will collect over its mission life, taking into account failures. Since both isolation and integrity are set in the requirements, the *imaging rate* will be the *distinguishing* capability parameter between different TPF architectures.

Recall that three different operational modes are modeled for TPF – surveying, medium spectroscopy, and deep spectroscopy. The *surveying* mode, which requires an SNR = 5 at a spectral resolution of 3, entails looking for planets around a large variety of stars. The *medium spectroscopy* mode, which requires an SNR = 10 at a spectral resolution of 20, encompasses looking for strong spectral lines of molecules, such as CO₂ and H₂O, that could indicate the presence of life on the observed planets. Finally, the *deep spectroscopy* mode, which requires an SNR = 25 at a spectral resolution of 20, searches for O₃ spectral lines.

To compute the imaging rate of a TPF architecture, the total time required to obtain a single image must be calculated for each mode of operation. This total imaging time (T_T) is the sum of the integration time (T_i), overhead time (T_o), and time lost due to mission inefficiency (T_m).

$$T_T = T_i + T_o + T_m \tag{Equation 104}$$

The integration time for the different spectroscopy modes is driven by the required SNRs and spectral resolutions. The values for these parameters for the different spectroscopy modes are directly obtained from the requirements document and are given in Table 19.

Also listed in the table are the science objectives that correspond to the different spectroscopy modes.

Table 19. Detection Requirements for the Different Spectroscopy Modes

Spectroscopy Level	Science Goal	SNR	Spectral Resolution
Survey	Detect Planet	5	3
Medium	Detect Atmosphere	10	20
Deep	Habitable Life?	25	20

The following inputs are required to compute integration time.

- The required SNR
- The spectral resolution
- The aperture configuration matrix
- The interferometer's operating orbit
- The wavelength of interest

The required SNR and the spectral resolution are obtained from Table 19. The aperture configuration matrix is the $N \times 6$ output matrix produced by the Aperture Configuration Macro-Module. The interferometer's operating orbit is obtained directly from the Design Vector, while the operating wavelength is set to 12 microns in the Constants Vector.

The computation determines the rate at which photons are received by the interferometer from the different sources. Using these rates, the minimum integration time required for the specified SNR and spectral resolution can then be determined. The following sources contribute to the total photon count received by the instrument.

- The planet
- The parent star leakage
- The local zodiacal cloud
- The exo-zodiacal cloud
- The background noise

A noise source that is not captured is the dark current noise caused by using the infrared detector.

The physics behind this module is adapted from Appendix A in [Beichman et al., 1999] and is best explained with an example. In the following discussion, the integration time required for the 1-2-2-1 OASES interferometer located at an orbit of 5 AU and operating in the planet detection mode is determined by calculating the photon rate received from the different sources.

The target planet is modeled as an Earth-like planet located 10 parsec away from the instrument, which is consistent with the assumptions made in the Aperture Configuration

macro-module. Assuming also that the parent star is Sun-like, the temperature of the planet can be determined by Equation 105.

$$T_{planet} = 265a^{-0.5}L_*^{0.25} \quad \text{Equation 105}$$

The variable a is the orbital radius of the planet and L_* is the luminosity of the parent star with respect to the Sun. From this planet temperature, the brightness temperature of the planet can then be determined [Rohlf and Wilson, 1996] from Equation 106.

$$B_\nu(\nu, T_{planet}) = \frac{2h\nu^3}{c^2} \frac{1}{e^{h\nu/kT} - 1} \quad \text{Equation 106}$$

The variable ν is the observing frequency of interest, c is the speed of light, h is the Planck constant, and k is the Boltzmann constant. The number of photons collected from the planet can then be calculated by Equation 107.

$$Q_{planet} = \Theta(r, \theta) B_\nu(\nu, T_{planet}) \Omega_{planet} A_{tel} N_{tel} \eta h R^{-1} \quad \text{Equation 107}$$

$\Theta(r, \theta)$ is the transmissivity function of the interferometer, Ω_{planet} is the solid angle subtended by the planet, the product $A_{tel} N_{tel}$ is the total collecting area of the interferometer, η is the optical efficiency of the interferometer, and R is the specified spectral resolution, which is equivalent to $\lambda/\Delta\lambda$. The optical efficiency of the system is set at 0.04, as quoted in [Beichman et al., 1999]. Even though an Earth-like planet located at 1 AU from the parent star was assumed, the average response of the transmissivity function in the entire habitable zone (0.5 to 3 AU) is used to provide a more appropriate estimation of the expected photon rate. The results of these calculations indicate that the average photon rate from the planet is 0.1 photons/sec for the 1-2-2-1 interferometer operating in the planet detection mode.

A major source of noise for the TPF is parent starlight leakage. Since the parent star is approximately one million times brighter than the planet at the wavelength that is being considered (12 microns), the amount of starlight that leaks through may be sufficient to wreck the effort to detect the faint signal from the planet.

The rate of starlight coming through the null is given by Equation 108.

$$Q_{leak} = A_{tel} N_{tel} \eta h R^{-1} \iint \Theta(r, \theta) B_{\nu,*}(r, \theta) r dr d\theta \quad \text{Equation 108}$$

The brightness temperature of the parent star can be determined by assuming a constant surface temperature of 5800 K. The photon rate due to star light leakage, evaluated over the parent star, is 6.2×10^{-7} photons/sec for the current example.

Another important noise source introduced into the system is from local zodiacal dust. The capability module uses the zodiacal cloud model proposed by [Reach et al., 1995], where the

structure of the solar system dust is modeled as a fan shaped distribution. The amount of dust emission along the line of sight of the interferometer can be calculated by Equation 109.

$$I_v = \int B_v(T(r))\rho_o r^{-\alpha} e^{-\beta(z/r)^\gamma} dl \quad \text{Equation 109}$$

The variable ρ_o is the optical depth of the cloud, and r and z are the cylindrical coordinates within the cloud. The equilibrium temperature ($T(r)$) of the cloud can be determined by Equation 110, where r is the distance from the sun measured in AU.

$$T(r) = T_o r^{-\delta} \quad \text{Equation 110}$$

The different parameters that describe the zodiacal cloud in Equation 109 and Equation 110 are given in Table 20.

Table 20. Properties of the Zodiacal Cloud (Beichman et. al., 1999)

Property	Value
ρ_o	$1.14 \times 10^9 \text{ AU}^{-1}$
α	1.39
β	3.26
γ	1.02
Temperature at 1 AU (T_o)	$286 (L/L_o)^{0.25}$
δ	0.42

Using this zodiacal cloud model, the signal rate from the local zodiacal cloud can then be determined using Equation 111, where the integral extends to the edge of the primary telescope beam, $r_{max} = 0.66\lambda/D$. According to [Beichman et. al., 1999], this choice of r_{max} optimizes the SNR for a background-limited measurement of a point source. In the case of the OASES interferometer located at an orbit of 5 AU, the signal rate due to the local zodiacal cloud is 0.27 photons/sec.

$$Q_{lz} = A_{tel} N_{tel} \eta h R^{-1} I_v(LZ) \iint \Theta(r, \theta) r dr d\theta \quad \text{Equation 111}$$

The determination of the exo-zodiacal cloud photon count rate is similar to what is shown in the previous section. Since no information is available for the zodiacal cloud in the targeted systems, the same cloud model [Reach et al., 1995] is used again. Therefore, the photon rate the interferometer sees is determined by Equation 112.

$$Q_{ez} = A_{tel} N_{tel} \eta h R^{-1} \iint I_v(r, \theta) \Theta(r, \theta) r dr d\theta \quad \text{Equation 112}$$

The integral extends from the surface of the parent star to the edge of the primary telescope beam. A total photon count rate of 13 photons/sec will be seen by the OASES interferometer.

Another noise source that is included in the formulation is the background noise. This error comes about since the planet must be detected against a non-flat field of corrugations in the target field. The flat field error used in this formulation is $f = 10^{-5}$, while the flat field photon rate is calculated from Equation 113, where the dark current rate is discussed below. For this OASES example, the flat field photon rate is 1.8×10^{-9} photons/sec.

$$Q_{flat} = f^2(Q_{LZ} + Q_{EZ} + Q_{dark} + Q_{planet}) \quad \text{Equation 113}$$

The last noise source considered in this module is the detector dark current noise. The value for this source was obtained from [Beichman et. al., 1999] and is estimated to be 5 photons/sec.

The total noise is the quadratic sum of all the individual components and is given by Equation 114, where τ is the integration time.

$$S_{noise}^2 = (Q_{leak} + Q_{LZ} + Q_{EZ} + Q_{dark} + Q_{planet} + Q_{flat})\tau \quad \text{Equation 114}$$

Since the SNR of the exo-planet is given by Equation 115, the minimum integration time required is therefore calculated using Equation 116.

$$SNR = Q_{planet}\tau/S_{noise} \quad \text{Equation 115}$$

$$\tau = \left[SNR \sqrt{(Q_{leak} + Q_{LZ} + Q_{EZ} + Q_{dark} + Q_{planet} + Q_{flat})} / Q_{planet} \right]^2 \quad \text{Equation 116}$$

For the example OASES interferometer, the minimum integration time required to obtain the specified SNR and spectral resolution is 3.7×10^4 sec. Table 21 summarizes the different components that contribute to the minimum integration time calculation for this example.

Table 21. Signal and Noise Source Components for the OASES Interferometer

Parameter	Value
Planet photon rate (Q_{planet})	0.1 photons/sec
Parent star leakage rate (Q_{leak})	6.2×10^{-7} photons/sec
Local zodiacal photon rate (Q_{LZ})	0.27 photons/sec
Exo zodiacal photon rate (Q_{EZ})	13 photons/sec
Dark current (Q_{dark})	5 e ⁻ /sec
Flat Field Error (Q_{flat})	1.8×10^{-9} photons/sec
Minimum Integration time (τ)	3.7×10^4 sec

In addition to physics, the TPF imaging time calculations must also consider operations issues such as overhead time and operations downtime. Overhead time for an observation is the time allotted for constellation slewing, aperture configuration, array rotation, etc. JPL estimates this overhead time as 6 hours for each survey and 5.33 hours for every 24 hours of spectroscopy [Beichman et. al., 1999]. The time lost to mission inefficiency is computed in the operations module and is a function of the total number of spacecraft in the system. An architecture that contains more spacecraft is inherently more complex to control, and will therefore lose more imaging time due to the resolution of anomalies. Table 22 summarizes the three elements that go into the imaging time calculation for each mode of operation.

Table 22. Imaging Time Components

Mode of Operation	Integration Time	Overhead Time	Operations Downtime
Surveying	SNR=5	6 hours	Operations module
Medium Spectroscopy	SNR=10	5.33 hours per day	Operations module
Deep Spectroscopy	SNR=25	5.33 hours per day	Operations module

Finally, once the total imaging time has been computed for a mode of operation, the imaging rate (C_i) in that mode may be determined by inverting the total imaging time.

$$C_i = \frac{1}{T_i} \tag{Equation 117}$$

This imaging rate must be computed for each mode of operation for each possible operational state of the interferometer, taking into account failures. For example, a six collector nulling interferometer may function with all six collectors operational (State 1), five operational collectors after a single failure (State 2), and four operational collectors after two failures (State 3). Table 23 lists these imaging rates for both SCI and SSI TPF architectures. Both architectures contain six collectors, two meters in diameter each, and are located in a 1 AU orbit. While both architectures have the same imaging rate in State 1, the SSI maintains a higher imaging rate in the degraded states. This is because the collectors in an SSI may be reconfigured to new “optimal” positions after a failure, while the collectors on an SCI are fixed in sub-optimal positions after one or more failures.

Table 23. Surveying Imaging Rates (surveys per month) for Each Operational State of a 6 Collector TPF Architecture

Architecture	State 1	State 2	State 3
SCI	78.3	43.1	37.6
SSI	78.3	44.8	38.0

Trade Space

The GINA modules calculate the metrics used to evaluate the results of the trade studies. The Adaptability Module (Section 7.6.5) provides the capability to perform a wide range of trade studies and sensitivity analyses.

7.6.2 Performance Module

Module Motivation

While the capability module calculates metrics such as the imaging rate of each operational mode at any point in time, the performance module calculates how well these metrics are satisfied over the mission lifetime. For the TPF, performance is expressed as the total number of images the system produces over the mission design life. However, to calculate this quantity, the additional complication of taking into account all of the possible failures that may occur within the system must be addressed. As individual collectors fail over time, the imaging rate of the system will decrease in order to maintain the same pre-failure level of integrity (ie. the TPF must still achieve the same SNR for each operational mode, despite failures).

Module Description

The Performance Module uses Markov reliability modeling techniques to determine both the probability that the system will continue to function over a given amount of time and the likelihood with which the system will function in different partially failed states throughout the mission. A Markov model must be created for each proposed architecture. From the Markov model, a system of differential equations is developed, as shown in Equation 118, where $\dot{\vec{P}}$ is the time rate of change of the state probability vector, A is the state coefficient matrix comprised of component failure rates, and \vec{P} is the state probability vector.

$$\dot{\vec{P}} = A\vec{P} \tag{Equation 118}$$

The solution to this set of linear first order, partially coupled ordinary differential equations determines the probability of the system being in any given state at a particular time. Coupling the outputs of the reliability model with the outputs of the capability model yields the total performance (total number of images) of the system. The coupling equation is called the utility function (Equation 119).

$$E(T) = \int_0^T \sum_{i=1}^n C_i P_i(t) dt \tag{Equation 119}$$

E is the total number of images, T is the mission lifetime, n is the total number of operational states, C is the capability in each state i , and P is the probability of being in each operational state i as a function of time t .

This section presents an example of how to create a Markov model for a TPF architecture and how to apply this information to the design of the system architecture. Markov models have been traditionally used to evaluate the reliability of complex systems. In order to apply a Markov modeling methodology, the states of the system must be time dependent,

sequential, and mutually exclusive. If the system satisfies these requirements, then a set of differential equations can be written to model the evolution of the system. By taking advantage of the Markov property, which states that given full knowledge of the current state of the system, one can predict all future states by integrating the set of differential equations, irrespective of the past states of the system [Gelb, 1974]. The example creates a Markov model for the case of an eight collector nulling interferometer. The Markov models for architectures with 4 to 12 collectors were implemented in the same manner.

The first step is to develop a fault tree diagram illustrating all the possible different modes of failure for each design (Figure 57). Recall that the minimum functionality required for a nulling interferometer is one combiner and four collectors. Thus, the eight collector TPF architecture fails when the combiner fails or when any five collectors fail.

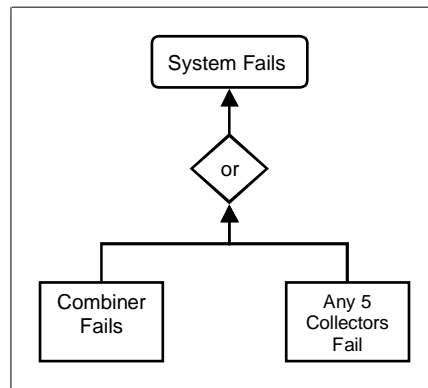


Figure 57. Fault Tree for an Eight Collector TPF Architecture

From the fault trees, a Markov model illustrating each possible state of the system may be created for each architecture. Figure 58 illustrates the Markov model for the eight collector architecture. This model contains five possible functioning states, which all require a functional combiner.

- State 1: All eight collectors are working.
- State 2: Seven of the eight collectors are working.
- State 3: Six of the eight collectors are working.
- State 4: Five of the eight collectors are working.
- State 5: Four of the eight collectors are working.

Otherwise, the system is in a state of failure since the nulling (isolation) requirement can no longer be met.

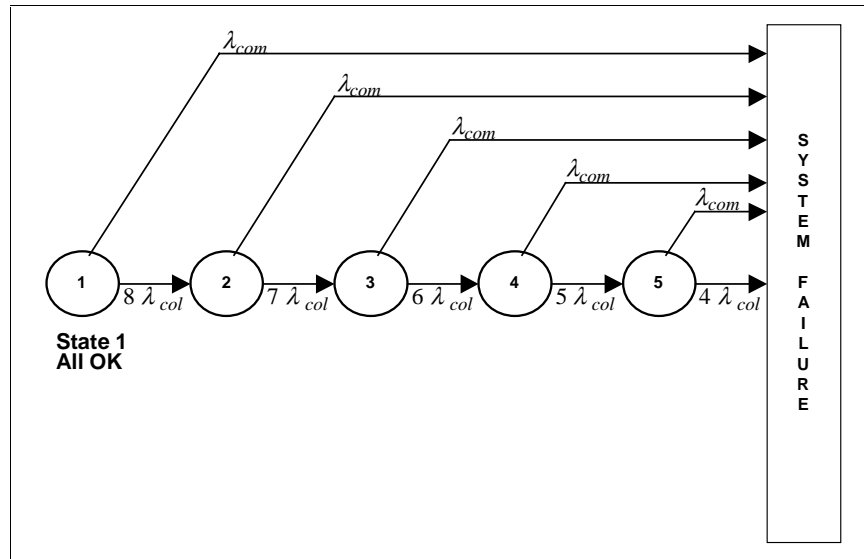


Figure 58. Markov Model State Diagram for the 8 Collector TPF Architecture

From the Markov model state diagram, a system of differential equations can be written to determine the probability of the system being in any given state at any given time. This is done by representing each possible state of the system in the Markov model as a node in a network. To determine the differential equation for a particular state, the flow into and out of the node representing that state is balanced. The eight collector TPF architecture requires a set of five partially coupled linear first order differential equations to model the system (Equation 120).

$$\begin{bmatrix} \dot{P}_1 \\ \dot{P}_2 \\ \dot{P}_3 \\ \dot{P}_4 \\ \dot{P}_5 \end{bmatrix} = \begin{bmatrix} -(\lambda_{com} + 8\lambda_{col}) & 0 & 0 & 0 & 0 \\ 8\lambda_{col} & -(\lambda_{com} + 7\lambda_{col}) & 0 & 0 & 0 \\ 0 & 7\lambda_{col} & -(\lambda_{com} + 6\lambda_{col}) & 0 & 0 \\ 0 & 0 & 6\lambda_{col} & -(\lambda_{com} + 5\lambda_{col}) & 0 \\ 0 & 0 & 0 & 5\lambda_{col} & -(\lambda_{com} + 4\lambda_{col}) \end{bmatrix} \begin{bmatrix} P_1 \\ P_2 \\ P_3 \\ P_4 \\ P_5 \end{bmatrix} \quad \text{Equation 120}$$

Knowledge of the failure rates for the combiner (λ_{com}) and collector (λ_{col}) are required to solve for the state probabilities. For this work, it was assumed that a combiner has a mean-time-to-failure (mttf) of 10 years and a collector has an mttf of 15 years. The failure rate (λ) is the inverse of the mttf (Equation 121).

$$\lambda = \frac{1}{mttf} \quad \text{Equation 121}$$

The system's initial conditions are also required for the solution. In every case, the initial conditions (ie. at $t=0$ in the beginning of the operational mission) are a 100% probability of being in state 1 and a 0% probability of being in all successive states.

The plot in Figure 59 illustrates the results for the eight collector example. The Markov model gives the exact probability of being in any of the five operational states as a function of time through the five year (60 month) TPF mission. Each of these five operational states will have a different imaging rate. Markov models for TPF architectures containing four to twelve collectors were created and solved with the same assumed failure rates. The results (state probability matrices) were saved in Matlab “.mat” files. The TMAS software calls and loads the appropriate “.mat” file based on the number of collectors entered in the Design vector.

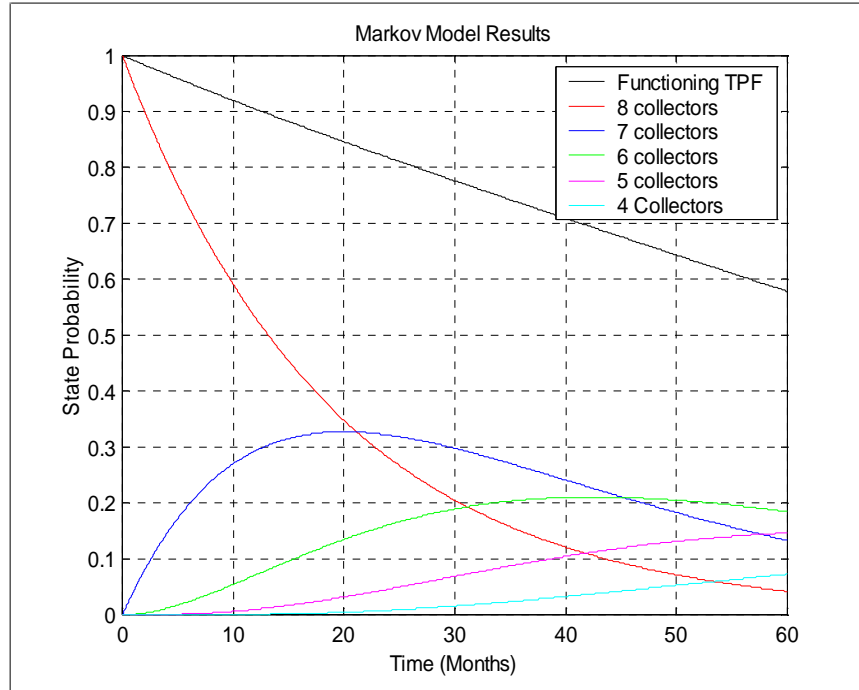


Figure 59. Markov Model Results for the Eight Collector TPF Architecture

The total system performance of a TPF configuration can now be calculated using the imaging rate (C) in each operational mode in each possible functioning state (capability module) and the probability of being in each possible functioning state over the mission lifetime (Markov model).

Table 24 lists JPL’s scientific utilization plan for TPF. With this utilization plan as the basis, a daily TPF mission profile (Table 25) was created using the following two assumptions:

1. During each year, each phase is executed sequentially. For example, in year one all of the surveys must be completed before beginning the medium spectroscopy, and all of the medium spectroscopy must be completed before beginning the deep spectroscopy. This simplifies the modeling process.
2. The time allocated by JPL to “astrophysical imaging” is shared evenly between medium and deep spectroscopy, since astrophysical imaging is not modeled in the TMAS.

Table 24. TPF Scientific Utilization Plan (Beichman et. al. 1999)

Operational Mode	Year 1	Year 2	Year 3	Year 4	Year 5
In-Orbit Checkout	0.2	0	0	0	0
Planet Survey	0.5	0.5	0.2	0.1	0.1
Medium Spectroscopy	0.1	0.2	0.4	0.4	0.3
Deep Spectroscopy	0.1	0.1	0.1	0.2	0.2
Astrophysical Imaging	0.1	0.2	0.3	0.3	0.4

Table 25. TPF Daily Mission Profile (cumulative from mission start)

Year	In-Orbit Checkout	Planet Survey	Medium Spectroscopy	Deep Spectroscopy
1	Days 1-73	74-256	257-313	314-365
2		366-547	548-658	659-730
3		731-804	805-1004	1005-1095
4		1096-1132	1133-1333	1334-1460
5		1461-1498	1499-1680	1681-1825

The total number of images a TPF architecture produces is the sum of the number of images it produces in each operational mode each year. Using the mission profile in Table 25 for the limits of integration (the time step is one day), the total system performance is obtained by summing fifteen separate utility functions (Equation 122), where i is an index indicating a particular operational state, n is the total number of operational states, C_s is the survey mode imaging rate, C_m is the medium spectroscopy mode imaging rate, C_d is the deep spectroscopy mode imaging rate, and P is the probability of being in any state i as a function of time (t).

$$\begin{aligned}
 \text{Total \# Images} = & \int_{74}^{256} \sum_{i=1}^n C_{si} P_i(t) dt + \int_{257}^{313} \sum_{i=1}^n C_{mi} P_i(t) dt + \int_{314}^{365} \sum_{i=1}^n C_{di} P_i(t) dt + \int_{366}^{547} \sum_{i=1}^n C_{si} P_i(t) dt + & \text{Equation 122} \\
 & \int_{548}^{658} \sum_{i=1}^n C_{mi} P_i(t) dt + \int_{659}^{730} \sum_{i=1}^n C_{di} P_i(t) dt + \int_{731}^{804} \sum_{i=1}^n C_{si} P_i(t) dt + \int_{805}^{1004} \sum_{i=1}^n C_{mi} P_i(t) dt + \\
 & \int_{1005}^{1095} \sum_{i=1}^n C_{di} P_i(t) dt + \int_{1096}^{1132} \sum_{i=1}^n C_{si} P_i(t) dt + \int_{1133}^{1333} \sum_{i=1}^n C_{mi} P_i(t) dt + \int_{1334}^{1460} \sum_{i=1}^n C_{di} P_i(t) dt + \\
 & \int_{1461}^{1498} \sum_{i=1}^n C_{si} P_i(t) dt + \int_{1499}^{1680} \sum_{i=1}^n C_{mi} P_i(t) dt + \int_{1681}^{1825} \sum_{i=1}^n C_{di} P_i(t) dt
 \end{aligned}$$

Trade Space

The GINA modules calculate the metrics used to evaluate the results of the trade studies. The Adaptability Module (Section 7.6.5) provides the capability to perform a wide range of trade studies and sensitivity analyses.

7.6.3 Cost Module

Module Motivation

The cost module estimates the total TPF architecture lifecycle cost by summing the computed payload, bus, launch, and operations costs.

Module Description

The combiner payload cost (C_{com}) is computed in millions of U.S. dollars as a function of the diameter (D_{com}) of the science light entering the combiner instrument (0.2 m for TPF) [Larson and Wertz, 1992].

$$C_{com} = (122.758)D_{com}^{0.562} \quad \text{Equation 123}$$

Based on the projected mirror costs for the Next Generation Space Telescope, the collector payload costs (C_{col}) were estimated in millions of U.S. dollars as a function of the collector diameter (D_{col}).

$$C_{col} = (0.7243)D_{col}^{2.69} \quad \text{Equation 124}$$

The spacecraft bus cost model estimates the total cost involved in designing, manufacturing, integrating, and testing each spacecraft bus. This cost will generally be proportional to the mass, power, and other subsystem requirements of the spacecraft. Over the years, several governmental organizations have created Cost Estimation Relationships (CERs) for satellite buses that show how the cost properties of a spacecraft bus vary with the subsystem parameters of the bus. These CERs are based on the historical data of past satellite programs and work on the assumption that future costs will reflect historical trends.

The two most commonly used CERs are the U.S. Air Force's Unmanned Spacecraft Cost Model (USCM) and the Aerospace Corporation's Small Satellite Cost Model (SSCM). The SSCM is valid for satellites approximately 500 kg or less and is based on 1990's technology. The USCM database contains much larger satellites, but is based on older 1970's and 1980's technology [Bearden, 1998].

The original intention was to use several of the CERs from the SSCM, and then compute the theoretical first unit (TFU) cost of each spacecraft bus via a weighted average algorithm. However, it soon became apparent that the bus masses for TPF would greatly exceed 500 kg. Therefore a mass (M) CER from the USCM was used to compute the TFU cost of each spacecraft bus (C_{bus}) in millions of U.S. dollars [Larson and Wertz, 1992].

$$C_{bus} = (0.185)M^{0.77} \quad \text{Equation 125}$$

The launch cost is strictly a function of the launch vehicle selected to deploy the TPF architecture. Table 26 lists the vehicles considered in the launch vehicle module and their

associated costs. If a particular TPF architecture requires a larger launch vehicle than currently exists, the module automatically declares the launch cost to be \$300 million.

Table 26. Launch Vehicle Costs

Launch Vehicle	Cost (\$ Millions)
Delta II	50
Zenit	85
Delta III	85
Delta IV	100
Ariane V	150
Titan IV	250
“Future Vehicle”	300

Finally, the TPF architecture operations costs are computed directly in the operations macro-module. The total operations cost is comprised of ground system development and maintenance costs, transit operations costs, on-station checkout costs, and science operations costs. These costs also scale with the complexity of the particular TPF architecture as explained in the Operations Macro-module section.

The total lifecycle cost ($C_{lifecycle}$) is calculated from Equation 126.

$$C_{lifecycle} = C_{payload} + C_{bus} + C_{launch} + C_{operations} \quad \text{Equation 126}$$

$C_{payload}$ is the sum of all the combiner and collector payload costs, C_{bus} is the sum of all the bus costs, C_{launch} is the total launch cost, and $C_{operations}$ is the total operations cost.

Trade Space

The GINA modules calculate the metrics used to evaluate the results of the trade studies. The Adaptability Module (Section 7.6.5) provides the capability to perform a wide range of trade studies and sensitivity analyses.

7.6.4 Cost per Function Module

Module Motivation

The Cost Per Function (CPF) metric provides a clear measure of the cost of an architecture versus its performance. It is a measure of the cost to achieve a common level of performance and includes expected development, launch, and operations costs.

Module Description

For the TPF, the cost per function is defined as the cost per image (CPI), and is calculated by dividing the total number of images obtained by the interferometer into the total lifecycle cost.

$$CPI = \frac{C_{lifecycle}}{\text{Total \# Images}}$$

Equation 127

- As the system design trade-space is explored, the CPI may be used as one metric to determine the relative performance of competing TPF system architectures.

Trade Space

The *CPI* metric provides a mechanism for evaluating the following design trades.

- **Orbit:** Placing the TPF farther from the sun increases the imaging rate as the interferometer looks through less of the local zodiacal cloud, thus improving total system performance. However, placing TPF further away costs more since a larger, more expensive launch vehicle is required to deploy the system. Which orbit provides the best balance?
- **Number of Collector Apertures:** Increasing the number of apertures improves the system performance by increasing the total collecting area, increasing system reliability, and allowing for fine-tuning of the null. However, more apertures also increases the construction, testing, launch, and operations costs. Which number of apertures provides the best balance?
- **Architecture Type:** SCI architectures tend to have a lower total mass and are thus cheaper to launch, but SSI architectures tend to provide better performance due to their reconfiguration capability. Which one provides the best value for the TPF mission?
- **Aperture Collector Diameter:** Larger apertures provide better images, but also cost more. What size provides the best balance?

7.6.5 Adaptability Module

Module Motivation:

In GINA, adaptability is a measure of how flexible an architecture is in response to changes in design assumptions and mission requirements. In one sense, adaptability may be thought of as the sensitivity or elasticity of the cost per function of a particular architecture to incremental changes in an assumption or requirement. For the TPF mission, potential assumptions that could be altered to measure architecture sensitivity include component costs and component reliabilities. In another sense, adaptability may be thought of as the flexibility of a particular architecture to adapt to a new set of mission requirements, such as a longer mission design life. An example of flexibility for TPF might be the ability of an SSI architecture to transition from a planetary detection mission to a mission of astrophysical imaging. This latter interpretation of adaptability is not modeled by TMAS.

A sensitivity analysis measures how a change in a single architecture assumption or requirement affects the entire system “performance” in terms of the system metrics. Sensitivity analyses are conducted because, in reality, point design do not remain frozen, but evolve over time. This occurs because the actual values for the architecture variables (Constants Vector) used in the implementation of a design will be different from the theoretical values used during the conceptual design phase of the project. A sensitivity analysis allows the user to assess ahead of time how such changes will affect the capability, reliability, and cost of the system; and whether or not such variations will change the choice of the “best” architecture.

Module Description:

The adaptability metric is defined as the sensitivity, or elasticity, of the cost per function of an architecture to incremental changes in a particular design parameter. Elasticity is a tool commonly used in the field of economics to determine the responsiveness of the demand for a product to a change in price of the product [McEachern, 1994]. For TPF, elasticity (E) may be thought of as the responsiveness of the cost per image of a particular architecture to a change in value of an architecture design parameter (x).

$$E_x = \frac{CPI / CPI}{x / x}$$

Equation 128

Because TPF is a large, complex, non-linear design problem with many design variables, finite differencing is the only way to calculate the sensitivity of the CPI to the design parameter(s) of interest. Thus, the simulation must be re-run for each parameter to which the sensitivity will be calculated. After obtaining the new CPI , the sensitivity or elasticity is calculated by Equation 128.

The process for evaluating the CPI sensitivity of a particular architecture to the diameter of the truss members can be illustrated by an example. The architecture selected for this example is a four aperture linear symmetric SCI in a 1 AU orbit with 2 meter diameter apertures. With the truss member diameter default value of 2 cm, the system has a CPI of \$1.00 million. If the truss member diameter is changed to 3 cm, the system CPI is 1.05 million. Thus, the elasticity of the CPI to the truss member diameter is 0.122, meaning that the total system value is relatively insensitive to a small change in the diameter of the truss members. In this manner, the sensitivity of any TPF architecture may be computed for many different design parameters.

Trade Space:

The Adaptability Module is the tool with which many of the possible trade studies can be executed.

This page intentionally left blank.

8.0 Architectural Design Evaluation Results

This Chapter demonstrates the results we obtained from exploring the trade space with the TPF mission analysis software (TMAS). First, the TRW, Lockheed Martin, and Ball Aerospace benchmark cases used to determine the quality of TMAS are presented. Next come the actual trade study results. We did not have time to complete a full test matrix, and thus a single optimal design was not found. Rather, we chose to explore each axis of the design vector independently, and thus the trades are made between the entries of the design vector and our capability metrics. A useful metric for comparing very different architectures is the cost per image (CPI) metric, assuming that all images (i.e. surveys) meet the required SNR and nulling requirements (ie. the integrity and isolation requirements). Important trends have become visible and the first indications of “optimal” design corners are becoming apparent. These are illustrated in the two combined cases presented at the end of this Chapter.

8.1 Benchmark Configuration Results

Before the TMAS software can be used to explore the tradespace for TPF, a series of test cases need to be conducted to ensure that the end results are within reason. A total of four test cases, corresponding to the TPF designs by Ball, TRW, and Lockheed Martin, were examined to create multiple benchmark comparisons for the TMAS software. The results from TMAS were compared to the TPF system parameters from each point design to see which estimates had significant differences, and to explain the reason why these differences exist. The overall goal in this benchmarking process was to gain confidence in the results from TMAS, not to match them with the design parameters from other companies.

The first benchmark test case concerns the TPF design by the Ball Aerospace and Technologies Corporation. An illustration of their TPF design is given in Figure 60.

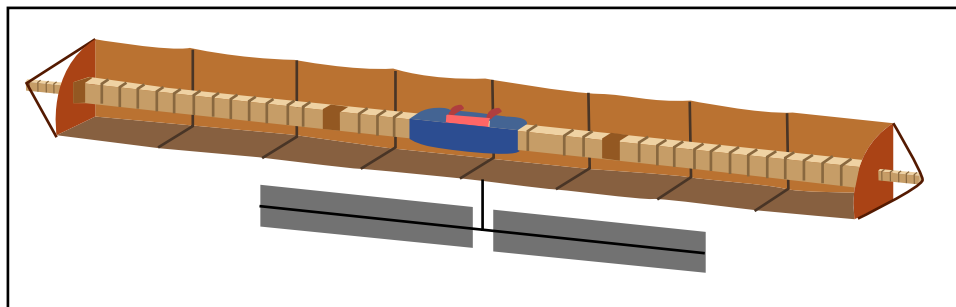


Figure by MIT OpenCourseWare.

Figure 60. Ball Design for TPF

The Ball design is an SCI interferometer with a total of four apertures (the outer aperture diameter is 0.5 m while the inner aperture diameter is 1.5 m) located at 5 AU. The mass and power estimates for the Ball design are listed with the same estimates from TMAS in Table 27.

Table 27. Ball SCI Benchmark

Parameter	Ball Estimate	TMAS Estimate	% Difference	Reason
Structure	987.6	1080.1	9.37	Good
Power	344.6	516.3	49.83	Solar array vs. RTGs and different power estimates
C&DH	39.3	33.0	16.03	Good
Comm	68.1	40.0	41.26	More power so less mass
Thermal	24.5	391.1	1496	Ball includes sun-shields in the structure mass
ADCS	124.0	185.0	49.19	More structural mass so more ADCS needed
Propulsion	392.4 (19.4)	9.68	97.53 (50.10)	Ball included transfer propulsion requirement
Payload	836.0	1040.0	24.40	Both values are only rough estimates
Propellant	791.6 (200)	54.8	93.08 (72.60)	See propulsion
Total, Bus, dry	1980.5 (1607.5)	2256.2	13.92 (40.35)	(adjustment for propulsion discrepancy)
Total, S/C, dry	2816.5 (2443.5)	3296.2	17.03 (34.90)	
Total, S/C, wet	3608.1 (2643.5)	3351.0	7.13 (26.76)	Not bad
Average Power	795.5	1939	143.7	Different power estimates (payload, thermal, etc.)

The notable differences in this case concern the communications, thermal, power, and propulsion/propellant estimates. The communications subsystem mass from TMAS is lower than the Ball estimate because the TMAS code specifically attempts to limit this subsystem mass by providing it with more power. The power subsystem discrepancy is mainly caused by the different power demand estimates but is also affected by the chosen power source. However, the most significant differences between the TMAS and Ball estimates concern the thermal and propulsion subsystems. The thermal subsystem used in the Ball design almost exclusively employs passive cooling strategies in the form of sun shields, whose mass is included in the structural mass estimate. The TMAS thermal module uses a combination of sun shields and cryocoolers to size the thermal subsystem, causing it to estimate a greater total mass. The discrepancy in the estimate for the propulsion subsystem is due to the fact the Ball design includes an additional thruster with propellant that would be used to travel to the mission orbit. The TMAS propulsion neglected this consideration, so the transfer propulsion system mass has been removed from the Ball estimates to account for the modeling differences. The important results from this benchmark concern the total mass comparisons between the Ball and TMAS estimates. For the most part, the TMAS estimates are reasonably similar to those from Ball, making this a successful test of the TMAS software.

The next test cases compare the TMAS software with the TRW TPF designs. Figure 61 gives an illustration of the TRW structurally connected design for TPF.

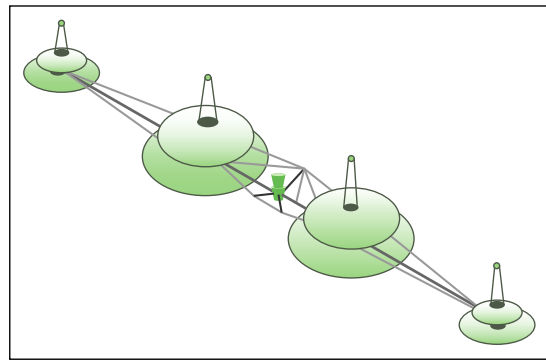


Figure by MIT OpenCourseWare.

TRW design for TPF

Figure 61. TRW Design for TPF

The TRW TPF study analyzes both SCI and SSI architectures using four collector spacecraft located at 5 AU. The mass and power estimates for an SCI architecture are listed with the TMAS estimates in Table 28.

Table 28. TRW SCI Benchmark

Parameter	TRW Estimate	TMAS Estimate	% Difference	Reason
Structure	719.4	1207.1	67.8	TRW uses ultra lightweight truss with guy wire supports
Power	169.5	516.2	204.5	TRW uses lightweight solar concentrator
CD&H	41	69.0	68.3	Small total difference
Comm	71.2	40	43.8	Small total difference
Thermal	265	493	86	
Propulsion	118.2	9.5	92	TRW included transfer propulsion requirement
Payload	924.3	1118	21	Good
Propellant	250	53.5	78.6	See propulsion
Total, Bus	753.3	1094	45.2	
Total, S/C (dry)	2309.8	3602.5	56	
Total, S/C (wet)	2559.8	3656	42.8	Reasonable
Average Power	2536.8	1939	23.6	Good

In this case, the major discrepancies between the TRW and TMAS estimates concern the spacecraft structure and the power and propulsion subsystems. The main reason for these differences is that the TRW design attempts to minimize mass using an ultra lightweight truss and lightweight solar concentrators. The TMAS modules account for certain technological advances, but do not reach the same level as TRW. In addition, the propulsion subsystem in the TRW design accounts for the transfer requirement similar to the Ball design while the TMAS software does not consider this requirement. Overall, the comparison of the total mass and power estimates again supports the validity of the results from the TMAS software. The TPF trade study by TRW also includes the analysis of an SSI architecture. Table 29 lists the mass and power estimates for TRW and TMAS.

Table 29. TRW SSI Benchmark

Parameter	TRW Estimate	TMAS Estimate	% Difference	Reason
Structure	289.7	885.4	205.6	
Power	192.7	1135.3	489.5	TRW uses lightweight solar concentrator and has lower power estimates
CD&H	33.2	69.0	107.8	Small total difference
Comm	24.6	44.6	81.3	Small total difference
Thermal	10.4	530.3	4999	TRW does not include sun shields
Propulsion	55.4	306.4	453	Class has heavier buses and electric prop is used
Payload	676.2	1095	61.9	
Propellant	312.5	550.9	76.2	See propulsion
Total, Bus	426.5	2544.4	496.6	
Total, S/C (dry)	2808.7	4250.1	51.3	
Total, S/C (wet)	3121.2	4801	53.8	Reasonable
Average Power	346.2	6425	1756	Drastically different power estimates (electric prop)

This test case shows a greater number of significant discrepancies between the TRW and TMAS estimates. The most important reason for this is the drastic difference between the two power demand estimates. The TMAS software incorporates an electric propulsion subsystem for an SSI architecture which requires a significant level of power to operate properly. Even with these different design assumptions between TRW and TMAS, the overall spacecraft mass estimates are again reasonably close to prove that the TMAS results are logical.

The final benchmark test case concerns the TPF study conducted by Lockheed Martin. The Lockheed Martin design is a structurally connected interferometer with four apertures located at 1 AU. The comparisons of the mass, power, and cost estimates between the Lockheed Martin and TMAS designs are given in Table 30.

Table 30. Lockheed Martin SCI Benchmark

	LM Estimate	Class Estimate	% Difference	Reason
Total S/C Mass	1750	3098	77.03	LM did not make a detailed model of the TPF spacecraft
Average Power	1500	1939	29.27	Same as above
Total Cost	608	755	24.18	Good

This is the only test case that provides an explicit cost estimate for TPF, which is quite close to the total cost calculated in the TMAS program. Aside from the total cost estimate, the remainder of the Lockheed Martin analysis is not a useful benchmark because the Lockheed Martin design makes only a rough approximation of the total mass and power demand for

PF while the TMAS software models each component of the entire spacecraft in greater detail. Once again, the TMAS software successfully benchmarks against the TPF design from another company.

Overall, the benchmark test cases proved the validity of the TMAS software and gave us confidence in its results. The benchmark cases specifically concentrated on mass and power estimates because the Ball, TRW, and Lockheed Martin team did not conduct a detailed analysis of the trade space available to TPF. These companies were more interested in constructing a point design for TPF and evaluating its performance. The TMAS software takes a different approach by focusing on the trade space analysis rather than specifying a specific design for TPF. Now that the TMAS software has been successfully tested, a detailed exploration of the TPF trade space can be conducted.

8.2 Trade Study Results

The key objective of this project is to develop a framework in which the trade studies between different architecture designs can be conducted. Taking a first step towards achieving this objective, the team decided upon a test matrix where the results from the different cases can be compared when only one parameter in the Design Vector is varied at a time. In doing so, we are able to determine the trends by which certain parameters (cost, mass, etc.) change as a function of only one parameter. Even though, given enough time and computing power, we could have performed an exhaustive search for the “optimal” solution based upon the metric we chose to compare, understanding these single dimension trends gave us considerable insight as to what the sensitive parameters are and at the same time, confidence in our model. An exhaustive search of the trade space should only be performed once these key trades are understood. Based upon these results, it may be possible to reduce the search space from the large number of designs.

In order to compare the different test cases, the team has chosen two architectures (SCI and SSI) as baseline cases to which results from the other cases could be compared. The Design Vector parameters for these two baseline cases are listed in Table 31. Table 32 lists the range over which each parameter is varied in the trade studies.

Table 31. Baseline Cases

Design Vector Parameter	Value
Orbit	1 AU
Aperture Size	2 m
Number of Apertures	4
Interferometer type	Linear Symmetric (SCI & SSI)

Table 32. Range Over Which Each Parameter Varies

Design Parameter	Values
Vector	
Orbits	1, 1.5, 2, 2.5, 3, 3.5, 4, 4.5, 5, 5.5, 6
Aperture size	0.5, 1, 1.5, 2, 2.5, 3.0, 3.5, 4.0
Number of Apertures	4,6,8,10,12
Interferometer type	Linear, Two-dimension

8.2.1 Orbit Trade Study

The orbital trade study was conducted on both an SCI and an SSI of the following configuration: 4 apertures, 2 meters diameter each, linear symmetric arrangement.

Image Distribution vs. Orbit

At orbits closer to the sun, the number of images is limited by the lower SNR caused by the local zodiacal dust. In these orbits, the density of the dust relative to the light gathering power of the 2 meter collectors causes the integration time to be longer for each image. The plateau at approximately 1200 images represents the maximum number of images for this configuration based on factors other than orbit, such as instrument theoretical capabilities and other noise sources. For the same aperture configurations, the total number of images as a function of orbit is independent of whether the spacecraft is SCI or SSI.

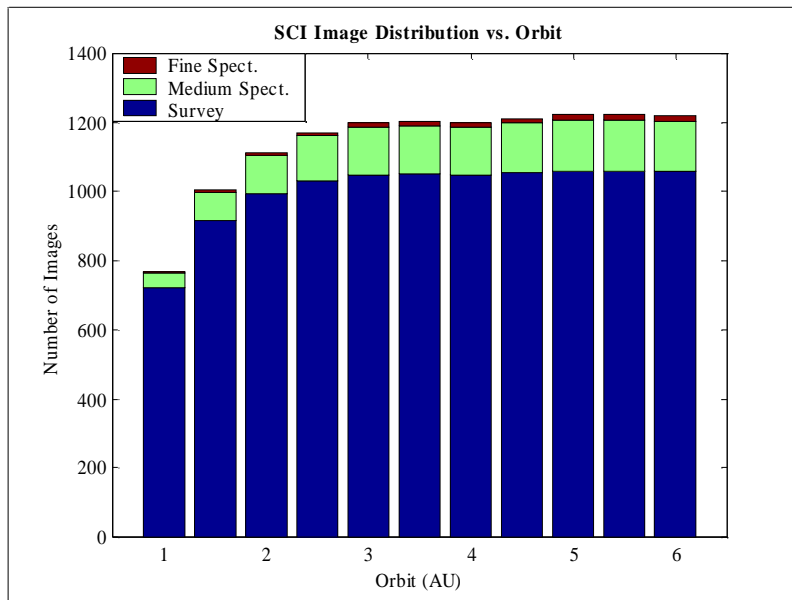


Figure 62. Image Distribution vs. Orbit

Cost Distribution vs. Orbit

As the orbital radius increases, the most sizable increases in cost are due to launch vehicle selection. Both the mass of the spacecraft and the V requirements increase as the orbit

increases, but it is the V requirement that drives the cost increases in the SCI case. (See the next section for more information on the mass trade.)

Development and payload costs do not show any dependence on orbit, while spacecraft bus and operations costs show the expected increases with higher orbits, primarily due to the longer mission lifetime.

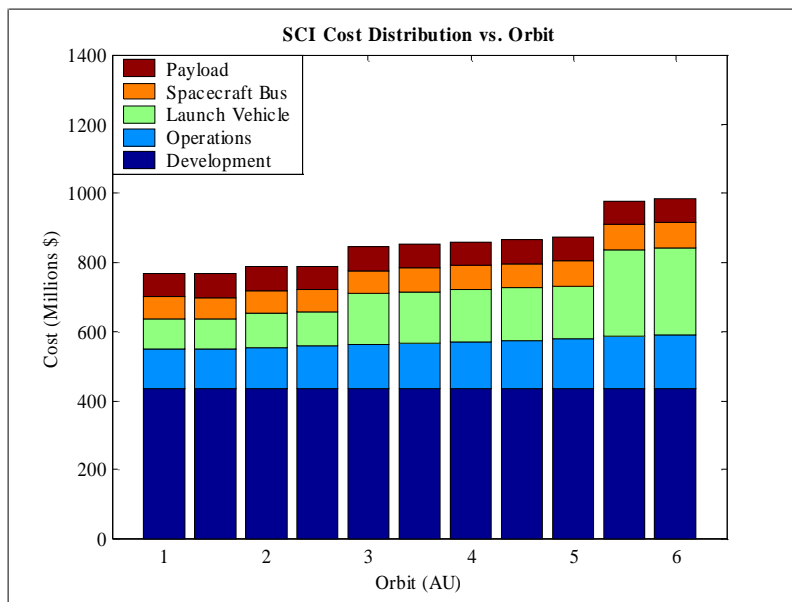


Figure 63. Cost Distribution vs. Orbit

Total Mass Distribution vs. Orbit

As expected, the total mass of the spacecraft increases with orbital radius. The effect is much more pronounced for the SSI architecture. In this case, the propulsion systems on the separate spacecraft require a large amount of power relative to the rest of the spacecraft instruments to operate efficiently. Thus, as the orbit increases, the size of the solar arrays required to provide this amount of power will grow until the TMAS determines that an RTG of an equivalent or smaller mass can provide the necessary power. Propellant mass showed only a slight increase with orbit, indicating that rather than increasing propellant mass, it is more efficient to increase the power required by the propulsion system and to take the mass increase in the power system.

The payload mass is not a function of orbit by the definition of this test case. The effect of orbit on bus mass is relatively small. In general, there is a slight positive correlation, but at the transition from solar arrays to RTGs, there is a more noticeable jump due to the loss of the solar arrays as a layer in the passive cooling scheme.

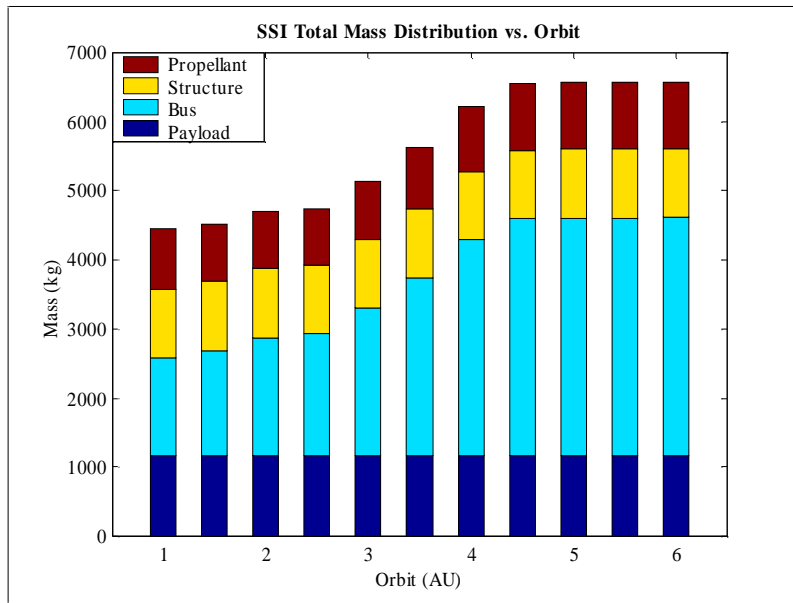


Figure 64. Total Mass Distribution vs. Orbit

Total Mass vs. Orbit by Architecture

The difference is due to the greater total bus mass associated with the multiple spacecraft in the SSI case. Not only do the multiple spacecraft require a greater initial mass, but the rate of increase with orbit is also greater due to the higher power requirements of the multiple propulsion systems. The dip in the graphs at 2.5 AU is due to a change in the thermal control scheme resulting from the lower solar heat flux.

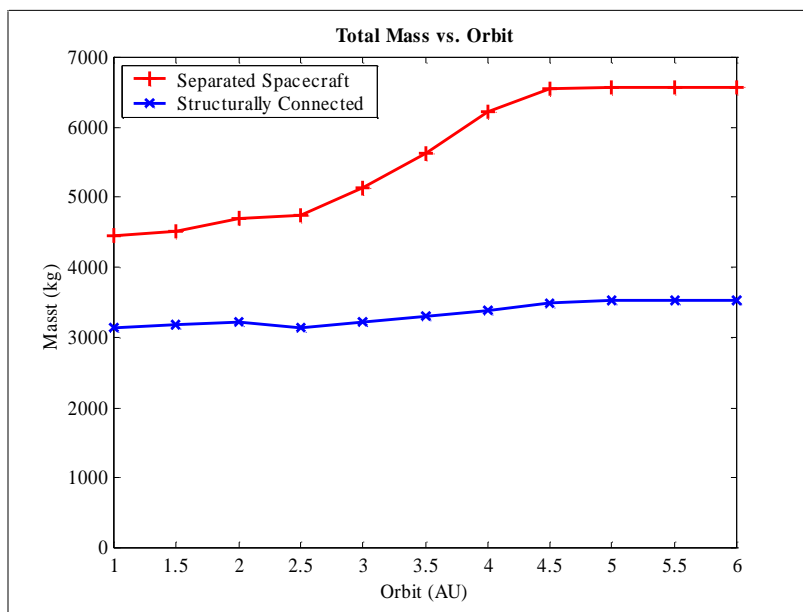


Figure 65. Total Mass vs. Orbit

Cost per Image (CPI) vs. Orbit

The total cost per image tends to increase at both ends of the orbital range, indicating that the optimum orbit (for the selected architecture) is within our range of consideration. However, one factor not included in the TMAS is an explicit evaluation of the potential effects of placing the TPF in the asteroid belt between 2.2 and 3.3 AU.

For low orbits, the higher CPI is largely due to the lower number of total images. As previously discussed, the lower number of images is due to the higher density of the local zodiacal dust that drives a longer integration time for each image.

For high orbits, the higher CPI is largely due to higher launch costs. As mentioned previously, the higher launch costs are driven by the increased mass and Delta V requirements for the higher orbits.

The higher CPI of the SSI relative to the SCI is primarily due to the greater total mass (higher launch costs) and to higher initial development costs. The development costs for the SSI case are higher due to the need to design (at least) two different spacecraft (collector and combiner) and to purchase more control system equipment rather than structural materials.

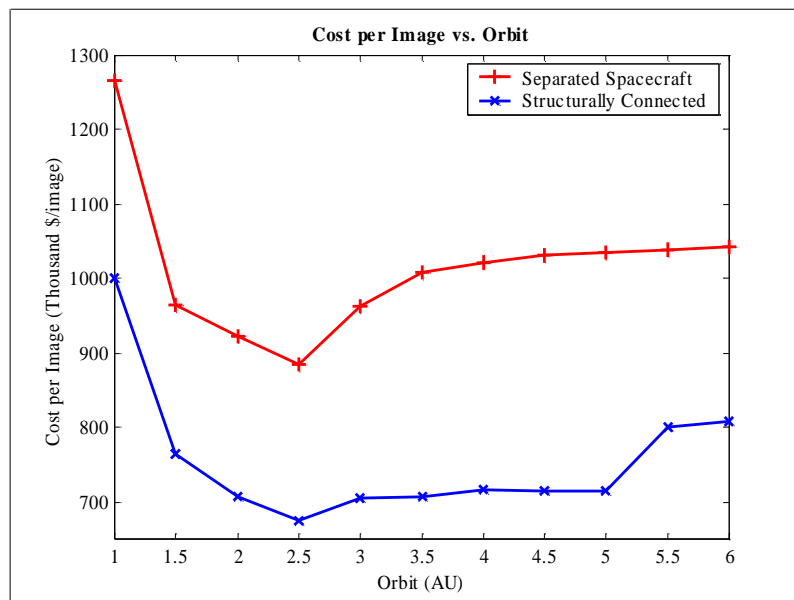


Figure 66. Cost Per Image vs. Orbit

8.2.2 Number of Apertures Trade Study

In this trade study, only the number of apertures parameter in the Design Vector is varied and the results are compared to the baseline cases.

SCI Image Distribution

The first plot shows the number of images increases with the number of apertures. The increase is most significant when the number of apertures increases from four to six. Besides producing better transmissivity functions (deeper and wider nulls) with higher number of apertures, this significant jump is seen mainly due to the assumptions made in the Markov model. In the Markov model, we assumed total mission failure will occur when there are less than four operational apertures. Hence, in the four aperture case, the expected number of images that can be obtained is lower since this design cannot tolerate any failures. However, as higher numbers of apertures are used, we do not lose the entire mission when some of its apertures fail as long as there are at least four operational apertures.

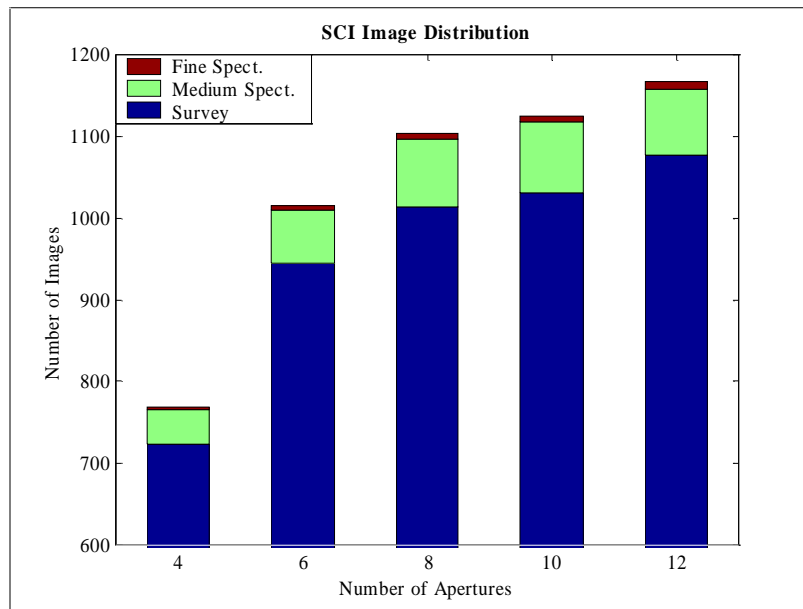


Figure 67. SCI Image Distribution

SCI Total Mass Distribution

The plot of the interferometer's mass as a function of the number of apertures shows the linear dependence of the total mass against the number of apertures. In all cases, the bulk of the interferometer's total mass is dominated by its dry mass, of which more than 50% of it is the structural mass. On the other hand, the contribution of the propellant mass to the total mass is small.

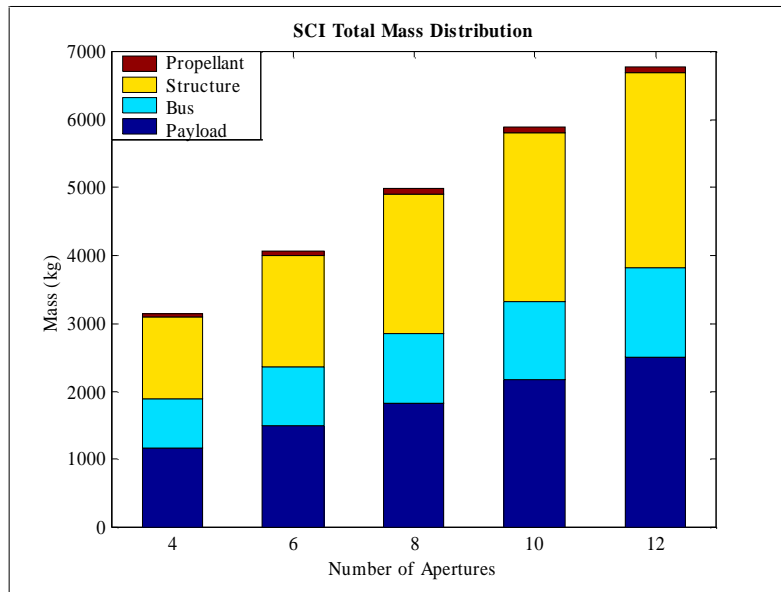


Figure 68. SCI Total Mass Distribution

SCI Cost Distribution

The total lifecycle cost for the SCI designs increases with the number of apertures in the design. Both the development and the operations costs for this architecture remain constant since there is only one structure. As the number of apertures is increased, larger launch vehicles are required. In the case of 4 apertures, a Delta 3 rocket is required, while for the 6 - 10 aperture cases, a Delta 4 is required, and the use of an Ariane 5 is required for the 12 aperture interferometer. Both the bus and the payload costs increase linearly with the number of apertures, which is also the trend observed with the bus and payload masses.

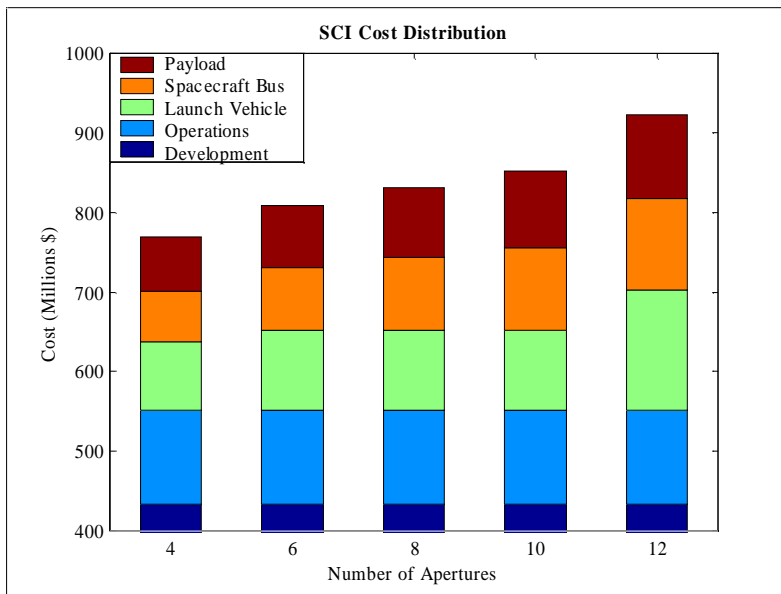


Figure 69. SCI Cost Distribution

SSI Image Distribution

Similar to the SCI results, the expected number of images increases with the number of apertures. Again, a sharp increase in the total number of images is again observed when the number of apertures is increased from four to six, and this can be attributed to the assumptions made in the Markov model. Note that except for the four spacecraft case, the expected number of images is higher than the results shown in the SCI design. This is mainly attributed to allowing the separated apertures to re-position to a different set of optimal imaging locations when one or more apertures fail. For example, the SSI apertures in an optimal six aperture configuration can be reconfigured to assume the optimal five aperture configuration when one aperture fails. This option, however, is not available to the SCI and will therefore explain the lower number of images obtained.

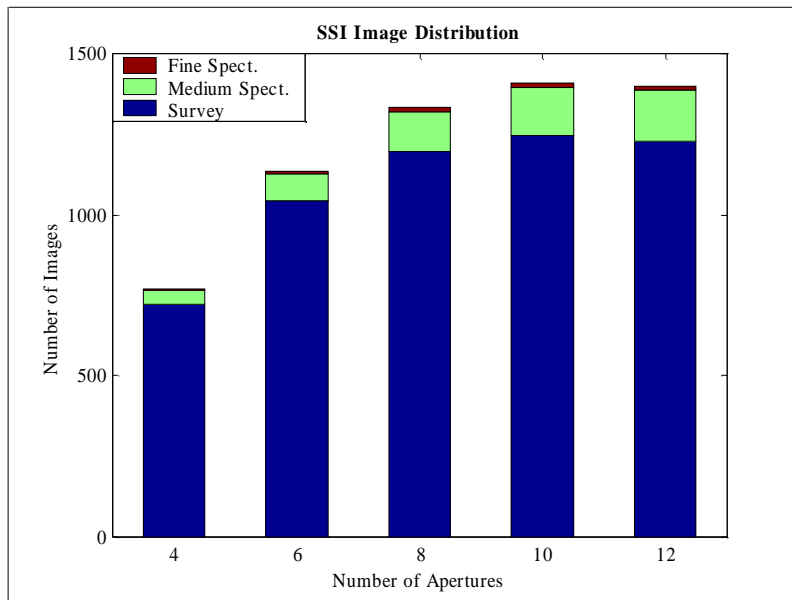


Figure 70. SSI Image Distribution

SSI Total Mass Distribution

Similar to the SCI design, the total mass of the interferometer is dominated by the dry mass of the interferometer. However, in this case the propellant mass makes up quite a significant portion of the total spacecraft mass. In reality, the amount of propellant required for the SSI is in fact lower, since one can take advantage of square maneuvering profiles where the spacecraft can be allowed to drift while no propellant is expended. The propellant calculation in this trade study assumes the spacecraft traverses a circular trajectory.

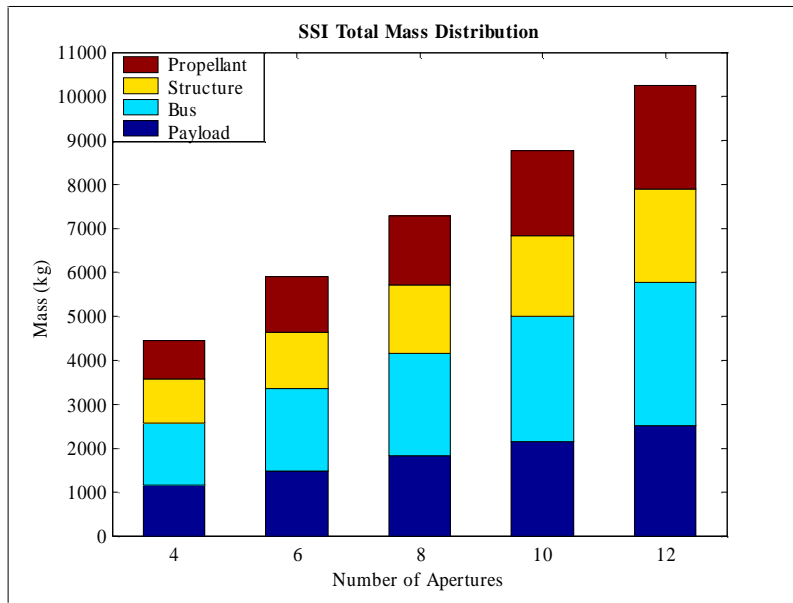


Figure 71. SSI Total Mass Distribution

SSI Cost Distribution

Except for the sudden jump in the launch vehicle cost, the lifecycle cost for this design increases approximately linearly with the number of apertures. The service of a Titan IV is required for the 12 aperture case, while the 8 and 10 aperture cases require an Ariane V launch vehicle and the 4 and 6 aperture interferometers require a Delta IV rocket.

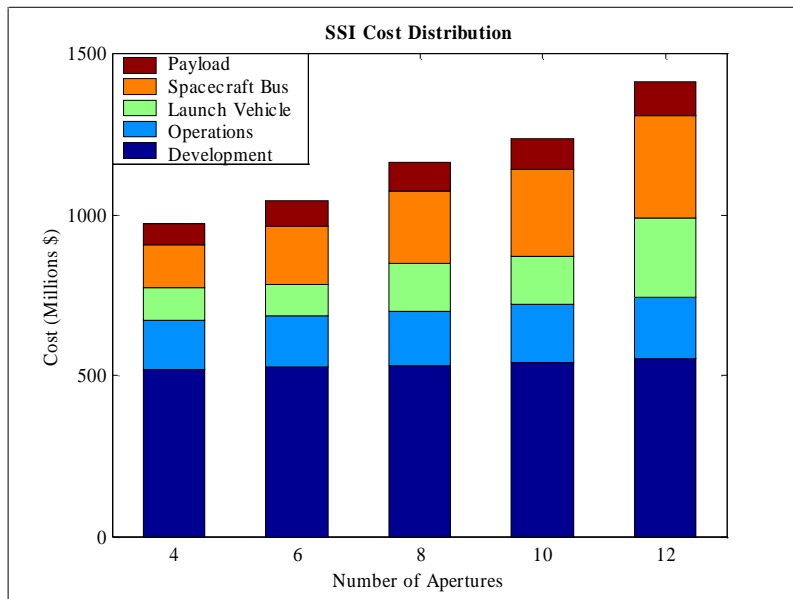


Figure 72. SSI Cost Distribution

Total Mass Distribution - SCI vs SSI

Comparison between the two architectures over the range of apertures shows a higher total mass in the SSI case. This is mainly attributed to the added spacecraft buses, structure, and propellant required for each aperture. In general, the SCI requires more structural mass but surprisingly, its overall dry mass is less than that required by the SSI. This lower dry mass in the SCI could be due to the rather short aperture separations required. In this analysis, we have considered planet detection as the key objective and a maximum baseline of only 120 m is required. However, if one were to take into consideration the second science requirement (astrophysical imaging) where milli-arcsec resolution imaging is required, aperture separations of at least 1 km are required. This will increase the structural mass of the SCI architecture significantly. Correspondingly, the amount of propellant required to maneuver the different spacecraft in the SSI case will increase too. The impact of varying the aperture separations has on the overall architectural mass should be investigated.

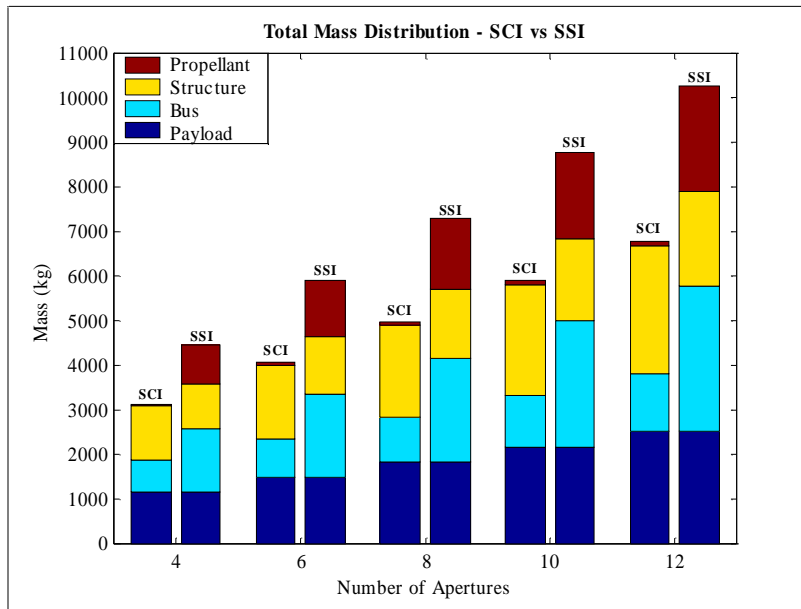


Figure 73. Total Mass Distribution

Cost Distribution - SCI vs SSI

Consistent with the trend observed in the architectural mass comparison, the lifecycle cost of the SSI is higher than the SCI. This is true especially for designs with a high number of apertures. This higher SSI cost can be attributed to several factors:

- more massive design (from mass comparison),
- larger launch vehicles required,
- more complex operations scenario, and
- higher development cost as SCI is probably a more technologically mature design than an SSI design.

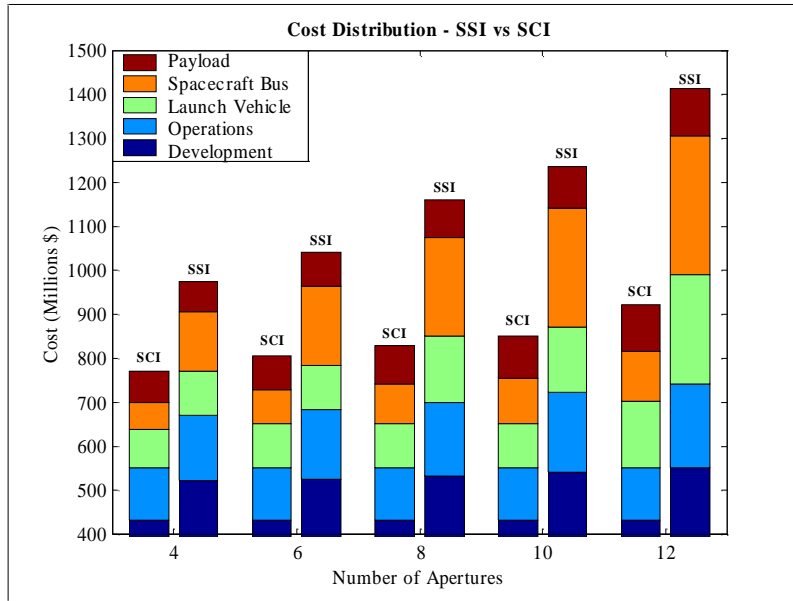


Figure 74. Cost Distribution

Cost per Image - SCI vs SSI

Even though the SSI has a higher lifecycle cost, comparisons between the architectures should be performed based upon the design's cost per function metric. Figure 75 shows the cost per image for the two architectures. Even though we observe rather significant differences in the architecture's lifecycle cost, the difference in the cost per image metric is not as high. This is mainly due to the higher number of images that can be expected from the SSI design. In both cases, the "optimal" solution is to use the 8 aperture configuration.

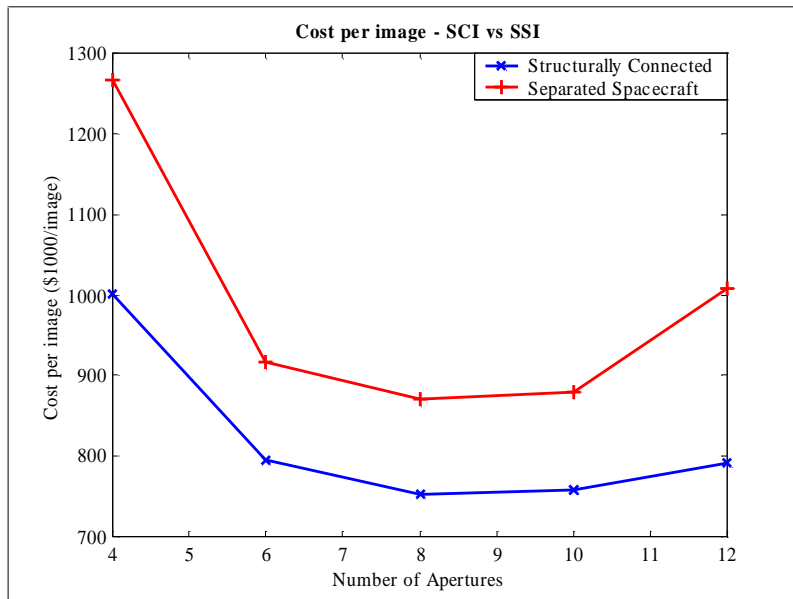


Figure 75. Cost Per Image

8.2.3 Interferometer Type Trade Study

The architectures of interest for the systems level analysis of TPF are: the SCI and SSI, one and two-dimensional cases. All architectures evaluated are symmetric designs. These four interferometer choices were traded for the (constant) configuration of 4 apertures, each having a 2 meter diameter; orbiting at 1 AU.

Image Distribution vs. Interferometer Type

The number of images appears to be more dependent on the aperture configuration than on architecture type. In this case, the one-dimensional architectures out perform the two-dimensional ones. This is a counter-intuitive result because we naturally expect the two dimensional configuration to be more efficient. But the two-dimensional case does not null as well the one-dimensional case.

We would also expect the SSI case to be more efficient, a distinct architecture advantage. This trade, however, does not show the graceful degradation capability of the SSI configuration. The four aperture SSI (based on our failure analysis) is the smallest SSI configuration allowed. So a single collector failure will cause a system failure. If a 3 or 2 collector array was feasible, then the SSI architectures would gain an advantage. This advantage would also become clear if our baseline design consisted of more than four spacecraft.

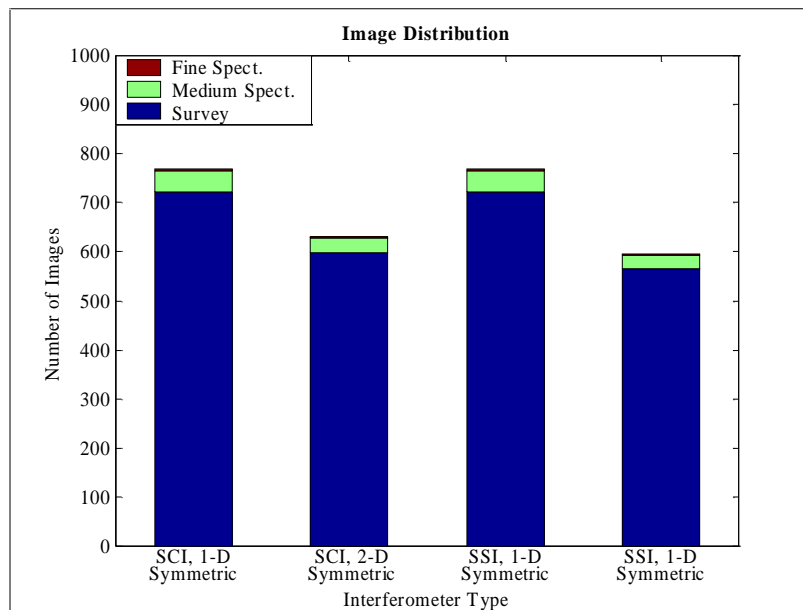


Figure 76. Number of Images

Total Mass Distribution vs. Interferometer Type

The total mass of the SSI architecture is clearly larger than the total mass of the SCI architecture. There are several contributors to the additional SSI mass. Some examples include the fact that:

- each collector spacecraft requires its own bus,
- the propulsion system must operate over a large range of thrust which is inherently inefficient, and
- the structural mass savings (initially thought to be considerable) is minimal.

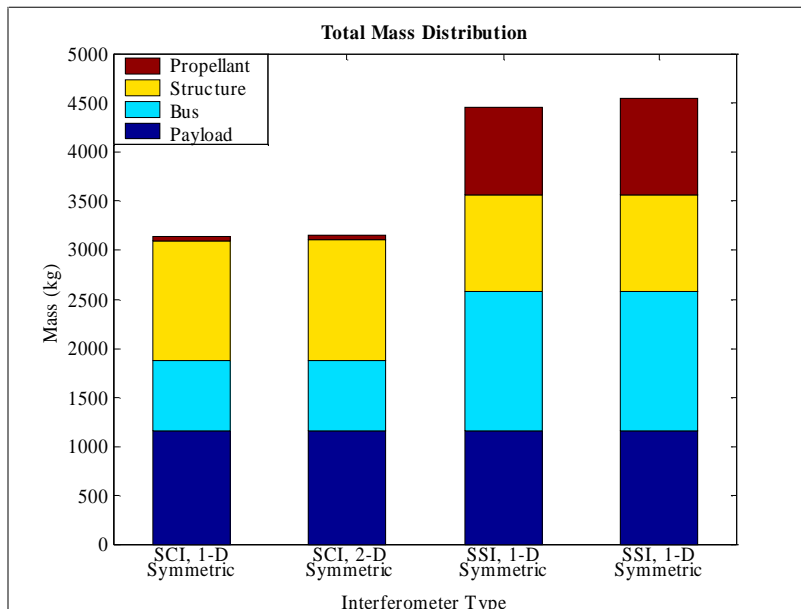


Figure 77. Total Mass (kg)

Cost Distribution vs. Interferometer Type

The cost distribution appears to scale with mass and complexity, so the SSI architecture is duly penalized. The largest increases in cost come with extra development cost (presumably due to complexity) and with extra bus cost (due to the increase in bus mass). The net difference in mass between the SCI and SSI architectures is small enough, though, that there is negligible launch vehicle penalty. As mass increases, we are sure to see a launch vehicle effect on the interferometer trade.

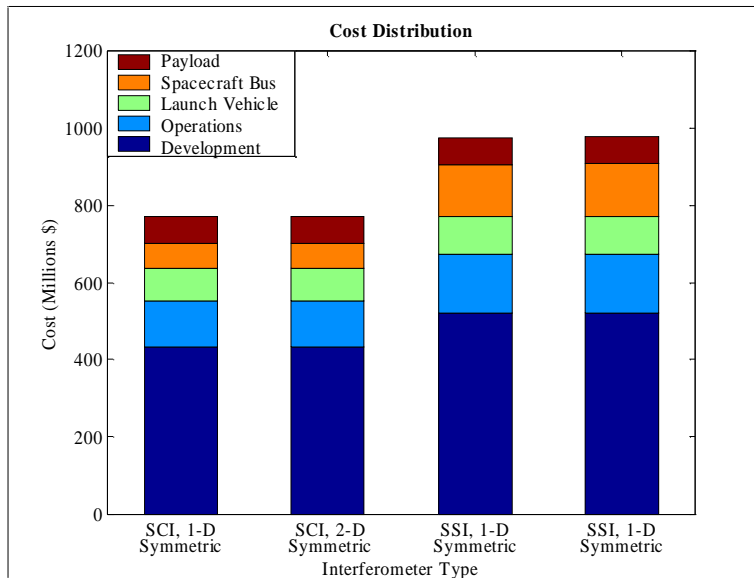


Figure 78. Cost Distribution (\$M)

Cost per Function vs. Interferometer Type

The cost per function is a combined metric attempting to capture both the performance and the cost we pay for that performance. In this case, the one-dimensional SCI architecture has the “best” cost per function. This is quite obvious because the one-dimensional SCI case matches the performance of the one-dimensional SSI case for the cost of the two-dimensional SCI case. The “best” architecture will likely change as the design vector changes. It is difficult to project the changes of the cost per function, because it incorporates both image distribution and cost (mass and complexity) effects. Please review the former sections to estimate these changes.

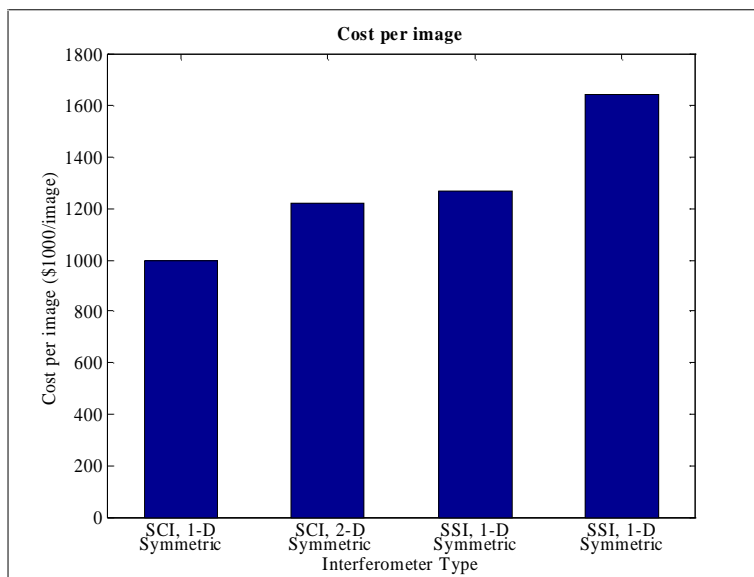


Figure 79. Cost Per Image (\$M/Image)

8.2.4 Aperture Diameter Trade Study

This study analyzes the effect on the system performance and cost due to variations in the aperture diameter, keeping all other design variables fixed.

First of all we notice, as expected, that the payload cost increases as the aperture size increases. The payload cost can be split into a fixed component and a component that varies with the mirror size. This variable component is proportional to the aperture diameter raised to the 2.67.

The operations/development cost is largely independent of the aperture size, and it is indeed constant in the above plots. Moreover, we notice that this cost component is considerably bigger in the SSI case, due to the increased complexity of the SSI system over the SCI.

The bus costs are higher in the SSI case, since we have to duplicate components for each and every one of the independent spacecraft; and increase with the aperture size, since bigger mirrors require more capabilities from the bus (e.g. thermal system). The SSI and SCI bus costs can be seen to differ by a constant term.

Finally, the launch costs are essentially the same for the two cases. However, we notice that for $D=4\text{m}$ in the SSI case, we have a jump in the launch cost. This is due to the fact that the total system mass exceeds the capabilities of the previously selected launcher, and requires a more expensive launch system.

As a consequence of the above trends, the total costs in both the SSI and SCI cases grow more than quadratically with the aperture size. The cost difference, on the other hand, appears to be constant, and is due mainly to the cost difference in the operations and development, and secondarily to different bus costs.

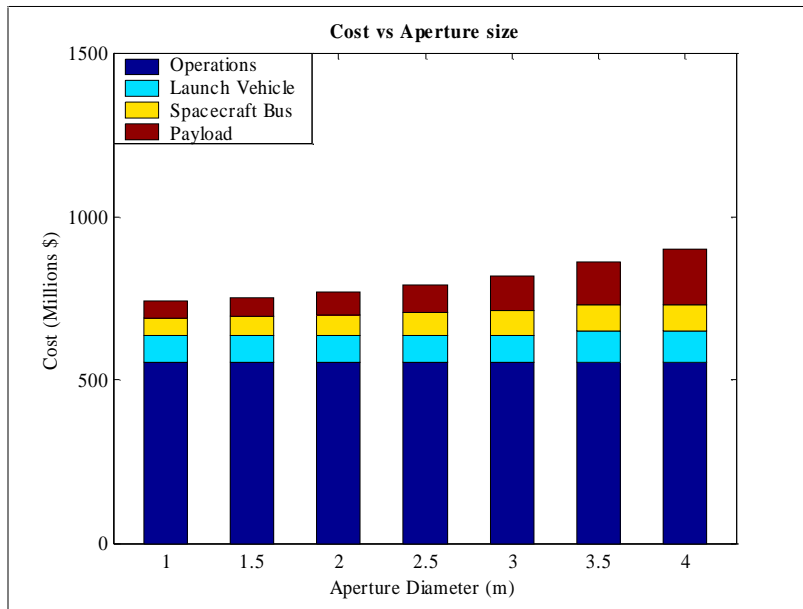


Figure 80. Cost vs. Aperture Size (SCI)

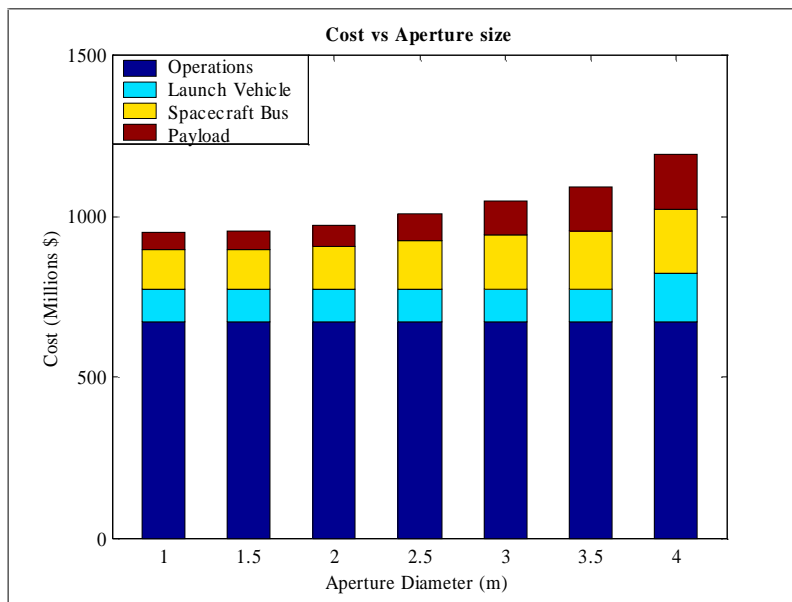


Figure 81. Cost vs. Aperture Size (SSI)

The increased collection area allows for a bigger harvest of photons from the target; as a consequence, the integration times required for each image will be reduced accordingly. Since we are considering a constant time delay between observations, it can be easily seen that as the aperture diameter grows, the total number of images per unit time goes to some asymptotic value. This effect is the same for both SSI and SCI cases.

The cost per image shows a generally decreasing behavior in the range we have considered, showing optimum values at the right end of the plot. The SSI case presents a very slight minimum at 3.5m, due to the increase in the launch cost for D=4m discussed in the above. Since the total cost increases as $D^{2.67}$, while the total number of images approaches a constant value, the cost per image will eventually increase at the same rate as the total cost. This means that the cost per image will have some minimum value, that from the plot above appears to be close to 4m. On the other hand, the cost difference approaches a constant value, as it will eventually be the ratio of two constants.

On the very limited trade space analyzed here, it appears that an SCI architecture with D=4m would be the optimum with respect to the aperture size.

8.2.5 Summary of Trade Studies

Orbit

Generally, the total number of images, mass, and cost increase as orbit increases. The number of images reaches the maximum of approximately 1200 images after about 3 AU because the effect of the local zodiacal dust becomes small. Therefore orbit does not influence the number of images any more. The same number of images is expected for both SSI and SCI architectures with the same number of apertures and same sized aperture diameters. SSI in general will have higher mass and cost. Since the total number of images is the same for both SSI and SCI, the ratio of total cost over the number images (the cost per image) is lower for SCI. The lowest cost per image occurs when the orbit is 2.5 AU for SCI. Unfortunately, 2.5 AU is located in the asteroid belt, so future work is required to see if this orbit is feasible for TPF.

Number of Apertures

Total number of images, mass, and cost increase as the number of apertures increases. SSI produces more images than SCI except when number of apertures is four. This trade study shows that the total mass, cost, and cost per image is higher for SSI designs than SCI designs. The lowest cost per image for both SCI and SSI is attained when the number of apertures is eight.

Size of Aperture

As the aperture diameter increases, the total number of images and total cost increases. Total cost increases as diameter to the power of 2.67, and the total number of images increases until it meets its asymptotic value. The total number of images for both SSI and SCI are the same for the same aperture diameter. The lowest cost per image occurs when the aperture diameter is 3.5 m for the SSI and 4 m for the SCI. Since the total number of image reaches a constant after 4 m, and the cost increases as the size of the aperture diameters increases; the cost per image will start to increase after 4 m.

Interferometer Type

The trade study of Interferometer type vs. metrics shows that the cost and mass of SSI designs are generally higher than SCI designs. One-dimensional designs have a higher

imaging rate than two-dimensional designs for both SSI and SCI architectures. Combining these two trends produces a result that an SCI one-dimensional architecture generates the lowest cost per image.

8.2.6 Combined Case Results

The different one-dimensional trades show the existence of local minima along single axes for the different trades. These minima, however, do not tell us anything about the global optimum solution. To determine the global optimum, the entire trade space must be search since one does not know the exact shape of the design surface. Due to time constraints, the team decided to perform simulations for two more case studies by combining the different local minimum configurations based upon the trade studies performed for the two interferometer types (SSI and SCI). The input variables and the results from the two combined designs are tabulated in Table 33.

Based upon the cost per image metric, the results given by these two cases are in fact the lowest in their respective interferometer types. In both cases the total mass of the array is rather large, to the point that no launch vehicle can provide the velocity increment required to place the interferometers into their operating orbits. In the case of the SSI, there exists the option of using multiple launch vehicles - this option was not explored in our study. Similar to the higher interferometer masses shown in Table 33, the life-cycle costs of the interferometers came out to be high too. However, due to the higher expected number of images, the cost per image of the interferometers turned out to be the lowest of all the architectures that we have studied.

It is important to note that the two architectures shown in Table 33 are not the architectures that give the global minimum to the cost per image metric. In fact, the different architectures that have been studied do not give any indication as to what the global minimum is. However, the architectures that are presented in Table 33 are the ones that give the best cost per function metric among the different architectures that we have studied. In order to determine the global optimum architecture, the entire trade space must be searched.

Table 33. Results for Combined Cases

Characteristic	SSI	SCI
Orbit	2.5 AU	2.5 AU
Aperture	2 meters each	2 meters each
Number of Apertures	8	4
Interferometer Type	Linear Symmetric	Linear Symmetric
Total Mass	12998 kg	7567 kg
Launch Vehicle	Too large	Too large
Number of Images	2182	2440
Total Cost	\$1.58 Billion	\$1.26 Billion
Cost per Image	\$727,000	\$518,000

8.2.7 Operational Trade Results

The previous trades varied one of the four parameters in the design vector to determine the effect of that parameter on the total system. Eventually, we wish to fill in our entire trade space by varying several parameters to arrive at an “optimal” solution for a chosen system metric. The operations trade-study captures the dynamics of the operational component while several variables are changed. Since operations cost and operationally-derived performance losses have such a large impact on total mission cost and performance, it behooves the mission designer to understand the coupling of operations with the other design vectors.

Crew Sizes vs. Time

Different staffing levels will be required at different times during the mission. The graph in Figure 82 shows the effect of time on the crew levels of four different configurations. The increase in complexity between the SCI and more complex SSI types increases the crew levels, despite learning curve effects of operating more similar spacecraft. Increasing the distance at which TPF operates (ex. from 1 to 5 AU) would tend to increase the transit time and cost.

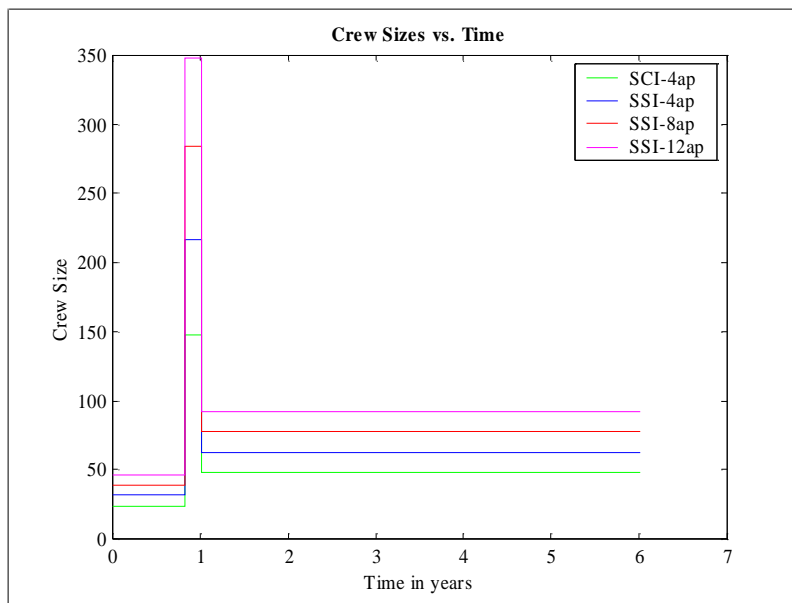


Figure 82. Crew Size vs Time (years)

Operations Cost Breakdown

In the graph in Figure 83 we witness the effect of increasing mission complexity on two different components of operational cost. Notice the large jump in yearly maintenance between the SCI and the least complex SSI. This represents the difficulty from switching from a single satellite operations scenario to a constellation and the attendant increase in control center size and capability. Also notice that further increases in complexity to 8 and 12 aperture SSI configurations have only a marginal effect on yearly maintenance. Labor

costs increase relatively linearly between the architectures shown. Steady-state maintenance and labor costs are relatively independent of final orbit.

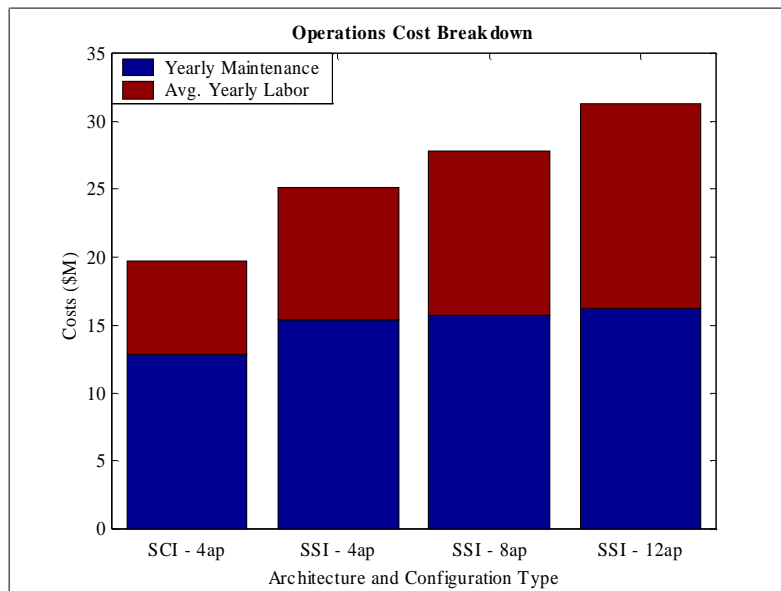


Figure 83. Operations Cost Breakdown

Mission Inefficiency vs. Orbit

The graph in Figure 84 shows the increase in mission inefficiency with orbit for three system configurations. The SCI closest to Earth has the least inefficiency while the most complex SSI farthest away has the most. Notice also that the rate of inefficiency increase is greatest for the SSI with 8 collector spacecraft.

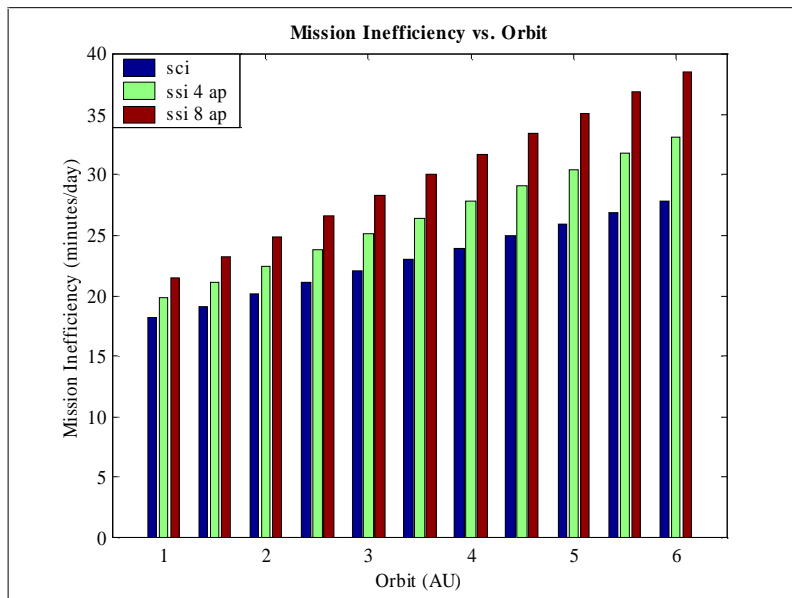


Figure 84. Mission Inefficiency vs. Orbit

9.0 Conclusions

9.1 TPF Architecture

Table 34 provides a summary of the best cost per image architectures from the 50 sample cases that were examined to explore the one-dimensional trades for both SSI and SCI scenarios. The composite architectures represent the architectures created from the individual minimum values from each one-dimensional trade. It must be stressed that these do not represent “optimal” designs – the full trade space has not yet been explored and cost per image (CPI) is not the only measure of the quality of a mission. A comparison of the SSI and SCI architectures reveals that the missions are rather different. The structurally connected architectures (SCI) consistently outperformed the separated spacecraft architectures (SSI) when applying the “cost per image” metric. This is due to the fact that the SCI provided good passive stability and led to advantageous total masses when only considering interferometer baselines required for planet detection (up to ~ 120 m). It must be mentioned, however, that the advantages of a separated spacecraft architecture (SSI) were not fully captured in the present study. Namely, the ability to re-position the apertures in order to optimize the transmissivity function or to compensate for aperture failures in the SSI case has not been fully modeled. Furthermore it is expected that the mass advantages of the SCI will be lost for very long baselines, where we expect a crossover between the SSI and the SCI case as explored by Surka and Stephenson. It is expected that this crossover will be visible if astrophysical imaging (baselines up to ~ 1000 m) were to be incorporated into the current methodology.

Table 34. Best Cost per Image for Sample Cases

Characteristic	SSI	SCI	SSI Composite	SCI Composite
Orbit	1 AU	2.5 AU	2.5 AU	2.5 AU
Aperture	2 meters each	2 meters each	3.5 meters each	4 meters each
Number of Apertures	8	4	8	8
Interferometer Type	Linear Symmetric	Linear Symmetric	Linear Symmetric	Linear Symmetric
Total Mass	7758 kg	3372 kg	12,998 kg	7567 kg
Launch Vehicle	Ariane 5	Delta 4	Too Large	Too large
Number of Images	1332	1171	2182	2440
Total Cost	\$1.16 Billion	\$789.9 Million	\$1.58 Billion	\$1.26 Billion
Cost per Image	\$871,267	\$674,000	\$727,000	\$518,000

9.2 TMAS

The team was able to successfully design and implement a software package to perform parametric evaluations of different TPF mission architectures. Adopting a modular programming protocol and using Matlab functions allowed multiple sections of the code (sub-modules) to be coded and tested in parallel instead of sequentially, thus drastically reducing the software development time. Interface control between both macro-modules and sub-modules appears to be the most difficult issue when developing such modular software, and was achieved through the use of N² diagramming techniques.

9.3 Lessons Learned

The first lesson learned is the need to compromise between model fidelity and simulation time. Balancing the complexity of the analysis model and the limited time available became an important issue throughout the entire program. This became most evident during the trade-study phase. The size of the test matrix was intentionally reduced in order to finish the one dimensional trade studies during the time remaining, even though the team would have preferred to explore the entire system architecture trade space.

Second, the team learned a great deal about the systems engineering process. Starting with the initial definition of the system design space, through initial evaluations of all feasible system architectures and down-selection to the best potential options, to the evaluation of the trade studies, this course provided valuable insight about the systems engineering process.

The N^2 diagram technique proved its worth by serving as an Interface Control Document to coordinate the integrated development of the software modules of the TMAS. The trade-study process allowed the team to observe the general trends and relationships between each design parameter and the corresponding outputs. Using these key relationships, more detailed trade studies can be performed in the future.

Throughout the course, team members gained the experience of participating in an integrated design team, including design and programming tasks, sharing responsibilities for making presentations, and creating engineering documentation.

9.4 Recommendations and Future Work

Our recommendation for the future is to refine and improve the fidelity of the software models, to conduct sensitivity analyses, and to examine the entire trade space using appropriate criteria to find the globally best architecture(s).

First, several items were not incorporated into the TMAS model due to time and resource limitations and are therefore recommended for future work. Although the software is already complex, increasing the fidelity of the modules will give more accurate solutions.

For the orbit transfer, the orbit module was based on the Hohmann's and Hill's transfer only. For future work, adding gravity assist or the low thrust electric propulsion trajectories to the orbit module will cut down the ΔV requirement and therefore cut down the launch cost.

For the launch vehicle module, only a single launch vehicle was considered for both SSI and SCI. For an SSI, multiple smaller launch vehicles can be used. For future work, the module can incorporate an option of using multiple launch vehicles if it cuts down the cost.

For the SSI case, only circular trajectories were considered for image maneuvering to simplify the calculations. If other trajectories are used, such as drift mode, propulsion can be saved and the cost will be decreased as a result.

For designing and integrating the bus module, more efficient optimization algorithms will help to reduce the complexity of the bus module and provide a better optimized bus design.

For the dynamics, optics, controls and structures (DOCS) module, a number of improvements are suggested for future work. First, the fidelity of the spacecraft structure and compliant trusses in the SCI case must be improved to provide better accuracy in the higher frequency range. Line-of-sight (LOS) jitter, wavefront tilt (WFT) and differential beam shear (DBS) are other ways in which the dynamics can adversely affect the signal-to-noise ratio (SNR) of the observatory. Furthermore, the incorporation of more disturbance sources, such as cryocoolers, should be considered. Finally a parametric model of the optical train, including optical delay lines, fast steering mirrors, and beam compressors would provide a more realistic estimate of the effects and limitations of optical control on the TPF performance.

For operations, optimizing the automation level remains as possible future work. Additionally, adding astrophysical imaging capability to the model is also recommended as a future work.

For the GINA module, many of the failure rates were assumed because we did not have enough information. Adding more reliability data to the model will result in more confident analysis and trade studies of architectures.

Many of the modules were generated assuming current resources and technology. If future technologies are considered, it could reduce the cost as well as the development time for TPF.

Additional module improvement suggestions have been made in the module description sections above.

Second, the effects on the cost and capability metrics were examined only for four of the most fundamental parameters. The TMAS provides the capability to conduct sensitivity analyses for many more parameters to determine the robustness of the mission architecture to changing initial conditions, mission profile, model assumptions, costs, etc.

Third, full trade space exploration is required to find the best architecture(s). The team was only able to carry out the single point trade studies, in which one element of the design vector was varied at a time to see its relationship with the outputs. This kind of trade-study suggests the key relationships and general trends, but does not give the best solutions.

This page intentionally left blank.

10.0 Acronyms

ADAM	ABLE Deployable Articulated Mast
ADCS	Attitude Determination and Control System
ASTRO	Architecting the Search for Terrestrial planets and Related Origins
AU	Astronomical Unit
BOL	Beginning-Of-Life
C&DH	Command and Data Handling
CER	Cost Estimation Relationship
COTS	Commercial Off-The-Shelf
CPF	Cost Per Function
CPI	Cost Per Image
DBS	Differential Beam Shear
DOCS	Dynamics, Optics Controls, and Structures
DS3	Deep Space 3 (Renamed Space Technology 3, ST3)
DSN	Deep Space Network
EOL	End-Of-Life
FEM	Finite Element Model
FIRST	Far Infra-Red and Sub-millimeter Telescope
FOV	Field of View
FSM	Fast Steering Mirrors
GINA	Generalized Information Network Analysis Methodology
GNC	Guidance, Navigation, and Control
GNC	Guidance, Navigation, and Control
HSI	Hybrid Spacecraft Interferometer
IPPD	Integrated Product Process Development
IR	Infrared
ISO	Infrared Space Observatory
JPL	Jet Propulsion Laboratory
L2	Lagrange 2
LEO	Low Earth Orbit
LOS	Line of Sight
LTI	Linear Time Invariant
MIT	Massachusetts Institute of Technology
MLI	Multi-Layer Insulation
mttf	Mean Time to Failure
NASA	National Aeronautics and Space Administration

NGST	Next Generation Space Telescope
NIR	Near Infrared
ODL	Optical Delay Line
OPD	Optical Pathlength Difference
PSD	Power Spectral Density
QC	Quality Control
QFD	Quality Function Deployment
RMS	Root Mean Square
RTG	Radioisotope Thermoelectric Generators
RWA	Reaction Wheel Assembly
SCI	Structurally Connected Interferometer
SIM	Space Interferometry Mission
SIRTF	Space Infra-Red Telescope Facility
SNR	Signal-to-Noise Ratio
SRTM	Shuttle Radar Topography Mission
SSCM	Small Satellite Cost Model
SSI	Separated Spacecraft Interferometer
ST3	Space Technology 3
TFU	Theoretical First Unit (cost)
TMAS	TPF Mission Analysis Software
TPF	Terrestrial Planet Finder
TSI	Tethered Spacecraft Interferometer
USCM	Unmanned Spacecraft Cost Model
WFT	Wavefront Tilt

11.0 References

- Athans, M., Lecture Notes for “6.245: Multivariable Control Systems”, MIT, Spring 1998, unpublished
- Bearden, David A., The Aerospace Corporation. Personal Communication. August 3, 1998.
- Beichman, C. A., Woolf, N. J., and Lindensmith, C. A., ed., "The Terrestrial Planet Finder (TPF): A NASA Origins Program to Search for Habitable Planets", JPL Publication 99-003, 1999.
- Boppe, C. W., “Integrated Product Process Development,” 16.870 Aerospace Product Design course note, 1997.
- Bracewell, R.N., and Macphie, R.H., “Searching for Non Solar Planets,” *Icarus* 38, 136,1979.
- Exploration of Neighboring Planetary Systems (ExNPS) Report, <http://origins.jpl.nasa.gov/library/exnps/ExNPS.html>, NASA JPL, August, 1996.
- Francis, B., et al., “Lockheed Martin TPF Final Review,” Lockheed Martin Missiles & Space TPF Conceptual Design Report, 1997.
- G. Mosier, M. Fermiano, et. al., “Fine Pointing Control for a Next generation Space Telescope”, http://ngst.gsfc.nasa.gov/public/unconfigured/doc_85_1/FinePointingControl.doc, 1999
- Gelb, Arthur. *Applied Optimal Estimation*. The MIT Press. Cambridge, MA., 1974.
- Larson, W.J. and Wertz, J.R., *Reducing Space Mission Cost*. Microcosm Inc. Torrance, CA., 1996.
- Larson, W.J. and Wertz, J.R., *Space Mission Analysis and Design*. Microcosm Inc. Torrance, CA., 1992.
- M. A. Dahleh, I.J. Diaz-Bobillo, “Control of Uncertain Systems – A Linear Programming Approach”, Prentice Hall, 1995.
- Makins, B., et. al., “TPF Mission Requirements Document,” 16.89 Space Systems Engineering Course, 1999.
- Malbet, F., Shao, M., and Yu, J., "Active optics and coronagraphy with the Hubble Space Telescope," *Astronomical Telescopes & Instrumentation for the 21st Century*, SPIE, March, 1994.
- McEachern, William A. *Economics – A Contemporary Introduction*. 3rd edition. South-Western Publishing Company. Cincinnati, Ohio. 1994.
- Noecker, C., et al., “Ball TPF Study,” Ball TPF Conceptual Design Report, 1997.
- Origins Home Page*, <http://origins.jpl.nasa.gov/>, NASA JPL, April, 1999.

Posner, E. C., "Relation between Communication Satellites and Deep-Space Communication," Proceedings of a Symposium on Space Communications Research & Development, March, 1988.

Rohlfs, K., Wilson, T. L, "Tools of Radio Astronomy," Springer, 1996.

Shaw, G.B., "The Generalized Information Network Analysis Methodology for Distributed Satellite Systems," PhD Thesis. MIT Department of Aeronautics and Astronautics. 1998.

Stephenson, R. L., Miller, D. W., and Crawley, E. F., "Comparative System Trades Between Structurally Connected and Separated Spacecraft Interferometers for the Terrestrial Planet Finder Mission," MIT Space Engineering Research Center (SERC) #3-98, 1998.

Surka, D. M. and Crawley, E. F., "A Comparison of Structurally Connected and Multiple Spacecraft Interferometers," MIT Space Engineering Research Center (SERC) #9-96, 1996.

Terrestrial Planet Finder Home Page, <http://tpf.jpl.nasa.gov/>, NASA JPL, April, 1999.

Wehner, M., Johnson, L., Kroening, K., and Moses, S., "TRW Terrestrial Planet Finder Study," TRW TPF Conceptual Design Report, 1997.

12.0 Authors

This document was created as part of the Space Systems Engineering course offered by the Massachusetts Institute of Technology (MIT) during the spring semester, 1999. It represents the culmination of the work performed by the 9 person class during the semester.

Appendix A. Electronic Requirements Document

ASTRO

Architecting the Search for Terrestrial planets and Related Origins

Title:	Mission Requirements Document
Version:	1.3
Date:	May 17, 1999
Document Manager:	Brian Makins
Authors:	Andrew Curtis, Olivier DeWeck, Emilio Frazzoli, Andre' Girerd, Troy Hacker, Cyrus Jilla, Edmund Kong, Brian Makins, and Sangwoo Pak

Revision	Date	Description
1.0	March 3, 1999	Initial Release for the TARR
1.1	April 7, 1999	Update for the PDR
1.2	May 10, 1999	Linked and Updated for the CDR
1.3	May 17, 1999	Edited for distribution copy

Space Systems Engineering - 16.89
 Department of Aeronautics and Astronautics
 Massachusetts Institute of Technology
 77 Massachusetts Avenue
 Cambridge, MA 02139

Mission Description

For almost two millennia, the scientific community has developed a list of fundamental questions regarding life and the formation of galaxies. Is life unique to Earth? How did life originate on earth? Are there habitable planets outside our solar system? The list goes on and on.

The National Aeronautics and Space Administration (NASA) has formed the Origins program, whose goal is to search for clues which may help answer such fundamental questions. The Terrestrial Planet Finder mission (TPF) is a key component in NASA's Origins program. The TPF mission is to conduct a search for Earth-like planets around nearby stars. This spaceborne observatory will directly detect and characterize these planets and other astrophysical phenomena by nulling the light of the parent star. The TPF mission will champion nulling interferometry technology to attain an unparalleled level of sensitivity, resolution, and starlight suppression.

Specifically, TPF is searching for answers to the following questions:

- Do any nearby planets satisfy our requirements for life?
- What are the frequency, atmospheric composition, and physical properties of planets outside our solar system?
- How do these planets differ from Earth?

TPF will also provide an exceptional opportunity to broaden our understanding of a wide range of astrophysical phenomena including star and planet formations, comets, distant starbursts and active galaxies.

ASTRO Project Scope

The ASTRO project goal is to identify and design the most appropriate mission architecture for TPF. To that end, the team will conduct a trade study of the mission architectures using a quantitative systems engineering methodology. Each architecture candidate, including structurally connected and separated spacecraft options, will be subject to the following requirements.

Requirements Document Scope

This document sets forth the scientific objectives, the system requirements, and the design requirements which must be accommodated by the spacecraft bus, payload, and operations design. Each requirements' source, intent, and expected verification technique have also been tabulated. This original issue contains a consistent set of requirements that will be used as a guide during the preliminary and critical design phases.

Motivation for an Electronic Format

Organizing requirements with computer programs, in a data base or even linked spreadsheets, is becoming the norm.

An electronic format offers several advantages that the standard document does not. Users can easily trace how a change in one requirement can affect the entire document; and they can access requirements at their preferred level of complexity.

The following electronic document uses hypertext links to organize the data. Hypertext is a very user friendly and accepted method that applies well to requirements. Some of the specific advantages follow:

Enables a Top Level Organization

Standard requirement documents are listed sequentially, proceeding to the lowest level before reaching the next top level. This organization provides an easy way to trace changes in requirements, but is somewhat cumbersome. The end user is not always interested in the lowest level of complexity.

A document with hypertext links allows the end user to navigate to the level of complexity of interest. If the user wants to go to a lower level, he/she can just click on that particular requirement.

Simplified Configuration Control

The electronic format helps to simplify the configuration control.

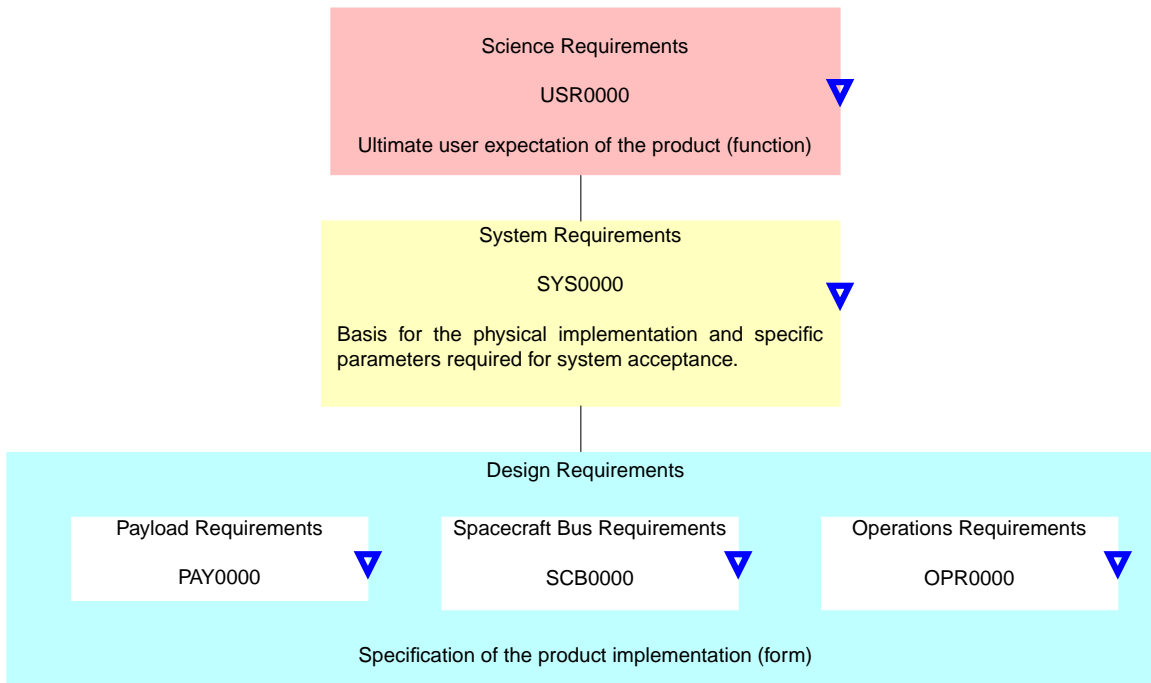
If a user wants to change a requirement he can isolate the children of that requirement. In fact, the top level organization ensures that each requirement has a defined parent - child relationship. This means that a change in a requirement will trace down to the lower levels and no rogue requirements will remain unchanged.

Source, Intent, and Verification

The context of any requirement is essential to its effectiveness. When requirements are browsed by those who are unfamiliar with the document, they can determine the intent and source of that requirement. This definitely helps in requirement refinement and re-writes.

For certain missions it is also essential to establish verification requirements. These state how to verify the given requirement, sometimes suggesting a specific approach.

The electronic format provides an easy way to store the intent and verification information. Databases are often used, but for this mission a table is just as effective. The "Intent and Verification" link is available below.



Top Level Requirement Flowdown

Top Level Back Previous Page Next Page Intent and Verification

◀◀ ◀ ▲ ▼ ▶▶

- 4 -

1. USR1000

▲ The system shall detect, locate and characterize Earth-like planets orbiting nearby stars, especially those in the habitable zone. ▼

2. USR2000

▲ The system shall be able to image approximately 750 astrophysical objects throughout its mission. ▼

User Needs / Science Requirements

 1. USR1000

1.1 USR1100
The system shall survey approximately 150 star systems located within 15 parsecs from our solar system.

1.2 USR1200
The mission shall detect each planet by isolating it from its parent star.

1.3 USR1300
The mission shall use spectroscopy to characterize planets.

1.4 USR1400
The habitable zone is the region around a parent star in which the existence of liquid water is likely.

1.4.1 USR1410
The habitable zone ranges from 0.5 AU for a K2 star system to 3 AU for a FO star system.

 2. USR2000

2.1 USR2300
The mission shall investigate specific types of astrophysical objects.

2.1.1 USR2110
Star formation regions, including accretion disks should be imaged

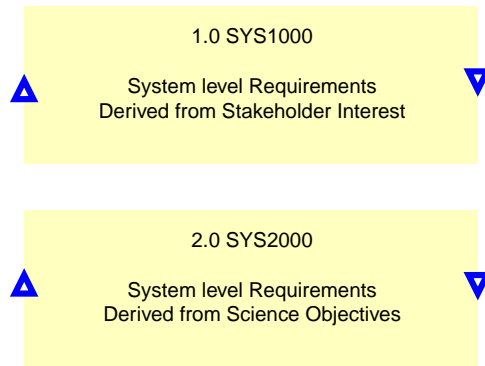
2.1.2 USR2120
Planetary formation around young stars should be imaged.

2.1.3 USR2130
Dying Stars should be imaged.

2.1.4 USR2140
Energy sources for distant starbursts and active galaxies should be imaged.

2.1.5 USR2150
Icy cores of comets should be imaged.

User Requirements - Level 2



System Requirements

 1.0 S1000

1.1 SYS1100
The system shall have a minimum lifetime of 5 years, after full operational capability is achieved.

1.7 SYS1700
The system shall be compatible with the launch and operational orbit environments.

1.2 SY1200
The system shall have a target launch date in 2010.

1.8 SYS1800
The system shall have a reliability of at least TBD at the end of 5 years.

1.3 SYS1300
The system lifecycle cost shall not exceed \$1 billion.

1.4 SYS1400
The system shall communicate all relevant data to Earth.

1.5 SYS1500
The system shall have an operational availability of not less than TBD.

1.6 SYS1600
The system shall accommodate new software during its operational life.

System Level Requirements - Derived from Stakeholder Requirements

 2.0 S2000

2.1 SYS2100
The system shall have a field of view (FOV) that spans from 0.4 arcseconds to 1.2 arcseconds
[1.4 USR1400 on page 6](#)

2.5 SYS2500
The system shall perform coarse level spectroscopy on about 50 planets and detail level spectroscopy on about 5 planets
[1.1 SYS1100 on page 8](#)
[1.3 USR1300 on page 6](#)

2.2 SYS2200
The system shall have a fraction of a milliarsecond angular resolution. 
[1.2 USR1200 on page 6](#)

2.6 SYS2600
The system shall perform spectral characterization in the thermal infrared spectrum ranging from 7 to 17 microns. 
[1.3 USR1300 on page 6](#)

2.3 SYS2300
The system shall suppress the light from a parent star by a factor of more than one hundred thousand.
[1.2 USR1200 on page 6](#)

2.7 SYS2700
The system shall have a minimum signal- to-noise ratio of 5 (unitless) for surveying, 10 (unitless) for coarse spectroscopy and 25 (unitless) for detailed spectroscopy. 
[1.2 USR1200 on page 6](#)
[1.3 USR1300 on page 6](#)
[Scientists' stake in "good data"](#)

2.4 SYS2400
The system shall operate in the thermal infrared spectrum, ranging from 2 to 30 microns.
[1.3 USR1300 on page 6](#)

2.8 SYS2800
The system shall have a minimum spectral resolution of 3 (unitless) for planet imaging and 20 (unitless) for spectroscopy.
[1.2 USR1200 on page 6](#)
[1.3 USR1300 on page 6](#)
[Scientists' stake in "good data"](#)

System Level Requirements - Derived from Science Objectives

 2.2 SYS2200

~~2.2.1 SYS2210~~
The system shall be able to provide a maximum separation of 120m for planet detection and spectroscopy and 1800m for astrophysical imaging.

 2.6 SYS2600

2.6.1 SYS2610
The system shall detect and resolve the following absorption lines from a candidate planet.

- 2.6.1.1 SYS2611
Carbon Dioxide, CO₂ at 15 microns
- 2.6.1.2 SYS2612
Water, H₂O from 7 to 17 microns
- 2.6.1.3 SYS2613
Ozone, O₃ at 9.6 microns
- 2.6.1.4 SYS2614
Methane, CH₄ spectrum
- 2.6.1.5 SYS2615
Carbon Monoxide, CO spectrum

2.6.2 SYS2620
The system shall determine for the following characteristics of a detected planet.

- 2.6.2.1 SYS2621
Size
- 2.6.2.2 SYS2622
Temperature
- 2.6.2.3 SYS2623
Density
- 2.6.2.4 SYS2624
Albedo
- 2.6.2.5 SYS2625
Orbit

System Requirements - Level 2

Top Level  Back  Previous Page  Next Page  Intent and Verification 

 2.7 SYS2700

2.7.1 SYS2710
The system shall correct for the following environmental noise sources.

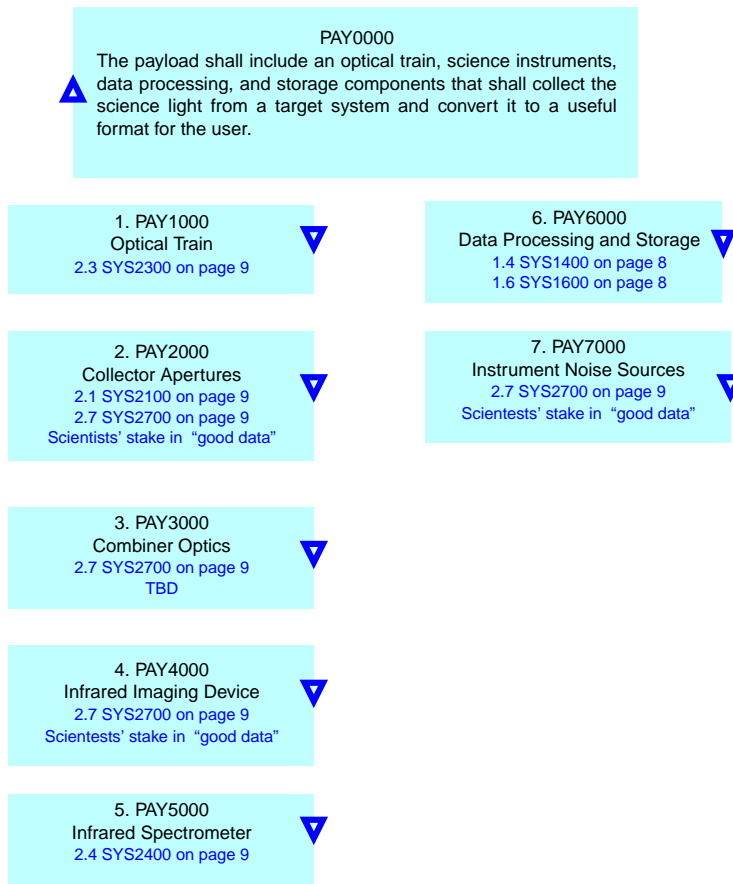
2.7.1.1 SYS2711
Local and Exo-zodiacal dust

2.7.1.2 SYS2712
Thermal disturbances

2.7.1.3 SYS7613
Miscellaneous background noise sources

2.7.1.4 SYS2714
Parent star leakage

System Requirements - Level 2



Payload Requirements Flowdown

Top Level Back Previous Page Next Page Intent and Verification



 1. PAY1000

1.1 PAY1100
The optical train shall have a differential path length control of at least $1/6000$.

 2. PAY2000

2.1 PAY2100
The collector apertures shall not exceed 4.0 m in diameter.

2.2 PAY2200
The collector apertures shall be at least 0.5 m in diameter.

 3. PAY3000

3.1 PAY3100
The combiner optics shall have a wavefront tilt of no more than TBD.

3.2 PAY3200
The combiner optics shall have a differential beam front shear of no more than TBD.

3.3 PAY3300
The combiner optics shall ensure that the difference in amplitude of the light - from the different paths - is within 1 part in 1000.

 4. PAY4000

4.1 PAY4100
The infrared imager shall collect photons from the combined science light into bins on a detector that will synthesize an image based photon count.

4.2 PAY4200
The infrared imager shall have a pixel size less than $30\ \mu\text{m}$ with a $3\ \mu\text{sec/pixel}$ readout time.

4.3 PAY4300
The infrared imager shall have less than 2 electrons per sec of dark current and at least a 50% quantum efficiency.

Payload Requirements Level 2

Top Level



Back



Previous Page



Next Page



Intent and Verification



 5. PAY5000

5.1 PAY5100
The infrared spectrometer shall separate the combined science light into its inherent wavelengths and detect the intensity of the resulting spectrum over the wavelength range.

5.2 PAY5200
The infrared spectrometer shall be tuned to the 7 to 17 μm wavelength range for planet characterization.

 6. PAY6000

6.1 PAY6100
The processing shall detect the signs of a planet from an image and the presence of strong absorption lines from a spectrum.

6.2 PAY6200
There shall be 20GB of memory capacity to store all images and spectra for 7 days, the average time between data downlinks with the ground station.

 7. PAY1000

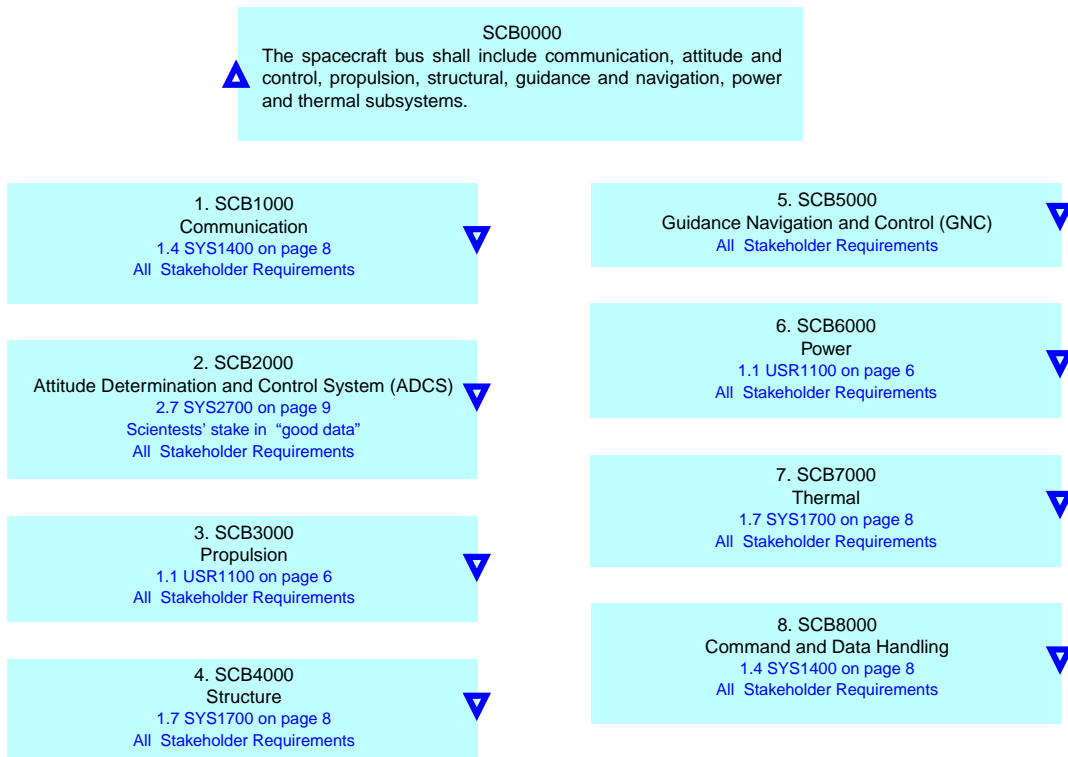
7.1 PAY7100
Digitization of photon energy shall be expected.

7.2 PAY7200
Detector Noise, including thermal distortions and dark current shall be expected.

7.3 PAY7300
Detector quantization shall be expected.

Payload Requirements Level 2

Top Level Back Previous Page Next Page Intent and Verification
    



Spacecraft Bus Requirement Flowdown

Top Level Back Previous Page Next Page Intent and Verification



 1. SCB1000

1.1 SCB1100
The communications system shall receive earth-origin command signals.

1.2 SCB1200
The communications system shall transmit health and status telemetry to its earth control segment at a sufficient data rate, as required by the earth control receiving system and operational tempo, respectively.

1.3 SCB1300
The communications system shall transmit science data at 400 kbps, as required by the earth control receiving system and operational tempo, respectively.

1.4 SCB1400
The communications system shall have a reliability of TBD over the mission nominal life.

Communication System Requirements

 2. SCB2000

2.1 SCB2100
The ADCS shall provide an inertial pointing accuracy of at least 7.5 arcsec during imaging maneuvers.

2.5 SCB2500
The ADCS shall provide attitude control modes as required by the launch, cruise, deployment, and science gathering operational phases.

2.2 SCB2200
The energy of the disturbance torque generated by the ADCS at frequencies greater than 3 Hz shall be less than TBD during imaging maneuvers.

2.6 SCB2600
The ADCS sensors and actuators shall have a dynamic range of at least 60 dB.

2.3 SCB2300
The ADCS shall perform attitude slewing maneuvers at a rate of at least TBD rad/s.

2.7 SCB2700
The ADCS sensors and actuators shall have a bandwidth of at least 3 Hz.

2.4 SCB2400
The ADCS shall provide an emergency safe attitude mode.

2.8 SCB2800
The ADCS shall have a reliability of TBD over the mission nominal life.

Attitude Determination and Control System Requirements

 3. SCB3000

3.1 SCB3100
The propulsion system shall provide the TBD ΔV to reach the TBD science orbit.

3.2 SCB3200
The propulsion system shall contain enough propellant - during the 5 year nominal life - for target reconfigurations and for daily momentum dumping.

3.3 SCB3300
The propulsion system's plume shall not infringe into the FOV of the science payload.

3.4 SCB3400
The propulsion system shall have a reliability of TBD over the mission nominal life.

Note:
The propulsion system parameters are determined by the type of architecture it must support. So, all TBD values will vary with the interferometer type.

Propulsion System Requirements

 4. SCB4000

4.1 SCB4100
The spacecraft structure shall provide orbital debris shielding for the payload and spacecraft subsystems.

4.5 SCB4500
The spacecraft structure shall provide electrical isolation between the spacecraft subsystems and the science payload

4.2 SCB4200
The spacecraft structure shall provide radiation shielding for the onboard electronics.

4.6 SCB4600
The spacecraft structure shall accommodate the dynamic loading and volume constraints of the launch vehicle.

4.3 SCB4300
The spacecraft structure should provide vibration isolation between the spacecraft subsystems and the science payload.

4.7 SCB4700
The structural mass fraction shall not exceed TBD.

4.4 SCB4400
The spacecraft structure should provide thermal isolation between the spacecraft subsystems and the science payload

4.8 SCB4800
The spacecraft structure shall have a reliability of TBD over the mission nominal life.

Structural System Requirements

Top Level Back Previous Page Next Page Intent and Verification
    

 5. SCB5000

5.1 SCB5100
The GNC system shall collect the navigational data input(s) and convert them into a position reference - with a TBD accuracy - for the spacecraft.

5.2 SCB5200
The GNC system shall generate a list of device commands to correct the spacecraft's current coordinates to the desired coordinates.

5.3 SCB5300
The GNC system shall have a reliability of TBD over the mission nominal life.

Guidance Navigation and Control System Requirements

 6. SCB6000

6.1 SCB6100

The power system shall provide continuous power to support the payload and bus activities throughout the nominal mission lifetime.

6.2 SCB6200

The power system shall be physically separated from the payload instruments to prevent contamination.

6.3 SCB6300

The power system shall have a reliability of TBD over the mission nominal life.

6.4 SCB6400

The power system shall provide at least 85% of the beginning of life (bol) power at the end of life (eol).

Power System Requirements

Top Level



Back



Previous Page



Next Page



Intent and Verification



 7. SCB7000

7.1 SCB7100
The thermal system shall maintain the temperature of the infrared imager and spectrometer below 5 (+/- 1) K during science gathering.

7.2 SCB7200
The thermal system shall maintain the temperature of the optical train below 35 (+/- 5) K during science gathering.

7.3 SCB7300
The thermal system shall maintain the temperature of the electronic components between 280 and 320 K for the mission nominal life.

7.4 SCB7400
The thermal system shall not compromise science gathering by outgassing.

7.5 SCB7500
The thermal system shall not radiate heat into the FOV of the science instruments.

7.6 SCB7600
The thermal system shall have a reliability of TBD over the mission nominal life.

Thermal System Requirements

 8. SCB8000

8.1SCB8100
The C&DH system shall gather, process, and format telemetry during standard spacecraft operations for downlink or use by an on-board computer.

8.2 SCB8200
The C&DH system shall interface with the communications subsystem from which it receives commands and to which it sends the formatted telemetry stream.

8.3 SCB8300
The C&DH system shall receive, validate, decode, and distribute commands to the appropriate subsystems.

8.4 SCB8400
The C&DH system shall have a reliability of "TBD" over the mission nominal lifetime.

Command and Data Handling Requirements

OPR0000
▲ The mission operations shall include launch, ground control, cruise, deployment, and science gathering phases.

1. OPR1000
Launch
1.2 SY1200 on page 8
1.7 SYS1700 on page 8 ▼

2. OPR2000
Cruise
1.4 SYS1400 on page 8
'Common Practice' ▼

3. OPR4000
Deployment
1.7 SYS1700 on page 8
'Common Practice' ▼

4. OP4000
Science Gathering
'Common Practice' ▼

5. OPR5000
Ground Control
'Common Practice' ▼

Operational Requirements Flowdown

Top Level Back Previous Page Next Page Intent and Verification
◀◀ ◀ ▲ ▼ ▶▶
- 24 -

 1. OPR1000

1.1 OPR1100
The launch system shall deliver the spacecraft safely to TBD orbit.

1.2 OPR1200
The launch operations staff shall prepare for the contingency of repairing the spacecraft before the cruise phase.

1.3. OPR1300
The launch operations staff shall manage the following activities:

- 1.3.1. OPR1310
Launch configuration
- 1.3.2 OPR1320
Final assembly and alterations
- 1.3.3 OPR1330
Spacecraft and payload verification tests
- 1.3.4 OPR1340
Continuous spacecraft health checks
- 1.3.5 OPR1350
Launch Vehicle separations
- 1.3.6 OPR1360
Configuration for cruise phase

Launch Requirements

 2. OPR2000

The cruise operations staff shall perform the following activities:

2.1 OPR2100

Continuous spacecraft health checks

2.2 OPR2200

Course monitoring / navigation to science orbit

2.3 OPR2300

Insertion to science orbit

Cruise Requirements

Top Level



Back



Previous Page



Next Page



Intent and Verification



 3. OPR3000

The deployment operations staff shall perform the following activities:

3.1 OPR3100
Continuous spacecraft health checks

3.2 OPR3200
Deployment of the appropriate (TBD) payload components

3.3 OPR3300
Initial calibration of the appropriate (TBD) science instruments

3.4 OPR3400
Test operations for the science gathering phase

Deployment Requirements

Top Level


Back


Previous Page

- 27 -

Next Page


Intent and Verification


 4. OPR4000

4.1 OPR4100
A process shall be developed to receive and rank requests for TPF observations.

4.2 OPR4200
A process shall be developed to efficiently schedule and conduct TPF operations.

4.3 OPR4300
A process shall be developed to permanently archive the data for future use.

4.4 OPR4400
A process shall be developed to disseminate science data to researchers and the public.

4.5 OPR4500
Continuous spacecraft health checks shall be performed.

4.6 OPR4600
Anomaly resolution and analysis shall be performed, if necessary.

Science Gathering Requirements

 5. OPR5000

5.1 OPR5100
The ground control support staff shall be adequately trained and informed.

5.2 OPR5200
operations tempo will be designed so that there will be a consistent, reasonable workload for the operations staff.

5.3 OPR5300
The operations software and equipment will be designed for ease of use.

Ground Control Requirements

Top Level


Back


Previous Page


Next Page


Intent and Verification


Requirement ID	Description	Reference Source	Intent	Verification
USR1000	Planet detection and characterization	Origins Roadmap	Science Objective	Useful Images
USR1100	Scope of the science gathering	Chapter 7 - TPF Book	Define scope within mission life	n/a
USR1200	Planet isolation from planet star	Chapter 2 - TPF Book	Specify the use of interferometry for direct planet detection	Useful Images
USF1300	Spectroscopy	Chapter 1 - TPF Book	Specify the use of spectroscopy for planet characterization	Analysis
USR1400	Habitable zone definition	Chapter 2 - TPF Book	Specify where to look for Earth-like planets	n/a
USR1410	Habitable zone specifics	TPF Book	Specify where to look for Earth-like planets	n/a
USR2000	Astrophysical Imaging	Chapter 9 - TPF Book	Science Objective	Useful Images
USR2100	Astrophysical Images of interest	Chapter 8 - TPF Book	Note the the astrophysical images of interest	Analysis
USR2110	Star formation	Chapter 1, 8 - TPF Book	Note interest in star formation	Operations trade
USR2120	Planetary formation	Chapter 1, 8 - TPF Book	Note interest in planetary formation	Operations trade
USR2130	Dying stars	Chapter 1, 8 - TPF Book	Note interest in dying stars	Operations trade
USR2140	Distant starbursts and active galaxies	Chapter 1, 8 - TPF Book	Note interest in starbursts and active galaxies	Operations trade
USR2150	Comets	Chapter 1, 8 - TPF Book	Note interest in comets	Operations trade

Intent and Verification for the Science Requirements

Requirement ID	Description	Reference Source	Intent	Verification
SYS1100	Minimum lifetime	Chapter 1 - TPF Book	Ensures TPF will have ample resources for the primary mission	Modeling & Modules
SYS1200	Operational by 2010	Chapter 1 - TPF Book	Provides target date and motivates work schedule	Schedule Milestones
SYS1300	Lifecycle cost	TBD	Keep program within NASA budget	Budget & Accounting
SYS1400	Communication	n/a - Standard practice	Communicate the data to the scientists	Systems Test
SYS1500	Operational availability	n/a - Systems methodology	Define top level requirement that will drive subsystem availability	Availability Analysis
SYS1600	Software Updates	n/a - Standard practice	Enable upgrades and ensures flexibility in case of partial failure	Upload Tests
SYS1700	Launch and orbit environments	n/a - Standard practice	Prevent damage during the launch phase	Launch Trade
SYS1800	Reliability	n/a - Systems methodology	Define top level requirement that will drive subsystem reliability	Reliability Analysis
SYS2100	Field of view	Derived - USR1210	Specify field of view in order to see the planet light	Analysis
SYS2200	Angular resolution	Chapter 8 - TPF Book	Specify the isolation capability, so we can image up to 15 parsecs	Analysis
SYS2210	Baseline separation	Derived - USR 1300/1100	Specify baseline separation for planets	Payload Trade
SYS2300	Starlight suppression	Chapter 1 - TPF Book	Specify the level of starlight suppression -- to see the planets	Analysis
SYS2400	Infrared range	Chapter 2 - TPF Book	Specify interferometry range for the spectra of interest	Analysis
SYS2500	Spectroscopy	Chapter 9 - TPF Book	Specify the use of spectroscopy to characterize planet atmospheres	Useful spectra
SYS2600	Spectral characterization	Chapter 1 - TPF Book	Specify fine spectroscopy	Analysis
SYS2610	Absorption lines	Chapter 4 - TPF Book	Specify the molecules that may indicate life	n/a
SYS2611	Carbon dioxide spectrum	Chapter 4 - TPF Book	Search for planets with an atmosphere	Analysis
SYS2612	Water spectrum	Chapter 4 - TPF Book	Search for planets with water, believed essential for life	Analysis
SYS2613	Ozone valley	Chapter 4 - TPF Book	Search for planets with a potential for oxygen	Analysis
SYS2614	Methane spectrum	Chapter 4 - TPF Book	Search for planets with "advanced civilization"	Analysis
SYS2615	Carbon Monoxide spectrum	Chapter 4 - TPF Book	Search for planets with potential photosynthetic life	Analysis
SYS2620	Planet characteristics	TBD	Specify the planet's physical characteristics that are of interest	n/a

Intent and Verification for the System Requirements

[Top Level](#)
 [Back](#)
 [Previous Page](#)
 [Next Page](#)
 [Intent and Verification](#)



Requirement ID	Description	Reference Source	Intent	Verification
SYS2621	Size	TBD	Determine the planet's diameter	Analysis
SYS2622	Surface temperature	TBD	Determine the planet's surface temperature	Analysis
SYS2623	Density	TBD	Determine the planet's density or mass	Analysis
SYS2624	Albedo	TBD	Determine the planet's albedo (how well it reflects light)	Analysis
SYS2625	Orbit	TBD	Determine the planet's orbit about its parent star	Analysis
SYS2700	Signal-to-noise ratio	Chapter 6 - TPF Book	Specify the ratio of signal to noise that will result in meaningful data	Analysis
SYS2710	Noise Sources	Chapter 5,6 - TPF Book	Specify expected noise sources	n/a
SYS2711	Local and exo-zodiacal dust	Chapter 5,6 - TPF Book	Note the influence of zodiacal dust in design	Orbit trade
SYS2712	Thermal disturbances	Chapter 5,6 - TPF Book	Note the influence of thermal disturbances	Thermal trade
SYS2713	Astrophysical noise sources	Chapter 5,6 - TPF Book	Note the influence of astrophysical noise	Operations trade
SYS2800	Spectral resolution	Chapter 5 - TPF Book	Specify the spectroscopy operation	Analysis

Intent and Verification for the System Requirements

Requirement ID	Description	Reference Source	Intent	Verification
PAY1000	Optical Train	Derived - 1000 / 2000	Necessary payload component	n/a
PAY1100	Differential pathlength	Stephenson SERC Report	Specify baseline separation for planets versus astrophysical objects	Analysis
PAY2000	Collector Apertures	Derived - 1000 / 2000	Necessary payload component	n/a
PAY2100	Maximum size	Derived - USR1300 / 1310	Maximum aperture necessary to isolate a planet from its parent star	Analysis
PAY2200	Minimum size	Derived - USR1500 / 1600	Minimum aperture based on signal to noise & spectral requirements	Analysis
PAY2300	Combiner Optics	Derived - 1000 / 2000	Necessary payload component	n/a
PAY2310	Differential wavefront tilt	TBD	TBD	TBD
PAY2320	Differential beam front shear	TBD	TBD	TBD
PAY2330	Beam amplitudes	TBD	TBD	TBD
PAY2400	Infrared Imager	Derived - 1000 / 2000	Necessary payload component	n/a
PAY2410	Bins and photon count	Derived - 1000 / 2000	Specify the method for collecting and measuring light	Analysis
PAY2420	Pixel size	TPF TI Spreadsheet	Specify the imager precision	Analysis
PAY2430	Dark current and quantum efficiency	TPF TI Spreadsheet	TBD	TBD
PAY2500	Infrared Spectrometer	Derived - 1000 / 2000	Necessary payload component	n/a
PAY2510	Wavelength separation	Derived - 1000 / 2000	Necessary for spectral analysis, atmospheric analysis	Analysis
PAY2520	Wavelength range	TPF TI Spreadsheet	Defines the wavelength range that contains the relevant data	Analysis
PAY2600	Data Processing and Storage	Derived - 1000 / 2000	Necessary payload component	Analysis
PAY2610	Detection and absorption	Derived - 1000 / 2000	Defines onboard processing expectations	Testing
PAY2620	Storage capacity	Derived - 1000 / 2000	Defines onboard storage expectations - during communication lapses	Testing
PAY2700	Noise sources	TPF TI Spreadsheet	Specify expected noise sources	Payload Trade
PAY2710	Digitization	TPF TI Spreadsheet	Note digitization noise	Payload Trade
PAY2720	Detector noise	TPF TI Spreadsheet	Note detector noise	Payload Trade
PAY2730	Detector quantization	TPF TI Spreadsheet	Note quantization noise	Payload Trade

Intent and Verification for the Payload Requirements

Requirement ID	Description	Reference Source	Intent	Verification
SCB1000	Communication System	n/a	n/a	n/a
SCB1100	Earth originated commands	n/a - Standard practice	Communicate with the spacecraft	Simulation
SCB1200	Power and data rate for telemetry	Derived - Mission lifetime	Send health and status reports as they are needed	Flight Test
SCB1300	Power and data rate for science data	Derived - Gathering Rate	Transmit required science data	Simulation
SCB1400	Subsystem reliability	Derived - Reliability analysis	Ensure the system reliability requirement is met	Analysis
SCB2000	Attitude Determination and Control	n/a	n/a	n/a
SCB2100	Pointing accuracy	Derived - Saturation levels	Meet the required pointing accuracy	Test
SCB2200	Disturbance limit	Derived - Noise rejection of optics	Model disturbance to active optics	Test
SCB2300	Slew rate	Derived - Imaging schedule	Allow pointing over entire celestial sphere	Inspection / Simulation
SCB2400	Safe mode	Derived - Reliability analysis	Be prepared for emergencies, sun referenced	Inspection / Simulation
SCB2500	Launch and transit modes	Derived - Launch/cruise operation	Provide trajectory corrections during cruise	Inspection / Simulation
SCB2600	Dynamic range of equipment	Derived - TBD	Dimension the control layers	Test
SCB2700	Bandwidth of equipment	Derived - TBD	Dimension the control layers	Test
SCB2800	Subsystem reliability	Derived - Reliability analysis	Ensure the system reliability requirement is met	Analysis
SCB3000	Propulsion System	n/a	n/a	n/a
SCB3100	ΔV for science orbit	n/a - Standard practice	Place the spacecraft into orbit	Analysis
SCB3200	Propellant for mission life	Derived - Mission lifetime	Provide fuel for orbit corrections throughout mission	Analysis
SCB3300	Plume infringement	Derived - Physical contamination	Eliminate contaminates that could effect science results	Inspection
SCB3400	Subsystem reliability	Derived - Reliability analysis	Ensure the system reliability requirement is met	Analysis
SCB4000	Structural System	n/a	n/a	n/a
SCB4100	Orbital debris shielding	Derived - Orbit design	Protect instruments against any expected debris	Test / Analysis
SCB4200	Radiation shielding	MIL Specification	Protect against any expected radiation	Analysis / Test
SCB4300	Vibration isolation	Derived - Spatial resolution	Ensure pointing requirements are met	Test
SCB4400	Thermal isolation	Derived - IR detector sensitivity	Eliminate contaminates that could effect science gathering	Test

Intent and Verification for Spacecraft Bus Requirements

SCB4500	Electrical isolation	MIL Specification	Ensure safety and reliability of the bus	Test
SCB4600	Launch load and environment	Derived - Launch Vehicle	Limit structure to volume of launch vehicle fairing	Analysis
SCB4700	Structural mass fraction	Derived - ΔV, Payload Mass	Limit mass fraction of the spacecraft bus	Analysis
SCB4800	Subsystem reliability	Derived - Reliability analysis	Ensure the system reliability requirement is met	Analysis
SCB5000	Guidance Navigation and Control	n/a	n/a	n/a
SCB5100	Position accuracy	Derived - Ideal Trajectory	Ensure pointing requirements are met	Simulation
SCB5200	Device activation for corrections	Derived - Ideal Trajectory	Develop a plan to meet pointing requirements	Simulation
SCB5300	Subsystem reliability	Derived - Reliability analysis	Ensure the system reliability requirement is met	Analysis
SCB6000	Power System	n/a	n/a	n/a
SCB6100	Continuous power	Derived - Payload operations	Ensure the bus and payload are powered	Analysis / Simulation
SCB6200	Shielding	Derived - Payload sensitivity	Eliminate contaminants that could effect science gathering	Inspection
SCB6300	Subsystem reliability	Derived - Reliability analysis	Ensure the system reliability requirement is met	Analysis
SCB6400	End of life power	Derived - Power consumption	Provide energy for end-of-life disposal or extended mission	Analysis
SCB7000	Thermal System	n/a	n/a	n/a
SCB7100	IR temperature	Derived - IR detector sensitivity	Minimize thermal noise in the science instruments	Analysis
SCB7200	Optical train temperature	Derived - IR detector sensitivity	Minimize thermal noise in the science instruments	Analysis
SCB7300	Electronics temperature	MIL Specification	Extend electronics lifetime and reliability	Analysis
SCB7400	Outgassing	Derived - Physical contamination	Eliminate contaminants that could effect science results	Inspection
SCB7500	FOV and heat radiation	Derived - Thermal contamination	Eliminate contaminants that could effect science results	Inspection
SCB7600	Subsystem reliability	Derived - Reliability analysis	Ensure the system reliability requirement is met	Analysis
SCB8000	Command & Data Handling	n/a	n/a	n/a
SCB8100	Telemetry stream format	SMAD	Specify the telemetry stream format	Analysis
SCB8200	Communications commanded	SMAD	Specify the command structure	Analysis
SCB8300	Subsystem Decoder	SMAD	Specify the subsystem, data handling structure	Analysis
SCB8400	Subsystem reliability	Derived - Reliability analysis	Ensure the system reliability requirement is met	Analysis

Intent and Verification for Spacecraft Bus Requirements

Requirement ID	Description	Reference Source	Intent	Verification
OPR1000	Launch Phase	n/a	n/a	n/a
OPR1100	Deliver to orbit	Derived - Launch vehicle	Allow last chance, checkout before cruise phase	Analysis
OPR1200	Opportunity to repair	Derived - Launch vehicle	Allow last chance, checkout before cruise phase	Inspection
OPR1300	Manage tests and configuration	Derived	Define launch management responsibilities	Inspection / Demo
OPR1310	Launch configuration	Derived - Launch vehicle	Define responsibility for different launch possibilities	Inspection / Demo
OPR1320	Final assembly and alteration	Derived - TBD	Allow for in-orbit alterations	Inspection / Demo
OPR1330	Spacecraft and payload verification	Derived - System performance	Evaluate system performance at checkout	Inspection / Demo
OPR1340	Health checks	Derived	Evaluate system functionality	Inspection / Demo
OPR1350	Launch vehicle separation(s)	Derived - Launch vehicle	Ensure proper spacecraft separation	Inspection / Demo
OPR1360	Configuration for cruise	Derived - Cruise phase	Prepare the science equipment during cruise	Inspection / Demo
OPR2000	Cruise Phase	n/a	n/a	n/a
OPR2100	Health checks	Derived	Evaluate system functionality	Demonstration
OPR2200	Course navigation	Derived - Ideal Trajectory	Send course corrections to spacecraft	Demonstration
OPR2300	Insertion into science orbit	Derived - Ideal Trajectory	Complete commands necessary to enter science orbit	Demonstration
OPR3000	Deployment Phase	n/a	n/a	n/a
OPR3100	Health checks	Derived	Evaluate system functionality	Demonstration
OPR3200	Payload deployment	Derived - Payload Requirements	Deploy payload instruments that have been stowed	Demonstration
OPR3300	Initial calibration of payload	Derived - Payload Requirements	Ensure that data collection will be meaningful	Demonstration
OPR3400	Test gathering operations	Derived	Verify end-to-end system operation	Demonstration
OPR4000	Science Gather Phase	n/a	n/a	n/a
OPR4100	Rank science requests	Derived - Science objective	Choose science requests based on set criteria	Demonstration
OPR4200	Efficiently conduct requests	Derived - Science objective	Order science requests without compromising lifetime	Demonstration
OPR4300	Archive of science data	Derived - Science objective	Archive the data for future investigations	Test / Demo
OPR4400	Public relations	Derived - Science objective	Provide the end-users with the data	Test / Demo

Intent and Verification for Operational Requirements

OPR4500	Health checks	Derived	Evaluate system functionality	Demo
OPR4600	Anomaly resolution	Derived - Reliability analysis	Be prepared for emergencies, sun acquisition	Demo
OPR5000	Ground Control	n/a	n/a	n/a
OPR5100	Training and support	n/a - Standard practice	Prepare the staff for efficient operations	Test
OPR5200	Consistent work schedule	n/a - Standard practice	Provide an acceptable work environment / consistent stress	Demo
OPR5300	Software equipment - ease of use	n/a - Standard practice	Minimize operator confusion / training costs	Demo

Intent and Verification for Operational Requirements

[Top Level](#)



[Back](#)



[Previous Page](#)



[Next Page](#)



[Intent and Verification](#)



References

1. Public Website - <http://tpf.jpl.nasa.gov>
2. TPF Book - <http://tpf-lib.jpl.nasa.gov>
3. Origins Roadmap

Acronyms

1. ACDS - Attitude Determination and Control System
2. ASTRO - Architecting the Search for Terrestrial planets and Related Origins
3. BOL - Beginning of Life (Power)
4. EOL - End of life (Power)
5. FOV - Field of View
6. GNC - Guidance, Navigation, and Control
7. JPL - Jet Propulsion Laboratory
8. NASA - National Aeronautics and Space Administration
9. TPF - Terrestrial Planet Finder

[Top Level](#)



[Back](#)



[Previous Page](#)



[Next Page](#)



[Intent and Verification](#)



Appendix B. Results of the Aperture Configuration Module

The results for the different aperture configurations are tabulated below. Note that these results do not include configurations optimized with the aperture size set as a free parameter. In performing the optimization, it was observed that these second set of optimizations (aperture size as free parameter) seems to arrive at solutions with the same aperture size. This may be attributed to the phasing angles that were chosen for the apertures, which seems to make single aperture size configurations more preferential.

Linear Symmetric Arrays – Single Aperture Size

Aper. Num.	Aper. Length L_k (m)	Aper. Angle δ_k (rad)	Aper. Diam (m)	Phase Angle (rad)
1	5	0	1	0
2	5	π	1	2π
3	15	0	1	π
4	15	π	1	3π

Aper. Num.	Aper. Length L_k (m)	Aper. Angle δ_k (rad)	Aper. Diam (m)	Phase Angle (rad)
1	5	0	1	0
2	5	π	1	2π
3	17.5	0	1	$2\pi/3$
4	17.5	π	1	$8\pi/3$
5	32.5	0	1	$4\pi/3$
6	32.5	π	1	$10\pi/3$

Aper. Num.	Aper. Length L_k (m)	Aper. Angle δ_k (rad)	Aper. Diam (m)	Phase Angle (rad)
1	35	0	1	0
2	35	π	1	2π
3	20	0	1	$\pi/2$
4	20	π	1	$5\pi/2$
5	45	0	1	π
6	45	π	1	3π
7	5	0	1	$3\pi/2$
8	5	π	1	$7\pi/2$

Aper. Num.	Aper. Length L_k (m)	Aper. Angle δ_k (rad)	Aper. Diam (m)	Phase Angle (rad)
1	25	0	1	0
2	25	π	1	2π
3	37.5	0	1	$2\pi/5$
4	37.5	π	1	$12\pi/5$
5	47.5	0	1	$4\pi/5$
6	47.5	π	1	$14\pi/5$
7	10	0	1	$6\pi/5$
8	10	π	1	$16\pi/5$
9	57.5	0	1	$8\pi/5$
10	57.5	π	1	$18\pi/5$

Aper. Num.	Aper. Length L_k (m)	Aper. Angle δ_k (rad)	Aper. Diam (m)	Phase Angle (rad)
1	30	0	1	0
2	30	π	1	2π
3	40	0	1	$\pi/3$
4	40	π	1	$7\pi/3$
5	50	0	1	$2\pi/3$
6	50	π	1	$8\pi/3$
7	7.5	0	1	π
8	7.5	π	1	3π
9	60	0	1	$4\pi/3$
10	60	π	1	$10\pi/3$
11	20	0	1	$5\pi/3$
12	20	π	1	$11\pi/3$

Linear Arrays – Single aperture size

Aper. Num.	Aper. Length L_k (m)	Aper. Angle δ_k (rad)	Aper. Diam (m)	Phase Angle (rad)
1	41.25	π	1	0
2	28.75	0	1	π
3	41.25	0	1	2π
4	28.75	π	1	3π

Aper. Num.	Aper. Length L_k (m)	Aper. Angle δ_k (rad)	Aper. Diam (m)	Phase Angle (rad)
1	45.5	π	1	0
2	23	π	1	$4\pi/5$
3	32	0	1	$8\pi/5$
4	42	0	1	$12\pi/5$
5	5.5	π	1	$16\pi/5$

Aper. Num.	Aper. Length L_k (m)	Aper. Angle δ_k (rad)	Aper. Diam (m)	Phase Angle (rad)
1	17.5	0	1	0
2	32.5	0	1	$2\pi/3$
3	45	0	1	$4\pi/3$
4	7.5	0	1	2π
5	5	π	1	$8\pi/3$
6	20	π	1	$10\pi/3$

Aper. Num.	Aper. Length L_k (m)	Aper. Angle δ_k (rad)	Aper. Diam (m)	Phase Angle (rad)
1	30.36	0	1	0
2	27.14	π	1	$4\pi/7$
3	14.64	π	1	$8\pi/7$
4	54.64	π	1	$12\pi/7$
5	7.86	0	1	$16\pi/7$
6	17.86	0	1	$20\pi/7$
7	40.36	0	1	$24\pi/7$

Aper. Num.	Aper. Length L_k (m)	Aper. Angle δ_k (rad)	Aper. Diam (m)	Phase Angle (rad)
1	20	0	1	0
2	32.5	0	1	$\pi/2$
3	55	π	1	π
4	10	0	1	$3\pi/2$
5	7.5	π	1	2π
6	40	π	1	$5\pi/2$
7	65	0	1	3π
8	25	π	1	$7\pi/2$

Aper. Num.	Aper. Length L_k (m)	Aper. Angle δ_k (rad)	Aper. Diam (m)	Phase Angle (rad)
1	19.72	π	1	0
2	57.22	π	1	$4\pi/9$
3	32.22	π	1	$8\pi/9$
4	7.78	0	1	$4\pi/3$
5	45.28	0	1	$16\pi/9$
6	27.78	0	1	$20\pi/9$
7	55.28	0	1	$24\pi/9$
8	17.78	0	1	$28\pi/9$
9	44.72	π	1	$32\pi/9$

Aper. Num.	Aper. Length L_k (m)	Aper. Angle δ_k (rad)	Aper. Diam (m)	Phase Angle (rad)
1	47.5	π	1	0
2	45	0	1	$2\pi/5$
3	15	π	1	$4\pi/5$
4	5	π	1	$6\pi/5$
5	27.5	π	1	$8\pi/5$
6	42.5	0	1	2π
7	57.5	π	1	$12\pi/5$
8	32.5	0	1	$14\pi/5$
9	37.5	π	1	$16\pi/5$
10	55	0	1	$18\pi/5$

Aper. Num.	Aper. Length L_k (m)	Aper. Angle δ_k (rad)	Aper. Diam (m)	Phase Angle (rad)
1	17.5	0	1	0
2	15	π	1	$4\pi/11$
3	50	0	1	$8\pi/11$
4	40	0	1	$12\pi/11$
5	60	π	1	$16\pi/11$
6	5	0	1	$20\pi/11$
7	25	π	1	$24\pi/11$
8	35	π	1	$28\pi/11$
9	5	π	1	$32\pi/11$
10	47.5	π	1	$36\pi/11$
11	60	0	1	$40\pi/11$

Two Dimensional Symmetric Arrays – single aperture size

Aper. Num.	Aper. Length L_k (m)	Aper. Angle δ_k (rad)	Aper. Diam (m)	Phase Angle (rad)
1	15	$\pi/2$	1	0
2	15	$3\pi/2$	1	2π
3	5	0	1	π
4	5	π	1	3π

Aper. Num.	Aper. Length L_k (m)	Aper. Angle δ_k (rad)	Aper. Diam (m)	Phase Angle (rad)
1	15	2.79	1	0
2	15	5.93	1	2π
3	10	1.57	1	$2\pi/3$
4	10	4.71	1	$8\pi/3$
5	5	2.97	1	$4\pi/3$
6	5	6.11	1	$10\pi/3$

Aper. Num.	Aper. Length L_k (m)	Aper. Angle δ_k (rad)	Aper. Diam (m)	Phase Angle (rad)
1	15	1.75	1	0
2	15	4.89	1	2π
3	5	1.05	1	$\pi/2$
4	5	4.19	1	$5\pi/2$
5	15	0.35	1	π
6	15	3.49	1	3π
7	10	2.62	1	$3\pi/2$
8	10	5.76	1	$7\pi/2$

Aper. Num.	Aper. Length L_k (m)	Aper. Angle δ_k (rad)	Aper. Diam (m)	Phase Angle (rad)
1	5	1.57	1	0
2	5	4.71	1	2π
3	30	1.75	1	$2\pi/5$
4	30	4.89	1	$12\pi/5$
5	15	2.27	1	$4\pi/5$
6	15	5.41	1	$14\pi/5$
7	15	1.57	1	$6\pi/5$
8	15	4.71	1	$16\pi/5$
9	25	2.09	1	$8\pi/5$
10	25	5.24	1	$18\pi/5$

Aper. Num.	Aper. Length L_k (m)	Aper. Angle θ_k (rad)	Aper. Diam (m)	Phase Angle (rad)
1	5	2.62	1	0
2	5	5.76	1	2
3	15	1.92	1	$\pi/3$
4	15	5.06	1	$7\pi/3$
5	25	2.44	1	$2\pi/3$
6	25	5.59	1	$8\pi/3$
7	15	2.62	1	
8	15	5.76	1	3
9	15	0.87	1	$4\pi/3$
10	15	4.01	1	$10\pi/3$
11	35	2.27	1	$5\pi/3$
12	35	5.41	1	$11\pi/3$

Two Dimensional Arrays – Single aperture size

Aper. Num.	Aper. Length L_k (m)	Aper. Angle θ_k (rad)	Aper. Diam (m)	Phase Angle (rad)
1	4.75	1.66	1	0
2	10.89	3.33	1	
3	5.29	4.63	1	2
4	11.84	0.22	1	3

Aper. Num.	Aper. Length L_k (m)	Aper. Angle θ_k (rad)	Aper. Diam (m)	Phase Angle (rad)
1	11.56	0.22	1	0
2	10.91	1.90	1	4 /5
3	15.12	2.84	1	8 /5
4	9.32	4.09	1	12 /5
5	15.51	5.60	1	16 /5

Aper. Num.	Aper. Length L_k (m)	Aper. Angle θ_k (rad)	Aper. Diam (m)	Phase Angle (rad)
1	19.89	4.37	1	0
2	30.53	4.05	1	2 /3
3	34.89	4.37	1	4 /3
4	20.20	1.26	1	2
5	30.09	0.90	1	8 /3
6	35.11	1.22	1	10 /3

Aper. Num.	Aper. Length L_k (m)	Aper. Angle θ_k (rad)	Aper. Diam (m)	Phase Angle (rad)
1	41.32	2.98	1	0
2	34.86	5.81	1	4 /7
3	16.62	1.42	1	8 /7
4	27.77	6.21	1	12 /7
5	11.79	0.68	1	16 /7
6	30.27	3.12	1	20 /7
7	13.13	4.77	1	24 /7

Aper. Num.	Aper. Length L_k (m)	Aper. Angle θ_k (rad)	Aper. Diam (m)	Phase Angle (rad)
1	5.59	3.06	1	0
2	1.98	4.47	1	$\pi/2$
3	9.75	2.42	1	
4	22.04	5.56	1	$3\pi/2$
5	33.0	1.85	1	2
6	20.56	5.08	1	$5\pi/2$
7	27.06	1.43	1	3
8	22.09	4.04	1	$7\pi/2$

Aper. Num.	Aper. Length L_k (m)	Aper. Angle θ_k (rad)	Aper. Diam (m)	Phase Angle (rad)
1	13.54	3.32	1	0
2	16.72	5.81	1	$4\pi/9$
3	26.27	1.34	1	$8\pi/9$
4	11.91	4.20	1	$4\pi/3$
5	28.67	1.89	1	$16\pi/9$
6	8.81	0.76	1	$20\pi/9$
7	26.06	4.18	1	$24\pi/9$
8	12.37	2.16	1	$28\pi/9$
9	33.76	5.39	1	$32\pi/9$

Aper. Num.	Aper. Length L_k (m)	Aper. Angle θ_k (rad)	Aper. Diam (m)	Phase Angle (rad)
1	24.85	6.22	1	0
2	28.93	3.84	1	$2\pi/5$
3	32.83	1.20	1	$4\pi/5$
4	8.38	6.03	1	$6\pi/5$
5	20.32	3.61	1	$8\pi/5$
6	47.87	1.42	1	2
7	16.52	5.49	1	$12\pi/5$
8	39.71	3.88	1	$14\pi/5$
9	39.15	0.75	1	$16\pi/5$
10	41.46	4.13	1	$18\pi/5$

Aper. Num.	Aper. Length L_k (m)	Aper. Angle α_k (rad)	Aper. Diam (m)	Phase Angle (rad)
1	16.32	0.97	1	0
2	37.16	3.58	1	4 /11
3	28.25	2.57	1	8 /11
4	8.84	4.34	1	12 /11
5	8.03	0.14	1	16 /11
6	13.48	2.70	1	20 /11
7	42.54	0.45	1	24 /11
8	23.51	4.98	1	28 /11
9	28.21	0.23	1	32 /11
10	16.11	1.61	1	36 /11
11	33.76	4.23	1	40 /11

Appendix C. TMAS N² Diagram

Attached is a fold-out copy of the TMAS N² diagram and a complete table of the variables that were tracked.

TMAS N-Squared Diagram Interface Variabl

MODULE OUTPUTS

	VARIABLE NAME	UNITS	Allowable Range
Design Vector			
	DESIGNVECTOR		
1 - Orbit	orbit	AU	1 AU - 10 AU
2 - # Apertures	NumberApertures	#	4 to 12
3 - Architecture Type	interf_type	SCI, SSI, 1D, 2D, Sym, Non-Sym	
4 - Aperture Diameter	apert_diameter	meters	0.5 m - 4 m
Architecture Constants Vector			
	CONSTANTSVECTOR		Value
1 - Maximum Baseline	max_baseline	meters	120 m
2 - Number of Combiner Payloads	number_combiners	#	1
3 - Mission Design Life	MDL	years	5 years
4 - Science Data Rate	SDR	kbps	400 kbps
5 - SNR for Planet Detection	SNR1		5
6 - Spectral Resolution for Planet Detection	resolution1		3
7 - SNR for Medium Level Spectroscopy	SNR2		10
8 - Spectral Resolution for Medium Level Spectroscopy	resolution2		20
9 - SNR for High Level Spectroscopy	SNR3		25
10 - Spectral Resolution for High Level Spectroscopy	resolution3		20
11 - Wavelength of Interferometer Observation	lambda	meters	12e-6 m
12 - Science Light Beam Diameter	beam_diameter	meters	0.2 m
13 - Radius of Spacecraft Hub	r_hub	meters	2 m
14 - Required Bending Stiffness of Trusses	EI	Nm ²	1.00E+07
15 - Number of Flexible Modes To Be Included in Analysis	flex_modes	#	54
16 - Global Model Damping Ratio	zeta		0.001
17 - Scale Factor for OPD Performance to nm	sc		1.00E+09
18 - Gain at High Frequency for ODL	k_opd		1
19 - Bandwidth for Optical Control	fopd	Hz	100 Hz
20 - Radius of Truss Members for Hub and Combiners	r_bar	meters	0.02 m
21 - Radius of Beam Elements for High Gain Antennas	r_ant	meters	0.01 m
22 - Frequency Vector for Disturbance Analysis	f	Hz	(-3, 3, 1200)
23 - Nominal Reaction Wheel Speed	Ro	RPM	1000
24 - Variation in Reaction Wheel Speed	dR	RPM	1000
25 - PDF for RPM	pdf		Uniform, Gaussian
26 - Number of Reaction Wheels			4
27 - Euler Angles from S/C Axes to Reference Vectors	theta, alpha, gamma	degrees	0, 0, 0
28 - Distance From Each Wheel Frame 0 to Spine	d_wheel	meters	0.5 m
29 - Reaction Wheel Model	model		HST, FUSE, XTE
30 - Scale Factor for RWA Disturbance Magnitude	d_scale		1
31 - Number of Beam Finite Element Trusses	n_elpbay		4
32 - Rho	rho		0.0001
33 - Control Bandwidth	ControlBW		0.1
34 - Performance Bandwidth	PerfBW		1
35 - Rotation Rate	RotationRate		0.001
36 - Maximum CP Deviation	MaxCPDeviation		5
37 - Attitude Determination Bandwidth	AttDetBW		5
38 - Position Scale	PositionScale		0.01
39 - Angle Scale	AngleScale		pi/180/3600
40 - Maximum Number of Modes	MaxNumberOfModes		6
Environment			
	ENV		
1 - Solar Flux	solarflux	W/m ²	
2 - Solar Radiation Pressure	solarpressure	N/m ²	
3 - Gravity Gradient (GM/R ³)	gravitygradient	sec ⁽⁻¹⁾	
4 - Local Zodi Environment	zodiintensity	W/m ² /micron	

5 - Meteoroid Flux meteoroidflux impacts/m²/year

Aperture Configuration

AP_CONFIG

1 - Aperture Location Coordinates

Aper_mat

Matrix Column 1 = aperture number

#

Matrix Column 2 = aperture distance from combiner

m

Matrix Column 3 = aperture angle from combiner

radians

Matrix Column 4 = aperture diameter

m

Matrix Column 5 = delay phasing for nulling

radians

Matrix Column 6 = delay length for wavefront interference)

m

Payload

BUS

1 - Vector of Combiner and Collector Payload Masses

Mpay

kg

2 - Vector of Total Masses of the CD&H and

Mfixed

kg

3 - Vector Average Power Requirements for t

Pafixed

W

4 - Vector of Peak Power Requirements for t

Ppfixed

W

Power

BUS

1 - Power System Type (Solar Array or RTG)

PowerType

2 - Solar Array Power System Masses for All

Mpwr_sa

kg

3 - RTG Power System Masses for All Spacecr

Mpwr_rtg

kg

4 - Solar Array Areas (Vector)

A

m²

5 - RTG Cost

RTGcost

\$millions

6 - Vector of Average Power Requirements fc

AveragePower

W

7 - Vector of Peak Power Requirements for E

PeakPower

W

Thermal

BUS

1 - Total Mass of All Thermal System Components

Total_Thermal_Mass

kg

2 - Total Average Power Required by Thermal System

Total_Thermal_Pow

W

3 - Total Peak Power Required by Thermal System

Total_Thermal_Pow

W

4 - Thermal Mass Distribution Near Bus and

Thermal_Mass_Dist_

kg

5 - Watts Distribution of Power Requirement

Thermal_Power_Dis

W

6 - Watts Distribution of Peak Power Among

Thermal_Power_Dis

W

Propulsion

BUS

1 - Propulsion System Dry Mass

Mpopt

kg

2 - Propulsion System Wet Mass

Mdopt

kg

3 - Total Propulsion System Mass

MpropOpt

kg

4 - Propulsion System Power

Pp

W

Communications

BUS

1 - Transmit Antenna Diameter

Dt

meters

2 - Transmit Antenna Mass

Mt

kg

3 - Transmitter Mass

Mtt

kg

4 - Total Communication System Mass

McomOpt

kg

5 - Minimum Gimbal Distance

gd

meters

6 - Communication System Power

Pc

W

Structure

DOCS

1 - Global Stiffness Matrix

K

N/m

2 - Global Mass Matrix

M

kg

3 - FEM Gridpoint Locations

xyz

meters

4 - Boundary Condition Order Matrix

bco

5 - Element Connectivity Matrix

niall

6 - Total Spacecraft Mass

m_tot

kg

7 - Inertia Matrix wrt CG in s/c Frame

I_tot

kg m²

8 - Overall Deployed x-y-z Envelope

dim_depl

meters

9 - Stowed x-y-z Envelope

dim_stow

meters

10 - Normal Area if Sun Vector = Boresight	sun_area	m ²
11 - Input-Output Grid Points (Incl. Optics)	io_xyz	
12 - Description of IO Grid Points	io_descr	
13 - Short Model Description	model_info	
Truss Design		
1 - Truss Diameter	cmd	meters
2 - System Mass (truss+canister)	m_sys	kg
3 - Canister Mass Fraction	cmf	%
State-Space Plant		
1 - System State-Space Matrix	SYS_p	
2 - Mode-Shape Matrix	phi	
3 - Vector of Natural Frequencies	omeg	radians/sec
Attitude Control		
1 - H2 Control System Design (Plant)	ClPlant_2	
2 - H-Infinity Control System Design	ClPlant_inf	
3 - ADCS Mass	ADCSmass	kg
4 - ADCS Power	ADCSpower	W
Model Integration		
1 - SS System All Control Loops Open	SYS_zw0	
2 - SS System Only ADCS Loop Closed	SYS_zw1	
3 - SS System ADCS and Optics Loops Closed	SYS_zw2	
Performance Assesment		
1 - Dynamics Noise (OPD Delays)	dyn_delays	radians
Orbit Transit		
1 - Departure Delta V	Delta_V_depart	km/s
2 - Arrival Delta V	Delta_V_arrival	km/s
3 - Total Delta V	Delta_V_total	km/s
4 - Flight Time	flighttime	years
Launch		
1 - Launch Vehicle	launch_vehicle	
2 - Launch Cost	launch_cost	\$ Millions
Operations		
1 - Total Operations Cost	Ops_Cost_Total	\$ Millions
2 - Mission Inefficiency	Total_Mission_Ine	Hours/Day
3 - Spacecraft Transit Operations Crew Size	Transit_Crew_Total	people
4 - Spacecraft In-Orbit Checkout Operations	Checkout_Crew_Total	people
5 - Science Operations Crew Size	Science_Crew_Total	people
6 - Annual Operations Facility Maintenance Cost	Maint_Cost_Yearly	\$ Millions
7 - Total Pre-Launch Development Costs	Pre_Launch_Total_C	\$ Millions
8 - Total Post-Launch Operations Costs	Post_Launch_Total_	\$ Millions
Capability		
1 - Single Survey Integration Time in Each State	int_survey	seconds
2 - Single Medium Spectroscopy Integration	int_medspect	seconds
3 - Single Deep Spectroscopy Integration Time	int_deepspect	seconds
4 - Total Time Required to Obtain a Single	statel	seconds
5 - Total Time to Obtain a Single Medium Sp	state2	seconds
6 - Time to Obtain a Single Deep Spectrosc	state3	seconds
7 - Surveys Obtained Per Month in Each State (Vectrate1		images/month
8 - Medium Spectroscopies Obtained Per Month (Vectrate2		images/month

9 - Deep Spectroscopies Obtained Per Month (Vector) rate3 images/month

Performance

1 - Total Number of Surveys Over Mission Life number_surveys_total #
2 - Total Number of Medium Spectroscopies Over Mission Life number_medspect_tot #
3 - Total Number of Deep Spectroscopies Over Mission Life number_deepspect_tot #
4 - Total Number of Images Over Mission Life total_number_images #

Cost

1 - Combiner Payload Cost combiner_payload_cost \$ Millions
2 - Collector Payload Costs (Vector) collectors_payload_cost \$ Millions
3 - Total Payload Cost total_payload_cost \$ Millions
4 - Combiner Bus Cost combiner_bus_cost \$ Millions
5 - Collector Bus Cost (Vector) collector_bus_cost \$ Millions
6 - Total Lifecycle Cost total_lifecycle_cost \$ Millions

Cost Per Function

1 - Cost Per Function Metric (Image) Cost_Per_Image \$ Thousands

Adaptability

1 - Sensitivities %